TECHNISCHE UNIVERSITÄT MÜNCHEN

Fakultät für Physik
Lehrstuhl für Funktionelle Materialien

Magnetic hybrid films based on ultrahigh molecular weight diblock copolymers

Wei Cao

Vollständiger Abdruck der von der Fakultät für Physik der Technischen Universität München zur Erlangung des akademischen Grades eines

Doktors der Naturwissenschaften (Dr. rer. nat.)

genehmigten Dissertation.

Vorsitzende:	Prof. Dr. Andreas Weiler
Prüfer der Dissertation:	1. Prof. Dr. Peter Müller-Buschbaum
	2. Prof. Dr. Menno Poot

Die Dissertation wurde am 09.08.2021 bei der Technischen Universität München eingereicht und durch die Fakultät für Physik am 23.09.2021 angenommen.

Abstract

In the present thesis, magnetic hybrid films composed of ultrahigh molecular weight (UHMW) diblock copolymers (DBCs) and various types of magnetic nanoparticles (NPs) are investigated. The main focus is on the fabrication of superparamagnetic hybrid films for the application as magnetic switches and ferromagnetic hybrid films for the application in magnetic data storage. Small face centered cubic iron platinum (fcc-FePt) NPs are utilized for the hybrid system showing superparamagnetism. The influence of the FePt NPs on the film formation and structure evolution is investigated in situ with grazing-incidence small-angle X-ray scattering (GISAXS). Large iron oxide (Fe_3O_4) NPs are used for the hybrid system showing ferromagnetism. The localization of the large NPs inside the DBC and the corresponding magnetic properties are investigated as a function of the NP concentration. Moreover, ferromagnetic hybrid films with high coercivity above 3000 Oe are obtained by incorporating strontium hexaferrite ($SrFe_{12}O_{19}$) nanoplatelets into the UHMW DBC templates. Such magnetic hybrid film exhibits a perpendicular magnetic anisotropy before solvent vapor annealing (SVA), which is strongly weakened after SVA.

Zusammenfassung

In der vorliegenden Arbeit werden magnetische Hybridfilme aus ultrahochmolekularen (UHMW) Diblockcopolymeren (DBC) und verschiedenen Arten von magnetischen Nanopartikeln (NP) untersucht. Der Schwerpunkt liegt auf der Herstellung von superparamagnetischen Hybridfilmen für die Anwendung in Magnetschaltern und ferromagnetischen Hybridfilmen für die Anwendung in magnetischen Datenspeichern. Für das superparamagnetische Hybridsystem werden kleine kubisch flächenzentrierte Eisenplatin (fcc-FePt) NP verwendet, wobei der Einfluss dieser NP auf die Filmbidung und Strukturentwicklung in situ mittels Röntgenkleinwinkelstreuung unter streifendem Einfall (GISAXS) untersucht wird. Für das ferromagnetische Hybridsystem werden große Eisenoxid (Fe_3O_4) NP verwendet, wobei Lokalisation der NP im DBC und die entsprechenden magnetischen Eigenschaften in Abhängigkeit von der NP Konzentration untersucht werden. Darüber hinaus werden ferromagnetische Hybridfilme mit hoher Koerzitivfeldstärke über 3000 Oe erhalten, indem Strontiumhexaferrit ($SrFe_{12}O_{19}$) Nanoplättchen in die UHMW DBC Template eingebaut werden. Ein solcher magnetischer Hybridfilm zeigt vor der Lösungsmitteldampfbehandlung (SVA) eine senkrechte magnetische Anisotropie, die nach dem SVA stark abgeschwächt ist.

Contents

List of abbreviations

UHMW:	ultrahigh molecular weight
DBC:	diblock copolymer
NPs:	nanoparticles
PS-*b*-PMMA:	polystyrene-*block*-poly(methyl methacrylate)
N:	degree of polymerization
M_n:	number average molecular weight
M_w:	weight average molecular weight
f_B:	volume fraction of B block
c:	concentration
T_g:	glass transition temperature
D_c:	critical diameter of superparamagnetic nanoparticle
M_s:	saturation magnetization
M_r:	remanence
H_c:	coercivity
χ:	susceptibility
B:	external magnetic field
GISAXS:	grazing-incidence small-angle x-ray scattering
DWBA:	distorted-wave Born approximation
SDD:	sample-to-detector distance
R:	domain radius
D:	periodic domain distance
TEM:	transmission electron microscopy
OM:	optical microscopy
SEM:	scanning electron microscopy
AFM:	atomic force microscopy
FFT:	fast Fourier transform
XRR:	X-ray reflectivity
SQUID:	superconducting quantum interference device
SVA:	solvent vapor annealing
THF:	tetrahydrofuran

1 Introduction

Magnetic hybrid polymer films have attracted great research interests in applications such as magnetic sensors, switches and magnetic recording media [1–5]. The hybrid films possess a combined characteristic performance of polymers and magnetic nanoparticles (NPs). Polymers are lightweight, flexible and easy to fabricate while magnetic NPs exhibit controllable magnetic properties [6, 7]. For some applications, precise control over the alignment of the magnetic NPs is essentially required. For example, in magnetic sensors, the alignment of the magnetic NPs has a strong influence on the film's magnetic susceptibility, which is an important parameter of device sensitivity [5, 8]. Moreover, the ability to withstand demagnetization of magnetic recording media is also affected by the alignment of the magnetic NPs [9, 10].

Diblock copolymers (DBCs) have proven to be effective templates for controlling the alignment of magnetic NPs, due to their ability to form various periodic nanostructures, such as lamellae, cylinders and spheres via self-assembly [11–14]. To enhance the affinity of magnetic NPs to the DBC template, surface-modified selective NPs are normally used [15]. Moreover, with specific surface modification, the NPs can be preferentially incorporated inside a designated block of the DBC to achieve a controllable NP arrangement [16,17]. For example, Posocco et al. successfully localized small Fe_3O_4 NPs inside lamellar poly(methyl methacrylate) (PMMA) domains of polystyrene-*block*-poly(methyl methacrylate) (PS-*b*-PMMA) by functionalizing the NP surface with 3-methacryloxypropyltrimetho-xysilane (MPTS) chains [16]. Barandiaran et al. demonstrated that polystyrene-*block*-poly(4-vinylpyridine) (PS-*b*-P4VP) DBC templates with different structures (lamellae and cylinders) can be utilized as templates for the arrangement of small Fe_2O_3 NPs coated with PS chains [17]. Such kind of small magnetic NP-DBC hybrid films appear promising for magnetic sensors and switches. However, previously studied DBC templates are no longer suitable for high loading of small NPs. The low or intermediate molecular weights of the DBC have a microphase separation structure, which is too small to enable high loading with small NPs. The excess small NPs will be expelled from the target domain of the DBC template due to a significant conformational entropy loss of the polymer chains (polymer elastic penalty) associated with accommodating too many small NPs. As a result, well-aligned NP arrays are only available under the low load with NPs, which is an obstacle to

practical future applications. Moreover, the previously studied DBC templates also limit the application of large magnetic NPs in the field of data storage, due to the unfavorable ratio of polymer domain sizes and typical NP diameters.

Using ultrahigh molecular weight (UHMW) DBCs (number average molecular weight, $M_n > 500$ kg/mol) can be an effective approach to achieve a template with large domain sizes (diameters over 80 nm) for high loading of small magnetic NPs and incorporation of large magnetic NPs [18, 19]. However, the fabrication of ordered nanostructured films with UHMW DBCs is challenging. UHMW DBCs do not easily approach thermodynamic equilibrium to form ordered nanostructures because of their highly entangled chain conformations (very low chain mobility) [18]. To enhance the chain mobility and obtain ordered structures, solvent vapor annealing (SVA) is required [20–26]. The final morphology of UHMW DBCs can be tuned by the SVA conditions, such as polymer–solvent interaction parameters, annealing time and temperature [27–30]. Generally, compared to normal molecular weight DBCs with an average molar mass of $M_n < 500$ kg/mol, UHMW DBCs exhibit a very high segregation strength χN (χ: Flory-Huggins interaction parameter, N: total degree of polymerization) between A and B blocks, leading to an extremely large A/B interfacial tension [26, 31]. For the arrangement of magnetic NPs, such interfacial tension is no longer negligible [31]. The localization of NPs in a UHMW DBC template can be expected to be different from previously studied hybrid films formed from normal molecular weight DBC and small NPs. Moreover, the magnetic properties of the hybrid films not only depend on the characteristics of the magnetic NPs themselves, but also on the arrangement and the spatial localization of the magnetic NPs within the DBC template. To achieve a desirable magnetic behavior, it is of high significance to systematically study the hybrid system with UHMW DBCs. For example, the influence of NP concentration and SVA treatment on the DBC morphologies, the localization and alignment of the NPs inside the DBC template, and the kinetics of the magnetic hybrid films formation with different deposition methods should be studied.

In this thesis, magentic hybrid films based on UHMW DBC templates are investigated. The investigations include the self-assembly of the UHMW DBC template, the kinetics of printed superparamagnetic NP-DBC films, localization of large magnetic NPs inside the UHMW DBC template, and the kinetics of ferromagnetic NP-DBC films during spray deposition. The thesis starts with the theoretical background, which includes the basics theory of micro-phase separation of DBC, UHMW DBC, superparamagnetic and ferromagnetic behavior, and the fundamentals of the applied scattering techniques. Then, the characterization methods (structures and magnetic properties) and sample preparation are presented. The results and corresponding discussions are addressed in chapters 5 to 8. An overview of these research topics is shown in Figure 1.1. More details are as follows:

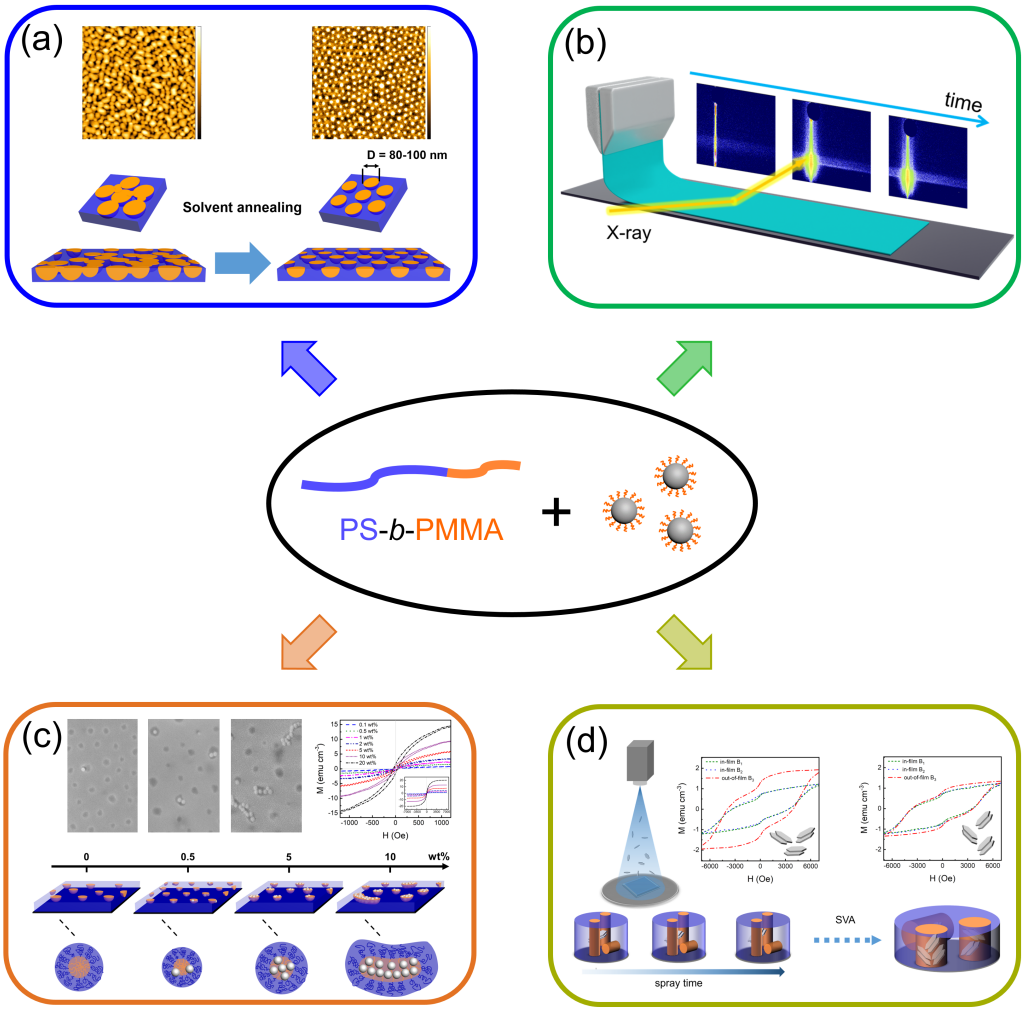

Figure 1.1: *Schematic overview of the research topics in the present thesis. (a) Self-assembly of a UHMW PS-b-PMMA DBC template. (b) Studying the kinetics of superparamagnetic hybrid film formation during printing via in situ grazing-incidence small-angle X-ray scattering (GISAXS) measurements. (c) Investigation on the localization of large magnetic NPs inside the UHMW PS-b-PMMA DBC template with various NP concentration. (d) Studying the kinetics of ferromagnetic hybrid film formation during spray deposition via in situ GISAXS measurements.*

To achieve a desirable template for hosting NPs, it is of great significance to systematically study the dependence of the structure evolution of UHMW DBC thin films on parameters such as film thickness and SVA time. As shown in Figure 1.1 a, an ordered nanostructure with large domain sizes can be achieved by using an asymmetric linear UHMW PS-*b*-PMMA DBC. The ordered nanostructure can be obtained through the control of the film thickness and the SVA time (chapter 5).

Based on the study of pure UHMW DBC thin films, superparamagnetic hybrid film

containing UHMW DBC and superparamagnetic NPs is fabricated for the application of magnetic switches [10]. Also to scale up the fabrication of superparamagnetic hybrid film, printing is applied. In chapter 6 (Figure 1.1 b), the study is focused on the fabrication of magnetic hybrid films with superparamagnetic behavior by printing. UHMW linear DBC PS-*b*-PMMA is used as a template to host small magnetic iron platinum (FePt) NPs with a concentration above 2 wt %. Due to the used UHMW DBC template with large domains, all FePt NPs are positioned inside the PMMA domains without overflow. Moreover, with in situ GISAXS, the kinetics of the UHMW DBC and FePt NPs during printing are investigated. The structure formation in different stages is monitored. As a reference, a pure DBC PS-*b*-PMMA film without magnetic NPs is printed using the same conditions. The scattering data suggest that the addition of NPs accelerates the solvent evaporation, so that the hybrid film exhibits a faster drying speed compared to the pure film. A relatively stable state is formed in both films when the solvent is almost evaporated.

The above printed small-sized magentic NP-DBC hybrid film shows superparamagnetic behavior at room temperature, which allows for a hysteresis-free switching when changing the external magnetic field. However, the absence of a hysteresis at room temperature limits their utilization in data storage. To enable magnetic data storage application, ferromagnetic films are required [32, 33]. Generally, small magnetic NPs are superparamagnetic while large magnetic NPs exhibit ferromagnetism. Thus, large magnetic NPs are used in the UHMW DBC system to prepare hybrid films with ferromagnetic behavior as shown in chapter 7 (Figure 1.1 c). The localization of the large NPs inside the DBC and the corresponding magnetic preoperties are investigated as a function of the NP concentration. At low NP concentrations, the NPs are located preferentially at the interface (between PS and PMMA domains) to minimize the interfacial tension, while they are preferentially located inside the PMMA domains to minimize polymer elasticity penalty at high NP concentrations [31]. Moreover, chain-like NP aggregates are formed inside the films at NP concentrations above 5 wt % and the superconducting quantum interference device (SQUID) data show that the hybrid film containing chain-like NP aggregates shows a weak magnetic anisotropy at an NP concentration of 10 wt %. All hybrid films exhibit ferromagnetic behavior with coercivity of around 50 Oe at room temperature.

To enhance the ability of magnetic hybrid films to withstand an external magnetic field without becoming demagnetized, magnetic films with high coercivity above 1000 Oe are required. In chapter 8 (Figure 1.1 d), strontium hexaferrite nanoplatelets are used as NPs in the magnetic hybrid system because they are hard magnetic materials with high coercivity [34, 35]. Also to enhance the magnetic response ability of hybrid films, it is necessary to obtain films with high thicknesses to have more magnetic NPs at a

fixed NP concentration. Here, instead of printing, spray deposition is applied. Since spray deposition is a layer-by-layer technique, film thickness can be controlled easily. During spray process, the kinetic of structure evolution is investigated by in situ GISAXS measurements. The spray process is operated in a dry-spray regime by the control of the temperature at 170 °C, resulting in a rapid drying of the deposited hybrid films. SQUID data show that ferromagnetic hybrid films with high coercivity are achieved. Moreover, solvent-controlled magnetic properties of the hybrid film are proven with SVA applied to the final deposited magnetic films. The hybrid film shows obvious magnetic anisotropy before SVA, while a weak magnetic anisotropy remains after SVA.

All the findings obtained in this thesis are systematically summarized in chapter 9. These results will pave the way for future development of flexible magnetic hybrid films. Moreover, a short outlook based on the present investigations is also provided for further studies.

2 Theoretical background

In this chapter, the related theoretical basics of diblock copolymers (DBCs), magnetic nanoparticles (NPs) and X-ray scattering techniques are presented. The basic concepts of DBCs, micro-phase separation behavior and ultrahigh molecular weight (UHMW) DBCs are addressed in Section 2.1. Magnetic NPs, ferromagnetic and superparamagnetic behaviors, as well as magnetic anisotropy are discussed in Section 2.2. In the last section, Section 2.3, an introduction to X-ray scattering techniques, especially grazing-incidence small-angle X-ray scattering for the study of inner film structure, is presented.

2.1 Diblock Copolymers

Diblock copolymers are polymers made up of two chemically dissimilar blocks, which are covalently bond with each other [36]. The diblock copolymer can be written as polyA-*block*-polyB and is denoted as PA-*b*-PB. For example, polystyrene-*block*-poly(methyl methacrylate) is denoted as PS-*b*-PMMA. The structure of a diblock copolymer composed of blocks from two different monomers, A and B, is shown in Figure 2.1.

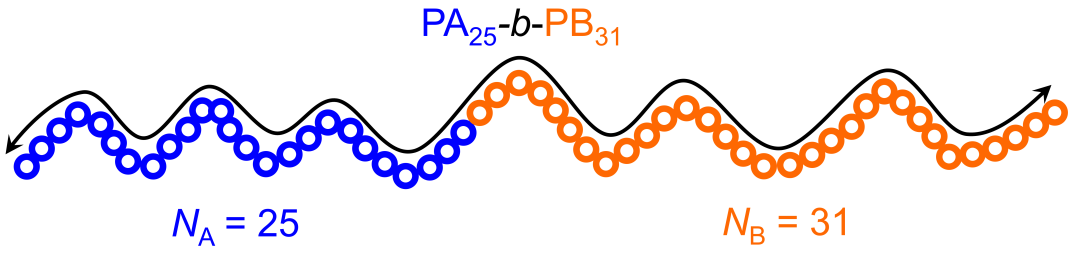

Figure 2.1: *Schematic of a diblock copolymer with blocks of two monomers (A and B). The degree of polymerizations of each block is $N_A = 25$ and $N_B = 31$.*

In Figure 2.1, the total number of repeating units gives the degree of polymerization, N. N can be calculated as the sum of N_A and N_B, where N_A and N_B are the degree of polymerization of the A and B blocks, respectively. To characterize a DBC, two important

average molecular weights are presented, which are the number average molecular weight (M_n) and the weight average molecular weight (M_w). They are calculated as follows

$$M_n = \frac{\sum_i M_i n_i}{\sum_i n_i} \tag{2.1}$$

$$M_w = \frac{\sum_i M_i^2 n_i}{\sum_i M_i n_i} \tag{2.2}$$

where M_i and n_i represent the molecular weight and the number of molecules, respectively. Normally, not all polymer chains in the sample have the same molecular weight due to the statistical polymerization process. However, the chains follow a distribution, which is known as polydispersity (PDI). The PDI can be calculated by

$$PDI = \frac{M_w}{M_n} \tag{2.3}$$

2.1.1 Micro-phase separation

For polymer blends, the phase separation is related to the changes of free energy of mixing, ΔG_m. According to the Flory-Huggins theory [37, 38], ΔG_m can be calculated by

$$\Delta G_m = k_B T n(\frac{f_A}{N_A} \ln f_A + \frac{f_B}{N_B} \ln f_B + f_A f_B \chi) \tag{2.4}$$

where k_B, T and n are the Boltzmann's constant, temperature and number of moles of polymers, respectively. f_A and f_B are the volume fractions of blocks A and B in the DBC. χ represents the Flory-Huggins interaction parameter between polymers A and B, which can be calculated by

$$\chi = \frac{\chi_H}{T} + \chi_S \tag{2.5}$$

where χ_H represent the enthalpic contribution and χ_S represent the entropic contribution. They can be obtained by

$$\chi_H = -T\frac{\partial_\chi}{\partial T} \tag{2.6}$$

$$\chi_S = \frac{\partial}{\partial T}(\chi T) \tag{2.7}$$

For $\chi < 0$, mixing is promoted. In the case of $\chi > 0$, mixing is unfavorable because the entropic contribution is mostly positive.

In equation (2.4), the last term on the right side is the enthalpic contribution and the first two terms are the entropic contribution. The phase separation is related to the value of χN (segregation strength), because the enthalpic term scales with χ and the entropic term with N^{-1}. If the segregation strength is negative or small, mixing is favorable. However, microphase separation occurs to minimize the free energy if the segregation strength is increased above a critical value $(\chi N)_c$. For example, the critical value of the segregation strength for symmetric polymer blends is 2.

However, the Flory-Huggins theory cannot well describe the phase separation behavior of DBCs because the two blocks of a DBC are covalently bonded [36]. Such covalent bond prevents macroscopic demixing in a DBC, resulting in microphase separation. For a symmetric DBC, $(\chi N)_c$ is around 10.5 based on the mean-field theory [36, 39].

For $\chi N < 10.5$, the interactions between polymer blocks are quite weak. The blocks mix and a disordered phase is formed.

For $\chi N \approx 10.5$, a phase transition from disorder to order occurs. However, the segregation strength is still weak. The regime is referred to the weak segregation limit (WSL). The composition profile is approximately sinusoidal as shown in Figure 2.2a, indicating the blocks still mix at the domain interfaces. The domain spacing (D_{wsl}) is scaled as $N^{1/2}$.

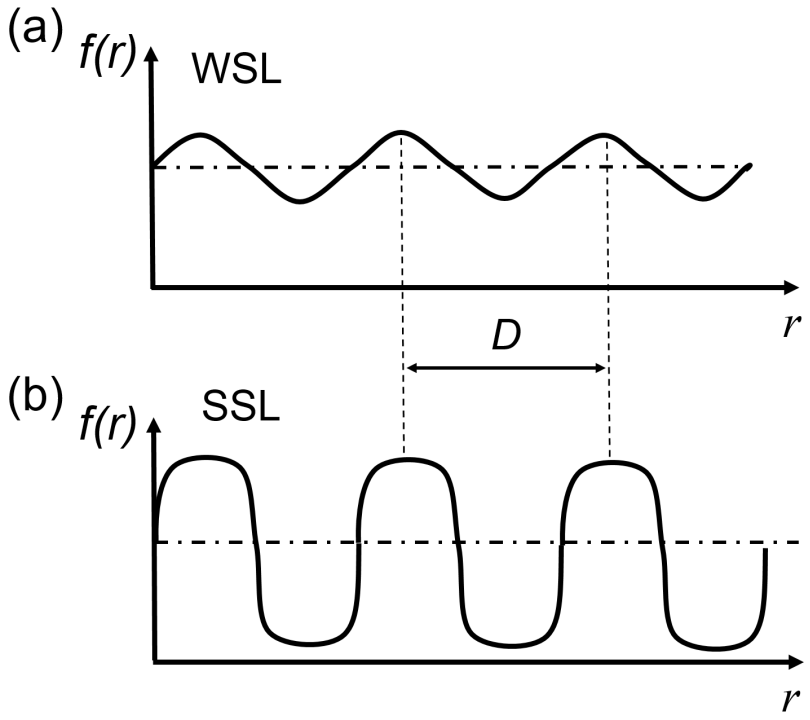

Figure 2.2: *One-dimensional composition profiles in two different limiting regimes: (a) weak segregation limit (WSL) and (b) strong segregation limit (SSL). f(r) and r are the local volume fraction and the distance from an arbitary molecule, respectively. D refers to the domain spacing. The image is adapted with permission from reference [36] Copyright 1990 Annual Reviews Inc..*

For $\chi N \gg 10.5$, the segregation strength is strong and well defined interfaces are formed. In this regime, strong segregation limit (SSL) theory is applied (Figure 2.2b). The domain spacing (D_{ssl}) is scaled as

$$D_{ssl} \sim aN^{2/3}\chi^{1/6} \tag{2.8}$$

where a is the characteristic segment length.

As discussed previously, the microphase separation behavior of a DBC depends on the value of χN. Moreover, the block volume fraction of the used DBC has a strong influence on the type of microphase separation [39, 40]. Thus, the morphologies of DBCs can be predicted by considering the relationship between the combined impact of the block volume fraction and segregation strength according to the self-consistent mean-field theory. A theoretical phase diagram is presented in Figure 2.3.

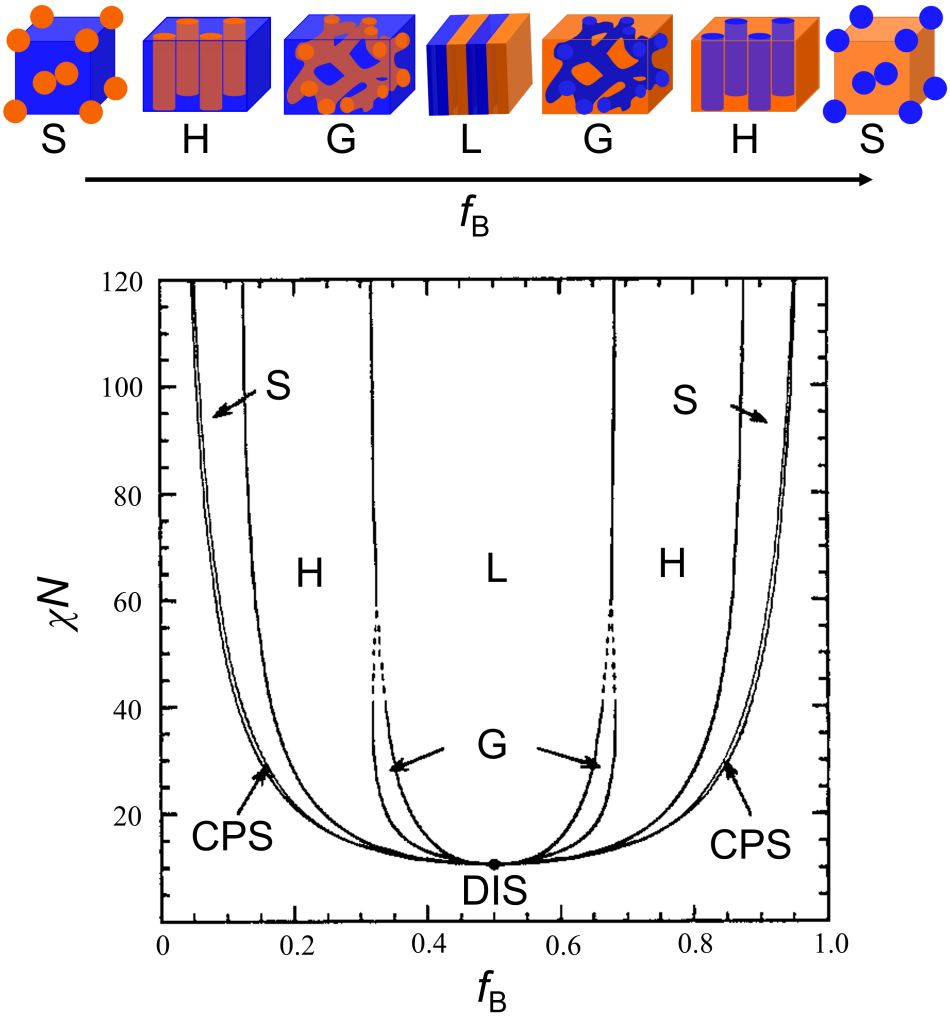

Figure 2.3: *Theoretical phase diagram of DBCs. The image is adapted with permission from reference [39] Copyright 1996 American Chemical Society. DIS: disordered, CPS: close packed spheres, S: body centered cubic spheres, H: hexagonally packed cylinders, G: gyroid, L: lamellae. 3D illustration of the DBC (PA-b-PB) morphologies are depicted above the phase diagram and are adapted with permission from reference [41] Copyright 2006 American Chemical Society. Blocks A and B are colored in blue and orange, respectively.*

As shown in Figure 2.3, a disordered phase is formed at $\chi N < 10.5$, while ordered

morphologies are formed at $\chi N > 10.5$ due to microphase separation. The type of morphology is influenced by the block volume fraction, f_B (volume fraction of B block). For a DBC, PA-*b*-PB, f_B is calculate by

$$f_B = \frac{V_B}{V_A + V_B} \tag{2.9}$$

where V_A and V_B are the volumes of A and B blocks, respectively.

At $f_B < 0.17$, close packed or body centered spheres (S) are formed with B spheres dispersed in a matrix of A blocks. At $0.17 < f_B < 0.30$, hexagonally packed cylinders (H) with B cylinders inside the A matrix are obtained. At $0.30 < f_B < 0.50$, a structure with B gyroid (G) in the A matrix can be achieved. At $f_B \approx 0.50$, lamellae (L) with alternating blocks B and A are formed. With further increasing f_B, the morphologies are similar but inverted, and block B now is the matrix [42].

2.1.2 Diblock copolymer thin films

For applications, DBC thin films are highly required and have gained great interest in bottom-up nanofabrications. The self assembly of DBC thin films is affected strongly by the substrate surface [43–46], and the film thickness effect (associated with the DBC period) [47–50], as well as thermal and solvent vapor annealing conditions [51–55]. Thus, the discussion in this section is mainly focused on the above mentioned factors.

Substrate surface effects

Substrate surface energy and chemistry have strong influence on the self assembly of DBCs and thus on the orientation of the film's morphology (for cylinders and lamellae) [44, 46]. Preferential surfaces encourage the presence of a preferred block at the surface, leading to a segregation of the preferred block to the substrate surface. As a result, the domains are oriented parallel to the film surface. For example, Shin et al. fabricated a lamellar poly(styrene-*block*-isoprene) (PS-*b*-PI) film, which is aligned parallel to the substrate surface even in film thickness of 40 L_0 (inter-domain distance) by using a strongly preferential substrate surface (Figure 2.4a) [45]. In contrast, neutral surfaces allow the presence of two blocks at the surface. Kim et al. modified a substrate surface with PS-*r*-PMMA random copolymers to reduce the interaction difference between each of the two blocks, PS and PEO, and the substrate [56]. Consequently, the cylindrical PEO domains are controlled and align perpendicular to the substrate surface as shown in Figure 2.4c. The sample with a native oxide layer exhibits parallel cylinders with respect to the substrate surface in the film (Figure 2.4b). This behavior can be ascribed to the fact

that the interfacial energy $\sigma_{substrate\text{-}PEO}$ is lower than the interfacial energy $\sigma_{substrate\text{-}PS}$, leading to the segregation of the PEO chains to the substrate surface which then form parallel cylinders.

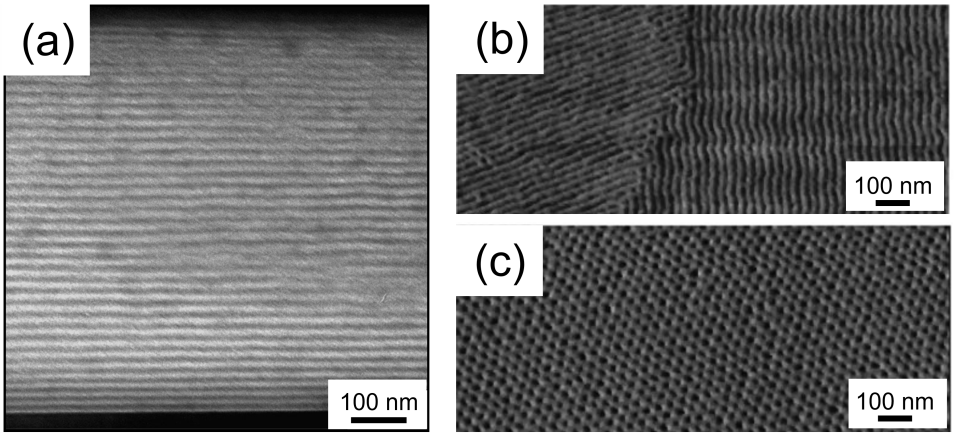

Figure 2.4: *(a) Cross-sectional TEM image of a lamellar PS-b-PI film, which was spin-coated on a PS-modified substrate. The image is adapted with permission from the reference [45] Copyright 2008 American Chemical Society. SFM images of PS-b-PEO films, which were spin-coated on a (b) unmodified substrate and a (c) substrate modified with PS-r-PMMA random copolymers. The images are adapted with permission from the reference [56] Copyright 2008 WILEY-VCH Verlag GmbH & Co. KGaA, Weinheim.*

Film thickness effect

The morphology of the DBC thin film is not only influenced by the substrate surface, but also by the free surface associated with the top surface of the film exposed to air. Two interfaces (substrate/DBC and DBC/air) are presented inside all DBC thin films as shown in Figure 2.5.

A block that exhibits affinity to the substrate surface or free surface wets the corresponding interface, resulting in a preferential orientation of the domains. However, such influences are limited by the film thickness. Literature shows that the DBC morphology is influenced by the relation between the film thickness (t) and inter-domain distance of DBC (L_0) [29, 57, 58].

To illustrate this, the lamellar morphology of a DBC film which can be presented in two regimes is considered.

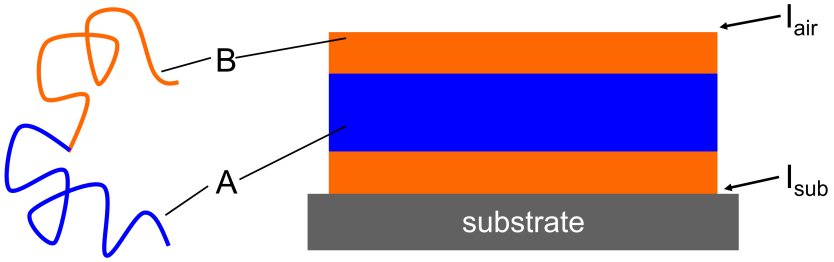

Figure 2.5: *Schematic of a PA-b-PB DBC thin film. Blue and Orange colors correspond to the A and B blocks, respectively. I_{air} represents the DBC/air interface and I_{sub} represents the substrate/DBC interface. The image is adapted with permission from reference [29] Copyright 2002 The American Physical Society.*

(1) At $t \geq L_0$, a parallel asymmetric structure (with respect to the substrate surface) is formed in case two blocks show affinity to opposite interfaces (Figure 2.6a). While a symmetric lamellar structure is supported if one block shows affinity to both interfaces (Figure 2.6b).

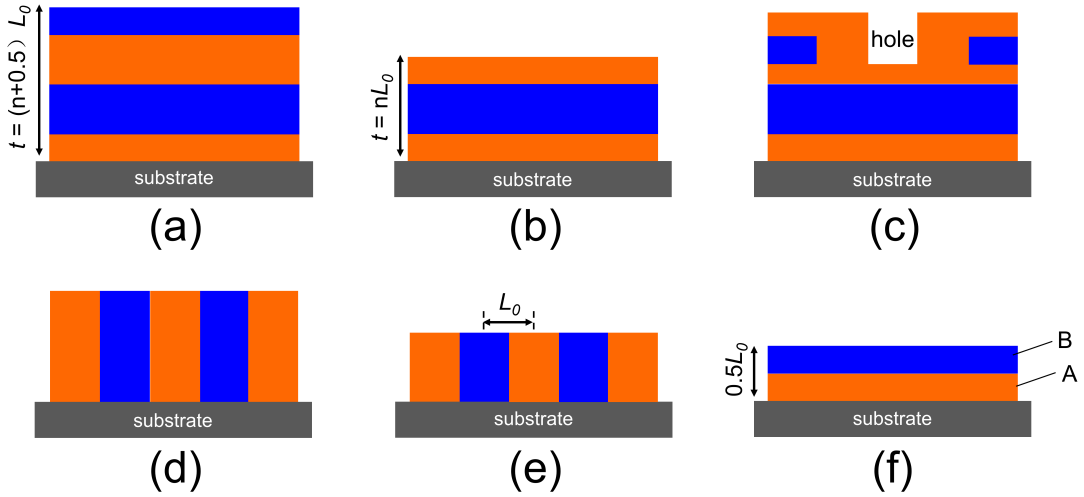

Figure 2.6: *Schematic of the morphology of a lamellar PA-b-PB DBC thin film. Blue and orange colors correspond to the A and B blocks, respectively. The resulting morphology occurs based on the relation between the film thickness (t) and inter-domain distance of the DBC (L_0). For $t \geq L_0$, (a) parallel asymmetric lamellar, (b) parallel symmetric lamella or (c) parallel lamella with defects (holes) can be observed. At $t < L_0$, (e) perpendicular lamella or (f) parallel half-lamella (if $t = 0.5L_0$).*

The morphologies occur since the free energy of the system is minimized by the maximization of the favorable contact [59, 60]. To maximize the conformational entropy of the polymer chains by allowing L_0 to be presented, stable asymmetric and symmetric structures are formed at $t = (n + 0.5)L_0$ (n is an integer) and at $t = nL_0$, respec-

tively [43, 61–63]. However, defects, such as holes, appear on the film surface if the film thickness cannot match the above requirements for t and L_0 (Figure 2.6c). The depth of holes depends on the amount of excess polymers on the surface. If niether of the two blocks have a preferential affinity to the interface, a perpendicular orientation of the lamella is favored (Figure 2.6d) [64].

(2) For $t < L_0$, the parallel lamellar structure with respect to the substrate surface is no longer favored, because a parallel structure would incur entropic penalty and the DBC period L_0 cannot be presented well. However, a perpendicular lamellar structure (with respect to the substrate surface) can satisfy the DBC period L_0 in lateral direction (Figure 2.6e). Thus, the conformational entropy of the polymer chains can be maximized [29, 59, 65]. But for t = $0.5L_0$, a parallel half-lamellar structure is favorable [58]. As shown in Figure 2.6f, A block aggregates at the substrate surface while B block is attracted to free surface. In this case, a parallel half-lamellar structure is supported to reduce the unfavorable contact between the two immiscible blocks. Moreover, the period size can be achieved.

For a DBC film with a cylindrical morphology, the effect of the film thickness is similar to that of the lamellar morphology as discussed above. The orientation of cylinders changes with a change in the film thickness [66]. However, DBCs with a spherical morphology, the film thickness primarily influences the packing arrangement of spheres in the DBC system [48, 50, 67]. Hexagonal (HEX) symmetry is stable in the monolayer, while body-centered cubic (BCC) symmetry is preferred for thicker films [67]. HEX and BCC symmetries are presented in Figure 2.7.

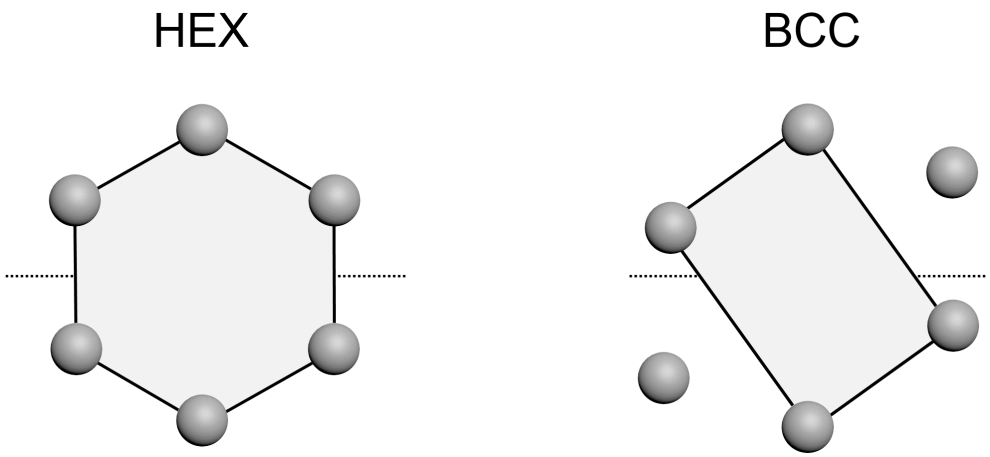

Figure 2.7: *Schematic of the packing arrangement of spheres in the DBC system. The images are modified with permission from the reference [67] Copyright 2007 The American Physical Society.*

The correlation between packing arrangement and film thickness can be attributed to the competition between interfacial and stretching energies. The interfacial energy is minimized though uniform interfacial curvature, while the stretching energy is minimized when the extension of the polymer chains is uniform [67]. For example, Stein et al. studied the packing of sperical DBC as a function of the number of layers (n) based on the self-consistent field theory (SCFT) [67]. For films with 1-3 layers, HEX symmetry is observed. The HEX symmetry is preserved when n increases to 4 and is broken at n = 5. At a higher n, a BCC symmetry is favorable.

Thermal and solvent vapor annealing conditions

Thermal annealing is a common approach utilized to enhance the structural order of DBC. The mobility of the polymer chains can be increased with thermal annealing, so that the DBC can easily approach thermodynamic equilibrium to form ordered structures by microphase separation [68–71]. Moreover, thermal annealing also can be utilized to tune the surface properties of a DBC thin film. For example, Han et al. studied the surface morphology of a PS-*b*-PMMA film with a thickness of 175 nm at different annealing temperatures [44]. They found that a neutral free surface could be obtained for the PS-*b*-PMMA film at an annealing temperature of 230 °C. As shown in Figure 2.8, fewer parallel cylinders appear on the surface as the temperature increases. Finally, at 230 °C, all the cylinders are aligned perpendicularly on the top surface (Figure 2.8c).

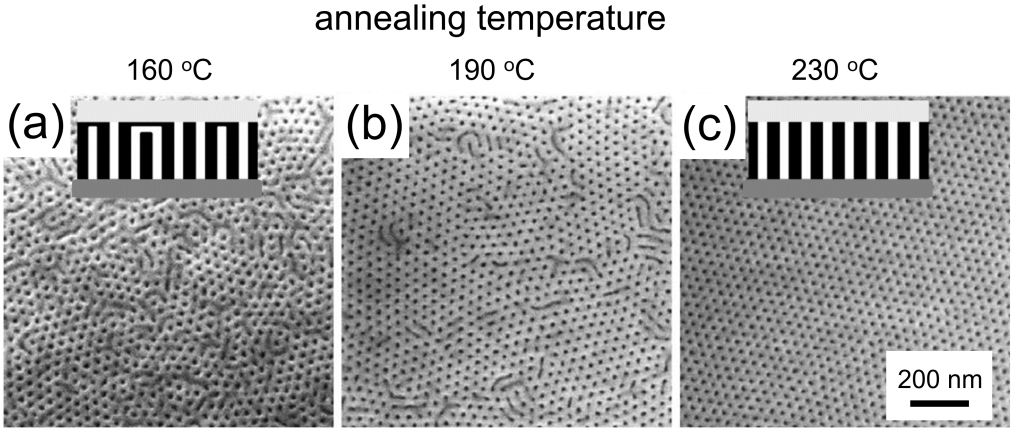

Figure 2.8: *SEM images of a cylindrical PS-b-PMMA film with a thickness of 175 nm at different annealing temperatures. The annealing temperatures are indicated on the top of each image. The images are modified with permission from the reference [44] Copyright 2009 American Chemical Society.*

Solvent vapor annealing (SVA) is also an effective method to achieve a desired morphology within a DBC film [52, 72–75]. Here, the discussion of SVA is mainly focused on three

parameters: solvent selection, annealing time and solvent removal rate. The selection of the solvent has a strong influence on the final morphology of the DBC film [73, 76]. For example, Xuan et al. studied the morphology of a DBC PS-*b*-PMMA film after SVA with different solvents, including acetone and toluene [76]. An ordered morphology with hexagonally packed PMMA domains in a PS matrix (Figure 2.9a and b) is obtained for the film annealed with acetone (strongly PMMA selective), while the film annealed with toluene (slightly PS selective) exhibits a morphology with small PMMA protrusions (Figure 2.9c and d). This can be attributed to the fact that the free surface preference for the lower surface energy PS block could be overcome by applying a solvent (acetone) that prefers the PMMA block [76].

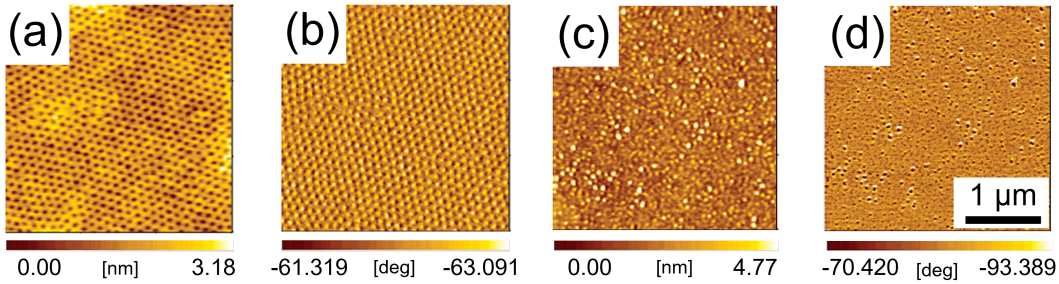

Figure 2.9: *AFM height images of PS-b-PMMA films annealed with (a) acetone and (c) toluene vapors. (b) and (d) are the corresponding phase images of (a) and (c), respectively. The images are modified with permission from the reference [76] Copyright 2004 American Chemical Society.*

A suitable annealing time is required for the formation of ordered morphologies in DBC systems [77]. If the applied annealing time is not long enough, the rearrangement of polymer chains into ordered structures cannot be readily realized [23]. Normally, the structure order of the DBC can be enhanced with longer annealing time to achieve thermodynamic equilibrium for obtaining ordered structures by microphase separation. However, in some cases, too long annealing time is not helpful for generating ordered structures [77, 78]. This might be due to the dynamic change of interfacial interactions caused by the continual solvent absorption [77]. For example, Kim et al. studied the surface morphology of a lamellar PS-*b*-PMMA film annealed with tetrahydrofuran (THF) for various times [51]. They found that the ordering of the lamellae is enhanced with increasing the annealing time during the early stage (Figure 2.10a-d). However, there is a significant loss in the ordering of the DBC structure when the annealing time is increased to 60 min and longer (Figure 2.10f and g), because the film might got unstable and dewet.

The solvent removal rate is the rate of solvent extraction from the DBC films after the SVA process. Literature shows that the structure orientation of DBCs can be influenced

by the solvent removal rate [79–81]. In cylinder-forming DBC systems, perpendicular cylinders are normally formed if the solvent removal rate is high, while a low solvent removal rate leads to the formation of parallel cylinders in DBC films [77]. For example, Hao investigated the influence of solvent removal rate on the morphology of a cylindrical DBC film using lattice Monte Carlo simulations [82]. It was found that the perpendicular structure tends to form at a high solvent removal rate, because the solvent removal rate dominates the relaxation time of the DBC system. A low rate allows time for the adequate relaxation of the system, and the morphology, such as orientation, formed in the early stage of SVA can be changed through a rearrangement of the polymer chains. In contrast, at a high solvent removal rate, the morphology can be maintained because the relaxation of the DBC system is insufficient and film morphology is frozen.

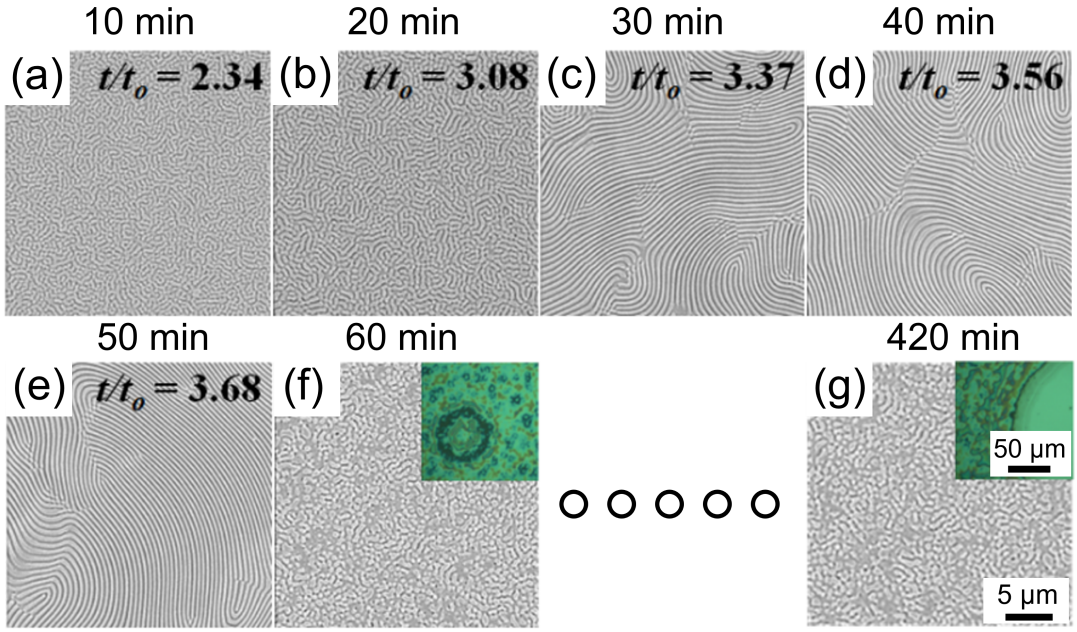

Figure 2.10: *SEM images of a lamellar PS-b-PMMA film annealed with THF at different times. The annealing times are indicated on the top of each image. t/t_0 is the swelling ratio of the PS-b-PMMA film during SVA. The images are modified with permission from the reference [51] Copyright 2016 American Chemical Society.*

2.1.3 Ultrahigh molecular weight (UHMW) diblock copolymers

DBCs form different periodic structures such as lamellae, cylinders and spheres due to microphase separation and they have proven to be suitable templates for the arrangement of various NPs [31, 83–85]. For the incorporation of selective NPs into a DBC PA-*b*-PB template, literature shows that there are three competing effects [31]. First is the

reduction of AB interfacial tension between the polymer blocks by localization of the NPs at the AB interface. Second is the enthalpic gain arising from the localization of the NPs in the target domains. The final effect is the decreases of polymer elastic penalty arising from the localization of the NPs in the center of the target domains. The first two effects scale with R^2 while the last effect scales with R^3, where R is the radius of the NPs. Thus, small and medium NPs are located at the interface between the A and B blocks and the center of target block B, respectively (Figure 2.11a and b). Large NPs are expelled from the target domain (A block) as shown in Figure 2.11c, because such DBC templates cannot provide enough space in a domain to accommodate such particles. [84]. Expulsion is due to the fact that the incorporation of large NPs in a domain causes a significant conformational entropy loss of the polymer chains. Thus, templates from normal molecular weight DBCs are not suitable for large NPs. Moreover, the normal templates are also not suitable for high loading of small or medium NPs. To address this limitation, DBC templates with large domains, such as those achieved with ultrahigh molecular weight (UHMW) DBCs, should be utilized.

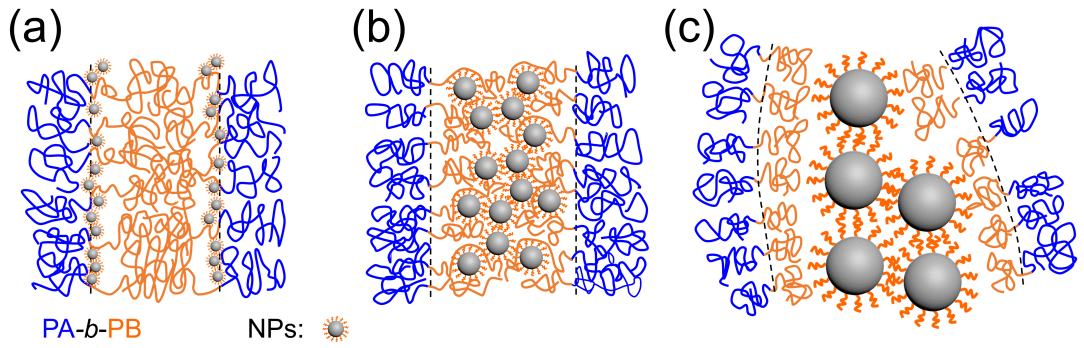

Figure 2.11: *Position of the NPs inside a DBC template depending on the NP size. (a)Small NPs are located at the interface between the A and B blocks. (b)Medium-sized NPs are located in the center of the A block. (c)Large NPs are expelled from the target domain (B block).The images are modified with permission based on the reference [83] Copyright 2004 American Chemical Society.*

UHMW DBCs are DBCs that have a number average molecular weight (M_n) greater than 500 kg/mol [18, 19]. Nanostructures with large domain sizes (diameters over 80 nm as shown in Figure 2.12) can be realized and are convenient for the incorporation of large NPs, as well as high load of small NPs [86, 87]. However, the fabrication of ordered nanostructured films with UHMW DBCs is challenging. UHMW DBCs do not easily approach thermodynamic equilibrium to form ordered nanostructures because of their highly entangled chain conformations. To enhance the chain mobility and obtain ordered structures, a post-treatment, such as SVA, is required [20–22, 25].

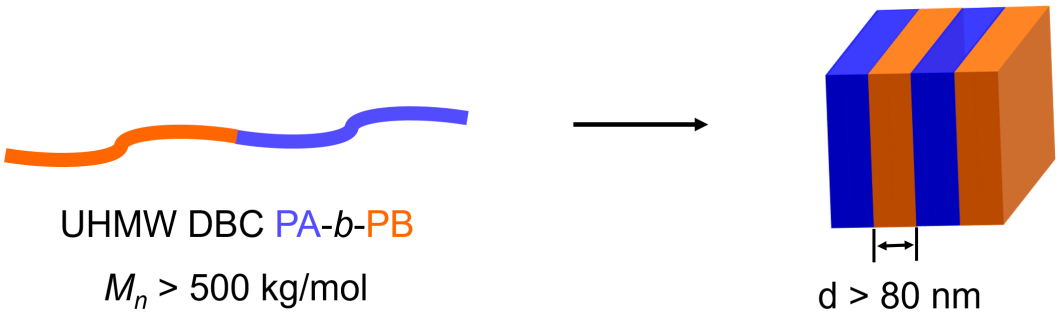

Figure 2.12: *Schematic of fabricating large domain sized nanomaterial from a UHMW DBC (PA-b-PB).*

Kim et al. fabricated highly ordered lamellar PS-*b*-PMMA films with large domains by using a SVA process as shown in Figure 2.13 [88]. For a thermally annealed UHMW DBC PS-*b*-PMMA film (M_n = 733 kg/mol), disordered structures are observed without SVA as shown in Figure 2.13a and e (an enlarged view of Figure 2.13a), while ordered lamellar structures were achieved after SVA for 1.5 h, as shown in Figure 2.13b and f (an enlarged view of Figure 2.13b).

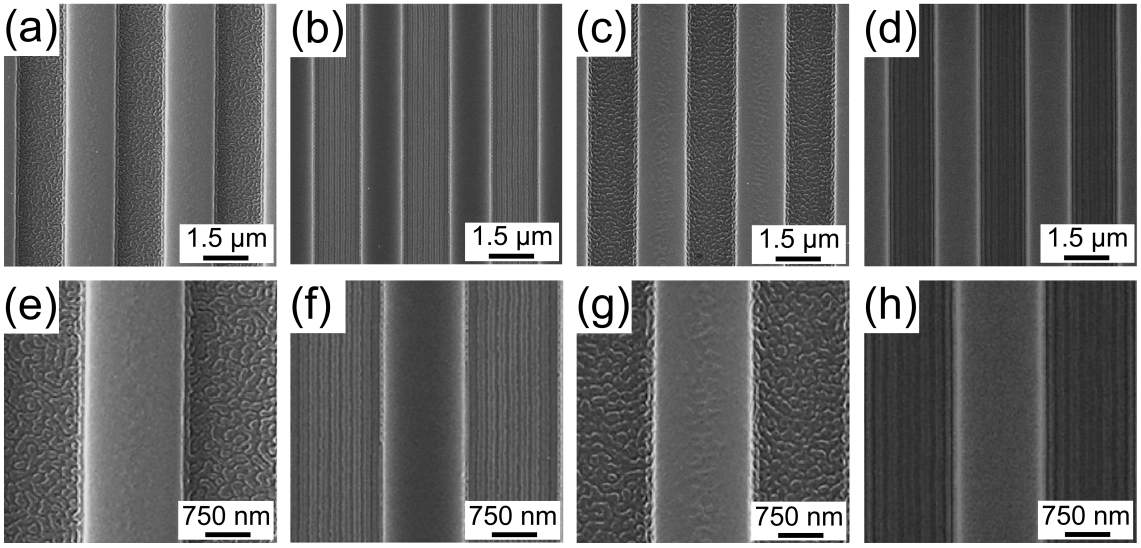

Figure 2.13: *SEM images of lamellar UHMW PS-b-PMMA films in the topographic confinement. Thermally annealed PS-b-PMMA film with M_n of 733 kg/mol (a,e) without and (b,f) with SVA of 1.5 h. Thermally annealed PS-b-PMMA film with M_n of 1000 kg/mol (c,g) without and (d,h) with SVA of 10 h. The images are modified with permission from the reference [88] Copyright 2013 American Chemical Society.*

For a thermally annealed UHMW DBC PS-*b*-PMMA film with higher M_n (1000 kg/mol), disordered structures are present without SVA (Figure 2.13c and g). However, compared

to the film with M_n of 733 kg/mol, a longer annealing time (10 h) is required to obtain ordered structures for the film with a higher M_n. Since the rearrangement of the PS-*b*-PMMA is hindered more severely with increasing molecular weight, longer annealing time is required.

Like normal molecular weight DBCs, UHMW DBCs can also form various periodic morphologies through manipulation of the volume fraction of one block in the DBC system. For example, Appold et al. reported the fabrication of UHMW DBC polyisoprene-*block*-poly(4-methylstyrene) (PI-*b*-P4MS) films with different morphologies (cylinders and spheres) as shown in Figure 2.14 [89].

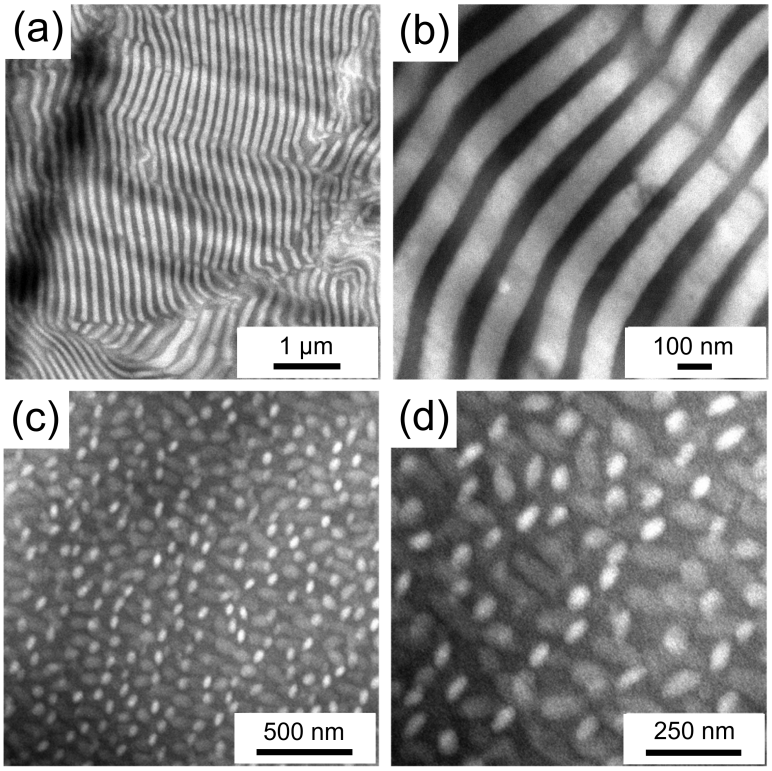

Figure 2.14: *TEM images of UHMW PI-b-P4MS films with different values of f_{P4MS} that show (a,b) lamellar and (c,d) spherical morphologies at different magnifications. The images are modified with permission from the reference [89] Copyright 2018 American Chemical Society.*

At a volume fraction of P4MS (f_{P4MS}) of 0.5, a lamellar morphology is observed in the DBC film (Figure 2.14a and b). However, the DBC film exhibits a spherical morphology at $f_{P4MS} = 0.14$ (Figure 2.14c and d). The domain sizes are greater than 90 nm in the above mentioned DBC PI-*b*-P4MS films.

2.2 Magnetic Nanoparticles

Magnetic nanoparticles (NPs) with diameters (D) ranging from a few to tens of nanometers have attracted great interest in applications such as catalysis, biomedicine, sensors and data storage due to their intriguing size dependent magnetic properties [5,90–93]. As described in the introduction, DBCs are utilized in this work as templates to control the arrangement of magnetic NPs in order to achieve desirable magnetic properties. However, the magnetic properties of the magnetic NPs-DBC hybrid films are still strongly depend on the the NPs themselves. Thus, it is of high significance to describe the properties of magnetic NPs, as well as some basic terms in this chapter.

2.2.1 Superparamagnetism and Ferromagnetism

Magnetic NPs exhibit intriguing size-dependent magnetic properties [94,95]. Figure 2.15 shows the schematic of size-dependent coercivity (H_c) of a magnetic NP. The value of coercivity represents the ability of a magnetic material to withstand an external magnetic field without becoming demagnetized. As shown in Figure 2.15, the magnetic NP acts as a single-domain magnet at $D < D_c$ (a certain critical size). In this case, the spins of free electrons in the NP are arranged in one direction by ferromagnetic coupling. For $D > D_c$, the NP exhibits multi-domain. D_c for a spherical magentic NP can be estimated by

$$D_c \approx 9\frac{\sqrt{AK}}{\mu_0 {M_s}^2} \tag{2.10}$$

where A, K and u_0 represent the exchange constant, effective anisotropy constant and vacuum permeability, respectively. M_s is the saturation magnetization.

Superparamagnetism

For a magentic NP with multiple domains, the alignment of magnetization directions in each domain is controlled by the domain wall energy and anisotropy energy KV (V is the domain volume). However, there is no domain wall for a NP with a single domain [96,97]. Thus, magnetization reversal of a single domain NP depends on KV. The magnetic anisotropy energy (E) of the single-domain NP is defined as

$$E = KV \sin^2\theta \tag{2.11}$$

where θ is the angle between the direction of magnetization ($\vec{M}$) and easy axis. The easy axis is the easy magnetization direction of a single domain magnetic NP. As shown in Figure 2.16, two energy minimums can be obtained at $\theta = 0$ and π, corresponding to the magnetization parallel and antiparallel to the easy axis. From parallel direction ($\theta = 0$) to antiparallel direction ($\theta = \pi$), the magnetization is separated by an energy barrier, described as $\Delta E = KV$. The flip behavior can be explained by Néel based on the competition between the anisotropy energy KV and the thermal energy k_BT [98], where k_B and T are the Boltzmann constant and temperature, respectively.

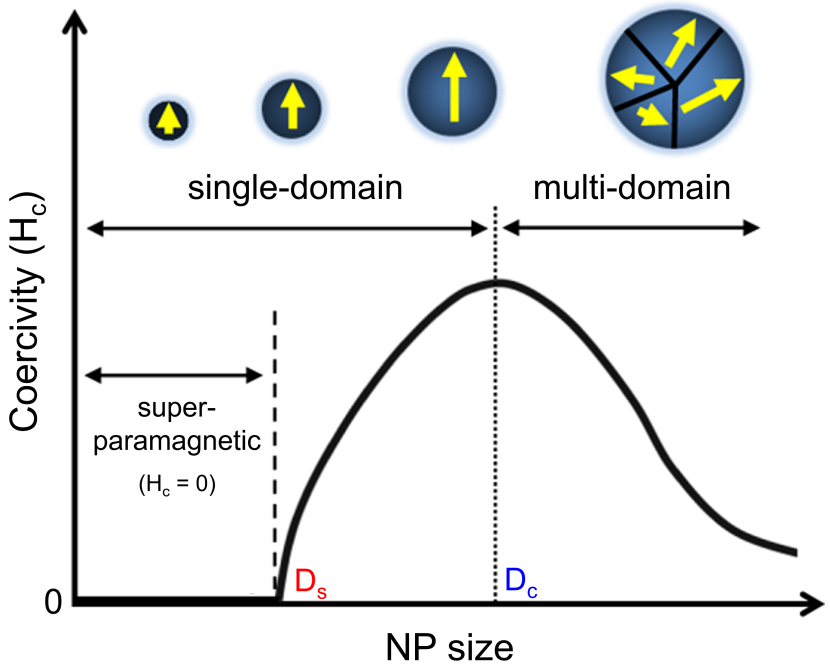

Figure 2.15: *Schematic of size-dependent coercivity (H_c) of a magnetic NP. D_c and D_s represent the size of magnetic NP reaching the single domain limit and spontaneous magnetization reversal limit, respectively. The image is modified with permission from reference [95] Copyright 2016 American Chemical Society.*

As the single domain NP size decreases further to a critical value D_s, the thermal energy k_BT overcomes the anisotropy energy KV [95]. As a result, a spontaneous magnetization reversal happens in the magnetic NP system at $D_c < D_s$, leading to the NP exhibiting superparamagnetic behavior. At $k_BT \approx KV$, the magnetization fluctuation between the two energy minima is related to the time scale of the measurement and can be described with a characteristic relaxation time (τ). According to the Néel-Brown equation [98], τ can be obtained by

$$\tau = \tau_0 \exp\left(\frac{KV}{k_BT}\right) \tag{2.12}$$

where $\tau_0 \sim 10^{-10}$ s is the inverse attempt frequency. Obviously, the magnetic behavior of the NPs is influenced strongly by the temperature T.

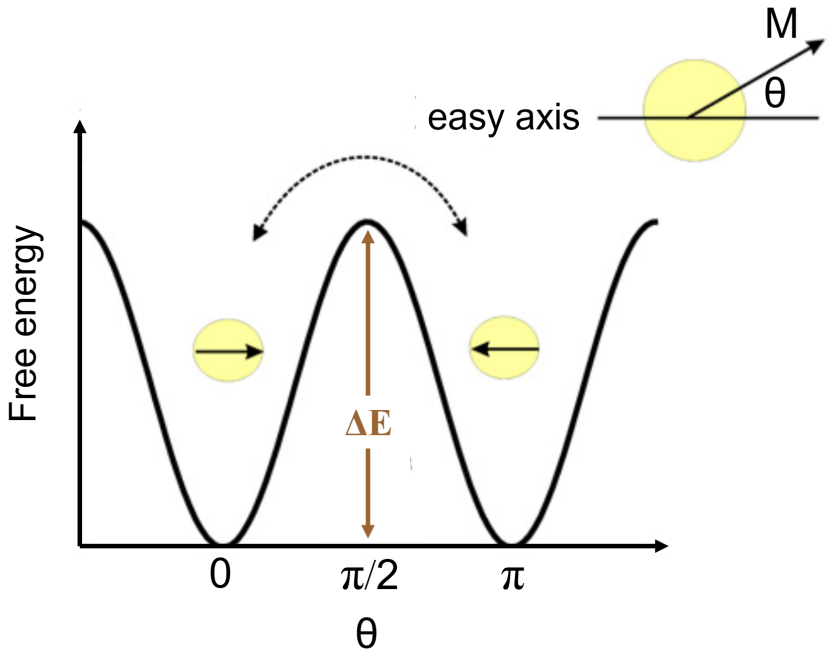

Figure 2.16: *Schematic presenting the free energy of a single domain NP versus magnetization direction. ΔE is the energy barrier for rotating the magnetization. θ is the angle between the magnetization $\vec{M}$ and the easy axis. The image is modified with permission from reference [97] Copyright 2009 IOP Publishing Ltd.*

In the system of superparamagnetic NP, a characteristic blocking temperature (T_B) exists [99]. At $T < T_B$, the magnetic moments are blocked and a hysteresis loop can be observed. With increasing T, the hysteresis loop becomes narrower and at $T > T_B$, the thermal energy is enough to overcome the anisotropy energy, leading to a spontaneous flipping of magnetic moments. As a result, the hysteresis disappears, as shown in Figure 2.17. T_B can be calculated by

$$T_B = \frac{KV}{k_B \ln(\tau_m/\tau_0)} \tag{2.13}$$

where τ_m is the experimental measuring time. Equation 2.13 is only valid for a NP system without interaction between NPs and size distribution.

As mentioned above, in the case of $T > T_B$, the magnetic moments fluctuate fast and cannot maintain their orientation. This leads to a spontaneous magnetization reversal of the NP in the absence of an external magnetic field (2.17a). When an external magnetic field is applied, the magnetic moments are aligned parallel to the direction of the magnetic field (Figure 2.17b). In a superparamagnetic system, coercivity (H_c) and remanence (M_r)

are 0. M_r is the remanent magnetization that remains after the magnetic field is removed. Such behavior can be applied for use in high-frequency magnetic inductors, because the energy loss that occurs then changing the direction of magnetic field with high frequency could be minimized by employing superparamagnetic materials [87].

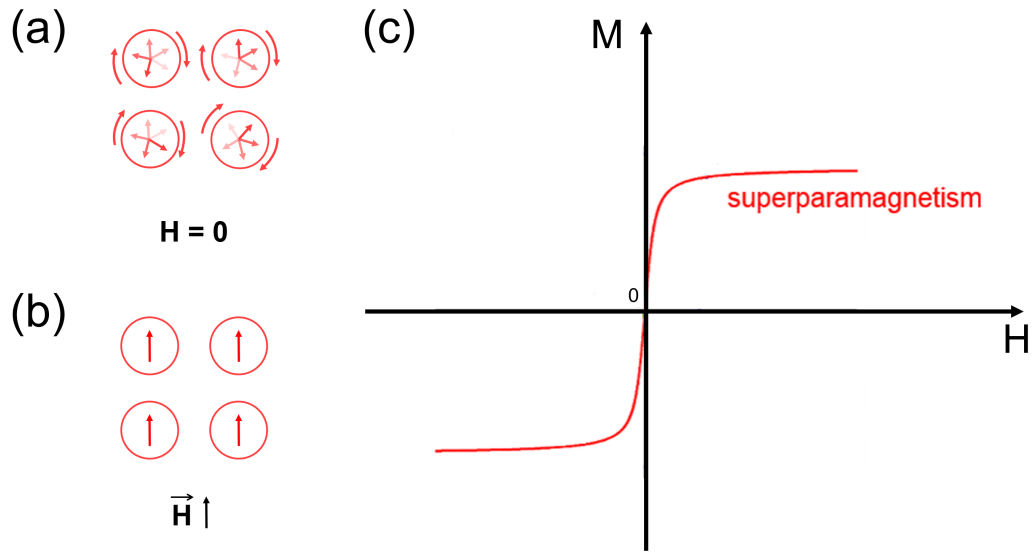

Figure 2.17: *States of the magnetic moments in domains of superparamagnetic materials (a) without and (b) with an external magnetic field. The black arrow in (b) indicates the direction of the magnetic field. (c)The M-H curve of a superparamagnetic material.*

Ferromagnetism

For application in data storage, superparamagnetic materials are not favorable due to the absence of a hysteresis at room temperature, while ferromagnetic materials are favorable because the hysteresis of ferromagnetic material exists at room temperature [32, 87]. In a ferromagnetic materal with multiple domains, the magnetic moments are oriented in one direction for each domain without an external magnetic field. However, the net magnetization of the material is zero as the orientation of the magnetic moments in different domains are randomly oriented with respect to each other (Figure 2.18a). When an external magnetic field is applied, all magnetic moments are aligned parallel to the direction of the magnetic field (Figure 2.18b).

Figure 2.18c shows the M-H (magnetization versus the strength of the magentic field) curve of ferromagnetic materials. As the strength of the magnetic field increases, the magnetization of the material increases and finally a saturation magnetization (M_s) is reached. When the applied magnetic filed is removed completely ($H = 0$), a remanent

magnetization (M_r) remains in the material. To reduce M_r to zero, a magnetic field equal to the coercivity (H_c) but opposite to the magnetization direction needs to be applied. As mentioned before, the value of coercivity represents the ability of a magnetic material to withstand an external magnetic field without becoming demagnetized [95]. Thus, it is an important parameter of magnetism in data storage applications. Moreover, a hysteresis loop is formed with further magnetization.

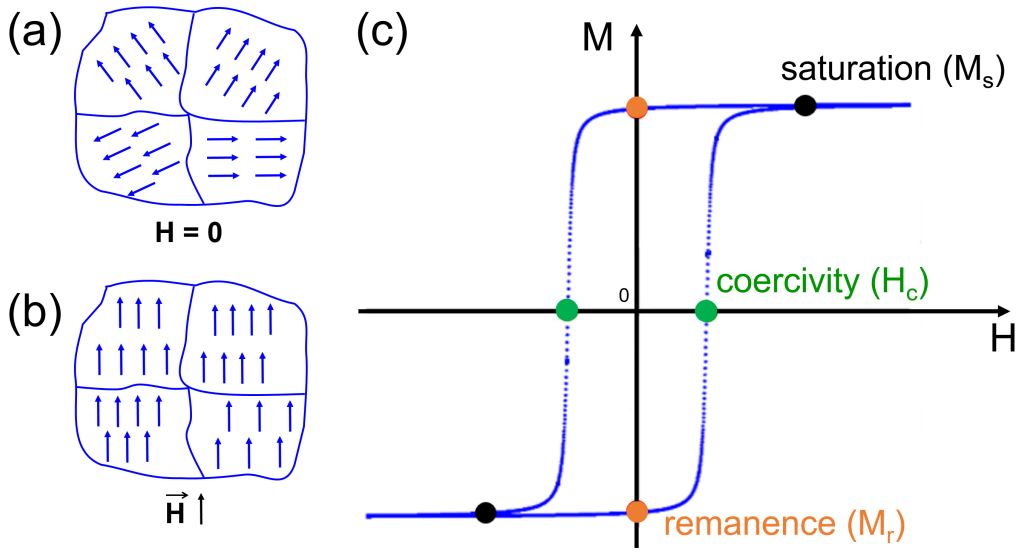

Figure 2.18: *States of magnetic moments in the domains of ferromagnetic materials (a) without and (b) with an external magnetic field. The black arrow in (b) indicates the direction of the magnetic field. (c)The M-H curve of ferromagnetic materials. Black, green and orange dots indicate the positions of saturation M_s, coercivity H_c and remanence M_r, respectively.*

2.2.2 Magnetic anisotropy

Magnetic anisotropy describes the fact that the magnetic properties of a material are different depending on direction. For the materials with magnetic anisotropy, their magnetic moments are aligned preferentially along the easy axis because of the energetic favor [100]. There are many types of magnetic anisotropy, such as shape anisotropy, magnetocrystalline anisotropy, magnetoelastic anisotropy and exchange anisotropy [101, 102]. The first two are the most common types considered in the study of magnetic thin films. Therefore, shape anisotropy and magnetocrystalline anisotropy are briefly introduced in here. Shape anisotropy describes magnetic materials with an asymmetric shape. A higher magnetization is shown along the easy axis because the demagnetizing field of the longer

axis is smaller than that of the shorter axis, which is caused by the induced poles at the surface of the NP being further apart. For a non-spherical NP, it is easier to magnetize along a long axis versus a short axis. In contrast, magnetocrystalline anisotropy states that the internal energy depends on the direction of spontaneous magnetization. The direction is related to the crystal structure of magnetic NP. For example, hexagonal cobalt shows uniaxial anisotropy, which makes the c-axis of the crystal the easy direction of internal magnetization at room temperature.

2.2.3 Magnetic nanoparticles

In the present thesis, superparamagnetic face-centered cubic (fcc) iron platinum nanoparticles (NPs) are selected for application in a high-frequency magnetic inductor. Large magnetic iron oxide NPs and strontium hexaferrite ($SrFe_{12}O_{19}$) nanoplatelets are used to achieve ferromagnetic films for applications in data storage and magnetic sensors.

Iron platinum NPs

Iron platinum (FePt) NPs are known to have two different crystal structures [103]. One structure is the chemically disordered fcc structure as shown in Figure 2.19a and denoted as fcc-FePt NPs [95, 103]. In the fcc lattice points, Fe and Pt atoms are distributed randomly. The other structure is the chemically ordered face-centered tetragonal (fct) structure (Figure 2.19b) denoted as fct-FePt NPs [95]. The fcc-structured FePt is magnetically soft and exhibits superparamagnetic behavior at NP size below 10 nm (Figure 2.19c). In contrast, the fct-FePt NPs below 10 nm are strongly ferromagnetic (Figure 2.19d) with a high coercivity [95, 104]. In the fct lattice, alternating atomic layers of Fe and Pt are stacked along the c-axis, which is the [001] direction.

In this case, fct-FePt NP has a large anisotropy constant K (as high as 1×10^7 J m^{-3}), which is caused by the strong 3d (Fe) and 5d (Pt) coupling. The large K makes the FePt NPs chemically much more stable and causes then to have a large coercivity at room temperature [104–106].

Figure 2.20 shows the schematic diagram of fct-FePt NPs formed by thermal annealing of fcc-FePt NPs [107]. To convert the fcc structure to the fct structure, thermal annealing with a high temperature T $\geq$ 500 °C is required [108–110]. Before annealing, a protective layer of robust oxide, such as magnesium oxide (MgO), is coated on the surface of the fcc-FePt NPs to prevent aggregation during sintering (thermal annealing). During annealing, an inert gas (such as Argon) needs to be used to prevent oxidation of the NPs [107].

The typical morphologies of the synthesized fcc-FePt NPs and fct-FePt NPs are shown in Figure 2.21a and b, respectively.

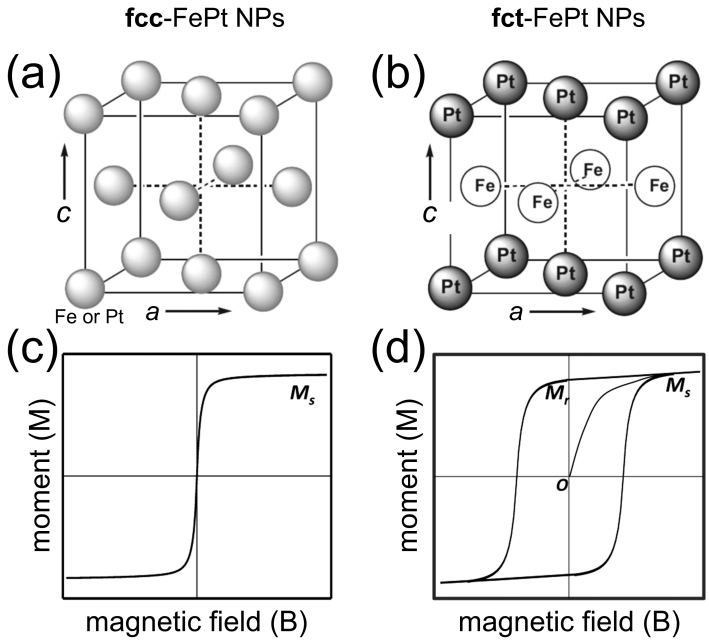

Figure 2.19: *Schematics of the structures of (a) fcc-FePt and (b) fct-FePt NPs. Magnetic hysteresis loops of (c) fcc-FePt (sub-10 nm) and (b) fct-FePt NPs. The image is modified with permission from reference [103] Copyright 2006 WILEY-VCH Verlag GmbH & Co. KGaA, Weinheim.*

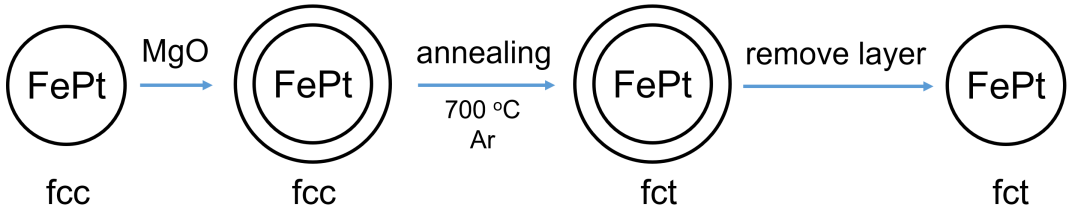

Figure 2.20: *Schematic diagram of fct-FePt NPs formed by the thermal annealing of fcc-FePt NPs. The image is modified with permission from reference [107] Copyright 2009 WILEY-VCH Verlag GmbH & Co. KGaA, Weinheim.*

In this thesis, fcc-FePt NPs are used rather than fct-FePt NPs, because the conditions for fct-FePt NPs synthesis are intensive and complicated as mentioned above. Moreover, the synthesized fcc-FePt NPs exhibit superparamagnetic behavior, which allows for a hysteresis-free switching when changing the external magnetic field.

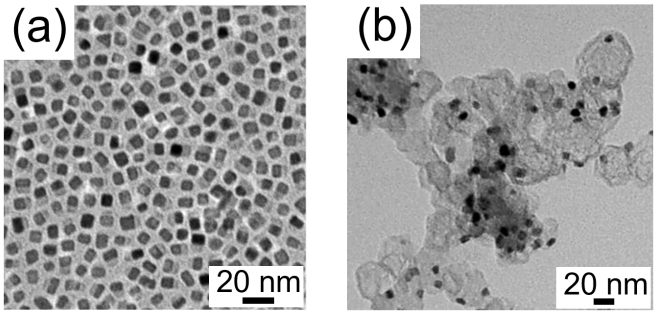

Figure 2.21: *TEM images of (a) fcc-FePt NPs and (b) fct-FePt NPs. The images are modified with permission from reference [110] Copyright 2015 American Chemical Society.*

Magnetic iron oxide NPs

Magnetic iron oxide NPs are soft magnetic materials and have been used in a variety of applications because of their controllable magnetism and chemical stability [95, 111, 112]. The most used two types of iron oxide NPs in NP-DBC system are magnetite Fe_3O_4 and maghemite γ-Fe_2O_3 NPs. They have a similar cubic structure which cannot be distinguished by standard resolution X-ray diffraction [113]. Magnetite Fe_3O_4 shows a cubic crystal structure with a unit cell composed of 56 atoms (16 Fe^{3+} ions, 8 Fe^{2+} ions and 32 oxygen atoms). The unit cell contains eight cubic units with a lattice d-spacing of 0.8396 nm. The Fe^{3+} ions are split between 1/4 of the octahedral sites and 1/8 of the tetrahedral sites and Fe^{2+} ions occupy 1/4 of the octahedral sites [114]. Like magnetite, maghemite γ-Fe_2O_3 exhibits a cubic crystal structure with a lattice d-spacing of 0.8330 nm. However, only Fe^{3+} ions and vacancies are existed inside the maghemite. To minimize the electrostatic energy of the crystal, they prefer to order in the octahedral sites [113,114].

For the fabrication of iron oxide NPs with different sizes, numerous methods are available, such as aqueous phase synthesis, organic phase reaction and metal-oleate decomposition method [95]. Aqueous phase synthesis is the coprecipitation of Fe^{2+} and Fe^{3+} ions by a base in an aqueous solution, which is a common method for lab-scale and mass fabrications [95]. Organic phase reaction is the high-temperature organic phase decomposition of an iron precursor and a promising method for obtaining mono-disperse NPs [111]. As shown in Figure 2.22a, mono-disperse Fe_3O_4 NPs with size of 6 nm are obtained via the reductive thermal decomposition of $Fe(acac)_3$ in an organic solvent (benzyl ether) [111]. Larger NPs can be achieved by using the 6 nm NPs as seeds (Figure 2.22b).

Metal-oleate decomposition method utilizes a Fe-oleate complex as the starting precursor and allows the fabrication of mono-disperse magnetic iron oxide NPs on a large scale [112, 115, 116]. For example, Park et al. reported the fabrication of monodisperse iron oxide NPs on an ultra large scale (Figure 2.23a) [117].

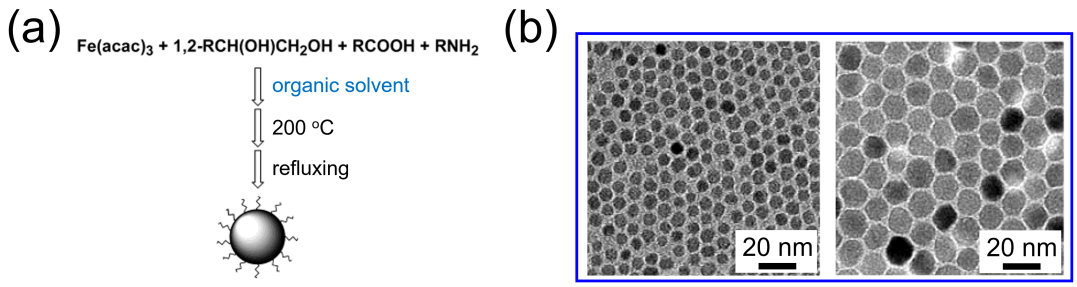

Figure 2.22: *(a) Scheme for the fabrication of mono-disperse Fe_3O_4 NPs. (b) TEM images of the obtained mono-disperse Fe_3O_4 NPs with different sizes (left and right are 6 nm and 12 nm, respectively.). The images are modified with permission from reference [111] Copyright 2004 American Chemical Society.*

Metal–oleate complexes (precursors) were obtained from the reaction of metal chlorides with sodium oleate (Na-oleate). The precursors were then thermally decomposed in a solvent with a high boiling point to produce highly mono-disperse iron oxide NPs. The size of the iron oxide NPs can be controlled by using different solvents with different boiling points. Large NPs are obtained by employing solvents with higher boiling points.

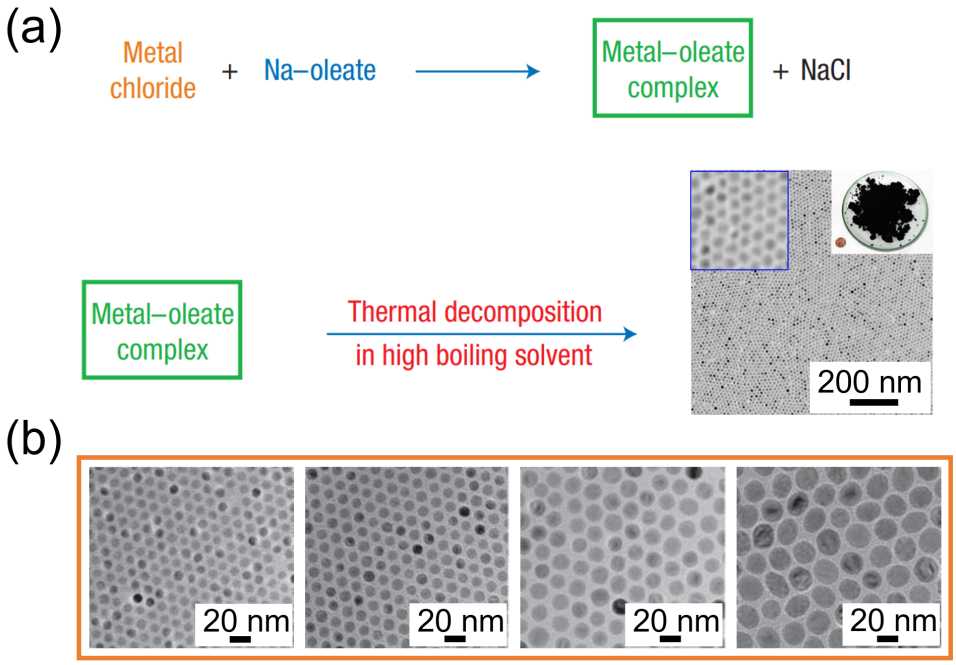

Figure 2.23: *(a) Scheme for the fabrication of mono-disperse iron oxide NPs on a large scale. (b) TEM images of the obtained mono-disperse iron oxide NPs with different sizes ((from left to right: 9 nm, 12 nm, 16 nm and 22 nm).The images are modified with permission from reference [117] Copyright 2004 Nature Publishing Group.*

As shown in Figure 2.23b, iron oxide NPs with diameters of 9 nm, 12 nm, 16 nm and 22

nm are obtained using solvents of octyl ether (287 °C), 1-octadecene (317 °C), 1-eicosene (330 °C) and trioctylamine (365 °C), respectively. By using X-ray absorption spectroscopy (XAS) and X-ray magnetic circular dichroism spectroscopy (XMCD), the compositions of the iron oxide NPs in the form of $(\gamma\text{-}Fe_2O_3)_{1-x}(Fe_3O_4)_x$ can be estimated. x = 0.57, 0.68, 0.86 and 1.00 correspond to the NPs with sizes of 9, 12, 16 and 22 nm, respectively.

For iron oxide NPs, small sized NPs show superparamagnetic behavior ($H_c = 0$) at room temperature [87, 95]. However, the absence of a hysteresis limits their application in data storage [95]. As shown in Figure 2.24, the critical diameter for Fe_3O_4 NPs, below which the NPs are superparamagnetic, is around 20 nm [118]. Thus, larger iron oxide NPs with a diameter above 20 nm are required to be considered for utilization in data storage.

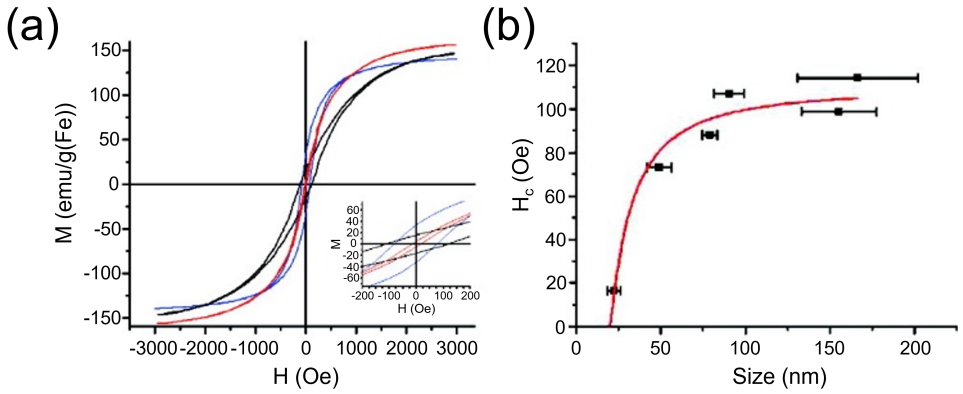

Figure 2.24: *(a) M-H curves of Fe_3O_4 NPs with different sizes at 300 K (red, blue and black curves indicates 22 nm, 80 nm and 160 nm, respectively).(b) NP size-dependent H_c.The images are modified with permission from reference [118] Copyright 2009 American Chemical Society.*

Strontium hexaferrite nanoplatelets

Strontium hexaferrite nanoplatelets ($SrFe_{12}O_{19}$) are hard magnetic materials with high coercivity and high magnetic anisotropy [34, 35, 119, 120]. Unlike soft magnetic materials, the fabrication of $SrFe_{12}O_{19}$ nanoplatelets (hard magnetic materials) requires high temperatures above 1000 °C [119]. As shown in Figure 2.25a, the $SrFe_{12}O_{19}$ nanoplatelets are platelet-like with a large diameter to thickness ratio. To better disperse the nanoplatelets in the solution, the surface of the nanoplatelets can be positively charged to prevent the formation of aggregates, as done by Kushnir et al. [119]. The nanoplatelets have a high uniaxial magnetic anisotropy with the easy magnetization axis (c-axis) perpendicular to their large facets. TEM images of the prepared $SrFe_{12}O_{19}$ nanoplatelets with different

sizes are shown in Figure 2.25b (D = 40 nm , t = 4 nm), c (D = 70 nm , t = 8 nm) and d (D = 60 nm , t = 8 nm). D and t are the average diameter of the large facet and average thickness of the nanoplatelets, respectively. Moreover, Kushnir et al. prepared a monolayer magnetic film with a fixed orientation of the nanoplatelets by utilizing a negatively surface charged glass substrate as shown in Figure 2.25e. Controlled orientation was achieved through the electrostatic attraction between the negative charges of the substrate surface and the positive charges of the nanoplatelets. The magnetic hysteresis loop of the monolayer film is shown in Figure 2.25f (red curve). The magnetic hysteresis loop of a film without controlled orientation of the $SrFe_{12}O_{19}$ nanoplatelets is also presented as a reference in Figure 2.25f (blue curve). As expected, the monolayer magnetic film exhibits a wider hysteresis loop with a higher H_c versus the film containing randonly oriented nanoplatelets.

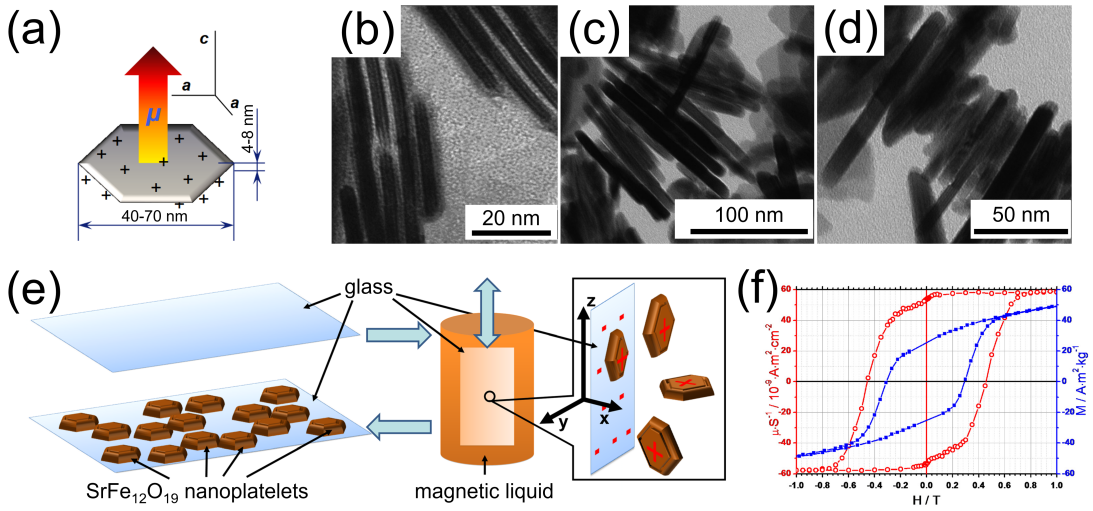

Figure 2.25: *(a) Schematic of a $SrFe_{12}O_{19}$ nanoplatelet. D and t represent the diameter of the large facet and thickness of the nanoplatelet. a and c represent the horizontal and vertical directions, respectively. TEM images of the obtained $SrFe_{12}O_{19}$ nanoplatelets with different sizes: (b) D = 40 nm and t = 4 nm, (c) D = 70 nm and t = 8 nm, and (d) D = 60 nm and t = 8 nm. (e) schematic of the fabrication of a monolayer magnetic film with a fixed orientation of the nanoplatelets on a negatively surface charged glass substrate. (f) Magnetic hysteresis loops of the monolayer magnetic film and reference film with randomly oriented nanoplatelets. Red and blue curves represent the monolayer magnetic film and reference film, respectively.The images are modified with permission from reference [119] Copyright 2014 WILEY-VCH Verlag GmbH & Co. KGaA, Weinheim.*

2.3 Scattering techniques

As discussed in the introduction, the arrangement of magnetic NPs can be controlled by DBC templates. The morphologies of the DBC and magnetic NPs play a vital role in understanding the whole hybrid system and influence the resulting magnetic properties. For the investigation of surface morphologies, real-space imaging methods (such as SEM and AFM) can be applied. However, real-space imaging methods cannot probe the entire morphology of the magnetic NP-DBC hybrid film. To study the inner morphology of a hybrid film with a large volume, X-ray scattering can be utilized. The scattering characterization method is non-destructive and can probe the structural information of the sample with high statistical relevance. In section 2.3.1, scattering basics are discussed and introductions to X-ray reflectivity (XRR) and grazing-incidence small-angle X-ray scattering (GISAXS) are presented in section 2.3.2 and section 2.3.3, respectively.

2.3.1 Scattering basics

X-rays have a wavelength ranging from 0.01 nm to 10 nm. The electric field vector $\overrightarrow{E}(\overrightarrow{r})$ can be described as an electromagnetic plane wave

$$\overrightarrow{E}(\overrightarrow{r}) = \overrightarrow{E}_0 \exp(i\overrightarrow{k_i}\overrightarrow{r}) \tag{2.14}$$

where $\overrightarrow{E}_0$ represents the polarization direction and amplitude of the electric field. $\overrightarrow{k_i}$ and $\overrightarrow{r}$ are the wave and position vectors, respectively.

The propagation of an electromagnetic wave that passes through a medium with a specific $n(\overrightarrow{r})$ (refractive index of the medium) can be described by the Helmholtz equation [121]

$$\Delta\overrightarrow{E}(\overrightarrow{r}) + k^2 n^2(\overrightarrow{r})\overrightarrow{E}(\overrightarrow{r}) = 0 \tag{2.15}$$

where k is the modulus of the wave vector and is given as $k = \left|\overrightarrow{k}\right| = \frac{2\pi}{\lambda}$. λ is the wavelength. The refractive index $n(\overrightarrow{r})$ can be described with the dispersion $\delta(\overrightarrow{r})$ and the absorption $\beta(\overrightarrow{r})$ of the material

$$n(\overrightarrow{r}) = 1 - \delta(\overrightarrow{r}) + i\beta(\overrightarrow{r}) \tag{2.16}$$

where $\delta(\overrightarrow{r})$ and $\beta(\overrightarrow{r})$ can be written respectively as

$$\delta(\vec{r}) = \frac{\lambda^2}{2\pi}\rho(\vec{r}) = r_e\frac{\lambda^2}{2\pi}\rho_e(\vec{r}) \tag{2.17}$$

$$\beta(\vec{r}) = \frac{\lambda^2}{2\pi}\mu(\vec{r}) \tag{2.18}$$

where ρ is the scattering length density (SLD) of the penetrated medium and $r_e = 2.814 \times 10^{-5}$ $\AA$ is the classical electron radius. ρ_e and μ are the electron density and the linear absorption coefficient of the investigated materials, respectively. Therefore, the SLD is dependent on the electron density of the related elements. In X-ray scattering experiments, scattering contrasts between different components in a matrial are a result of the varying SLD of the components.

The specular and diffuse scattering geometries are depicted schematically in Figure 2.26. The X-ray beam is incident on a film with a certain incident angle (α_i), and the reflected beam leaves the film at a certain exit angle (α_f). For specular scattering geometry, the beam stays in the xz-plane and $\alpha_i = \alpha_f$ (Figure 2.26a). However, the reflected beam is not limited to the xz-plane but with an additional angle ψ_f displayed in the xy-plane for the diffuse scattering geometry (Figure 2.26b).

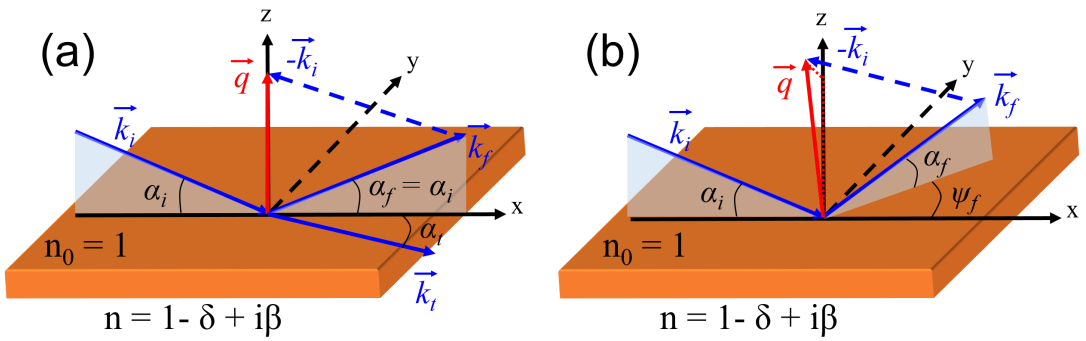

Figure 2.26: *Basic definitions of angles and directions in (a) specular scattering and (b) diffuse scattering geometries. The incoming, reflected and transmitted X-ray beams are marked as $\vec{k}_i$, $\vec{k}_f$ and $\vec{k}_t$, respectively. The incident angle is represented by α_i and α_f is the exit angle. ψ_f is the angle between the projection of the specular reflected beam and the scattered beam onto the xy-plane.*

The scattering vector represents the difference between the incident and scatted wave vectors and is defined as

$$\vec{q} = \vec{k}_f - \vec{k}_i \tag{2.19}$$

In the present thesis, only elastic scattering is considered. $\vec{q}$ indicates a direction change of the scattered beam associated with the incident beam. The modulus of the $\vec{q}$ stays constant such that $\left|\vec{k}_i\right| = \left|\vec{k}_f\right| = \frac{2\pi}{\lambda}$.

As shown in Figure 2.26a, the X-ray beam can be either reflected or transmitted at the interface between the air and the film. The angle of the transmitted beam (α_t) is related to the incident angle α_i and described by Snell's law

$$n_0 \cos(\alpha_i) = n \cos(\alpha_t) \tag{2.20}$$

where $n_0 = 1$ and n are the refractive indices of air and film, respectively. At $\alpha_t = 0$, the X-ray beam is fully reflected. In this case, the incident angle is defined as the critical angle α_c of the studied material ($\alpha_i = \alpha_c$). According to the small angle approximation and Equation 2.20, n^2 can be obtained by

$$n^2 = \cos^2(\alpha_c) \approx 1 - \alpha_c^2 \tag{2.21}$$

In addition, assuming $\beta \ll \delta$ and in combination with equation 2.17, the critical angle α_c can be given as

$$\alpha_c \approx \sqrt{2\delta} = \lambda\sqrt{\rho/\pi} \tag{2.22}$$

At $\alpha_i < \alpha_c$, the beam is fully reflected and the scattering signal is mostly surface sensitive. The penetration depth of the beam increases significantly when α_i is creased above α_c. In the case of $\alpha_i > \alpha_c$, the beam can usually penetrate the whole film.

2.3.2 X-ray reflectivity (XRR)

In this thesis, X-ray reflectivity (XRR) is applied to obtain the film thicknesses. XRR refers to the case of $\psi_f = 0$ and records the specular scattering as a function of the incident angle (α_i). Herein, $\alpha_i = \alpha_f$. As shown in (Figure 2.26 a), the scattering vector $\overrightarrow{q}$ is oriented always along the z-axis. Thus, only the z-component q_z is collected and calculated by [122]

$$q_z = \frac{4\pi}{\lambda} \sin(\alpha_i) \tag{2.23}$$

In the case of an X-ray beam impinging on the interface of materials A and B, the beam is split into two parts, which are transmitted and reflected beams. As discussed previously, the angle of the transmitted beam can be described by Snell's law Equation 2.20. The ratio of the amplitudes of the reflected and transmitted beams can be addressed by the Fresnel reflection coefficient (r^F) and transmission coefficient (t^F), respectively. The reflectivity (R^F) and transmission (T^F) are described as

$$R^F = |r^F|^2, \quad T^F = |t^F|^2 \tag{2.24}$$

So far, interface roughness is not considered in the above discussed scattering behavior, which are based on the assumption that the interfaces are perfectly smooth. The deviation from a smooth surface can be described by the interfacial roughness and expressed by the root-mean-square surface roughness σ_{rms} [123]

$$\sigma_{rms} = \sqrt{\frac{1}{N_{\sigma_{rms}}} \sum_{i=1}^{N_{\sigma_{rms}}} \Delta z_i^2} \tag{2.25}$$

where $N_{\sigma_{rms}}$ shows the number of the sampling spots along the interface and Δz_i represents the deviation from a specific sampling spot i to the average interface. If the roughness below the film thickness, an exponential function of Névot-Croce factor could be used to improve and correct the Fresnel reflection coefficient [124]. However, such correction cannot be used if the roughness is on the order of or even above the film thickness.

Figure 2.27 shows typical XRR data of a PS-*b*-PMMA DBC film spin-coated on a silicon (Si) substrate. At $\alpha_i < \alpha_c^{DBC}$, the beam is totally reflected. At $\alpha_i = \alpha_c^{DBC}$ and $\alpha_i < \alpha_c^{Si}$, an intensity minimum for PS-*b*-PMMA and silicon can be observed.

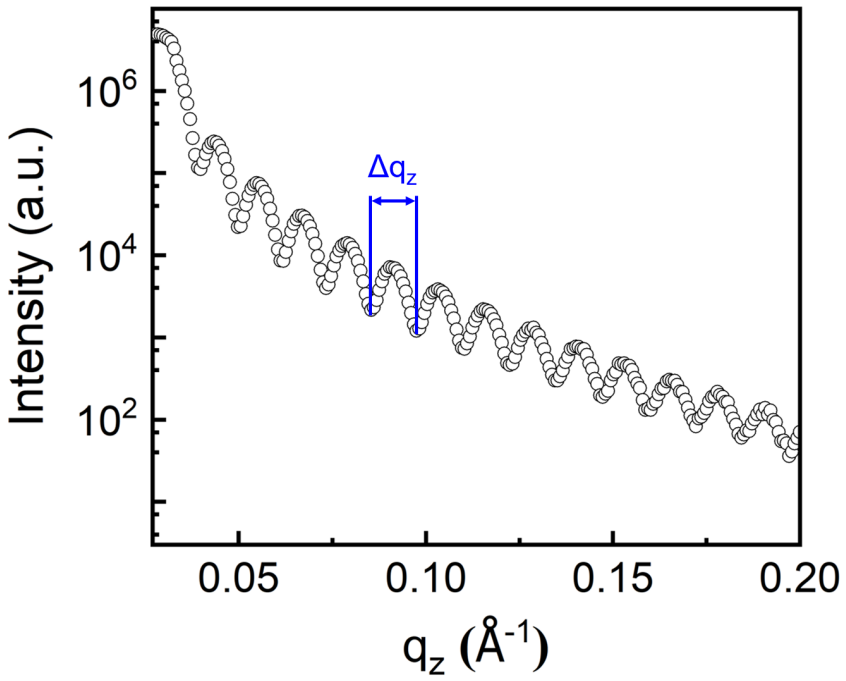

Figure 2.27: *XRR data of a PS-b-PMMA DBC film on a supported silicon substrate. Δq_z shows the distance between two neighboring intensity minima and revels information about the film thickness.*

At $\alpha_i > \alpha_c^{Si}$, intensity oscillations (named Kiessig fringes) appear and provide information about the film thickness given by t [125]

$$t \approx \frac{2\pi}{\Delta q_z} \tag{2.26}$$

where Δq_z is the distance between two neighboring intensity minima, corresponding to the distance between two valleys in the fringes, as shown in Figure 2.27.

Data analysis is performed by Parratt algorithm based software to fit the XRR data.

2.3.3 Grazing-incidence small-angle X-ray scattering (GISAXS)

Grazing-incidence small-angle X-ray scattering (GISAXS) is a powerful and non-destructive technique used to investigate the structures of thin films. The large footprint of the X-ray beam (originating from the shallow grazing incident angle) allows for the probing of a large film volume and therefore good statistical information on the film morphology can be obtained. Moreover, GISAXS is an excellent technique for in situ investigations because GISAXS measurements can be performed with a high time resolution (such as 0.1 s per frame). In GISAXS, the X-ray scattering is considered to be elastic and the scattering vector $\overrightarrow{q}$ is given as [126]

$$\vec{q} = \frac{2\pi}{\lambda}\begin{pmatrix} q_x \\ q_y \\ q_z \end{pmatrix} = \frac{2\pi}{\lambda}\begin{pmatrix} \cos(\alpha_f)\cos(\psi) - \cos(\alpha_i) \\ \cos(\alpha_f)\sin(\psi) \\ \sin(\alpha_f) + \sin(\alpha_i) \end{pmatrix}. \tag{2.27}$$

In GISAXS measurements, the incident angle α_i and the exit angle α_f are small, indicating $q_x \approx 0$ and can be ignored. According the the commonly used distorted wave Born approximation (DWBA) [127,128], the diffuse scattering can be treated as a perturbation of an ideal system. In the case of an ideal system with a smooth interface, the lateral structure and the film roughness are described as the perturbations. Thus, the differential cross section of the scattering can be denoted as

$$\frac{d\sigma}{d\Omega} = \frac{S\pi^2}{\lambda^4}\left(1 - n^2\right)^2 \mid T_i \mid^2 \mid T_f \mid^2 P_{diff}(\vec{q}) \propto P_{diff}(\vec{q}) \tag{2.28}$$

with the illuminated area S and the diffuse scattering factor $P_{diff}(\vec{q})$ [129]. The Fresnel transmission coefficients of the incident and scattered beams are denoted as T_i and T_f, respectively. If the incident angle is equal to the critical angle of the studied material, the Fresnel transmission coefficients can reach a maximum. In the scattering map, a characteristic intensity maximum called material sensitive Yoneda peak can be observed. Thus, horizontal line cuts performed at the Yoneda peak position of the material allows for the quantitative analysis of the lateral structures via modeling.

In this thesis, the modeling is based in the framework of the DWBA using the effective interface approximation (EIA) [127]. For a system with N identical objects in a geometrical arrangement, the diffuse scattering factor $P_{diff}(\vec{q})$ can be given by [130]

$$P_{diff}(\vec{q}) \propto N|F(\vec{q})|^2 S(\vec{q}) \tag{2.29}$$

with form factor $F(\overrightarrow{q})$ describing the shape and size of the scattering objects, and structure factor $S(\overrightarrow{q})$ relating to the spatial arrangement of the scattering objects and presents the objects at a certain distance from one another.

As mentioned above, the diffuse scattering is based in the framework of DWBA, which considers four different scattering events [131]. The four terms are displayed schematically in Figure 2.28. The first mode is where the X-ray beam is directly scattered on the object (Figure 2.28a). The second occurs when the beam is reflected on the substrate first and then scattered on the object (Figure 2.28b). In the third mode, the beam is scattered first on the object and then reflected on the substrate (Figure 2.28c). The last mode describes a reflected-scattered-reflected beam (Figure 2.28d). Moreover, for the size distribution, a local monodisperse approximation (LMA) is applied. The LMA is based on the assumption that in local domains, which have the size of the coherence length of the X-ray beam, only objects of one type are found [132]. Thus no cross-correlation terms are considered. Though fitting of the data, average object sizes and center-to-center distances can be obtained.

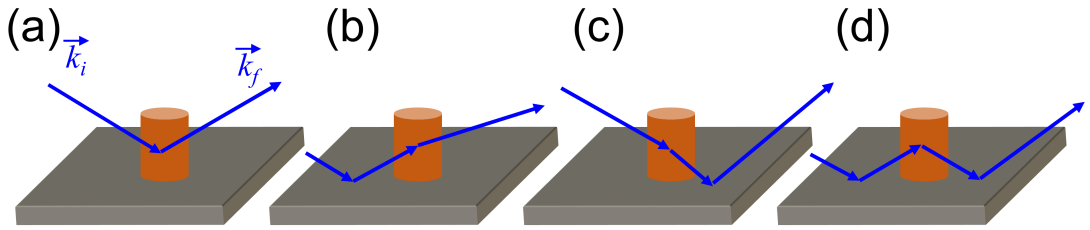

Figure 2.28: *Schematic of four different scattering events in the framework of DWBA. The X-ray beam is (a) scattered directly without reflection, (b) reflected first before scattering, (c) scattered first before reflection and (d) reflected before and after scattering.*

3 Characterization methods

In the present chapter, all characterization techniques, applied to probe magnetic NPs and thin films (pure DBC films and magnetic NP-DBC hybrid films), are described. The morphologies of various used magnetic NPs are studied by transmission electron microscopy. The surface structures of thin films are probed by optical microscopy (OM), scanning electron microscopy (SEM) and atomic force microscopy (AFM). The inner structures are investigated by grazing-incidence small-angle X-ray scattering (GISAXS). Moreover, the film thickness is measured by surface profilometry and X-ray reflectivity (XRR). The magnetic properties of the magnetic films are probed by superconducting quantum interference device (SQUID) magnetometry.

3.1 Structural characterizations

3.1.1 Transmission electron microscopy (TEM)

Transmission electron microscopy (TEM) is a technique in which an electron beam passes through a sample to form a graph. The chemical information and features in the range of a few nanometers can be obtained via TEM. Figure 3.1 shows the working principle of TEM. The electrons generated from the electron gun are focused into a thin beam. Then, the beam hits the specimen and passes through the specimen. This transmitted portion is focused and magnified by the objective lens and imaging lens into an image onto a fluorescent screen or a charge coupled device (CCD) camera.

In this thesis, TEM measurements with different parameters are carried out on different materials to obtain the best results. For FePt NPs in chapter 6, TEM is applied with a JEOL JEM-2100 electron microscope (200 kV, 0.14 nm resolution) and a Gatan Orius SC1000 camera (Binning 2, 1024 $\times$ 1024 pixels) in bright field mode. For Fe_3O_4 NPs in chapter 7, TEM experiments are carried out using a Zeiss EM 10 CR (60 kV)/ Olympus Megaview II / ITEM Software build 1276 operating at 60 kV in bright field mode. For $SrFe_{12}O_{19}$ nanoplatelets in chapter 8, TEM images are obtained using Carl Zeiss Libra 200MC and LEO 912 AB Omega microscopes.

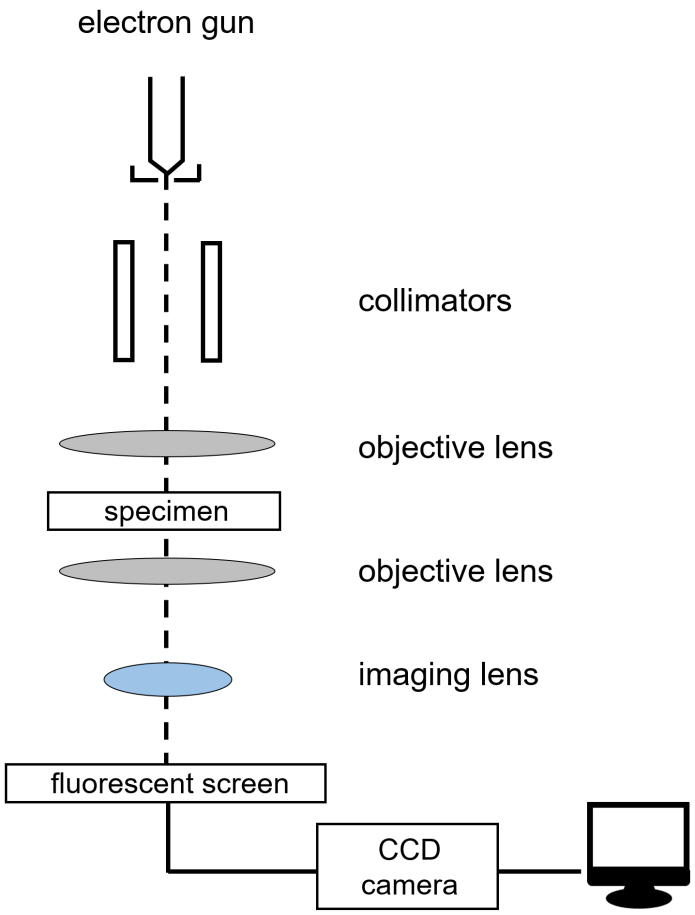

Figure 3.1: *Working principle of TEM.*

3.1.2 Optical microscopy (OM)

Optical microscopy (OM) is applied to examine the surface morphologies of the obtained films on the micrometer scale and check the film homogeneity, which is necessary for many applications. The used OM is an Axiolab A microscope (Carl Zeiss) combined with a charge coupled device camera (PixeLink USB Capture BE 2.6). The microscope is mounted with objectives for various magnifications, such as 1.25, 2.5, 10, 50 and 100–fold. The camera is equipped to record digital images (1280 $\times$ 1024 pixels).

Moreover, the resolution of each pixel is displayed in Table 3.1, which is used to calculate the real–space distance. In this thesis, the magnification of 10$\times$ is selected. The obtained images are processed and analyzed by ImageJ [133].

magnification[×]	resolution [μm/pixel]
1.25	6.26
2.5	3.11
10	0.82
50	0.17
100	0.082

Table 3.1: *Resolutions for various magnifications of the optical microscopy (OM).*

3.1.3 Scanning electron microscopy (SEM)

To study the film surface morphology at the nanoscale, scanning electron microscopy (SEM) is applied. Compared with OM, SEM can provide images with higher resolution (down to 10 nm). This is due to the fact that SEM is based on electrons rather than optical light in OM. The shorter electron wavelength provides a higher spatial resolution for the SEM. As a consequence, the film surface morphology at the nanoscale can be obtained by SEM measurements.

Figure 3.2 shows a simplified schematic of the SEM setup. Electrons are emitted through a field emission electrode. Then, electrons are accelerated by a voltage U_B with several kV and reach the anode. Afterwards, the generated electron beam is shaped by electromagnetic condenser lenses and gets focused on the respective sample. Compared with broad-shaped beams, an improved resolution could be achieved with narrow-shaped beams. Then, scanning coils are used to control the beam deflection, which is beneficial to scan the surface of the sample in a raster mode.

When the electron beam hits the film surface, secondary electrons from the area with small escape depth are released and can be collected via a detector with a small distance between the sample and detector. The intensity of the secondary electrons depends on many factors, such as incident angle between the beam and film surface, beam size and the surface morphology of the sample and sample-detector-distance. According to different materials and topography of the film surface, the collected electronic signals are converted to a monochrome image with different brightness. Moreover, backscattered electrons (large penetration depth) and characteristic X-rays (highest penetration depth) also exist. However, they do not contribute to the generation of the SEM images, because image acquisition for structural analysis is usually carried out by detecting secondary electrons with low energy. The electrons with a certain energy can be detected by using a de-acceleration bias voltage and controlling the position of the detector.

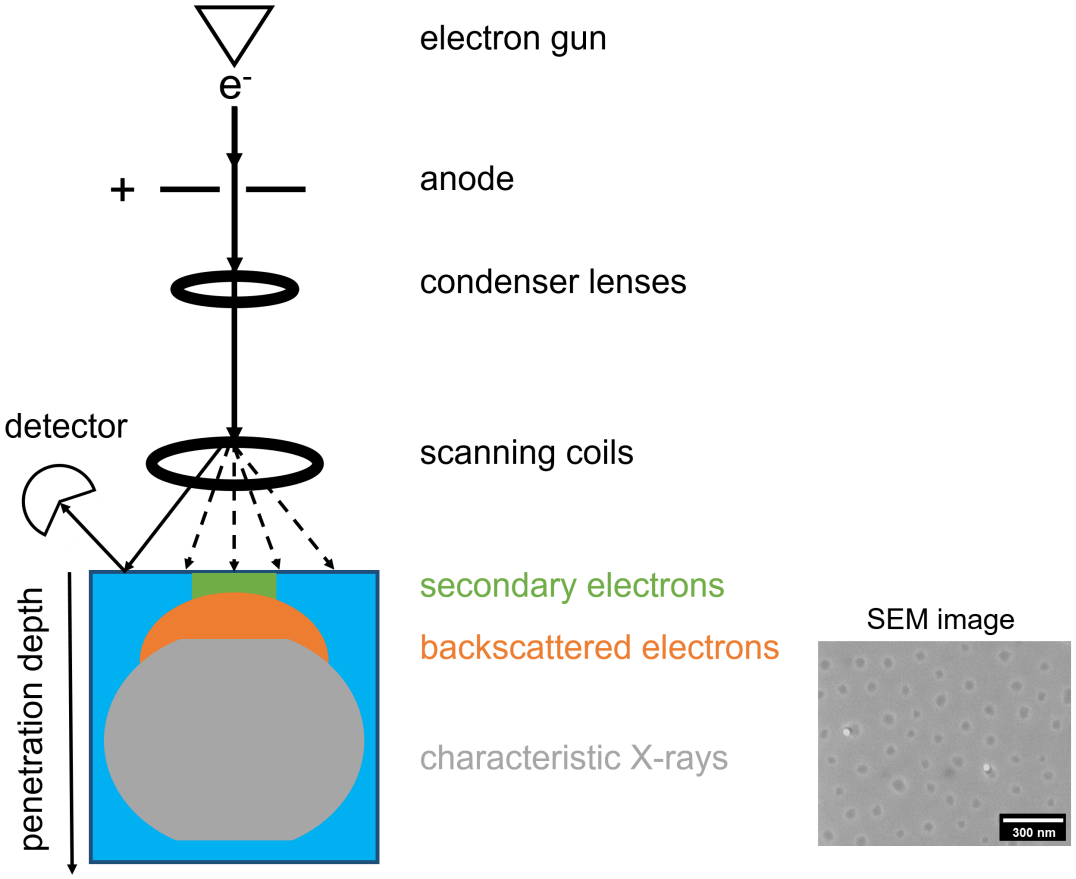

Figure 3.2: *Simplified schematic of the SEM setup. The obtained SEM image of a magnetic NP-DBC film is shown in the bottom right corner.*

In this thesis, SEM is performed using an NVision40 FESEM (Carl Zeiss AG) controlled by the software SmartSEM to probe the surface morphologies in nanoscale. An InLense detector is used for recording the signal of secondary electrons. A relatively low acceleration voltage of 1 kV is used during measurements because of the poor conductivity of the examined DBC film. The aperture size is 10 m. All obtained SEM images are analyzed with the software ImageJ [133].

3.1.4 Atomic force microscopy (AFM)

Atomic force microscopy (AFM) is a 3D mapping technique, topographic information of the film surface, such as height and roughness, is accessible. The working principle of AFM is based on the interaction between a shape AFM tip and the sample surface.

In Figure 3.3, a simplified sketch of the AFM instrument is illustrated. It shows an AFM feedback loop consisting of an xyz piezoelectric scanner, a cantilever with an AFM

tip, a laser beam, a photodiode detector and a feedback controller. The AFM tip is installed on the end of a cantilever and utilized for scanning the sample surface.

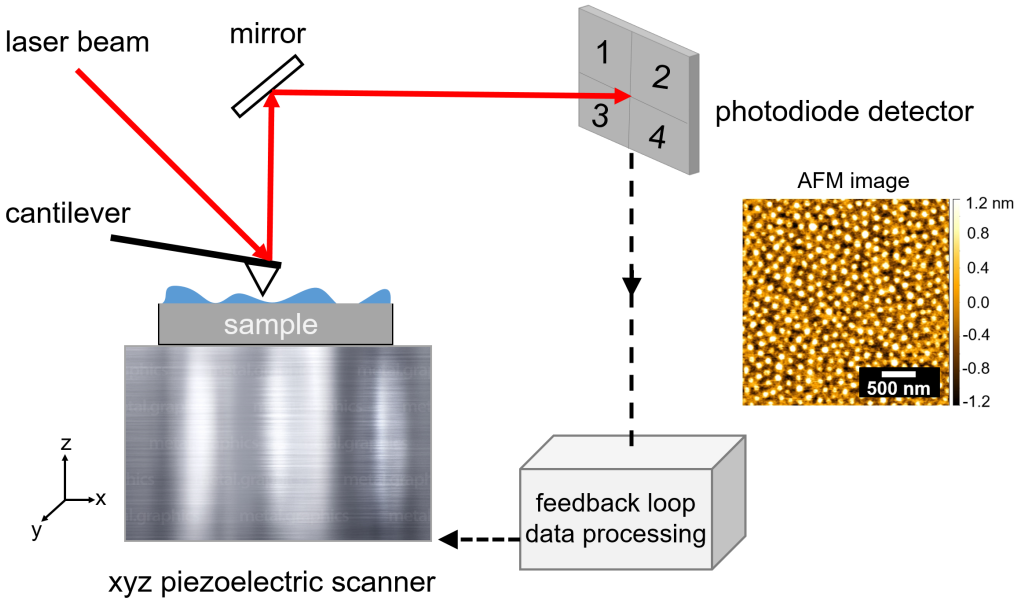

Figure 3.3: *Simplified sketch of the used AFM set–up. The sample is placed on an xyz piezoelectric scanner, which is used to realize 3D movement of the sample. The deformation of the cantilever is examined by a reflective laser beam recorded on a photodiode detector. The adjustment of the sample position and data processing can be realized through a feedback system.*

When the sample surface is scanned by the tip, interaction between the tip and the molecules on the sample surface produces, leading to a deformation of the cantilever based on Hooke's law [134]. According to the different interactions (forces) between the tip and the the sample surface, AFM measurements can be summarized into three basic modes, which are contact (repulsive force), non-contact (attractive force) and tapping modes (repulsive and attractive forces) as shown in Figure 3.4. The force type depends on the tip-surface distance and affects the deformation of the cantilever.

In this thesis, the AFM measurements are performed with a tapping mode using a MFP-3D instrument (Asylum Research) to probe the height profile of the film surfaces on the nanoscale. Such mode can record images with high resolution and minimize the possible damage to the sample surface during measurements. In contrast, the sample surface could be damaged by AFM measurements with a contact mode and the image resolution in the non-contact mode is limited. The curvature radius of the used AFM tip is 7 nm. The spring constant of the cantilever (OMCL-AC240TS-R3, Asylum Research) is 2 N m^{-1} with a resonance frequency of 70 kHz. During the measurements, the cantilever is driven first to oscillate close to its resonance frequency. Then, the tip touches the

sample surface repeatedly with high frequency. Due to the roughness and structure of the film surface, the tip-surface distance changes with scanning time, leading to changes in the tip-surface interaction. As a result, the amplitude of the oscillating cantilever is changed. As shown in Figure 3.3, such change can be examined by a reflective laser beam recorded on a photodiode detector. The detector is sensitive and is divided into four parts. Thus, the deformation of the cantilever is converted into electronic signals, which are then transfered to the feedback electronics. The feedback loop drives the movement of the sample stage in z-axis to keep an unchanged tip-surface distance. According to the motion of the stage, the height and phase images are obtained. All collected AFM images are analyzed with the software Gwyddion 2.42 [135].

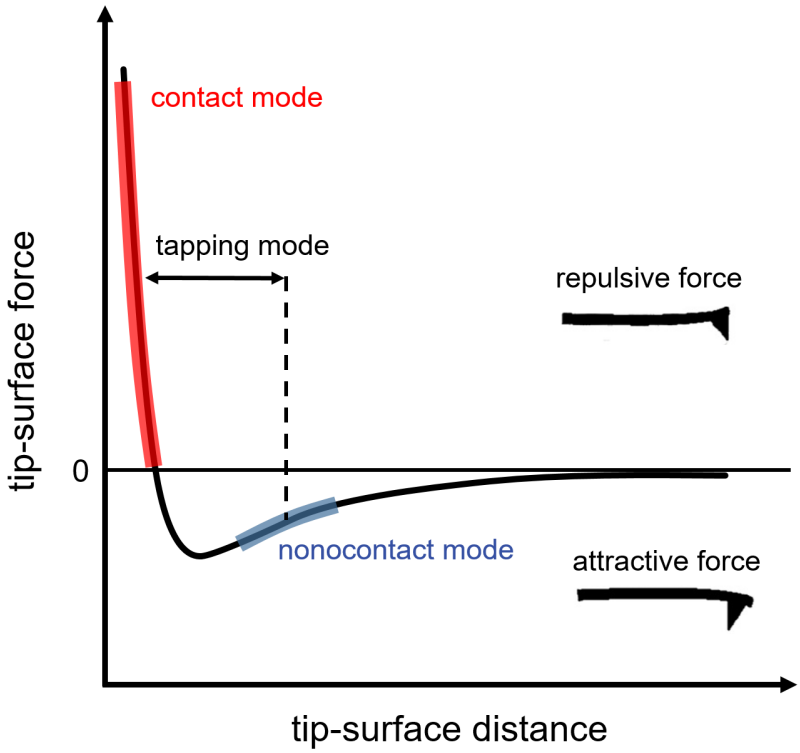

Figure 3.4: *Three main AFM operation modes (contact, non-contact and tapping modes) are presented based on the relationship between the tip-surface force and the tip-surface distance. The deformations of the cantilever under different forces are also present. The image is modified with permission from reference [136] Copyright 2013 IEEE Control Systems Society.*

3.1.5 Surface profilometry

Profilometry is a fast technique utilized to obtain the film thickness. The basic working principle of a profilometer is shown in (Figure 3.5) with a simplified sketch. A scratch is

made first on the film surface with the help of a clean tweezer before the measurement. Then, the sample is placed on the stage, the stylus with a diamond tip is put down to touch the film surface. To ensure a good contact between the film surface and stylus, a constant force is applied. Moreover, to allow the movement of the stage perpendicular to the direction of the scratch (see Figure 3.5), adjustment of the sample position is required before scanning. When the stage moves and the tip passes through the scratch, the height change of the film surface could be detected. The film thickness can be obtained by analyzing the collected height profile.

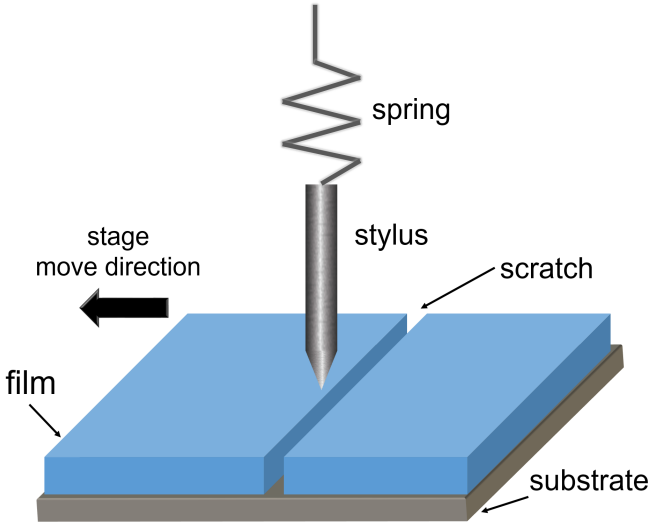

Figure 3.5: *Schematic of the profilometer. The film is scratched and placed on a movable stage. The stylus with a tip touches the film surface with a constant force. The scanning is realized by the movement of the stage, which is perpendicular to the direction of the scratch.*

In this thesis, a profilometry (DektakXT surface profiler, Bruker) is used to detect rough films. The scan speed and distance are 100 μm/s and 2 mm, respectively. The used contact force is 1 mN. For each sample, the obtained film thickness is an average value of 5 different measurement positions.

3.1.6 X-ray reflectivity (XRR)

X-ray reflectivity (XRR) is a non-destructive technique for the measurement of film thickness compared to the surface profilometry. This technique is based on specular reflection of X-rays and can be used to accurately obtain film thickness. The theoretical basics of XRR with more details can be seen in section 2.3.2.

For XRR measurements in this thesis, a Bruker D8–Advance is used. The measurement protocols are programed and controlled by XRDwizard and XRDcommander, respectively. As shown in Figure 3.6, XRR instrument is composed of three main parts (X-ray source, sample stage and detector). The X-ray beam ($\lambda = 0.154$ nm) is generated via a copper K_α-source and can be well defined by narrow slits, which are installed after the X-ray entrance and before the detector. Moreover, a knife-edge cutter is mounted over the sample with a short surface-to-edge distance to avoid excessive illumination of the sample. The XRR measurements are performed by changing 2θ from 0° to 5° with an increment size of 0.01°. To extract the film thickness from the corresponding XRR data, MOTOFIT package for IGOR is applied. [137].

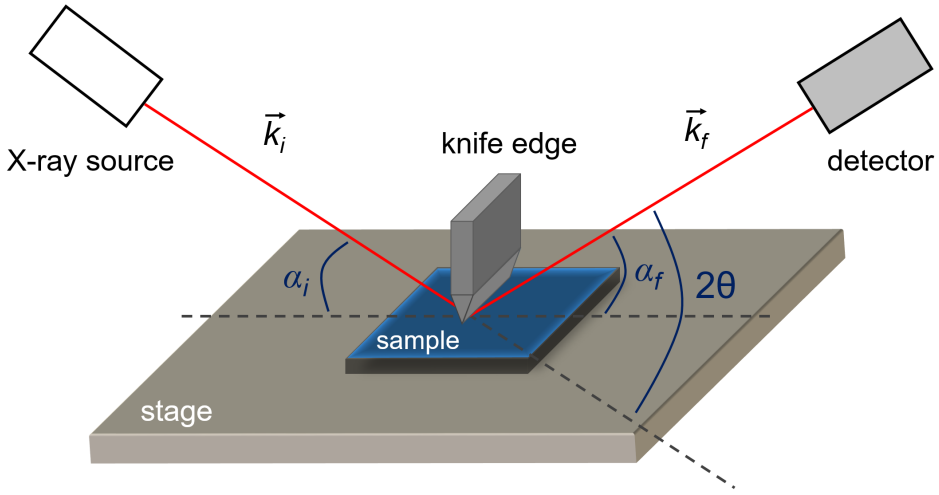

Figure 3.6: *Schematic overview of a setup used for XRR measurements. The X-ray beam is generated and impinges on the sample surface at an angle α_i. The reflected X-ray beam is recorded via a detector at an exit angle α_f. 2θ is the angle between the reflected X-ray beam and the incoming beam. $2\alpha_i = 2\alpha_f = 2\theta$. A knife edge is applied and approach to the sample surface to avoid overillumination at small angles.*

3.1.7 Grazing-incidence small-angle X-ray scattering (GISAXS)

As discussed above in the section 2.3.3 (theoretical basics), grazing-incidence small-angle X-ray scattering (GISAXS) is a non-destructive technique, which can probe the inner structure of the film with high statistical relevance. Figure 3.7 shows the schematic illustration of a setup for GISAXS measurements in reflection geometry. The X-ray beam impinges on the film with a incident angle α_i. To ensure that the full depth of film is probed, the incidence angle of the X-ray beam is set to larger than the critical angles of all materials inside the measured film. In general, $\alpha_i < 1^o$.

In this thesis, GISAXS measurements are performed at two different synchrotron facilities, which are Austrian SAXS beamline of the Elettra synchrotron source (Trieste, Italy) and MiNaXS/P03 beamline of PETRA III at DESY (Hamburg, Germany). The samples in chapter 5 are measured at the first facility, while the samples in other chapters (6, 7 and 8) are measured at the last facility. During the measurements, samples are placed on a stage that can be moved in 3D. The scattered signal is collected via a 2D detector. The sample-to-detector distance (SDD) is adjusted based on the structure sizes of the measured sample. To reduce the scattering noise from air, a vacuum flight tube with controllable length is applied and placed between the stage and the detector. Moreover, two beam stops are mounted in front of the detector to avoid oversaturation and protect the detector. One beam stop is installed at the position of the direct beam, and the other one is mounted at the position of the specular reflection. Table 3.2 shows the detailed parameters used for GISAXS measurements of samples in different chapters.

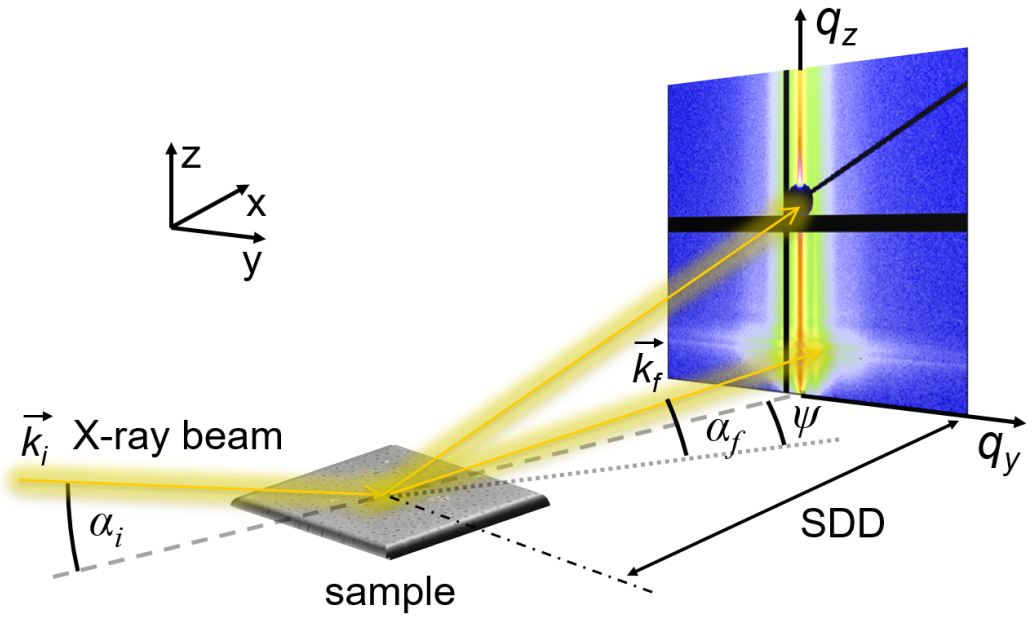

Figure 3.7: *Schematic illustration of a setup for GISAXS measurements in reflection geometry. The X-ray beam $\vec{k_i}$ impinges on the film under an incident angle α_i. For recording the scattered signal $\vec{k_f}$ with an exit angle α_f, a 2D detector is used. ψ is the angle between the scattered beam and incident beam in the xy-plane. SDD is the sample-to-detector distance.*

For a quantitative analysis of the lateral structures inside the film, horizontal line cuts of the 2D GISAXS data are made along the q_y direction via the software DPDAK (Gunthard Benecke, DESY Hamburg and MPIKG Potsdam) [138]. Then, the selected horizontal line cuts were modeled in the framework of the distorted-wave Born approximation (DWBA) using the effective interface approximation (EIA) as described in the section 2.3.3. In

our modeling, a spherical (or a cylindrical) geometry with a Gaussian size distribution of the scattering objects is assumed. From the model, the average object radii and their corresponding center-to-center distances are obtained.

chapter	λ **(nm)**	α_i **(°)**	**SDD (mm)**	**detector (type)**	**detector (pixel size)**	**synchrotron**
5	0.154	0.40	2083	Pilatus 1M	172 μm × 172 μm	Elettra
6	0.0993	0.35	4045	Lambda 750K	55 μm × 55 μm	DESY
7	0.0957	0.35	4994	Pilatus 1M	172 μm × 172 μm	DESY
8(in situ)	0.0965	0.40	4340	Pilatus 300K	172 μm × 172 μm	DESY
8(static)	0.0965	0.32	3554	Lambda 750K	55 μm × 55 μm	DESY

Table 3.2: *Detailed parameters used for GISAXS measurements of samples in different chapters.*

3.2 Characterizations of magnetic properties

SQUID magnetometry

Superconducting quantum interference device (SQUID) magnetometry (MPMS XL-7, Quantum Design, San Diego, CA, USA) measurements are conducted in a direct current (DC) mode for probing the magnetic properties of films as a function of temperature. A schematic view of the used SQUID instrument is displayed in Figure 3.8a. Before the magentic measurement, the measured sample is cut into a small size of 60 mm × 60 mm and then is fixed inside a long plastic straw. The plastic straw is a non-magnetic disturbance and is used as a sample holder to ensure that the sample's direction cannot be changed during the measurement. During the measurement, the direction of the applied external magnetic field is fixed and parallel to the long direction of the plastic straw. Thus, if the magnetic anisotropy of the sample needs to be measured, the direction of the sample with respect to the long direction of the plastic straw should be changed via a rotation of the sample (Figure 3.8b) before the measurement. The sample chamber is sealed and filled with liquid helium after the sample is placed in the center of a superconducting solenoid. Afterwards, an external magnetic field is applied and the magnetic signal from the sample is collected by a superconducting pick-up coil mounted around the sample. With a SQUID sensor connected to the coil, the magnetic flux from the sample can be converted into voltage signals. Such signals are amplified and displayed by the electronics

of a magnetometer. Moreover, the sample is oscillated with an amplitude of 3 cm in the perpendicular direction, leading to a change of magnetic flux in the coil. As a result, the output voltage changes in the SQUID and is proportional to the measured magnetic moments. In general, magnetic thin films exhibit small magnetic responses, especially for the films with low magnetic NP concentrations. Therefore, the instrument used needs to have extremely high sensitivity, which can be achieved by locking the readout frequency to the movement frequency [139].

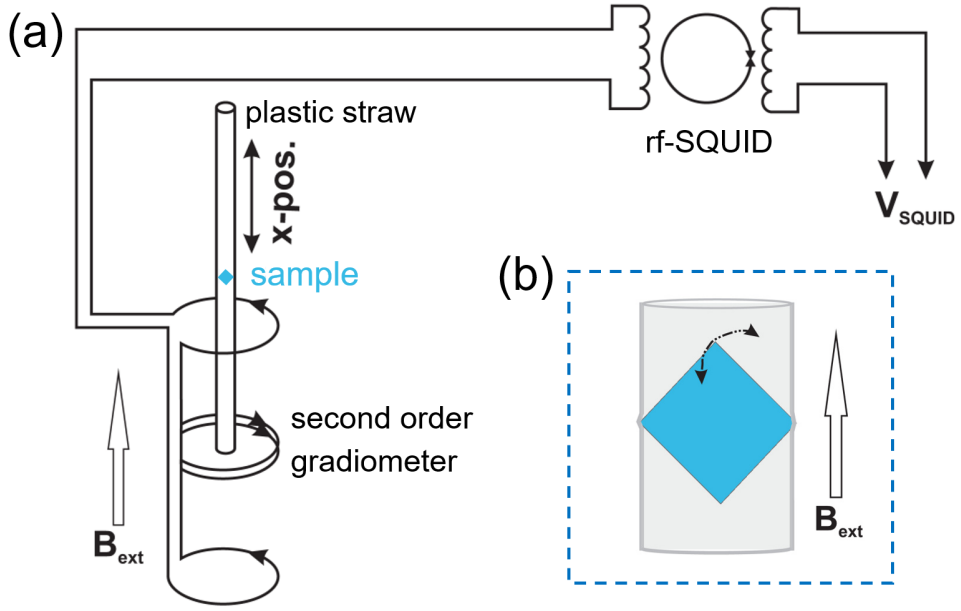

Figure 3.8: *(a) Schematic setup of a SQUID instrument. The sample (blue color) is fixed inside a long plastic straw. (b) Sketch of a sample mounted inside a plastic straw. The sample can be rotated from in-plane to out-of-plane for the measurement of magnetic anisotropy. The images are modified with permission from reference [140] Copyright 2018 AIP Publishing LLC.*

To study the influence of temperature on the magnetic properties, the samples are measured at various temperatures in the film plane, with an applied external magnetic field parallel to the sample surface. However, in chapter 7, the applied external magnetic field is rotated by 90^o in the film plane to study the alignment of chain-like NP aggregates in the film. In chapter 8, the nanoplatelets used have a high uniaxial magnetic anisotropy, leading to the hybrid film exhibits a magnetic anisotropic behavior when the nanoplatelets are not randomly aligned in the film. To verify this, the samples are measured in three orthogonal orientations (two in the film plane and one out of the film plane) by changing the direction of the applied external magnetic field. In the data analysis, the diamagnetic contribution from the silicon substrate is subtracted. From the obtained magnetization

curves, important magnetic parameters, such as magnetization saturation, coercivity, remanence and magnetic susceptibility, are extracted.

4 Sample preparation

In this chapter, the main materials and film fabrication techniques used for this thesis are introduced. In section 4.1, the main materials, polystyrene-*block*-polymethyl methacrylate (PS-*b*-PMMA) ultrahigh molecular weight diblock copolymers and various magnetic nanoparticles (NPs), such as iron platinum, iron oxide and strontium hexaferrite, are presented. The substrate and substrate cleaning prodedure (acid bath cleaning) are described in section 4.2. Finally, the film fabrication techniques and post-treatment method (solvent vapor annealing) are introduced in sections 4.3 and 4.4, respectively.

4.1 Materials

4.1.1 Ultrahigh molecular weight diblock copolymers

To obtain templates with large domain sizes and various desirable nanostructures, different ultrahigh molecular weight diblock copolymers (UHMW DBCs) are utilized. In this thesis, three types of UHMW PS-*b*-PMMA DBCs are employed. The chemical structure of PS-*b*-PMMA is presented in Figure 4.1.

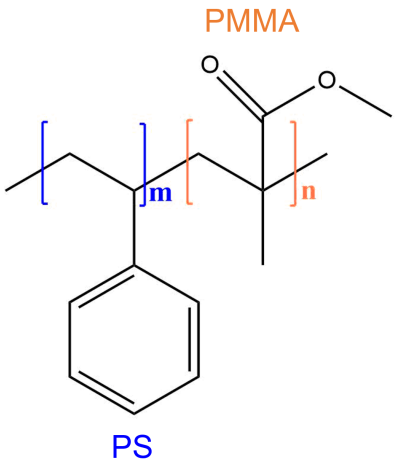

Figure 4.1: *Chemical structure of PS-b-PMMA DBC.*

All used PS-*b*-PMMA DBCs are synthesized via anionic block copolymerization of styrene and methylmethacrylate in tetrahydrofuran (THF) [89]. Table 4.1 shows the details of the UHMW PS-*b*-PMMA DBCs utilized in different chapters. The glass transition temperature (T_g) of PS block and PMMA block are 100 and 105 °C, respectively. According to the self-consistent field theory combined with a very high segregation strength χN (χ: Flory-Huggins interaction parameter, N: total degree of polymerization) between PS and PMMA blocks in UHMW DBC [31,86], spherical strucures are expected for the PS-*b*-PMMA with $f_{PMMA} = 0.07$ and 0.09 used in chapters 5 and 7, respectively. A cylinderical structure is expected for PS-*b*-PMMA ($f_{PMMA} = 0.173$) used in chapters 6 and 8.

chapter	**DBC**	M_n **(kg/mol)**	**PDI**	f_{PMMA}
5	PS_{10193}-*b*-$PMMA_{951}$	1062	1.15	0.07
7	PS_{11384}-*b*-$PMMA_{1290}$	1184	1.18	0.09
6 and 8	PS_{6690}-*b*-$PMMA_{1740}$	870	1.13	0.173

Table 4.1: *Details of used UHMW PS-b-PMMA DBCs.*

Exemplary synthesis of a UHMW PS-*b*-PMMA DBC with $M_n = 1062$ kg/mol (PS_{10193}-*b*-$PMMA_{951}$), which is taken from reference [86] and performed by Gallei group.

Materials. All solvents and reagents are purchased from Alfa Aesar, Sigma Aldrich, Fisher Scientific, ABCR and used as received unless otherwise stated. Deuterated solvents are purchased from Deutero GmbH, Kastellaun, Germany. THF is distilled from sodium/benzophenone under reduced pressure (cryo-transfer) prior to the addition of 1,1 diphenylethylene and *n*-butyllithium (*n*-BuLi) followed by a second cryo-transfer. Styrene and methylmethacrylate (MMA) are dried by stirring over calcium hydride (CaH_2) or trioctylaluminium and cryo-transferred prior to use. All syntheses are carried out under an atmosphere of nitrogen using Schlenk techniques or a glovebox equipped with a Coldwell apparatus.

Experimental section. In an ampule equipped with a stirring bar, 10 mg (0.24 mmol, 260 eq.) LiCl and 760 mg (7.26 mmol, 8013 eq.) neat styrene are dissolved in 60 mL of anhydrous THF. The solution is cooled to -78 °C before the polymerization is initiated by quick addition of 70 μL (0.91 µmol, 0.013 M solution in hexane, 1 eq.) s-BuLi with a syringe. After 1 h an aliquot of the solution is taken from the ampule for characterization of the PS segment and determined by adding methanol. Then, 64 μL (1.81 µmol, 0.028 M solution in hexane, 2 eq.) DPE is added to the active macroanions and the solution is stirred for 1 h at room temperature. After the solution is cooled for 1 h at -80 °C again 150

mg (1.50 mmol, 1653 eq.) MMA is added to the living chains and the solution is stirred for 24 h at -80 °C. After adding a small amount of degassed methanol, the polymer is poured into a 10-fold excess of water. The polymer is collected by filtration, washed with water and dried in vacuum (yield: 815 mg, 90 %). Figure 4.2 shows the molar mass distributions obtained by size-exclusion chromatography (SEC) measurements vs. PS standards in THF obtained for the $PS_{10193-precursor}$ (black line) and PS_{10193}-*b*-$PMMA_{951}$ (red line). Standard SEC is performed with a system composed of a 1260 IsoPump - G1310B (Agilent Technologies), a 1260 VW - detector - G1314F - at 254 nm (Agilent Technologies) and a 1260 RI-detector - G1362A - at 30 °C (Agilent Technologies), THF as the mobile phase (flow rate is 1 mL min^{-1}) on a SDV column set from PSS (SDV 103, SDV 105, SDV 106). Calibration is carried out using PS standards (from Polymer Standard Service, Mainz). For data acquisition and evaluation of the measurements, PSS WinGPC® UniChrom 8.2 is used.

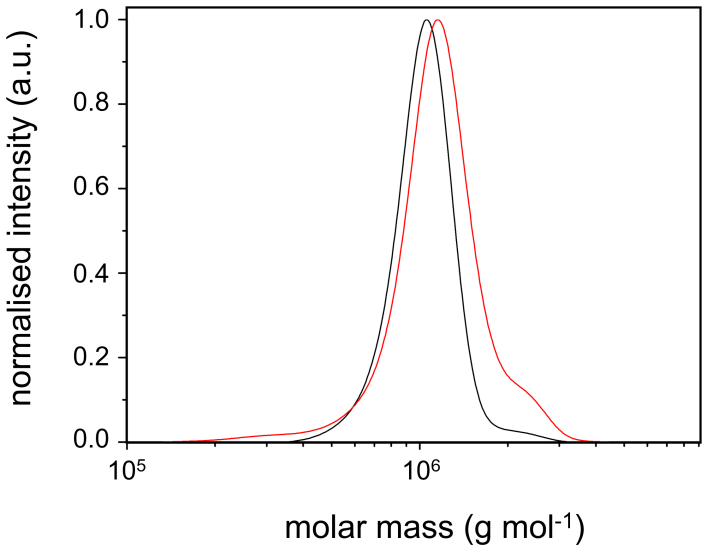

Figure 4.2: *Molar mass distributions obtained by SEC measurements vs. PS standards for the $PS_{10193-precursor}$ (black line) and PS_{10193}-b-$PMMA_{951}$ (red line). The image is modified with permission from reference [86] Copyright 2019 Nature Publishing Group.*

The synthesis other UHMW DBCs, PS_{11384}-*b*-$PMMA_{1290}$ and PS_{6690}-*b*-$PMMA_{1740}$, follows the similar method above but with some small changes on the amount of reagents and their ratios. Also these polymers were synthesized by the Gallei group.

4.1.2 Magnetic nanoparticles

In the present work, three types of magnetic NPs are studied. They are iron platinum NP, iron oxide NP and strontium hexaferrite nanoplatelet. To ensure that the magnetic

NPs can be preferentially located inside a designated block of the DBC template, surface-modified selective NPs are normally required [15, 16]. Thus, all the magnetic NPs used are coated with special organic layers on the surfaces.

Iron platinum NPs

The iron platinum (FePt) NPs are synthesized according to literature [110] by Sun group. They are coated with PMMA, and dissolved in toluene with a concentration of 2 mg mL^{-1}. The morphology of the FePt NPs is shown in Figure 4.3 (TEM images). The average NP radius is around 3.8 ± 0.4 nm (Figure 4.3c). Details of synthesis are shown as follows.

Materials. All solvents are received from commercial sources. Oleylamine (technical grade 70 %), 1-octadecene (90 %), oleic acid (technical grade 90 %), iron pentacarbonyl (Fe(CO)5 (99.999 %), α-bromoisobutyryl bromide (98 %), methyl methacrylate (MMA, 99 %) and tert-Butyl-α-bromisobutyrate (98 %) are purchased from Sigma Aldrich (St. Louis, MO, USA). Platinum(II) acetylacetonate (Pt(acac)2 (98 %) and anhydrous copper chloride (Cu(I)Cl (99.999 %) are purchased from ABCR (Karlsruhe, Germany) and (3-Aminopropyl)triethoxysilane (APTES, 98 %) from TCI Europe. N,N,N′,N′′,N′′-pentamethyldiethylenetriamine (PMDETA) is purchased from Merck KGaA. Prior to use in polymerization MMA is passed through a basic alumina column to remove the inhibitor. Toluene and TEA are dried over CaH_2 and freshly distilled before using. PMDETA and anisole are degassed and stored under argon in a glovebox.

Synthesis of FePt NPs. The synthesis of the FePt NPs are carried out according to the protocol from Li et al. [110]. 5 mL 1 octadecene, 0.13 g Pt(acac)2, 0.7 mL oleylamine and 0.65 mL oleic acid are added to a dry three-neck round bottom flask equipped with a KPG stirrer and an argon inlet. Afterwards the flask is heated up to 120 °C and degassed under an argon flow for at least 30 min. Then 0.11 mL of iron pentacarbonyl is added. In the next step the temperature is increased to 220 °C with a heating rate of 5 °C min^{-1} and kept for 1 h. After cooling to room temperature, 15 mL 2-propanol is added and the NPs are collected by centrifugation (8500 rpm). In addition, the particles are redispersed in hexane, mixed with 15 mL ethanol and again separated by centrifugation (8500 rpm). For further usage, the FePt NPs are redispersed in 30 mL of anhydrous toluene.

Synthesis of 2-bromo-2-methyl-N-(3-(triethoxysilyl)propyl) propenamide. For the synthesis of 2-bromo-2-methyl-N-(3-(triethoxysilyl)propyl) propenamide 150 mL of anhydrous toluene, 1.11 mL triethylamine (TEA) and 1.87 mL APTES are transferred in a dry 250 mL schlenk flask. After cooling the reaction mixture to 0 °C with an ice bath, 0.99 mL 2-Bromoisobutyrylbromide are added dropwise over 30 min. After the complete

addition the reaction mixture is stirred for 2 h at 0 °C and then at room temperature overnight. To isolate the final product, the reaction mixture is filtrated and the solvent evaporated under reduced pressure. Finally, a slightly yellowish oil is obtained.

Modification of FePt NPs with 2-bromo-2-methyl-N-(3-(triethoxysilyl)propyl) propenamide. 30 mL of a FePt-NP dispersion in toluene is added to a round bottom schlenk flask equipped with a mechanical stirrer under an argon atmosphere. Subsequently, 0.1 mL TEA and 0.2 mL 2-bromo-2-methyl-N-(3-(triethoxysilyl)propyl) propenamide are added and the mixture is stirred for 48 h at room temperature. Afterwards, 20 mL petroleum ether are added and the NPs are separated by centrifugation (8500 rpm), redispersed in toluene and re-precipitated by petroleum ether. This step is repeated for two times to remove unreacted initiator. After drying, the particles are redispersed in 25 mL of anisole.

Surface functionalization of FePt NPs with PMMA. 25 mL of the modified FePt NPs dispersion are added to a three-neck round bottom schlenk flask equipped with a mechanical stirrer and an argon inlet. After the addition of 10 mL MMA and 3 μL tert-Butyl-α-bromisobutyrate, the dispersion is heated up to 90 °C. The polymerization is initiated by the addition of 2 mL of a [CuI(PMDETA)Cl] solution (2 M in anisole). After 4 h the mixture is precipitated in an excess of methanol and separated by filtration. The precipitate is redispersed in THF, separated by centrifugation (23000 rpm) and washed three times with THF and two times with toluene. Finally, FePt NPs coated with PMMA are dispersed in toluene.

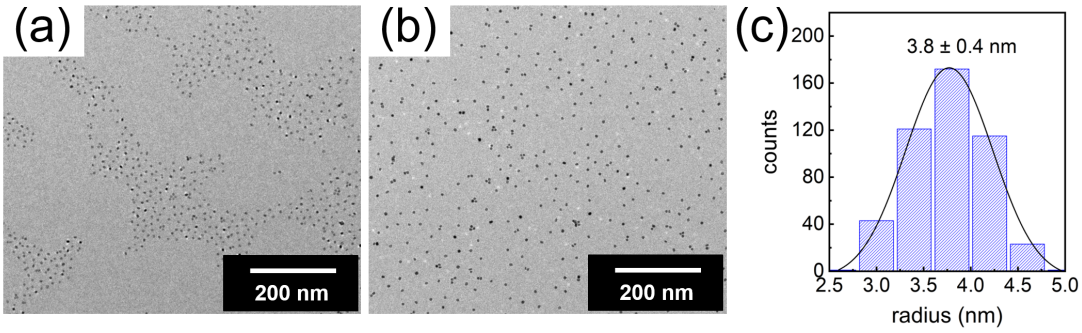

Figure 4.3: *TEM images of FePt NPs (a and b). Radius distribution of the FePt NPs is shown in (c). The image is reprinted with permission from reference [141] Copyright 2021 Wiley-VCH GmbH.*

The surface ligands (PMMA) of FePt NPs are examined by Fourier Transform Infrared Spectroscopy (FTIR), as shown in Figure 4.4. The peaks at 1143, 1720 and 2946 nm^{-1} are related to -C-O-, -C=O- and -C-H- groups, respectively. This reveals that the surface of FePt NPs is modified successfully with PMMA. Thus, the magnetic NPs can be preferentially located inside the PMMA domains of the UHMW PS-*b*-PMMA DBC films.

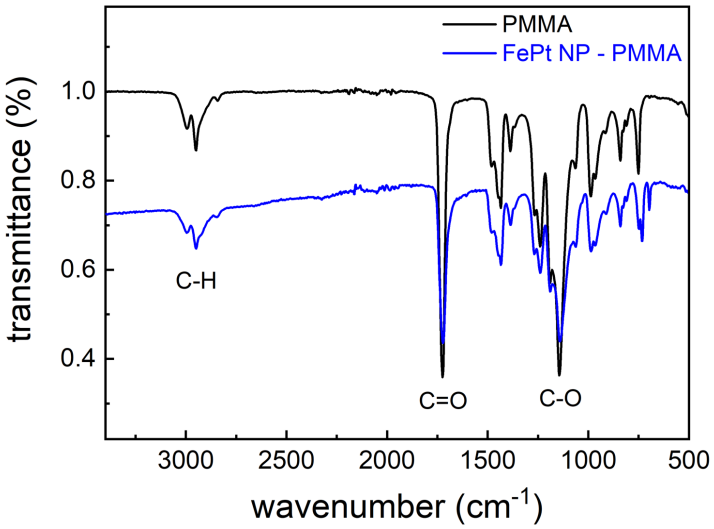

Figure 4.4: *FTIR spectra of PMMA (black curve) and FePt NPs coated with PMMA (blue curve). The image is reprinted with permission from reference [141] Copyright 2021 Wiley-VCH GmbH.*

Iron oxide NPs

Iron oxide NPs (Fe_3O_4) are purchased from Ocean NanoTech (San Diego, CA, United States). They are coated with carboxylic acid groups and dissolved in dimethylformamide (DMF) with a concentration of 5 mg mL^{-1}. The hydrogen bonding between the carboxylic acid ligands of NPs and the ester groups of PMMA allows a slightly higher selectivity of the NPs to PMMA blocks [142, 143]. The morphology of the parent iron oxide NPs is shown in Figure 4.5 (TEM images), and the average NP radius is around 14.3 ± 1.2 nm (Figure 4.5c).

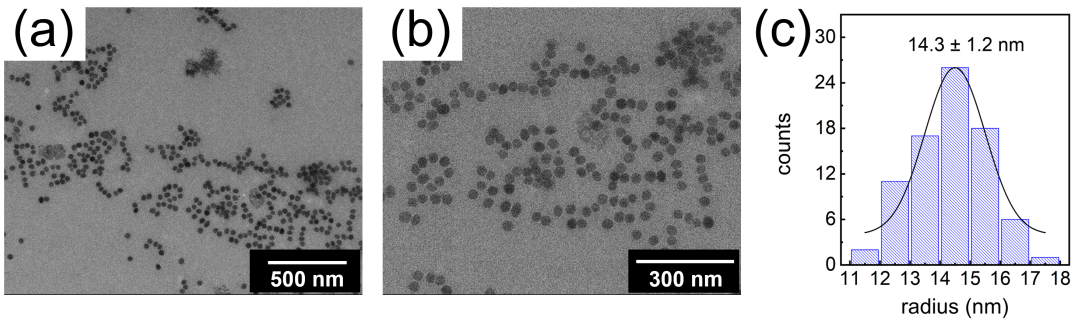

Figure 4.5: *TEM images of the parent iron oxide NPs with different magnifications (a and b). Radius distribution of the iron oxide NPs is shown in (c). The images are modified with permission from the reference [87] Copyright 2020 American Chemical Society.*

Strontium hexaferrite nanoplatelets

As discussed in the section 2.2.3 (magnetic nanoparticles), strontium hexaferrite ($SrFe_{12}O_{19}$) nanoplatelets have high coercivity. They are hard magnetic materials with a platelet-like shape and a high magnetic anisotropy. The $SrFe_{12}O_{19}$ nanoplatelets are synthesized according to literature [35] by Trusov group. They are coated with polyacrylic acid (PAA) according to the publication from Sehgal et al. [144], and dissolved in dimethylformamide (DMF) with a concentration of 2 mg mL^{-1}. Due to the hydrogen bonding between the ester groups of PMMA and the PAA ligands of magnetic nanoplatelets, the magnetic nanoplatelets should be preferentially located inside the PMMA domains of the UHMW PS-*b*-PMMA DBC films [145]. The morphology of the $SrFe_{12}O_{19}$ nanoplatelets is shown in Figure 4.6a-d (TEM images). As shown in Figure 4.6e and 4.6f, the nanoplatelets' average diameter of the large facet is around 39 ± 15 nm and average thickness is around 5.5 ± 1.1 nm. However, the nanoplatelet is not a standard disk. The large facet of the nanoplatelet can be treated as a rectangle with an average length of around 50 nm and an average width of around 28 nm.

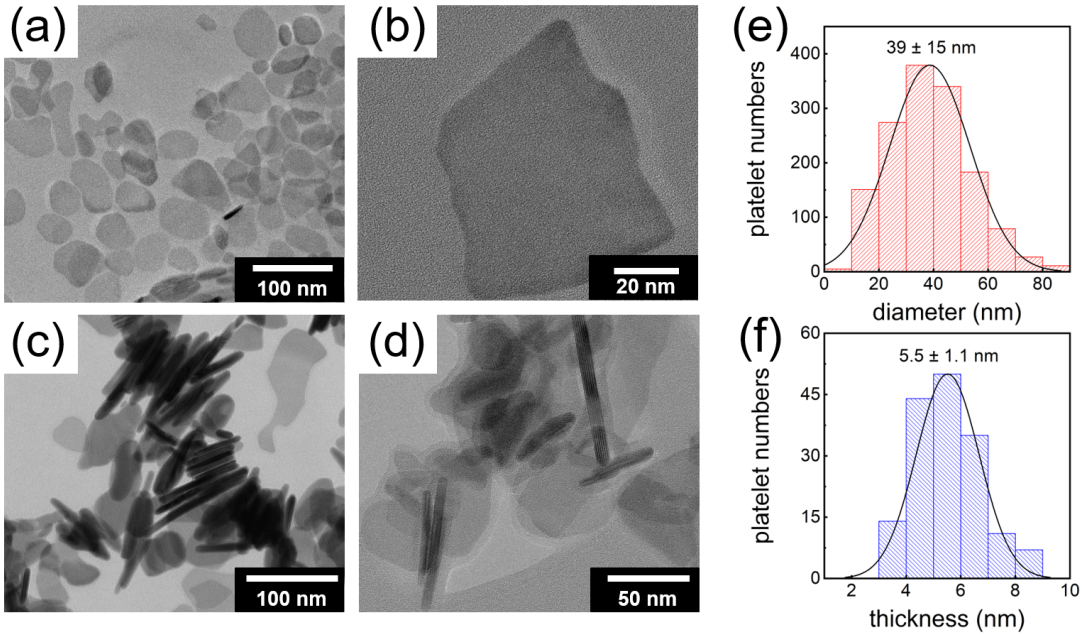

Figure 4.6: *TEM images of the $SrFe_{12}O_{19}$ nanoplatelets (a-d). (a and b) The large facet and (c and d) the thickness (height) of the nanoplatelets. Diameter distribution of the large facet and thickness distribution of the strontium hexaferrite nanoplatelets are shown in (e) and (f), respectively. The images are reprinted with permission from the reference [146] Copyright 2020 American Chemical Society.*

The surface ligands (PAA) of magnetic nanoplatelets are examined by FTIR, as shown

in Figure 4.7. The peaks observed at 1465 and 2913 nm^{-1} are related to -C-H_2- groupds, providing the existence of PAA in the film. Moreover, peaks at 1175, 1740, 2851 and 3438 nm^{-1} are also observed, related to -C-O-, -C=O-, -C-H- and -O-H- groupds, respectively. All these results reveal that the surface of magnetic nanoplatelets is coated with PAA.

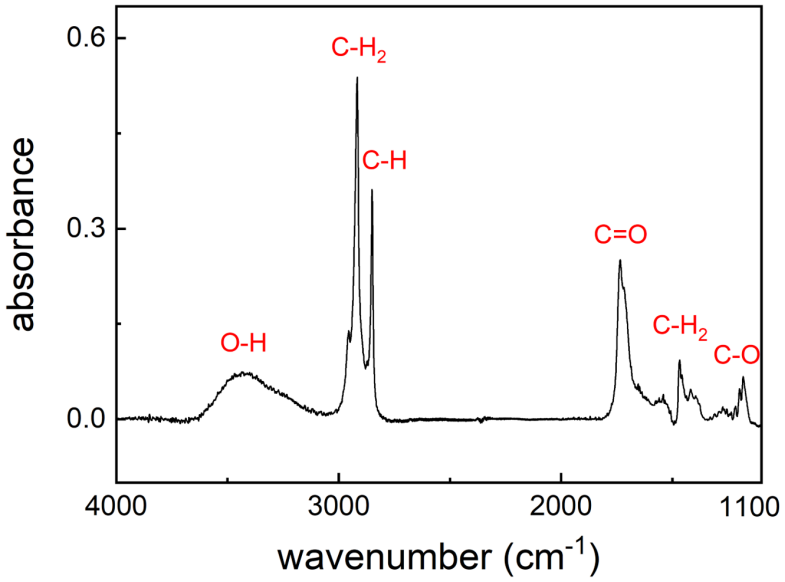

Figure 4.7: *FTIR spectra of the strontium hexaferrite nanoplatelets coated with PAA. The image is reprinted with permission from the reference [146] Copyright 2020 American Chemical Society.*

4.2 Substrates

Silicon substrates (Si, p-type, Silchem) with a thickness of 525 μm, (100) orientation and nature oxide layer are used for film deposition. They are cut into pieces with different sizes related to different film deposition methods, such as 15 mm × 15 mm for spin-coating, 25 mm × 80 mm for printing and 20 mm × 20 mm for spray deposition.

Acid bath cleaning

Before film fabrication and after cutting, all substrates undergo a cleaning step with an acid bath for better film deposition. They are immersed into a freshly prepared acid bath at 80 °C for 15 min. The acid bath is composed of 198 mL of H_2SO_4, 84 mL H_2O_2 and 54 mL H_2O. Finally, the substrates are thoroughly rinsed with deionized water (DI water), dried with nitrogen gas (N_2) and placed in a sealed sample box [147].

4.3 Film fabrication techniques

Since the UHMW PS-*b*-PMMA DBCs and all magnetic NPs are soluble in organic solvents, magnetic NP-DBC hybrid films can be fabricated easily via various techniques, such as spin-coating, solution-casting, spray deposition and printing. In this thesis, spin-coating, printing and spray deposition are applied and are described in the following sections 4.3.2, 4.3.3 and 4.3.4, respectively.

4.3.1 Solution preparation

To obtain homogeneous films, all materials (UHMW PS-*b*-PMMA DBC and magnetic NPs) need to be well dissolved in the selected solvents. Generally, toluene is considered as a good solvent for dissolving PS-*b*-PMMA with sufficient volatility [148,149]. However, toluene is a hydrophobic solvent, which cannot be combined with hydrophilic materials for extending applications. Thus, in the present work, a hydrophilic solvent, namely DMF, is applied for dissolving the materials conatining UHMW PS-*b*-PMMA DBC and magnetic NPs (Fe_3O_4 and $SrFe_{12}O_{19}$ nanoplatelets) in chapters 5, 7 and 8. While in chapter 6, toluene is used to prepare homogeneous films by printing to study the kinetic processes during printing. Since DMF has a boiling point of 153 °C [150], the drying time of the film prepared with DMF at room temperature is long, and it is difficult to obtain a homogeneous film via printing. Moreover, the kinetic processes of the film formation of the DBC and the magnetic NPs are investigated during printing.

UHMW PS-*b*-PMMA DBC

In chapter 5, DBC solutions in DMF with various concentrations (1.0, 3.0, 5.0, 10.0, 15.0 and 20.0 mg mL^{-1}) are prepared with shaking for 24 h to adjust the film thickness. To investigate the influence of solvent vapor annealing time on DBC morphology, eight solutions with a same DBC concentration (15.0 mg/mL) are prepared.

UHMW PS-*b*-PMMA DBC/FePt

In chapter 6, two UHMW PS-*b*-PMMA solutions with and without fcc-FePt NPs are prepared in toluene with a fixed PS-*b*-PMMA concentration of 7 mg mL^{-1}. For the PS-*b*-PMMA solution with fcc-FePt NPs, the weight ratio of NPs to PS-*b*-PMMA is 3 wt %. The UHMW PS-*b*-PMMA DBC is dissolved in toluene and shaken for 24 h before the addition of FePt NPs.

UHMW PS-*b*-PMMA DBC/Fe_3O_4

In chapter 7, for thin hybrid films: UHMW PS-*b*-PMMA DBC is dissolved in DMF and shaken for 24 h. Various concentrations of Fe_3O_4 NPs are added into the DBC solution with a fixed polymer concentration of 15 mg mL^{-1}. In this case, eight different weight ratios of Fe_3O_4 NPs to PS-*b*-PMMA (0, 0.1, 0.5, 1, 2, 5, 10, and 20 wt %) are investigated. In contrast, for thick hybrid films prepared for TEM measurement: mixed solutions PS-*b*-PMMA and Fe_3O_4 NPs) are prepared according to the preparation of thin films with a fixed polymer concentration of 15 mg mL^{-1}. However, only two different weight ratios of Fe_3O_4 NPs to PS-*b*-PMMA (0.5 and 5 wt %) are investigated.

UHMW PS-*b*-PMMA DBC/$SrFe_{12}O_{19}$

In chapter 8, a pure UHMW PS-*b*-PMMA reference solution and a UHMW PS-*b*-PMMA solution with $SrFe_{12}O_{19}$ nanoplatelets are prepared. The polymer concentration is fixed at 6 mg mL^{-1} with a solvent DMF. For the PS-*b*-PMMA solution with $SrFe_{12}O_{19}$ nanoplatelets, the weight ratio of nanoplatelets to PS-*b*-PMMA is 3 wt %. The UHMW PS-*b*-PMMA DBC is dissolved in DMF and shaken for 24 h before the addition of $SrFe_{12}O_{19}$ nanoplatelets.

4.3.2 Spin-coating

Spin-coating is a widely-used, fast and highly reproducible technique for fabrication of homogeneous thin films, especially for lab-scale thin film fabrication [151]. In this thesis (chapters 5 and 7), pure UHMW PS-*b*-PMMA DBC films and UHMW PS-*b*-PMMA DBC/Fe_3O_4 hybrid films are fabricated by spin-coating. The used spin coater is a Delta 6 RC TT device by Süss MicroTec Lithography GmbH. Figure 4.8a shows the schematic representation of the working principle of film fabrication via spin-coating. Firstly, a pre-cleaned substrate is placed on the center of a rotary plate and is sucked via a vacuum pump. Then, the solution is dropped and is covered on the whole surface of the substrate. Afterwards, the substrate with the solution is rotated under pre-set parameters. Finally, a film with a defined film thickness is achieved. In our experiments, the films are fabricated by spin-coating at 1200 rpm for 60 s with an acceleration time of 9 s in the presence of flowing nitrogen (N_2) gas. The nitrogen pressure is set to 1.8 bar to ensure a better evaporation of the solvent DMF for obatining homogeneous films. Figure 4.8b shows an AFM image of an UHMW PS-*b*-PMMA DBC film fabricated by spin-coating without any post-treatment. The obtained film displays a disordered surface structure with continuous domains. Since spin-coating is a fast established process, the DBC structure is frozen in

a short period of time. In this case, the UHMW PS-*b*-PMMA DBC does not approach thermodynamic equilibrium to form ordered structures by microphase separation.

The thickness (t) of spin-coated film can be obatined by [152, 153]

$$t = A\omega^{-1/2} c_o M^{1/4} \tag{4.1}$$

where A is an experimental parameter determined by the preparation system (such as the used spin coater and the actual environmental situations). ω, c_o and M are angular velocity, solution concentration and molar mass of the DBC, respectively.

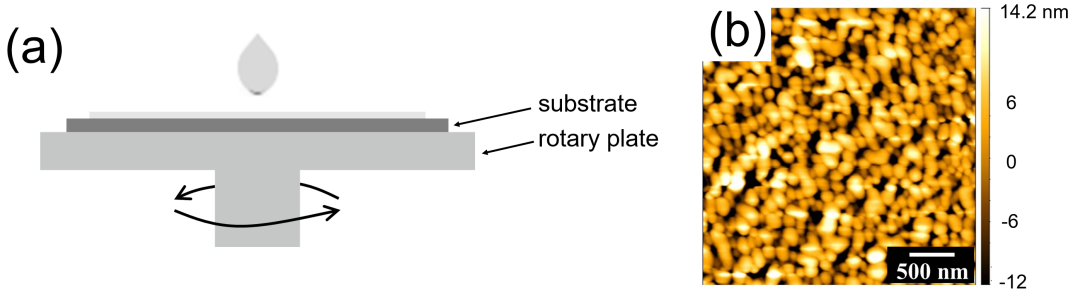

Figure 4.8: *(a) Schematic representation of the working principle of film fabrication via spin-coating. (b) AFM image of an UHMW PS-b-PMMA DBC film fabricated by spin-coating without any post-treatment.*

4.3.3 Printing

Printing is a solvent evaporation based scalable technique [99], which can provide the possibility of in situ investigation of the film formation process via GISAXS measurements. Figure 4.9 shows a schematic of the printing with simultaneous in situ GISAXS measurements, which is used to study kinetic processes during magnetic hybrid film (PS-*b*-PMMA and fcc-FePt NPs) formation via printing.

Printing is performed on a pre-cleaned silicon substrate with a custom-made slot-die coater and constructed in the context of a Master's thesis [152]. As shown in Figure 4.10a, a syringe pump provides a constant flow rate of the DBC or magnetic NP-DBC solution. The solution is transported through a polytetrafluoroethylene (PTFE) semitransparent tube to the printer head. An enlarged view of the printer head installed above the sample stage is shown in Figure 4.10b. The movement of sample stage is controlled by a motor. Then, the solution is guided through a solution guide mask and a meniscus guide mask for printing. The printing width is defined by the solution channel in the die and the

meniscus guide mask width. The two masks are attached inside a printer head, which can be seen clearly from Figure 4.11.

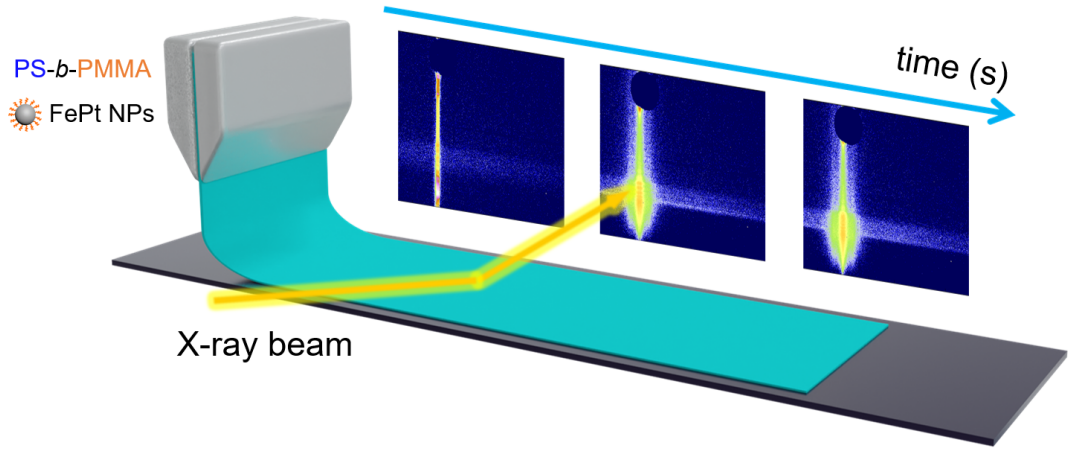

Figure 4.9: *Schematic of the printing with simultaneous in situ GISAXS measurements.*

The printer head is composed of solution inlets, front endplate, solution guide mask, meniscus guide mask and back endplat. The last four components can be seen clearly from Figure 4.11b.

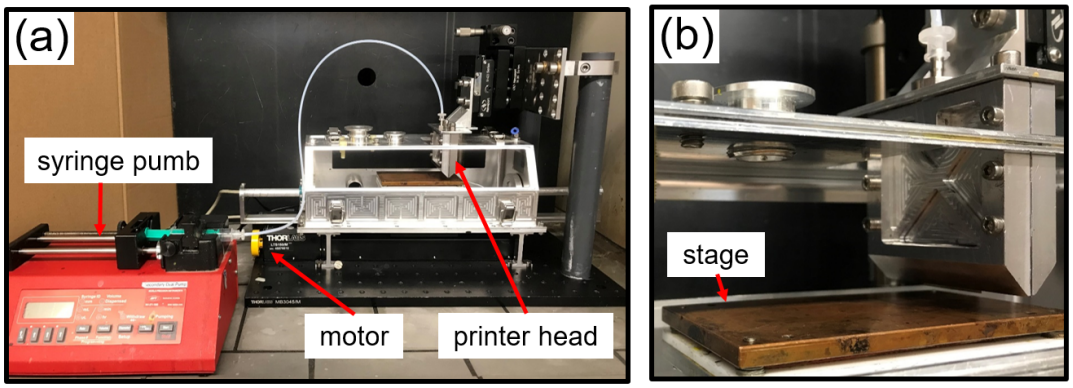

Figure 4.10: *(a) Photograph of the set-up for meniscus guided slot-die coating. (b) An enlarged view of the printer head installed above the sample stage. Selected components are labeled with red arrows in (a) and (b).*

In this thesis, all printed films are performed at ambient conditions. To achieve favorable thicknesses of the printed films, the solution flow rate, printing velocity and distance between the mask and the substrate are set to 0.1 mL min^{-1}, 5 mm s^{-1} and 0.5 mm, respectively.

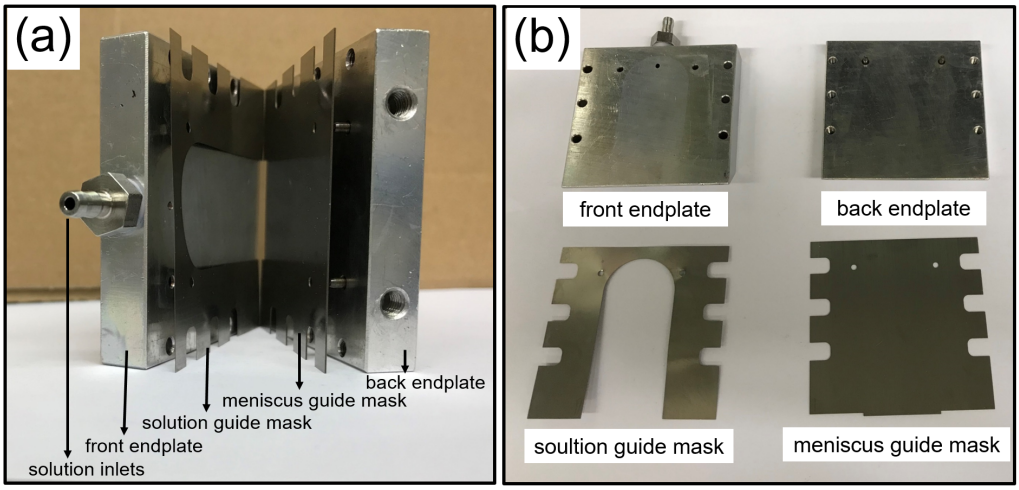

Figure 4.11: *(a) Photograph of the exploded printer head. The names of different components are shown in the figure accordingly. (b) Photographs of front endplate, back endplat, solution guide mask and meniscus guide mask.*

4.3.4 Spray deposition

Spray deposition, a technique, has obtained great attention because of its ability with large scale fabrication. Moreover, spraying can provide the possibility of in situ investigation of the film formation process via GISAXS measurements [13, 154]. A schematic of the spray deposition with simultaneous in situ GISAXS measurements is shown in Figure 4.12.

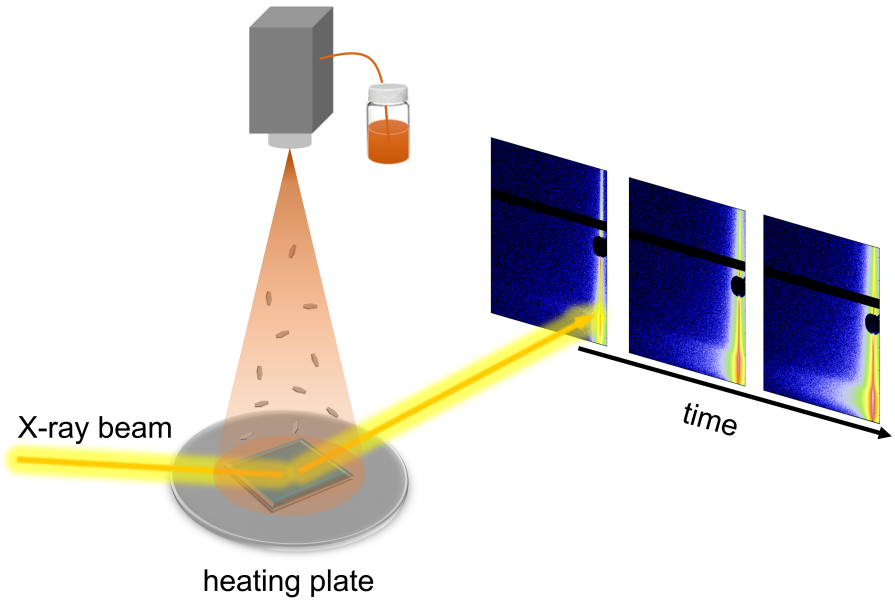

Figure 4.12: *Schematic of the spray deposition with simultaneous in situ GISAXS measurements.*

The details of spray deposition with simultaneous in situ GISAXS measurements in chapter 8 are shown follows. A spray gun (Compact JAU D55500, Spraying Systems Germany GmbH) is fixed on a custom made spray setup and orientated vertically to the pre-cleaned silicon substrate (20 mm × 20 mm). For the spray gun, an air atomizing nozzle (Stainless Steel 1.4404) is used. The distance between the substrate and the nozzle is set to 190 mm. To ensure a rapid evaporation of the solvent DMF (boiling point: 153 °C), the temperature of the substrate is controlled via a heating plate (DHS1100 Anton Paar) and set to 170 °C. For spray deposition, it is carried out by atomizing the polymer solutions with compressed nitrogen under a gauge pressure of 0.6 bar.

In the experiment, the spray protocol follows our previous work [155] with slight modifications as shown in Figure 4.13. One full spray cycle is defined as 0.1 s spray-on (spraying) and 2 s spray-off (waiting). In total, 20 full cycles are applied. The thickness values of the final deposited pure film and hybrid film are around 456 ± 52 nm and 514 ± 41 nm, respectively.

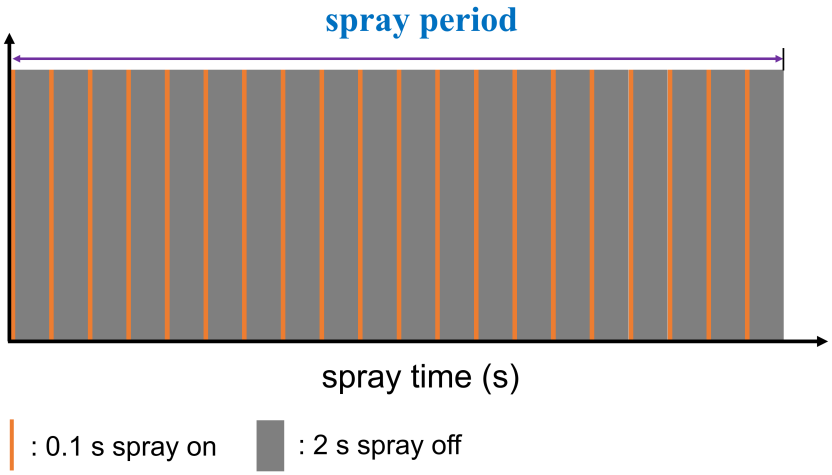

Figure 4.13: *Schematic of the used spray protocol (spray-on and spray-off) in this thesis.*

4.4 Post-treatment

As discussed in the introduction, the fabrication of ordered nanostructured films with UHMW PS-*b*-PMMA DBCs is challenging. UHMW PS-*b*-PMMA DBCs do not easily approach thermodynamic equilibrium to form ordered nanostructures even with a post-treatment of thermal annealing because of their highly entangled chain conformations (very low chain mobility) [18]. To address this issue, solvent vapor annealing (SVA) can be used. Through the SVA process, the mobility of the long polymer chains can be

effectively enhanced [20,86]. As a result, ordered structures in UHMW PS-*b*-PMMA DBC films and magnetic hybrid films can be realized if a suitable annealing time is applied.

Solvent vapor annealing

In this thesis, THF is used as a good solvent vapor for both blocks of PS-*b*-PMMA, which exhibits a small selectivity to PS [156]. As shown in Figure 4.14, a desiccator (volume, V = 942.3 cm^3 and surface area, S = 519.7 cm^2) is used for THF vapor atmosphere creation. Inside the desiccator, a porous plate on which the samples are placed, is positioned over the liquid solvent. The desiccator is tightly sealed with PARAFILM® M (Carl Roth GmbH+Co. KG), which consists mostly of polyolefin and paraffin waxes. The whole SVA process is carried out at room temperature and the solvent vapor pressure is saturated in equilibrium. After SVA, all films are removed from the desiccator as quickly as possible to allow for a preservation of the obtained nanostructures [157], rather than deswelling the films at slow rates [158].

During SVA, the UHMW PS-*b*-PMMA DBC film is swollen by THF molecules. The T_g of the PS-*b*-PMMA is decreased and the mobility of the long polymer chains in UHMW PS-*b*-PMMA DBCs is enhanced [86]. The mobile chains are able to adjust themselves to approach thermodynamic equilibrium to form ordered structures by microphase separation. The final morphology of the UHMW PS-*b*-PMMA DBC film mainly depends on three parameters, such as solvent selection, annealing time and solvent removal rate [74,159–161]. To simplify, a fixed solvent THF and a fast solvent removal rate are applied. For SVA process, the structural evolution of the obtained UHMW DBC thin films is investigated as function of increasing SVA time and shown in chapter 5.

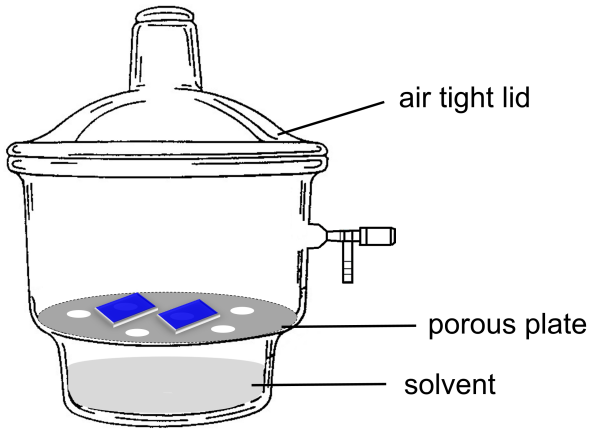

Figure 4.14: *A desiccator set-up utilized for SVA.*

5 Fabrication of ordered polymer template with a large domain size

Parts of this chapter have been published in the article: Self-Assembly in ultrahigh molecular weight sphere-forming diblock copolymer thin films under strong confinement [86] (Reprinted with permission from (W. Cao et al., *Sci. Rep.*, 2019, 9, 18269). Copyright (2019) Springer Nature. DOI: 10.1038/s41598-019-54648-3).

Ultrahigh molecular weight diblock copolymers (UHMW DBCs) continue to attract attention due to their ability to form periodic templates with large domain sizes [18,19]. By applying post-treatments, such as thermal annealing and solvent vapor annealing (SVA), the fabrication of ordered nanostructured films with UHMW DBCs can be achieved [19, 88]. For example, Kim et al. combined thermal annealing and SVA to achieve ordered large domain sized lamellar nanostructures of polystyrene-*block*-poly(methyl methacrylate) (PS-*b*-PMMA) films [88]. With SVA, Mokarian-Tabari et al. reported highly ordered hexagonally packed domain patterns of domain size above 100 nm based on an UHMW DBC poly(styrene-*b*-2-vinylpyridine) (PS-*b*-P2VP) [19].

Similar to DBCs with low or intermediate molecular weights, the type and size of the periodic nanostructure of UHMW DBCs are significantly influenced by the SVA conditions, such as polymer–solvent interaction parameters (A block-solvent and B block-solvent) as well as the swollen film thickness [11, 30, 162–164]. Moreover, the final morphology of UHMW DBCs is also determined by the film thickness in terms of thin films. However, systematic studies on the influence of film thickness and SVA on the morphology of UHMW DBC films are rarely reported [47–49]. It is of high significance to systematically study the influence of film thickness and SVA on the structure evolution of UHMW DBC thin films for a better application.

In this chapter, we exploit a hydrophilic solvent, namely dimethylformamide (DMF), for dissolving an asymmetric UHMW PS-*b*-PMMA DBC to fabricate ordered large-sized spherical nanostructured thin films. The structural evolution of the fabricated UHMW DBC thin films is systematically investigated as function of increasing film thickness and SVA time. Surface structures of the films are probed via AFM, and the buried structures are detected with GISAXS. Results show that an ordered nanostructure with an average half-sphere diameter of around 82 nm and an average inter-domain distance of around 151 nm can be achieved for the studied UHMW DBC thin films through the control of the film thickness and the SVA time.

5.1 Surface and inner morphologies

Films are fabricated by spin-coating at 1200 rpm for 60 s in the presence of flowing nitrogen (N_2) gas as described in chapter 4. If the flowing nitrogen gas is not applied, the surface of all films is heterogeneous and rough (Figure 5.1), especially at high concentrations (10.0, 15.0 and 20.0 mg/mL), owing to the use of the low volatile solvent DMF (boiling point, T_b = 153 °C) [156].

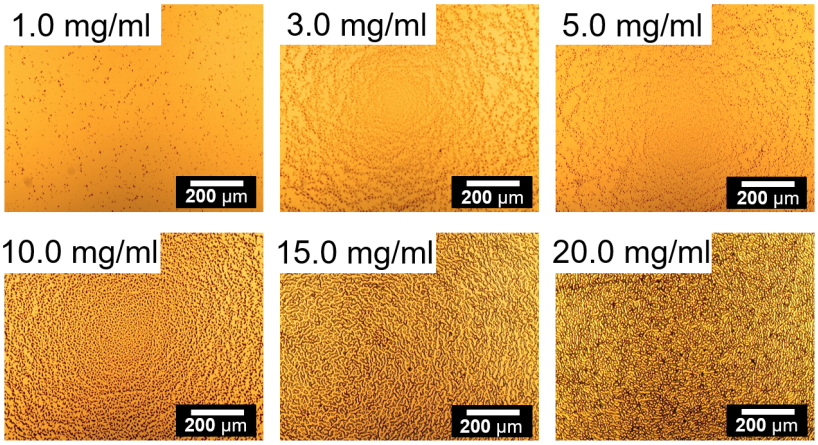

Figure 5.1: *Optical microscopy images of PS-b-PMMA films prepared at a fixed spin coating speed of 2500 rpm without use of N_2 gas at different PS-b-PMMA concentrations as indicated.*

In order to enhance the homogeneity of the films, we prepare the films via spin-coating combined with a fixed flow rate of N_2. As shown in Figure 5.2, homogeneous thin films can be achieved by decreasing the spin coating speed to 1200 rpm. We attribute this improvement to a complex competition between the N_2 gas (accelerated DMF volatilization) and the decrease of spin coating speed (decelerated DMF volatilization) [156, 165].

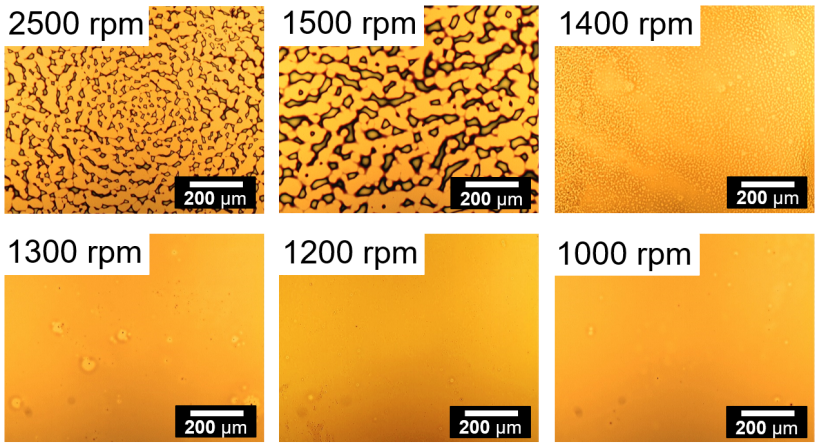

Figure 5.2: *Optical microscopy images of PS-b-PMMA films prepared with different spin coating speeds as indicated, using a fixed flow rate of nitrogen gas. The concentration of PS-b-PMMA is 15.0 mg/mL.*

5.1.1 Influence of film thickness

In previous studies, it was reported that increasing film thickness to a thin film monolayer, the half-spherical morphology is hexagonal packing in case of a normal molecular weight block copolymer film [47, 48, 50]. Moreover, a random island-like morphology is usually observed in thermally equilibrated films, due to the very high confinement effects between the film thickness (t) and inter-domain distance (L_0).

To investigate if these findings can be extended into the regime of UHMW DBCs, films with different film thicknesses have been prepared by spin coating on pre-cleaned substrates. The film thickness is controlled to be no more than 0.5 L_0 to obtain a thin film and the resulting system is highly confined.

The film thickness ($c > 3.0$ mg/mL) is measured by XRR (Figure 5.3a). Smaller concentrations ($c \leq 3.0$ mg/mL) lead to discontinuous and rough spin coated films (dewetting), which cannot be probed by XRR [166]. Therefore, surface profilometry is utilized as complementary measurement method for these films. Figure 5.3b shows the thickness of PS-*b*-PMMA thin films at different concentrations. The film thickness increases from 7 ± 2 nm nearly-linear to 91 ± 1.6 nm with increasing PS-*b*-PMMA concentration. Thus, also for UHMW PS-*b*-PMMA DBC the predictions from the spin coating equation are fullfilled [152].

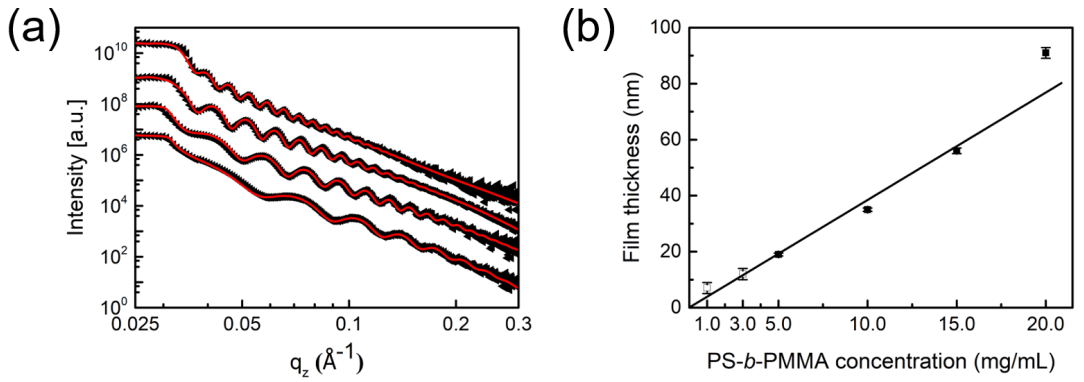

Figure 5.3: *(a) XRR data (symbols) with fits (red solid lines) of PS-b-PMMA films produced with different concentrations. Curves from bottom to top refer to PS-b-PMMA films with concentrations of 5.0, 10.0, 15.0 and 20.0 mg/mL DBC in DMF. (b) Film thickness plotted as a function of PS-b-PMMA concentration as measured by profilometry (empty box) and XRR (solid box). The solid line represents a linear correlation of film thickness and PS-b-PMMA concentration. (Reprinted with permission from [86]. Copyright 2019 Nature Publishing Group.)*

Surface morphology

As seen in Figure 5.4, AFM height images show the evolution of the film surface morphology with different film thicknesses after SVA (THF, 18.0 h), in which bright domains and a dark matrix are the PMMA and PS block segments, respectively. According to the self consistent field theory, the morphology of the DBC with a PMMA volume fraction of 0.07 should be sphere-type. This is confirmed by the previous study on thick DBC films (1 mm) of this UHMW DBC [26]. Moreover, the distribution of PMMA half-sphere size/distance for various film thicknesses are calculated statistically from the corresponding AFM images by using Image J 1.46r and shown in Figure 5.5. Relatively ordered nearly half PMMA spheres with a diameter (D) of 87 ± 11 nm (Figure 5.5b) and an inter-domain distance of 192 ± 27 nm (Figure 5.5e) are observed when the film thickness is 56 nm (Figure 5.4e).

For a better view of the phase separation structures of UHMW PS-*b*-PMMA DBC films, the corresponding AFM phase images are displayed in Figure 5.6. The half-spherical morphology follows locally a hexagonal packing ("hand"-drawn green hexagons in Figure 5.4e and 5.6e) but is irregular on a large scale (ring-like 2D fast Fourier transform pattern in Figure 5.6e). Since the film thickness (56 nm) is less than D (diameter of PMMA half-sphere, 82 nm), but higher than 0.5 D (41 nm), the arrangement of a full sphere is not favorable. Moreover, the morphology with half-spheres can maximize the conformational entropy of the polymer chains in the lateral direction [57, 58].

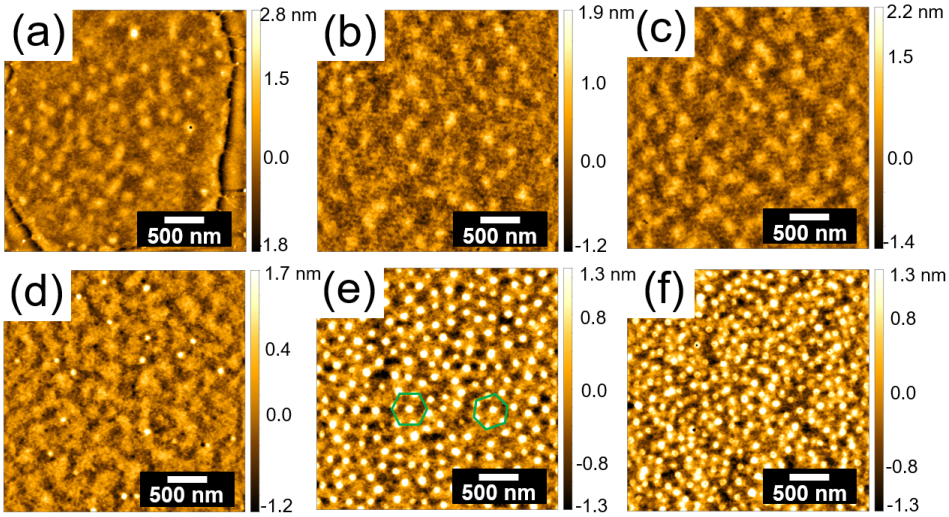

Figure 5.4: *AFM height images of PS-b-PMMA thin films with thickness of (a) 7 nm, (b) 12 nm, (c) 19 nm, (d) 35 nm, (e) 56 nm, and (f) 91 nm after SVA in THF for 18 h. The height bar is adapted individually as indicated. The green hexagons indicate that the positions of these half-spheres are not well located at the apex of the hexagon. (Reprinted with permission from [86]. Copyright 2019 Nature Publishing Group.)*

For thinner films (7 nm, 12 nm, and 19 nm), a disordered elongated structure is seen. No phase separation is found in the corresponding AFM phase images (Figure 5.6a, 5.6b, and 5.6c). This is related to the confinement effects between the film thickness and inter-domain distance, because the films are too thin to form a layer with spherical nanostructure [167]. Moreover, the effect of dewetting cannot be ignored, especially for the thinnest film (7 nm) [168]. A film edge (dark line) is seen in local areas in Figure 5.4a, indicating insufficient surface coverage and island formation [169].

As the film thickness increases to 35 nm, the elongated structures still exists while some half-spheres appear as well. Partial PMMA half-spheres randomly appear in the film, due to the film thickness which is not sufficient to support the formation of one layer of PMMA half-spheres. Moreover, the value of thickness is close to the value of the PMMA radius (around 44 nm at a film thickness of 56 nm), which increases the possibility of forming PMMA half-spheres.

Figure 5.5a shows that the obtained PMMA half-spheres in Figure 5.4d have a radius of around 39 nm, which is larger than the value of film thickness (35 nm). This indicates that the half-spheres might be compressed in the vertical direction. In a thicker film (91 nm, Figure 5.4f), the distance between neighboring PMMA half-spheres seems to be reduced as compared with the thickness of 56 nm. However, from the corresponding AFM phase image (Figure 5.6f), the distance (Figure 5.5f, 191 $\pm$ 24 nm) does not change and the

spherical size (Figure 5.5c, 83 ± 9 nm) only slightly decreases. Such difference between the height image and phase image might be attributed to the surface defects from PS chains.

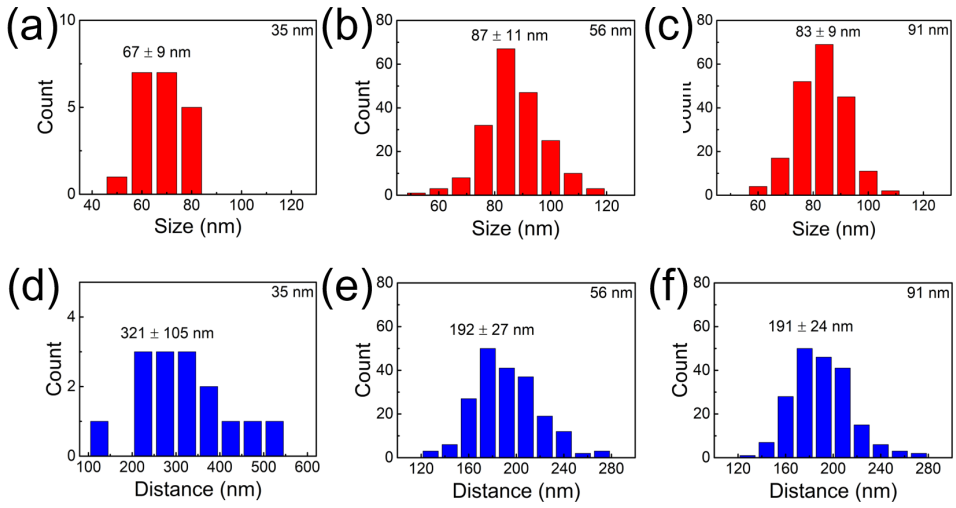

Figure 5.5: *Half-sphere size distribution (red bar chart) and distance distribution (blue bar chart) of PS-b-PMMA thin films (SVA time is 18.0 h) with thickness of (a + d) 35 nm, (b + e) 56 nm, (c + f) 91 nm. Distance is the distance between neighboring PMMA half-spheres. All of the data are calculated statistically from the corresponding AFM images by using Image J 1.46r. (Reprinted with permission from [86]. Copyright 2019 Nature Publishing Group.)*

In thicker film the polymer has sufficient space in the vertical direction to adopt an unperturbed chain conformation. In addition, "hand"-drawn green hexagons and ring-like 2D fast Fourier transform (FFT) pattern in Figure 5.6f confirm the only locally regular hexagonal packing of these PMMA half-spheres.

Inner morphology

In order to study the inner morphology of the films with high statistical relevance, all films are investigated by GISAXS after SVA in THF for 18 h [129]. The large footprint of the X-ray beam, which has its origin in the shallow grazing incidence angle, allows for probing a large film volume and therefore yields lateral structure information of the films with high statistical relevance. Horizontal line cuts of the 2D GISAXS data (Figure 5.7) are done at the Yoneda peak position of PS-*b*-PMMA. They reveal lateral structure sizes, as depicted in Figure 5.8. For quantitative analysis, the horizontal line cuts are fitted in the framework of the distorted-wave Born approximation (DWBA) using the effective interface approximation (EIA). In the model a half spherical geometry of the scattering

objects is assumed to match the AFM observations, which is based on the ratio of sphere diameter to film thickness [129].

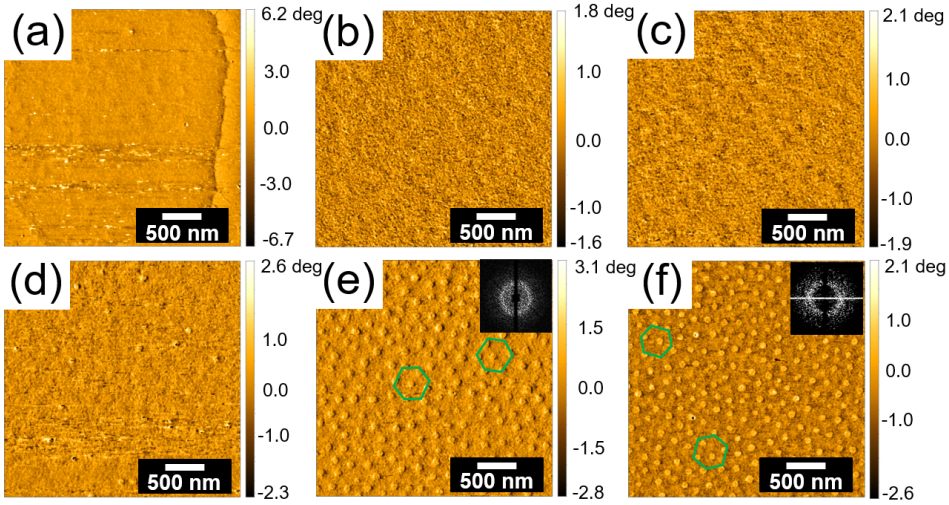

Figure 5.6: *AFM phase images of PS-b-PMMA thin films with thickness of (a) 7 nm, (b) 12 nm, (c) 19 nm, (d) 35 nm, (e) 56 nm, and (f) 91 nm after SVA in THF for 18 h. The green hexagons indicate that the positions of these half-spheres are not well located at the apex of the hexagon.On the top right corners, the insets show the corresponding 2D fast Fourier transform (FFT) patterns. (Reprinted with permission from [86]. Copyright 2019 Nature Publishing Group.)*

In case of a film thickness of 35 nm, compared to thinner films (7 nm, 12 nm, 19 nm), an additional half spherically shaped scattering object is needed to fit the data and to account for the presence of half-spheres as also seen in the AFM data. The form factors refer to the radius of the PMMA half-spheres, the structure factors describe the center-to-center distances of neighboring PMMA half-spheres (inter-domain distance). Moreover, a constant Ornstein-Zernike-like contribution is needed to describe the data at large q_y values, accounting for fluctuations on small scale [170, 171].

The fitted curves are shown as solid red lines in Figure 5.8a. The half-sphere radii and distances are extracted from the fits and shown in Figure 5.8b and 5.8c, respectively. For films with thicknesses $\leq$ 35 nm, a broad peak I around $q_y = 0.037$ nm^{-1} (marked with the green solid arrow in Figure 5.8a) is seen, which is the elongated (less ordered) PMMA nanostructure. The corresponding radius is about 52 nm and inter-domain distance is about 170 nm, respectively. For the film thickness $\geq$ 35 nm, another broad peak II is observed in the smaller q_y region (marked with the blue arrow in Figure 5.8a), which indicates the structure of the PMMA half-spheres.

As the film thickness increases from 35 nm to 56 nm, a layer of ordered half-spheres appears (AFM image, Figure 5.4e), the inter-PMMA half-spheres' distance decreases, resulting in the peak II moves to higher q_y value (shown in Figure 5.8a). The corresponding radius remains constant at about 41 nm, while the inter-domain distance decreases from 225 nm to 172 nm. For the thickest film (91 nm), the peak II becomes more prominent, indicating that an improved order is formed. The improved order is related to the larger available space in vertical direction (larger film thickness) for the arrangement of the polymer chains inside the film. The corresponding half-sphere radius and distance remain constant at around 41 nm and 172 nm, respectively.

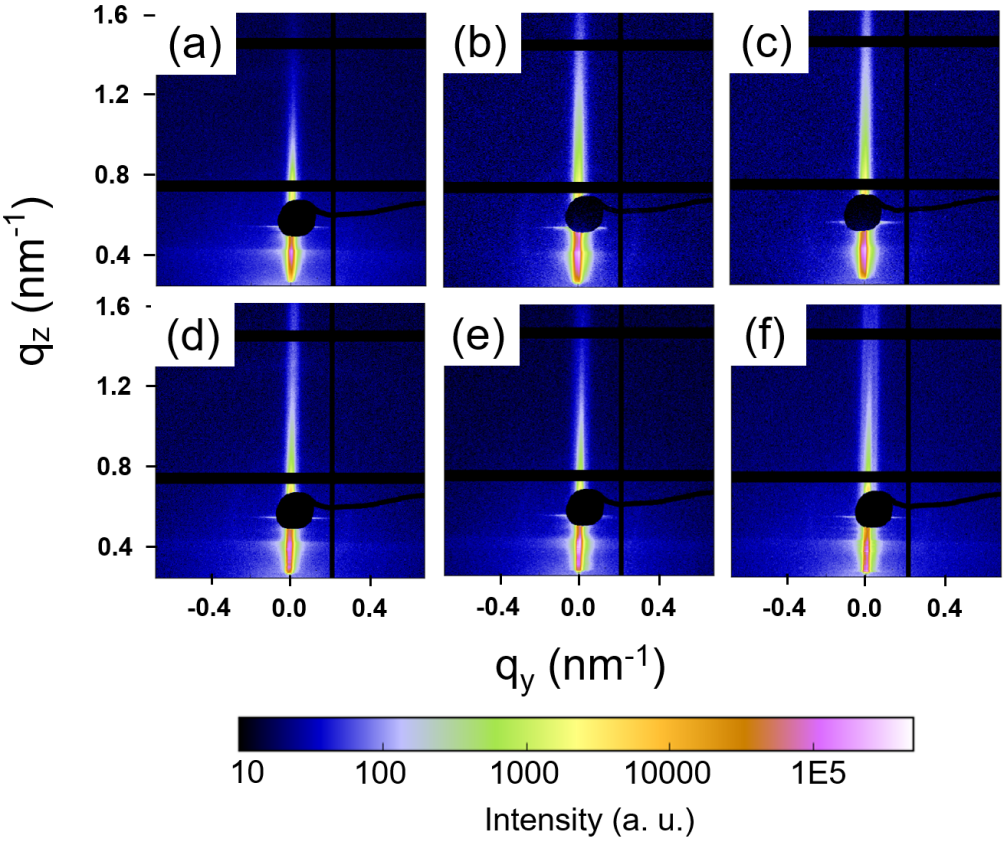

Figure 5.7: *2D GISAXS data of PS-b-PMMA thin films with thickness of (a) 7 nm, (b) 12 nm, (c) 19 nm, (d) 35 nm, (e) 56 nm, and (f) 91 nm after SVA in THF for 18 h. The specular peak is shielded by a beamstop. (Reprinted with permission from [86]. Copyright 2019 Nature Publishing Group.)*

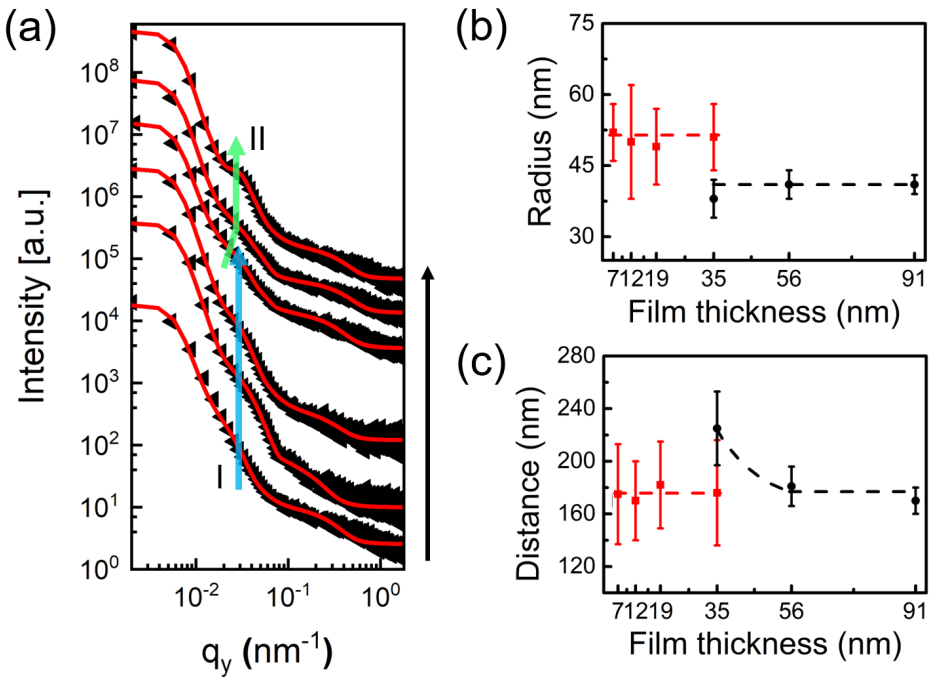

Figure 5.8: *Horizontal line cuts (q_y) from the 2D GISAXS data of the PS-b-PMMA thin films with different thicknesses after SVA in THF for 18 h. (a) Data (black dots) and fits (solid red lines) are shifted vertically along the y axis for clarity of the presentation (7 nm, 12 nm, 19 nm, 35nm, 56 nm, and 91 nm from bottom to top). The blue and green arrows serve as a guide to the eye for the main contributions I and II. (b) Radius and (c) distance of PMMA elongated structure (red) and PMMA half-spheres (black) determined from the fits of the GISAXS data plotted as a function of film thickness. The dashed lines in (b) and (c) serve as a guide to the eye. (Reprinted with permission from [86]. Copyright 2019 Nature Publishing Group.)*

5.1.2 Influence of SVA time

Surface morphology

The influence of the SVA time on the morphology of the PS-*b*-PMMA films with a thickness of 56 nm is investigated at room temperature. For SVA, THF is used as a good solvent vapor for both blocks of PS-*b*-PMMA and all films are removed from the desiccator as quickly as possible after SVA. Figure 5.9 shows AFM images of PS-*b*-PMMA thin films annealed in THF atmosphere for different times.

The as-prepared film (Figure 5.9a) displays a surface structure with large-sized continuous PMMA domains, since DMF is used for dissolving PS-*b*-PMMA which is a good solvent for PMMA versus PS [156]. The average size of the PMMA domains is around 122

± 36 nm (Figure 5.10a). However, with increasing annealing time from 0 h to 0.5 h, the PMMA domain size decreases while the PS phase increases. This change in the surface morphology can be explained by the rearrangement of polymer chains due to the solvent vapor annealing using THF which is a good solvent for both PS and PMMA. THF swells both blocks with slight PS selectively in the SVA process.

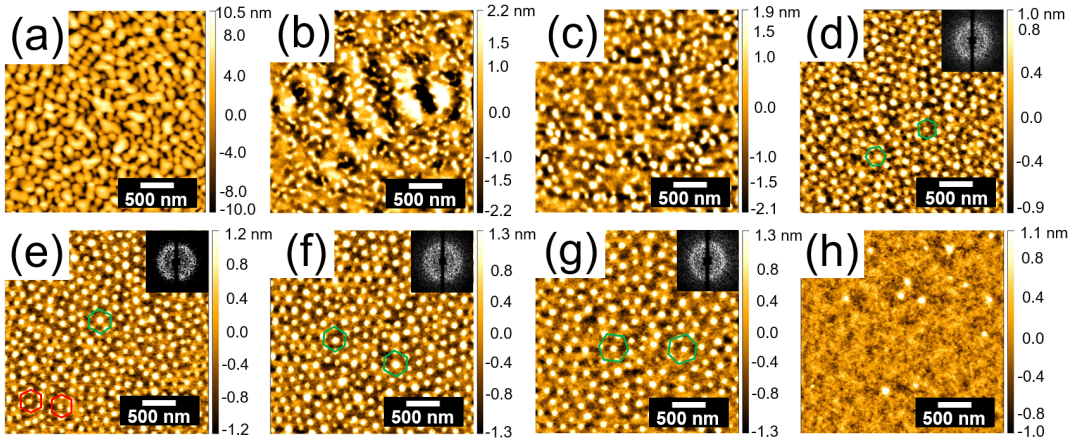

Figure 5.9: *AFM images of PS-b-PMMA thin films with a thickness of 56 nm for different SVA times. (a) 0 h, (b) 0.5 h, (c) 1.0 h, (d) 2.0 h, (e) 3.5 h, (f) 5.5 h, (g) 18.0 h, and (h) 31.0 h. The height bar is adapted individually as indicated. The green hexagons indicate that the positions of these half-spheres are not well located at the apex of the hexagon. The red hexagons indicate that the positions of these half-spheres are well located at the apex of the hexagon. On the top right corners in (d), (e), (f), and (g), the insets show the corresponding 2D fast Fourier transform (FFT) patterns. (Reprinted with permission from [86]. Copyright 2019 Nature Publishing Group.)*

As the annealing time increases from 0.5 h to 3.5 h, the morphology of the PS-*b*-PMMA films develops from a poorly ordered worm-like structure (Figure 5.9b) to an half-sphere structure with local order (Figure 5.9e). Moreover, a local hexagonal packing of half-spheres occurs when the annealing time increases to 2.0 h (Figure 5.9d, green hexagons). However, the hexagonal packing is irregular on large scale as seen from the ring pattern in the FFT analysis rather than having a 6-spot pattern. As the annealing time increases from 2.0 h to 3.5 h, the packing becomes locally more ordered, which can be confirmed by the red hexagons in Figure 5.9e. This transition can be explained by the enhanced mobility of long polymer chains in the swollen BCP films, which allows the polymer chains to approach the thermodynamically preferred arrangement [46, 53, 54]. For the annealing time of 3.5 h, a locally better ordered spherical structure can be obtained. From the surface morphology, one can see that the average half-sphere diameter is about 78 ± 13

nm (Figure 5.10e), and the average inter-domain distance is about 157 ± 20 nm (Figure 5.10m).

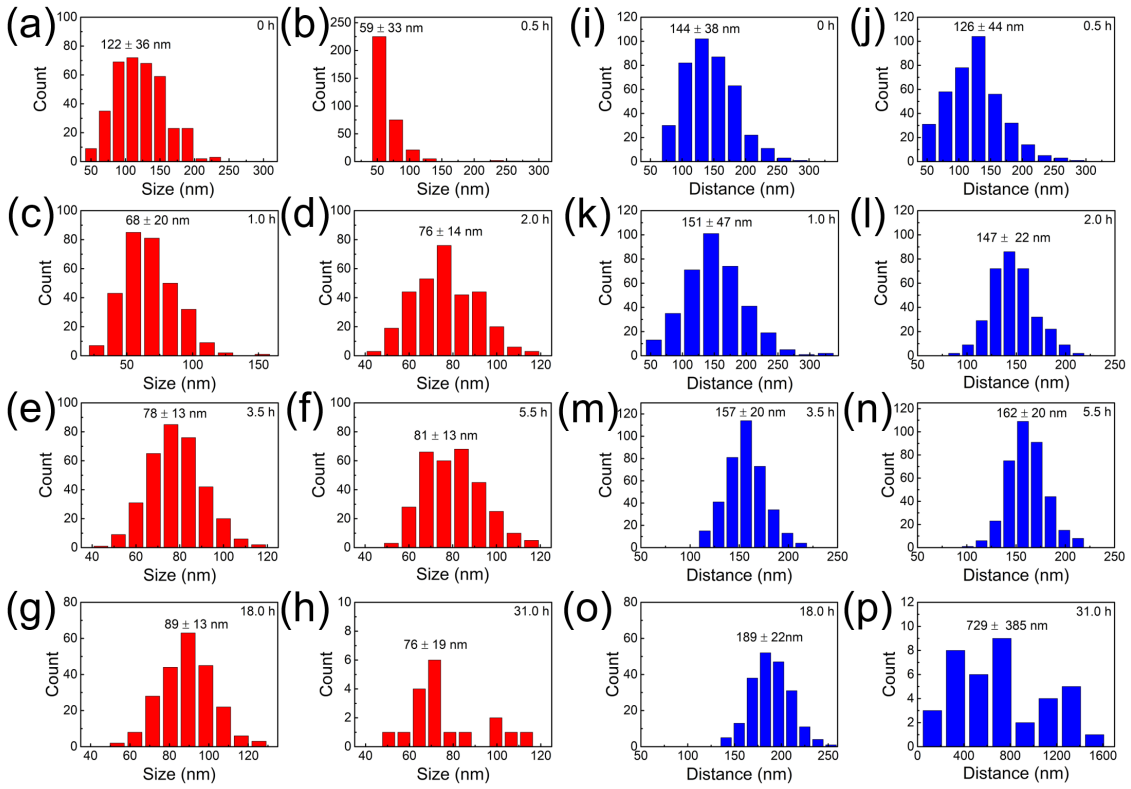

Figure 5.10: *Half-sphere size distribution (red bar chart) and distance distribution (blue bar chart) as a function of solvent annealing time in PS-b-PMMA thin films (56 nm). (a) and (i) 0 h, (b) and (j) 0.5 h, (c) and (k) 1.0 h, (d) and (l) 2.0 h, (e) and (m) 3.5 h, (f) and (n) 5.5 h, (g) and (o) 18.0 h, (h) and (p) 31.0 h. For disordered phase consecutive structures (a, b and c), Half-sphere size is the domain length for two orthogonal directions. For micro-phase separated half-spheres (d, e, f, g and h), half-sphere size is the domain diameter. Half-sphere distance is the distance between neighboring domains. All of the data are calculated statistically from the corresponding AFM images by using Image J 1.46r, with a total of at least 200 half-spheres or inter-domain distances being calculated on each image. For the PS-b-PMMA thin films with annealing time of 31.0 h, the amount of count is far less than 200 due to many half-spheres migrate inside the film. (Reprinted with permission from [86]. Copyright 2019 Nature Publishing Group.)*

As the annealing time increases, further swelling and chain stretching continues, which leads to an increasing inter-domain distance to 189 ± 22 nm (Figure 5.10o) for an annealing time of 18.0 h. The hexagonal packing is still irregular on large scale as indicated by the ring-like FFT pattern shown as inset in Figure 5.9e, 5.9f, and 5.9g. Moreover, the position of these half-spheres becomes more and more deviated from the apex of the

hexagon in Figure 5.9 (e, f, and g). However, the PS-*b*-PMMA film annealed for 31.0 h (Figure 5.9h) shows a dramatic disappearance in the spherical morphology. This change can be ascribed to the dynamic change of interfacial interactions and commensurability conditions caused by the continual solvent absorption [168]. During the SVA process, THF vapor is preferentially absorbed by the PS surface layer due to slight selectivity of THF towards PS ($\chi_{PS-THF} < \chi_{PMMA-THF}$) [21]. Therefore, part of the initially present PMMA half-spheres migrate into the film and PS dominates the film surface after a sufficient long annealing time, which is confirmed by the corresponding AFM phase image shown in Figure 5.11. The underlying process will be explained in more detail in the GISAXS analysis part.

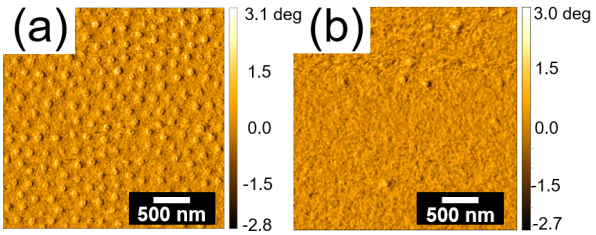

Figure 5.11: *AFM phase images of PS-b-PMMA thin films with a thickness of 56 nm for different SVA times: (a) 18.0 h and (b) 31.0 h. (Reprinted with permission from [86]. Copyright 2019 Nature Publishing Group.)*

Inner morphology

Figure 5.12 shows the 2D GISAXS data of PS-*b*-PMMA thin films after various SVA times. Horizontal line cuts for Figure 5.12 are performed like before (at the Yoneda peak position of PS-*b*-PMMA) and are displayed together with their corresponding fits (solid red lines) in Figure 5.13a. A broad peak (marked by the blue arrow) is observed. For the fitting of the horizontal line cut, the model as described before is used. The results of the extracted PMMA half-sphere radii and distances are depicted in Figure 5.13b and 5.13c, respectively.

For the non-solvent annealed reference sample, a shoulder-like feature around $q_y = 0.048$ nm^{-1} is observed. This peak becomes weaker, and it moves towards lower q_y values with increasing the annealing time to 0.5 h, which indicates the formation of less ordered nanostructures with larger inter-domain distance at the onset of annealing. The corresponding average inter-domain distance increases slightly from around 129 nm to 137 nm (Figure 5.13c) while the average half-sphere radius decreases from around 49 nm to 35 nm (Figure 5.13b). Such a decrease of the half-sphere size is caused by the

rearrangement of the polymer chains, which occurs when spin coated PS-*b*-PMMA films are placed in a new solvent-vapor atmosphere as we discussed above in AFM analysis (Figure 5.9a and 5.9b).

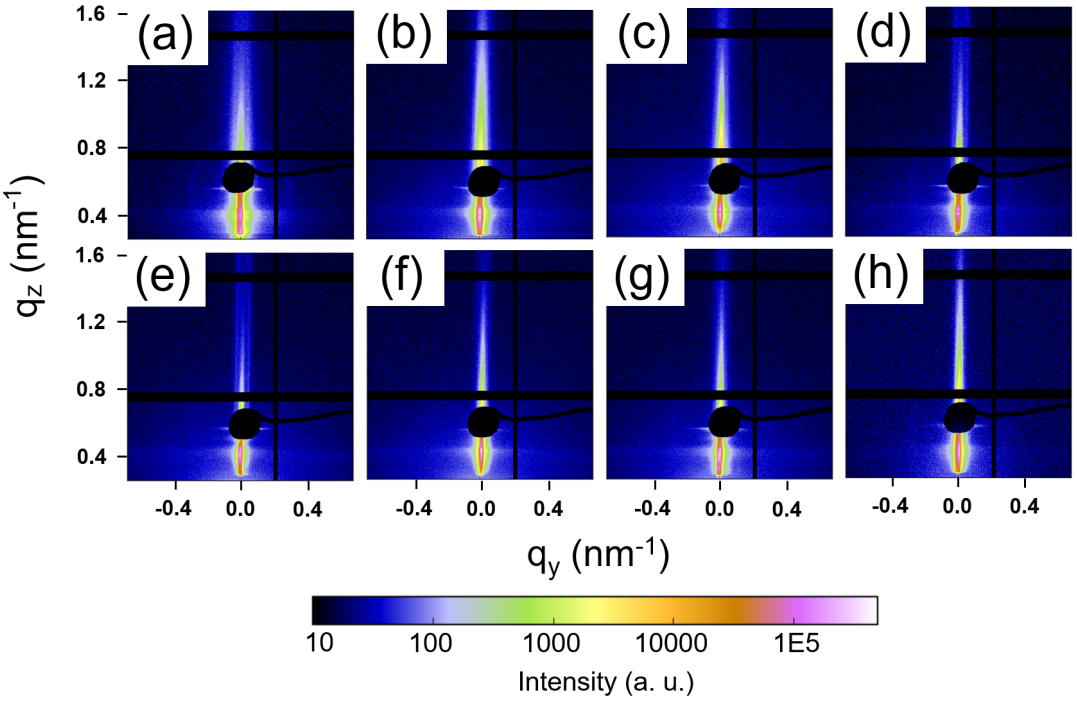

Figure 5.12: *2D GISAXS data of PS-b-PMMA thin films with a thickness of 56 nm for different SVA times. (a) 0 h, (b) 0.5 h, (c) 1.0 h, (d) 2.0 h, (e) 3.5 h, (f) 5.5 h, (g) 18.0 h, and (h) 31.0 h. The specular peak is shielded by a beamstop. (Reprinted with permission from [86]. Copyright 2019 Nature Publishing Group.)*

As the SVA time increases from 0.5 h to 3.5 h, the peak moves slightly to lower q_y values and becomes more prominent (Figure 5.13a). This change indicates the formation of a higher ordered structure with larger inter-domain distance with increasing the annealing time. The corresponding average inter-domain distance and half-sphere radius increases from around 137 nm to 151 nm (Figure 5.13c) and from around 35 nm to 41 nm (Figure 5.13b), respectively, since the degree of micro-phase separation in swollen BCP films is improved by the enhanced chain swelling and the increased mobility under THF solvent vapor [55].

As the annealing time further increases from 3.5 h to 18.0 h, the peak becomes weaker while it still shifts to lower q_y values. This shift is the result of a continuous extension of the polymer chains, especially for the PS block segments. Since the DBC used has a PS volume fraction of 93 %, the PS chain stretching has not reached maximum, which leads to the larger inter-domain distance distribution. The corresponding average inter-

domain distance increases from around 151 nm to 180 nm (Figure 5.13c) while the average half-sphere radius remains constant at around 41 nm (Figure 5.13b).

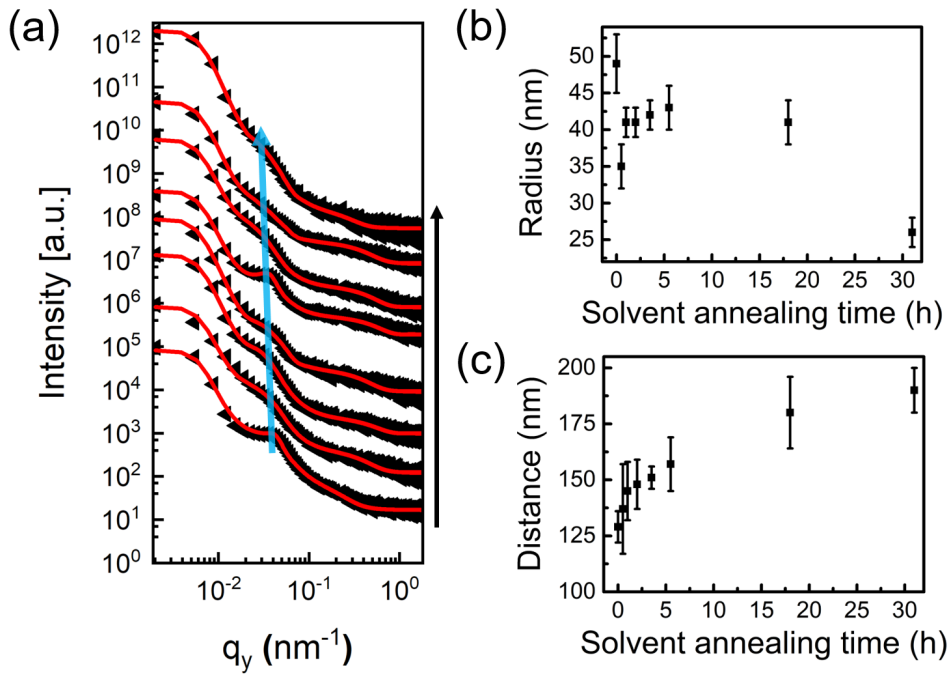

Figure 5.13: *Horizontal line cuts (q_y) from the 2D GISAXS data of the PS-b-PMMA thin films (56 nm) with increasing SVA time. Data (black dots) and fits (solid red lines) are shifted vertically for clarity of the presentation (0 h, 0.5 h, 1.0 h, 2.0 h, 3.5 h, 5.5 h, 18.0 h and 31.0 h from bottom to top). The blue solid arrow serves as a guide to the eye for the peak. Half-sphere (b) radius and (c) distance of PS-b-PMMA nanostructures determined from the fits of GISAXS data plotted as a function of SVA time. (Reprinted with permission from [86]. Copyright 2019 Nature Publishing Group.)*

Prolonging the annealing time (from 18.0 h to 31.0 h) results in a PS chain stretching close to equilibrium and a more prominent peak is seen in the line cuts at an annealing time of 31.0 h (Figure 5.13a). This indicates the formation of a higher ordered structure inside the film, which results from the rearrangement of polymer chains, causing part of the initially present PMMA half-spheres migrate into the film as discussed above in AFM analysis. The corresponding average inter-domain distance increases slightly from around 180 nm to 187 nm (Figure 5.13c) while the average radius remains constant at around 41 nm (Figure 5.13b) as before. The obtained radius of 41 nm indicates that the inner PMMA morphology is not full sphere, since the film thickness is only around 56 nm, which is not favorable to form full spheres with diameters of 82 nm. In our case, ellipsoid inside the film might be a reasonable morphology. Because at a swelling ratio of 1.7 (the initial 56 nm film swells to 91 nm where the nanostructure is in equilibrium), the

swollen film thickness (around 91 nm) is sufficient to accommodate a full sphere (diameter of 82 nm from GISAXS analysis) that may get "squished" into an ellipsoid upon solvent evaporation. Moreover, earlier work from Tang et al. shows that the half-sphere were formed only on the sample surface [50].

5.2 Evolution of morphology

To illustrate the entire morphology evolution of PS-*b*-PMMA thin films, a schematic model is shown in Figure 5.14 summarizing the findings of the AFM and GISAXS data analysis. On the left side of Figure 5.14, the schematic model illustrates the evolution of the film morphology with different thicknesses after SVA in THF for 18.0 h. At small film thicknesses (Figure 5.14a), a disordered structure inside the film is observed. This is the result of the confinement effects as observed with AFM measurements [172, 173]. Moreover, the film thickness is too small to support the formation of full-spheres or even half-spheres. At a medium film thickness (higher than 0.5 D, lower than 0.5 L_0, Figure 5.14b), vertical half-spheres with the poorly hexagonal packing fully cover the substrate. This is a typical arrangement to allow the characteristic structure (L_0) to be achieved in lateral direction. However, a similar structure with half-spheres aligned more ordered on the surface is seen at large film thicknesses (Figure 5.14c), instead of full-spheres. Since in the case where the film thickness is close to 0.5 L_0, a morphology with half-spheres is favorable for achieving the characteristic structure (L_0) in lateral and vertical direction.

The right side of Figure 5.14 shows the morphology evolution at various SVA times at room temperature in case of the film with a thickness of 56 nm. In case of the PS-*b*-PMMA thin film without any SVA (Figure 5.14d), a structure with a continuous PMMA phase appears due to the PS-*b*-PMMA thin film was fabricated under non-equilibrium conditions with the spin coating method [174]. As THF diffuses from the atmosphere into the film, a decrease in size and increase of the number of PMMA half-spheres occurs (Figure 5.14e). This is mainly attributed to the enhanced mobility of the polymer chains and a morphological rearrangement inside the thin films [51]. However, at this stage, there are still some island-like PMMA structures due to insufficient SVA time for highly entangled chain conformations in UHMW PS-*b*-PMMA thin films. When the film is treated in THF vapor for a certain time (i.e., 3.5 h), ordered half-spheres with hexagonal packing are obtained (Figure 5.14f). Thus, an annealing time of 3.5 h is sufficient for the self-assembly of the UHMW polymer chains. However, when the PS-*b*-PMMA film is annealed further, PS dominates the free surface. Part of the initially present PMMA half-spheres migrate into the film (Figure 5.14g) and become ellipsoids with same radius in film plane to minimize the energy of the system. This is confirmed by the AFM (surface

morphology is PMMA half-spheres) and GISAXS analysis (inner morphology is PMMA ellipsoids).

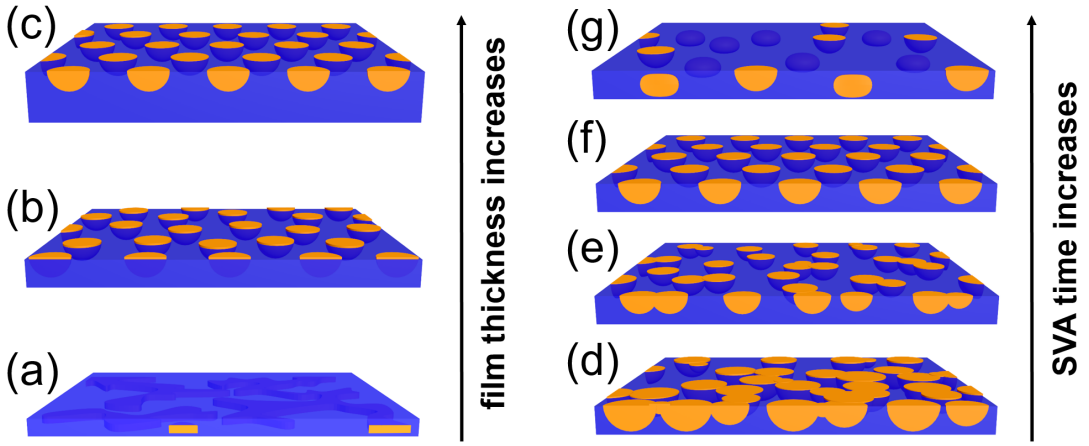

Figure 5.14: *Schematic model of the microstructure formation of PS-b-PMMA thin films (left) as function of film thickness and (right) as function of SVA time. The PS phase (green) forms the matrix in which PMMA domains (blue) are embedded. (Reprinted with permission from [86]. Copyright 2019 Nature Publishing Group.)*

5.3 Summary

The present chapter focuses on the fabrication of ordered polymer (DBC) templates with a large domain size. An asymmetric linear UHMW PS-*b*-PMMA DBC is used. To obtain a desired DBC template, the structural evolution of the fabricated UHMW DBC thin films is systematically investigated as function of increasing film thickness and SVA time.

DBC templates with ordered nanostructures and large domain sizes are fabricated by using spin-coating of an asymmetric linear UHMW PS-*b*-PMMA DBC combined with SVA. Over a large concentration range, we observe a linear dependence of the film thickness on the polymer concentration in the solution used for spin coating, which before was known for DBCs with smaller molecular weights. By applying an asymmetric UHMW DBC, we are able to tune the domain size and center-to-center distance of neighboring PMMA half-spheres to values larger than 80 nm and 150 nm, respectively, with SVA (THF) time of 3.5 h. As a function of film thickness ($\leq 0.5\ L_0$), the morphology changes from disorder to relativity ordered PMMA half-spheres (locally regular hexagonal packed) in a PS matrix. This is the result of the confinement effects between the film thickness and inter-domain distance. With increasing SVA time, a rapid morphology evolution of locally hexagonal packed half-spheres (from poorly ordered to locally ordered, and then

back to poorly ordered nanostructure) is observed, suggesting that a suitable SVA time is crucial for the formation of ordered nanostructures also in case of the UHMW DBC. Furthermore, when the annealing time increases to 31.0 h, PS dominates the entire film surface.

The obtained DBC-based large-sized nanomaterials will pave the way for future applications. For example, using the UHMW DBC will provide large inter-domain distance for application of photonic band gap structures (in the field of visible light). In addition, such UHMW DBC template has sufficient space for embedding large-sized NPs, such as large magnetic iron oxide NPs with diameters above 20 nm.

6 In situ study of magnetic hybrid polymer film during printing

Parts of this chapter have been published in the article: In situ study of FePt nanoparticles-induced morphology development during printing of magnetic hybrid diblock copolymer films [141] (Reprinted with permission from (W. Cao et al., *Adv. Funct. Mater.*, 2021, 2107667). Copyright 2021 Wiley-VCH GmbH. DOI: 10.1002/adfm.202107667).

In the previous work (chapter 5), ordered DBC templates with a large domain size are fabricated by using a linear UHMW PS-*b*-PMMA DBC. Such templates can be well utilized to host magnetic NPs to prepare magnetic hybrid NP-DBC films. For the wet chemical fabrication of magnetic hybrid NP-DBC films, various methods such as spin coating, solution casting, spray coating and printing, have been developed [175–177]. For instance, Konefał et al. prepared magnetic hybrid films by spin coating, in which Fe_3O_4 NPs were dispersed uniformly inside the P4VP domains of the DBC polystyrene-*block*-poly(4-vinylpyridine) PS-*b*-P4VP [175]. Hammond et al. fabricated nanocomposite films containing a cylindrical PS-*b*-P2VP DBC and spindle type hematite (α-Fe_2O_3) NPs via a solution casting method [176]. The alignment of the α-Fe_2O_3 NPs can be improved by employing a uniaxial external magnetic field during solution casting. In previous studies from Müller-Buschbaum group, various methods, like spin coating, spray coating and printing, were utilized to prepare magnetic NP-DBC films with different morphologies and magnetic properties [13, 177, 178]. Among these fabrication methods, printing has obtained increasing attention because of its large-scale production capability in industrial applications [179, 180]. Moreover, printing is an effective method to obtain homogeneous films with smooth surfaces on a macroscopic level compared to other methods such as spray coating. To achieve a favorable morphology, it is necessary to have a systematic investigation on the morphological evolution of hybrid NP-DBC films during printing process.

During the printing process, GISAXS has been proven to be an effective approach to track the morphology evolution without destroying the films [181, 182]. For instance, Liu et al. utilized in situ GISAXS measurements to study the morphology evolution in slot-die printed polymer-based active layers during the film formation process [179]. With in situ GISAXS, Marques et al. and Gu et al. followed the structure evolution during printing in polystyrene-*block*-poly(2-vinylpyridine) DBC and polyisoprene-*block*-polystyrene-*block*-poly(4-vinylpyridine) triblock terpolymer, respectively [183, 184]. In previous studies from the Müller-Buschbaum group, the kinetics of printed different films, such as PbS quantum dot stacking and bulk heterojunction films, were in-depth investigated via in situ GISAXS [185, 186].

So far, concerning magnetic NP-DBC hybrid films, less attention has focused on the kinetics of printed magnetic hybrid films during the film formation process. The kinetics of the magnetic hybrid films and the arrangement of the magnetic NPs during the printing process are rarely investigated. Most studies focused on the final printed magnetic NP-DBC hybrid films [10, 177].

In this chapter, the slot-die printing technique is applied to fabricate magnetic hybrid films by using an UHMW DBC PS-*b*-PMMA to host magnetic iron platinum (FePt) NPs. With in situ GISAXS, the kinetics of the magnetic hybrid NP-DBC films and the arrangement of the magnetic NPs during solvent evaporation are investigated. The structure formation in different stages of the film formation is monitored. As a reference, a pure DBC PS-*b*-PMMA film without magnetic NPs is printed under the same conditions. The surface structures and magnetic properties of the printed films are probed by SEM and SQUID magnetometry, respectively. The in situ GISAXS data suggest that the addition of NPs accelerates the solvent evaporation, leading to a faster film formation of the hybrid film compared to the pure DBC film. A metastable state is formed in both films when the solvent is almost evaporated. Compared with the pure film, such metastable state remains longer in the hybrid film due to the presence of the FePt NPs, which limits the reorganization of polymer chains. SQUID data shows that the printed magnetic hybrid NP-DBC film is superparamagnetism and is benefical to scale up the magnetic film fabrication for magnetic sensors [13].

6.1 Printing

Two UHMW PS-*b*-PMMA solutions with and without FePt NPs are prepared in toluene with a fixed DBC concentration of 7 mg mL^{-1}. For the PS-*b*-PMMA solution with FePt NPs, a NP concentration (weight ratio between NPs and PS-*b*-PMMA) of 3 wt %

is studied. PS-*b*-PMMA and FePt NPs are synthesized by the Gallei group and are detailed in section 4.1 (materials). The whole printing is performed on a pre-cleaned silicon substrate (with a size of 25 mm × 70 mm) with a custom-made slot-die coater at room temperature. To achieve a favorable film thickness, the solution flow rate, printing velocity and distance between the mask and the substrate are set to 0.1 mL min^{-1}, 5 mm s^{-1} and 0.5 mm, respectively. Details can be seen from the chapter 4 (sample preparation).

To track the structure evolution of the printed films, GISAXS measurements are performed at the DESY synchrotron (P03, Hamburg, Germany) in situ during the printing (Figure 4.10). The scattering signal is recorded on a 2D detector Lambda 750 K with a pixel size of 55 μm × 55 μm (X-Spectrum GmbH) with 20 cycles. Each cycle consisted of 0.1 s X-ray exposure time and 2.0 s waiting time. To track the morphology of films over a large area and to avoid beam damage, the in situ GISAXS measurements are carried out at different spots of the film through moving the sample. The X-ray wavelength and incidence angle of the X-ray beam are 0.0993 nm and 0.35^o, respectively. The sample-detector distance is set to 4045 mm.

6.2 Surface morphology

SEM is applied to examine the surface morphology of the printed final pure and hybrid films. The SEM images of the printed pure PS-*b*-PMMA film at low and high magnifications are shown in Figure 6.1a and 6.1c, respectively. The bright matrix and dark domains correspond to PS and PMMA blocks [187]. Due to the use of UHMW DBC, a very high segregation strength χN between PS and PMMA blocks is obtained. According to the self-consistent field theory, such very high segregation strength leads to the realization of a cylindrical morphology of the DBC, although the PMMA volume fraction of DBC is only 0.172 [31]. Thus, PMMA cylinders dispersed in the PS matrix are expected as microphase separation structure. In Figure 6.1a and 6.1c, indeed parallel and perpendicular PMMA cylinders are observed. The average half-length of the parallel PMMA cylinders and average radius of the PMMA cylinders are about 27 ± 5 nm and 59 ± 11 nm, respectively.

For the hybrid NP-DBC film, magnetic FePt NPs (brighter spots) are observed in addition. The NPs are positioned inside the PMMA domains as shown in Figure 6.1b and 6.1d. In the hybrid film, the FePt NPs have a higher selectivity to the PMMA domains *versus* the PS phase because the FePt NPs are functionalized with PMMA chains. Moreover, less parallel PMMA cylinders are observed in the hybrid system (Figure

6.1d) compared with the pure film (Figure 6.1c). The parallel PMMA cylinders are marked with blue rectangles in Figure 6.1c and 6.1d. Such decreased number of parallel cylinders can be attributed to the presence of a polymer-rich layer during the solvent evaporation and a strong interaction between the polymer and the functionalized FePt NPs [188, 189]. It has been reported that a polymer-rich layer at the interface of liquid and vapor was formed during solvent evaporation of polymer solution [189]. The formed layer can attract more NPs to the interface if the interaction $F_{NP-polymer}$ is higher than the interaction $F_{NP-solvent}$. In case of the present study, the used FePt NPs are functionalized with PMMA chains and the DBC is PS-*b*-PMMA. Thus, the interaction $F_{NP-polymer}$ is strong enough to move the NPs to the interface, causing more flipping of the PMMA domains from parallel to vertical orientation. Moreover, driving FePt NPs to the film surface can reduce the entropy loss of the polymer chains [13]. The formation of more upstanding PMMA cylinders can minimize the surface energy of the hybrid system, which is achieved by decreasing the contact area between air and PMMA (functionalized on NP surface) due to a higher surface energy of PMMA ($\gamma_{PMMA} = 41$ mN m^{-1}) compared with that of PS ($\gamma_{PS} = 40$ mN m^{-1}) [190, 191].

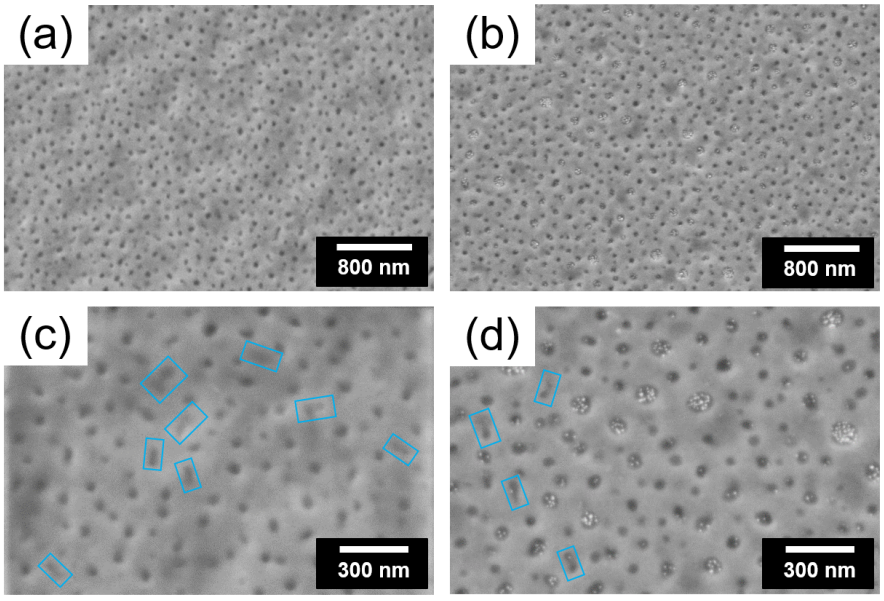

Figure 6.1: *SEM images of printed films of (a) pure PS-b-PMMA reference film and (b) hybrid film containing 3 wt % of FePt NPs at (a, b) low and (c, d) high magnifications. The parallel PMMA cylinders are marked with blue rectangles in the high magnification images. (Reprinted with permission from [141]. Copyright 2021 Wiley-VCH GmbH.)*

6.3 Morphology evolution during printing

To study the impact of FePt NPs on the morphology evolution of PS-*b*-PMMA DBC film and the arrangement of the NPs during the film formation process, the film printing is combined with in situ GISAXS (as shown in Figure 4.10). Printing is done at room temperature. During printing, the DBC solution flows out along a solution guide mask and is then spread evenly on the substrate via movement of the sample holder [185]. For the in situ GISAXS measurements, we define the moment when the sample holder stops as $t = 0$ s.

6.3.1 Pure DBC film

For the pure PS-*b*-PMMA film without FePt NPs, selected 2D GISAXS data at various times are displayed in Figure 6.2. With increasing time, the overall signal intensity in the Yoneda peak region increases first due to the evaporation of solvent and then remains relatively stable in the later stages [186]. The DBC structure is developing along with the solvent evaporation.

To extract the DBC morphology changes during printing, horizontal line cuts of the 2D GISAXS data are performed as indicated in Figure 6.2 with a red rectangle at $t = 0$ s. Figure 6.3a shows selected horizontal line cuts (black dots) of the printed pure PS-*b*-PMMA film at selected times from the in situ printing. All horizontal line cuts are displayed in an 2D intensity mapping for the pure PS-*b*-PMMA film in Figure 6.3b [126]. For the pure DBC film, it can be seen that the intensity along the q_y direction becomes relatively stable after $t = 18.9$ s (marked with a white dashed line), indicating that the solvent is almost evaporated and a relatively stable film is formed.

For a quantitative insight, horizontal line cuts are modeled based on the effective interface approximation (EIA) and the distorted wave Born approximation (DWBA) [129,192]. The corresponding fits and obtained radii of the pure PS-*b*-PMMA film are summarized and plotted in Figure 6.3a and 6.3c, respectively. Two main structures (I and II) are observed (Figure 6.3a). Structures I and II are form factors of the PMMA domains (perpendicular PMMA cylinders and parallel PMMA cylinders along the radius direction) and of the elongated PMMA structure (parallel PMMA cylinders along the length direction), respectively. In the initial stage ($t \leq 18.9$ s), structure I shifts to higher q_y values with increasing time, indicating that the average radius of the PMMA domains decreases over time. In more detail, the average radius of the PMMA domains decreases from 117 ± 12 to 28.1 ± 1.5 nm. Such a decrease in the PMMA domain size is similar to the reported observations of the drying process of a block copolymer film [184]. The polymer chains

shrink due to the solvent evaporation over time, leading to a decrease in PMMA domain radius.

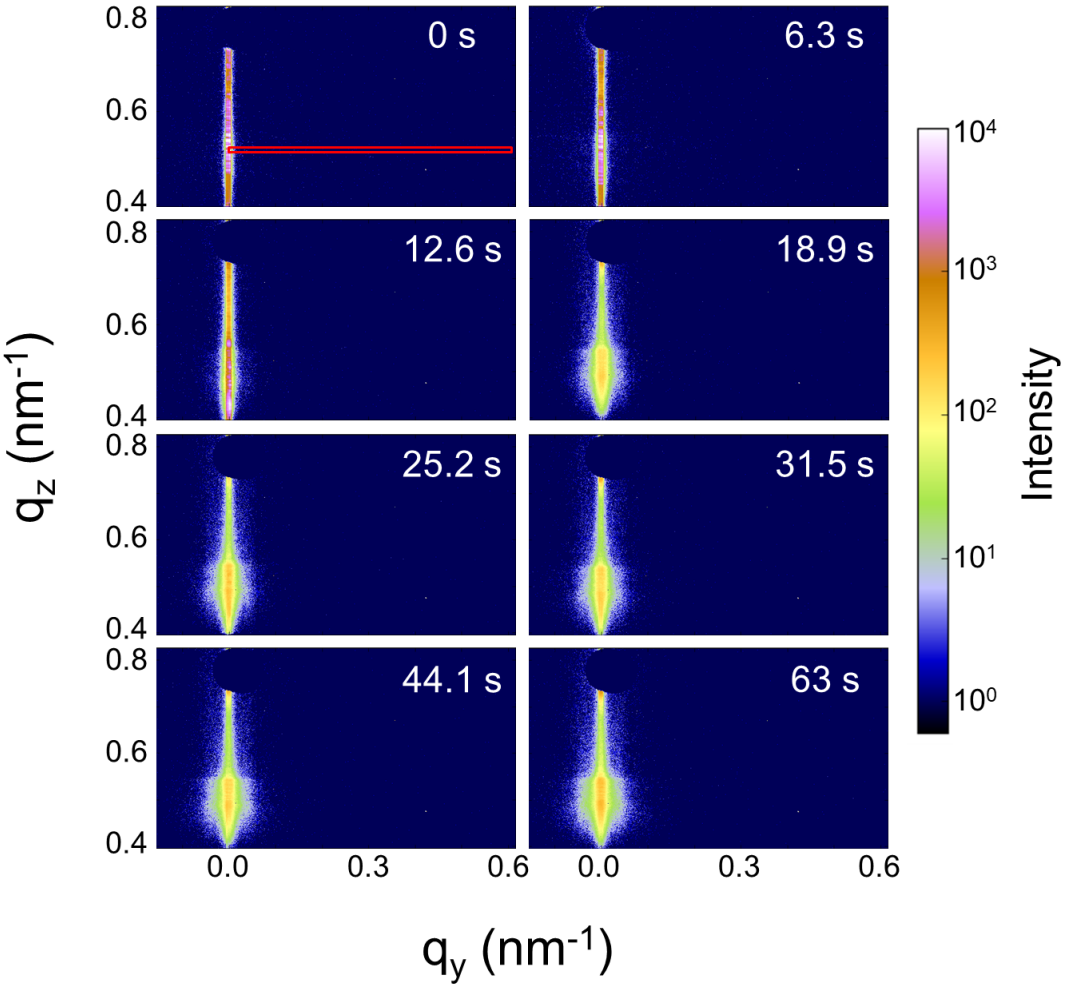

Figure 6.2: *Selected 2D GISAXS data of the pure DBC reference film measured during in situ printing at different times as indicated (top right corner). (Reprinted with permission from [141]. Copyright 2021 Wiley-VCH GmbH.)*

As the solvent is almost evaporated, the film changes from a wet state to a solid-like state and the mobility of polymer chains is strongly suppressed due to the lack of sufficient solvent molecules. Thus, structure I remains constant with further increasing time (after 18.9 s) with an average radius of the PMMA domains of 28.1 ± 1.5 nm. Looking in more detail, structure I turns out to be metastable in the time range from 18.9 s to 27.3 s as seen from the increasing error bars in Figure 6.3c, which indicate a loss in order. Such reorganization of the polymer chains is caused by a small amount of residual solvent inside the DBC film [184]. For $t > 27.3$ s, the error bars remain constant and since the average radius of the PMMA domains also remains constant within in the error bars, a final stable

DBC film is obtained. Besides structure I, in the lower q_y region (0.010 – 0.015 nm^{-1}), an additional scattering feature (denoted as structure II, shown as a purple arrow in Figure 6.3a) is observed at $t \leq 6.3$ s. It arises from the form factor of elongated PMMA structures, which are ascribed to the parallel PMMA cylinders seen in the SEM images. As time increases to 18.9 s, this structure II shifts to higher q_y values. The corresponding average radius of the elongated PMMA structure decreases from 124 ± 17 to 61 ± 8 nm. For $t \leq 18.9$ s, structure II remains constant as discussed for structure I. Error bars do not change for structure II.

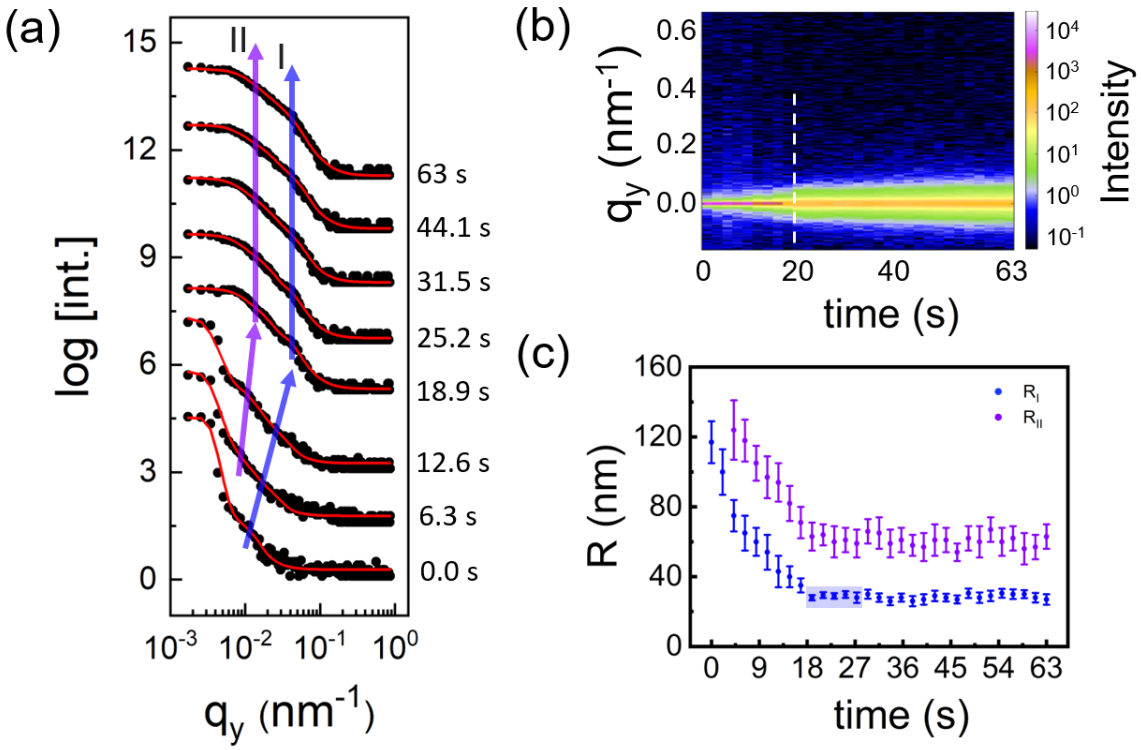

Figure 6.3: *(a) Selected horizontal line cuts of the 2D GISAXS data during printing of the pure PS-b-PMMA film at selected times (0.0 s, 6.3 s, 12.6 s, 18.9 s, 25.2 s, 31.5 s, 44.1 s, and 63.0 s from bottom to top). The fits are shown with red lines and shifted along the y axis together with their corresponding cuts. The form factors of PMMA domains and PMMA elongated structure are denoted with I (blue arrow) and II (purple arrow), respectively. (b) 2D mapping of all horizontal line cuts obtained from the 2D GISAXS data during printing of the pure PS-b-PMMA film. (c) Radius of the PMMA domains (R_I) and PMMA elongated structure (R_{II}) obtained from the fits. The semi-transparent color area indicates a metastable state. (Reprinted with permission from [141]. Copyright 2021 Wiley-VCH GmbH.)*

6.3.2 Hybrid film

For the hybrid film containing 3 wt % FePt NPs, the selected 2D GISAXS data at various times are displayed in Figure 6.4. Similar to the observations in the pure PS-*b*-PMMA film, the overall intensity in the Yoneda peak region increases first with increasing time, while it remains relatively stable at an earlier time compared to the pure film.

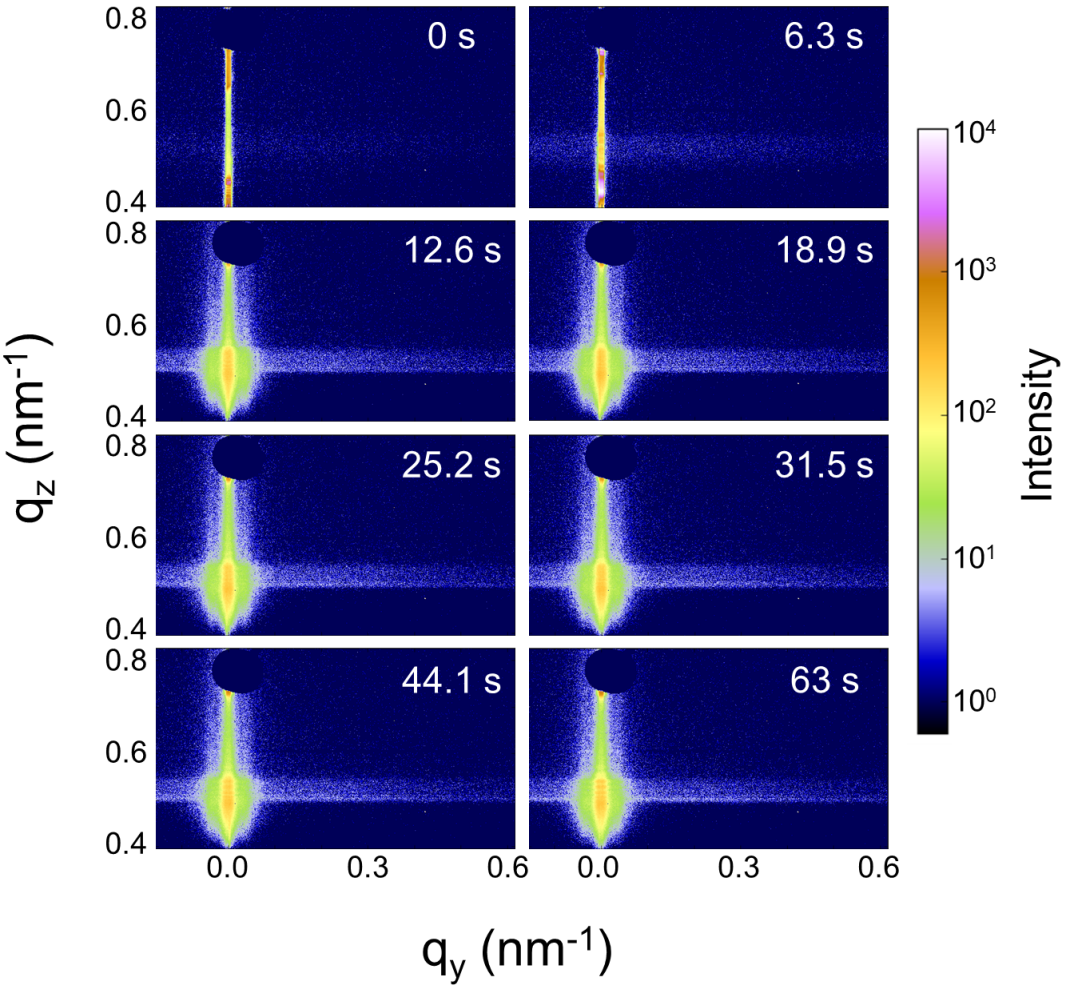

Figure 6.4: *Selected 2D GISAXS data of magnetic hybrid film measured during in situ printing at different times as indicated (top right corner). (Reprinted with permission from [141]. Copyright 2021 Wiley-VCH GmbH.)*

Figure 6.5a shows selected horizontal line cuts from the 2D GISAXS data of the hybrid NP-DBC film and the corresponding fits. The 2D intensity mapping from all horizontal line cuts of hybrid NP-DBC film is shown in Figure 6.5b. Obviously, a relatively stable hybrid film is formed already at t = 12.6 s (Figure 6.5b), which is faster as compared to the pure PS-*b*-PMMA film (t = 18.9 s). This indicates that the addition of FePt NPs

accelerates the majority of the solvent evaporation, which will be explained further below. For modelling of the horizontal line cuts, three characteristic structures are required. Two structures resemble the PMMA domains (perpendicular and parallel orientation) and the third structure the FePt NPs.

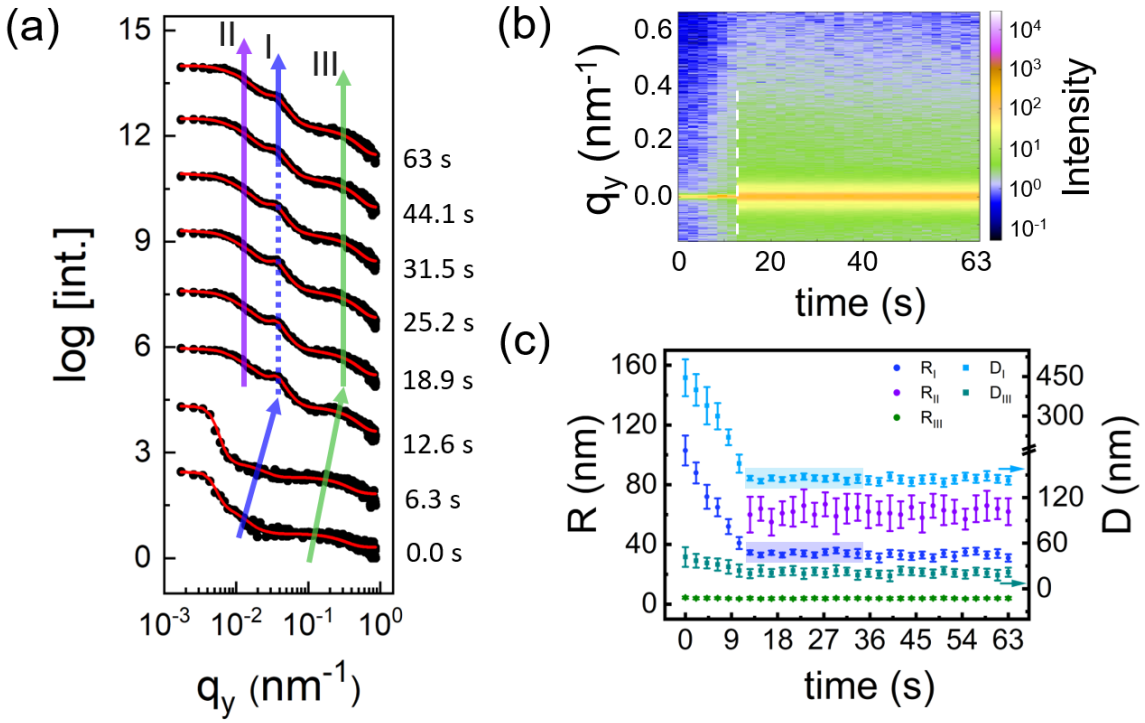

Figure 6.5: *(a) Selected horizontal line cuts of the 2D GISAXS data during printing of the hybrid film containing 3 wt % FePt NPs at selected times (0.0 s, 6.3 s, 12.6 s, 18.9 s, 25.2 s, 31.5 s, 44.1 s, and 63.0 s from bottom to top). The fits are shown with red lines and shifted along the y axis together with their corresponding cuts. The structure factors of PMMA domains and FePt NPs are denoted with structures I (blue arrow) and III (green arrow), respectively. The form factors of PMMA elongated structure are denoted with II (purple arrow). (b) 2D mapping of all horizontal line cuts obtained from the 2D GISAXS data during printing of the hybrid film. (c) Radius of the PMMA domains (R_I), PMMA elongated structure (R_{II}) and FePt NPs (R_{III}) and distance of the PMMA domains (D_I) and of nearest neighbor FePt NPs (D_{III}) obtained from the fits. The semi-transparent color areas indicate a metastable state. (Reprinted with permission from [141]. Copyright 2021 Wiley-VCH GmbH.)*

As shown in Figure 6.5a, in the hybrid film formation the evolution of structure I is similar to that of pure film. However, structure I of the hybrid film remains constant at $t \leq 12.6$ s, while in case of the reference film this happens at $t \leq 18.9$ s. Thus, the hybrid film dries faster compared to the pure film in terms of forming a metastable film

during printing. Since the used solvent toluene exhibits a higher selectivity to PS *versus* PMMA, the solvent prefers to move to the surface to evaporate through the PS phase. The polymer-solvent interaction parameter is $\chi_{PS-toluene} = 0.34$ and $\chi_{PMMA-toluene} = 0.45$ [156]. Less parallel PMMA cylinders are formed due to the presence of the NPs and more PS is at the surface of the hybrid film compared with the pure DBC film as observed from the SEM images. Thus, the solvent molecules have more chances to evaporate in the hybrid system.

As the solvent evaporates faster, one might expect a less ordered DBC structure in the hybrid film *versus* the pure film, especially for the used UHMW DBC [18]. In general, having long polymer chains requires more time to phase separate into ordered structures [18]. However, instead of getting a less ordered DBC structure, structure I shows higher order at $t \leq 12.6$ s for the hybrid film containing 3 wt % FePt NPs (marked with blue arrow in Figure 6.5a) compared with the pure film (marked with blue arrow in Figure 6.3a). Such increased order of the DBC structure in the hybrid film originates from the reduced number of parallel PMMA cylinders (as seen in SEM) due to the addition of the FePt NPs. The more parallel PMMA cylinders are present, the more they disturb the DBC structure [146], because they are distributed in the film with random orientations as shown in SEM images.

With further increasing time, again an increase in the error bars of structure I is observed (from 12.6 to 33.6 s, marked with semi-transparent colors in Figure 6.5c). The respective metastable state of the hybrid film is longer (21.0 s) as compared to the pure DBC (8.4 s). Obviously, the presence of the FePt NPs limits the movement of the polymer chains, while residual solvent molecules enable a local reorganization of the polymer chains [193]. Moreover, to better model the structure I with a relatively ordered structure, a structure factor is required to describe the interdomain distance of the PMMA domains. As shown in Figure 6.5c, the average center-to-center distance of the PMMA domains decreases in the beginning of the film formation and remains constant around 146 ± 5 nm (Figure 6.5c) at $t \leq 12.6$ s. Comparing the final printed films, the PMMA domains (structure I) are larger for the hybrid film (average radius 33.4 ± 2.7 nm, Figure 6.5c) compared with the pure DBC film (28.1 ± 2.5 nm, Figure 6.3c) due to the space required for accommodating the FePt NPs inside the PMMA domains.

Similar to the pure DBC film, a constant structure II (elongated PMMA structure) is seen at lower q_y values after a relatively stable film has formed ($t \leq 12.6$ s). The corresponding average radius of the elongated PMMA structure remains constant at around 63 ± 8 nm (Figure 6.5b). However, we do not see a decrease of structure II at the early stage of the solvent evaporation, which is different to the observation in the pure DBC film. Such difference can be explained by the formation of fewer parallel PMMA cylinders

in the hybrid film compared with the pure DBC film due to the addition of the FePt NPs. As a result, these parallel PMMA cylinders are located sparsely inside the semi-dry film and do not have a sufficient scattering contribution to be seen in the GISAXS measurements. With further solvent evaporation, the number of parallel PMMA cylinders per unit volume gradually increases and finally passes the threshold to be detectable in the GISAXS data at $t \leq 12.6$ s.

At the studied NP concentration, the FePt NPs are no longer dispersed only as isolated NPs but also aggregate. Consequently, for the hybrid film, one more structure factor is required to model the inter-domain distance of neighboring FePt NPs, which is denoted as structure III (marked with a green arrow in Figure 6.5a). The form factor representing the radius of NPs remains constant during the entire film formation, since the size of the FePt NPs does not change during the printing [17, 162]. Information about the PMMA chains located on the NP surface during printing is gained from analyzing the nearest neighbor distance of the NP. As seen in Figure 6.5a, the structure III shifts to higher q_y values with increasing until 12.6 s, which is similar to the changes of structure I. The corresponding average nearest neighbor distance of the FePt NPs decreases from 42 $\pm$ 13 nm to 20 $\pm$ 6 nm (Figure 6.5c), while the average FePt NP radius is 3.9 $\pm$ 0.6 nm (Figure 6.5c). When $t \leq 12.6$ s, structure III remains constant due to the absence of mobility of NPs caused by an almost complete evaporation of the solvent.

6.4 Morphology evolution

A side view sketch illustrates the film formation of the DBC without (Figure 6.6a) and with FePt (Figure 6.6b) NPs during the print process. Initially, a wet (W) film is deposited. During the drying process, both PS and PMMA chains shrink as the solvent evaporates, leading to a decrease in the size and the center-to-center distance of the PMMA domains. Due to the presence of SiO_x on the Si substrate, which is preferentially wetted by the PMMA block, parallel PMMA cylinders should form [194, 195]. In case of the pure DBC printing, parallel PMMA cylinders are observed during the wet (W) stage in the GISAXS measurements. Similar to the PMMA domains, the size and center-to-center distance of these parallel PMMA cylinders decrease over time. In contrast, in the hybrid film printing parallel PMMA cylinders are not observed during wet (W) and wet-dry (W-D) stages via GISAXS measurements. They appear at the last stage, namely the dry (D) stage as explained by the formation of less parallel PMMA cylinders in the hybrid film compared with the pure film as discussed before. Importantly, the hybrid film exhibits a faster drying speed than the pure DBC film due to the different selectivity of the solvent to PS and PMMA and the different proportions of PS and PMMA on the surface for pure

and hybrid films. The final dry (D) films differ in their characteristic domain sizes due to the presence of the NPs in the hybrid film.

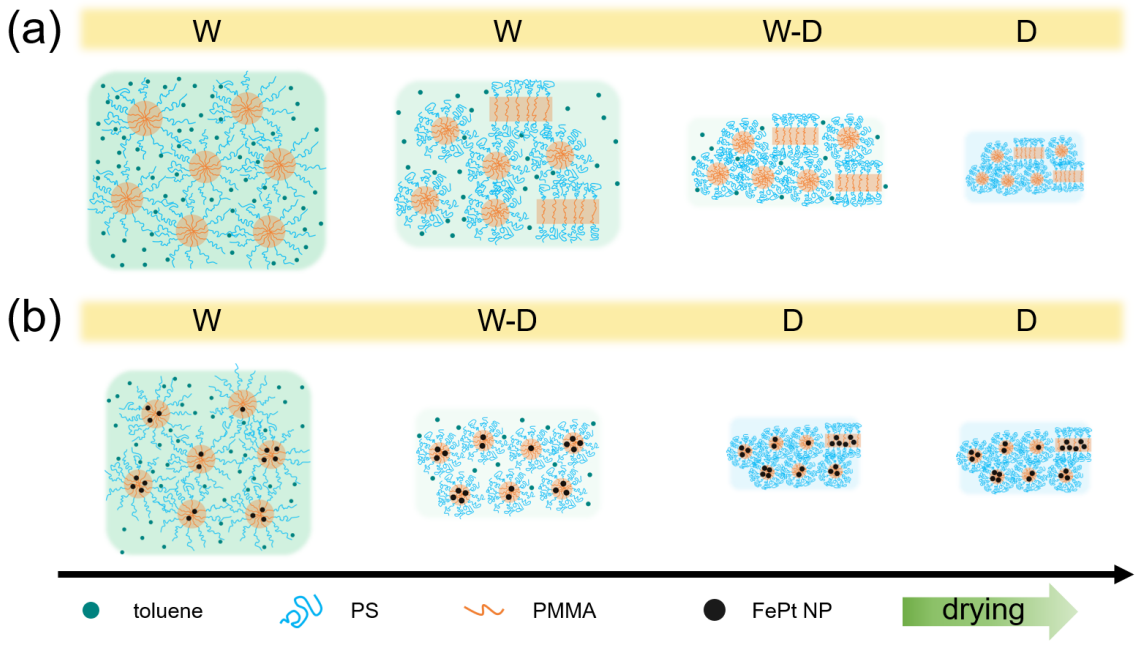

Figure 6.6: *Side-view sketch of the morphology evolution during printing for (a) pure and (b) hybrid films from a wet state (W) to a wet-dry state (W-D) to a dry state (D), in which the solvent is almost evaporated. The green dots only represent the amount of solvent (toluene). (Reprinted with permission from [141]. Copyright 2021 Wiley-VCH GmbH.)*

6.5 Magnetic properties

For the analysis of the magnetic properties of the final printed hybrid film, measurements are performed at different temperatures via a SQUID magnetometer. Figure 6.7a shows magnetization curves of the printed hybrid film for temperatures between 2 and 300 K. At 2 and 10 K, the magnetization curves exhibit a hysteresis loop. With increasing temperature, the hysteresis loop narrows and finally disappears, indicating a superparamagnetic behavior of the printed hybrid film [8]. To further quantify the relationship between magnetic properties and temperature, the corresponding saturation magnetization (M_s), coercivity (H_c) and magnetic susceptibility (χ) are shown in Figure 6.7b.

As the temperature increases, M_s decreases due to thermal fluctuations [196], which leads to faster fluctuations in magnetic moments and higher random anisotropy in the magnetic domains with increasing temperature. As a result, lower M_s values are obtained at higher temperatures. Due to the superparamagnetic behavior of the used fcc-FePt NPs,

H_c decreases sharply first and then remains constant with a value of almost zero [197]. At low temperatures (2 and 10 K), the thermal energy is too small to overcome the anisotropy energy and the magnetic moments are blocked along the applied external magnetic field [10]. As the temperature increases, such blocked behavior is weakened, resulting in a decrease of H_c. While at high temperatures ($T \geq 50$ K), the anisotropy energy can be overcome by the high thermal energy [95]. In this case, magnetic moments can spontaneously reverse themselves when the external magnetic field is removed, leading to an H_c of almost zero.

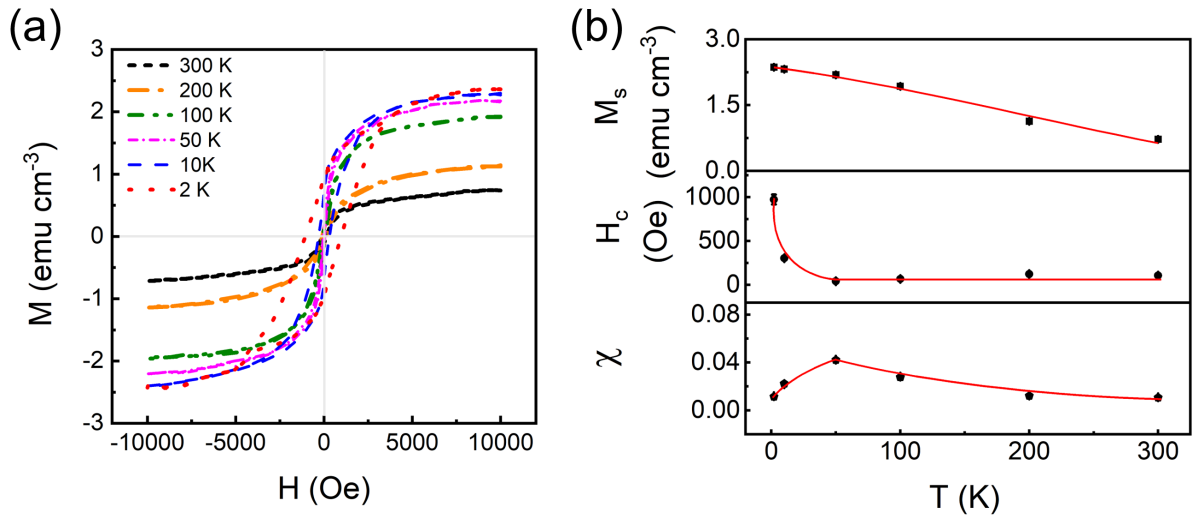

Figure 6.7: *(a) Magnetization curves of the printed hybrid film obtained at various temperatures plotted against magnetic field (from -10000 to 10000 Oe). (b) Saturation magnetization (M_s), coercivity (H_c), and magnetic susceptibility (χ) versus temperature obtained from the magnetization curves. The solid red lines serve as guides to the eye. (Reprinted with permission from [141]. Copyright 2021 Wiley-VCH GmbH.)*

In addition, a non-monotonic temperature dependence of the χ is observed as shown in Figure 6.7b. With increasing the temperature from 2 to 50 K, χ increases from 0.0115 ± 0.0012 to 0.0421 ± 0.0007. This increase results from a faster fluctuation of the magnetic moments, yielding an enhanced magnetic response at a higher temperature [13]. However, when the magnetic moments can be spontaneously reversed, a further increase in temperature causes the magnetic moments to fluctuate quite fast and become more difficult to be aligned or controlled by an external magnetic field with a previous used strength [198]. Thus, χ decreases as the temperature increases from 50 to 300 K.

According to the changes in H_c and χ (Figure 6.7b), the characteristic blocking temperature (T_B) of the superparamagnetic hybrid film is expected to be between 10 and 50 K. To quantify the T_B, field-cooling (FC) and zero-field-cooling (ZFC) measurements

are performed for the printed hybrid film at an applied external magnetic field of 100 Oe. Figure 6.8 shows the obtained FC and ZFC curves in the range of 2 to 300 K. A peak is observed at a temperature of around 24 K (marked with an arrow), indicating the T_B of the printed hybrid film is 24 K [199]. Thus, the hysteresis loops are observed at temperatures (2 and 10 K) below 24 K and disappear at temperatures above 24 K, such as 50, 100, 200 and 300 K (Figure 6.7a).

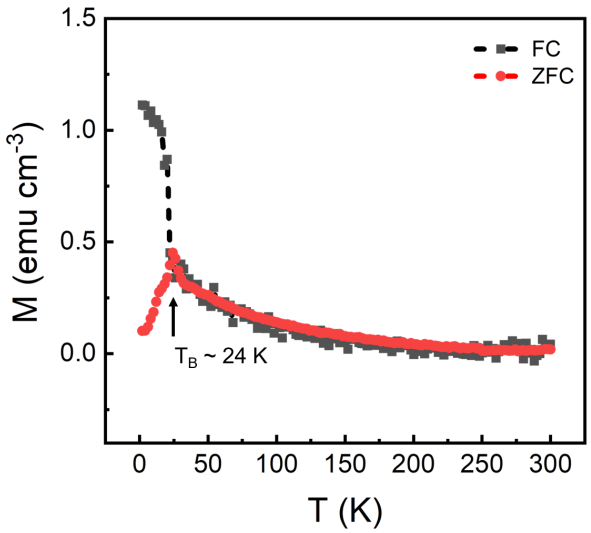

Figure 6.8: *FC (black square) and ZFC (red sphere) curves for printed hybrid film obtained at a magnetic field of 100 Oe. (Reprinted with permission from [141]. Copyright 2021 Wiley-VCH GmbH.)*

6.6 Summary

In this chapter, the influence of the presence of FePt NPs on the film formation of UHMW PS-*b*-PMMA DBC film is investigated in situ during printing of magnetic hybrid DBC film. A printed pure DBC PS-*b*-PMMA film serves as a reference to understand the impact of the NPs. The structure formation is monitored with in situ GISAXS measurements.

For both films, pure and hybrid, the size of PMMA domains decreases as the solvent evaporates from the initially deposited wet film. Compared to the pure film, the hybrid film exhibits a faster shrinkage of the PMMA domains due to the addition of NPs, which accelerates the solvent evaporation. As a result, a faster formation of a metastable state is observed in the hybrid film compared with the pure film. The metastable state changes slightly as the time increases due to the reorganization of polymer chains enabled by a small amount of residual solvent molecules inside the printed film. Since the presence of

the FePt NPs hinders the reorganization of the polymer chains, a longer metastable state is observed during the printing of hybrid film compared with the pure film. In addition, less parallel oriented microphase separation structures of the DBC are formed in the hybrid film compared to the pure film, which results in a higher ordered structure of the hybrid film when the solvent is almost evaporated. Similar to the PMMA domains, the size of the parallel DBC microphase separated structure is decreased as the solvent evaporates from the pure film. However, we do not see the similar shrinkage at the beginning of the solvent evaporation in case of the hybrid film because of the formation of less parallel PMMA cylinders in the hybrid film compared with the pure film. This leads to a weak scattering contribution, which is not detected in the GISAXS measurements of the hybrid film. Moreover, magnetic data reveal that the printed hybrid film is superparamagnetic, which is important for the fabrication of magnetic films used in magnetic sensors on a large scale.

Overall, this chapter provides insights for the future optimization of printed magnetic NP-DBC hybrid films, as well as the hybrid systems based on DBC and other types of non-magnetic NPs.

7 Self-assembly of large magnetic nanoparticles in UHMW diblock copolymer

Parts of this chapter have been published in the article: Self-assembly of large magnetic nanoparticles in ultrahigh molecular weight linear diblock copolymer films [87]. (Reprinted with permission from (W. Cao et al., *ACS Appl. Mater. Interfaces*, 2020, 12, 7557−7564.). Copyright 2020 American Chemical Society. DOI: 10.1021/acsami.9b20905).

In the previous work (chapter 6), a magnetic hybrid film containing UHMW PS-*b*-PMMA and small-sized FePt NPs is fabricated. By applying an UHMW DBC template with a large domain size, all FePt NPs are positioned inside the PMMA domains without excess of NPs into the other block. SQUID data indicates that the hybrid film is superparamagnetic which makes this film class promising for a hysteresis-free switching when changing the external magnetic field. However, the absence of a hysteresis at room temperature limits their utilization in data storage. To enable application in the field of magnetic data storage, magnetic films containing ferromagnetic NPs are required [32,33].

For ferromagnetic NPs, larger iron oxide NPs with a diameter above 20 nm can be utilized. The critical value for iron oxide NPs, below which the NPs are superparamagentic, is around 20 nm [33]. Unlike FePt NPs, the iron oxide NPs can be more easily synthesized and are commercially available nowadays. In literature, many reports related to the investigation of iron oxide NP-DBC hybrid films can be found [15, 17]. For example, Upadhyaya et al. demonstrated that poly(methacrylic acid)-*block*-poly(methyl methacrylate) (PMAA-*b*-PMMA) DBCs with different structures (spheres, worms, and vesicles) can be utilized as templates for the arrangement of Fe_3O_4 NPs coated with quaternized poly(2-(dimethylamino)ethyl methacrylate) [15]. In previous studies from the Müller-Buschbaum group, DBCs with different morphologies, like spherical polystyrene-*block*-poly(methyl methacrylate) (PS-*b*-PMMA), lamellar poly(styrene-d_8)-*block*-poly(n-butyl methacrylate) (PSd_8-*b*-PBMA) and cylindrical polystyrene-*block*-poly(N-isopropyl

acrylamide) (PS-*b*-PNIPAM), were used to template maghemite (γ-Fe_2O_3) NPs with PS chains [164, 178, 200]. However, the investigation mostly focused on iron oxide NPs with diameters below 20 nm, leading to iron oxide NP-DBC hybrid films with superparamagnetic behavior at room temperature. Such films cannot be utilized in data storage [32].

In this chapter, larger iron oxide NPs with a diameter of 27.0 $\pm$ 0.6 nm, above the critical value of 20 nm, are utilized to obtain ferrimagnetic properties. An asymmetric UHMW linear DBC PS-*b*-PMMA, which yields perpendicularly aligned large PMMA half-spheres inside the PS matrix, is used to template the large iron oxide NPs. The iron oxide NPs are purchased from Ocean NanoTech (San Diego, CA, United States). To enhance the compatibility between the NPs and the DBC, the NPs are coated with carboxylic acid ligands. The hydrogen bonding between the carboxylic acid ligands of NPs and the ester groups of PMMA allows a slightly higher selectivity of the NPs to PMMA blocks [142, 143]. The surface structure of the NP-DBC hybrid films is investigated as a function of the NP concentration by using AFM, SEM, and TEM. To probe the buried structures, GISAXS is applied. The magnetic properties of the hybrid films are probed with a SQUID magnetometer. We observe a change in the position of the NPs inside the UHMW DBC thin films depending on the NP concentration. At low NP concentrations, they are located at the interfaces (between the PS and PMMA domains), and at high NP concentrations, they are positioned preferentially inside the PMMA domains. SQUID data indicates that all hybrid films are ferromagnetic and thus are promising for potential applications in magnetic data storage.

7.1 Film surface morphology

7.1.1 Largescale morphology

For many applications the film homogeneity is necessary. The film homogeneity is examined via optical microscopy as a function of the NP concentration on a large scale (Figure 7.1). At low NP concentrations ($<$ 2 wt %), the films are homogenous. Only small dots, which are NP aggregates, can be observed. As the NP concentration increases (2 and 5 wt %), the size of NP aggregate increases, and the film uniformity is reduced. Further loading of NPs (10 and 20 wt %) leads to a formation of network-like agglomerates, which are covering the film surface, and result from the attractive forces among the magnetic NPs [200]. As a consequence, the films become rough.

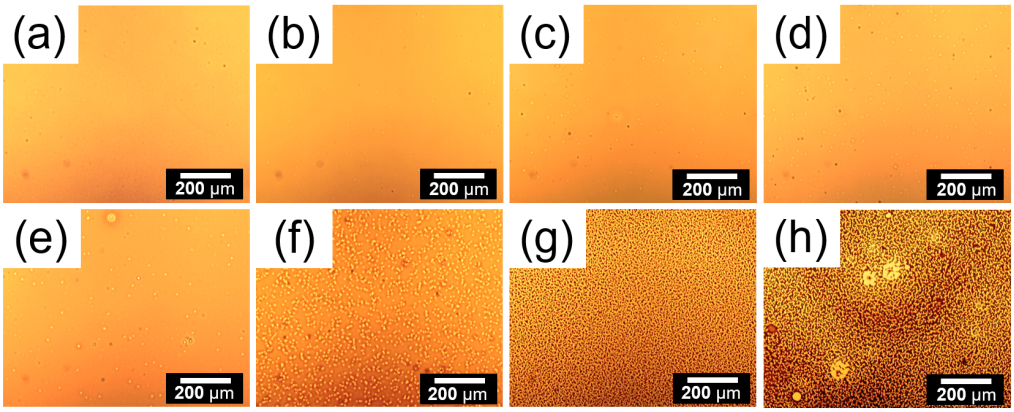

Figure 7.1: *OM images of hybrid films with increasing iron oxide NP concentration: (a) 0, (b) 0.1, (c) 0.5, (d) 1, (e) 2, (f) 5, (g) 10 and (h) 20 wt %. (Reprinted with permission from [87]. Copyright 2020 American Chemical Society.)*

7.1.2 Nanoscale morphology

To study the film surface morphology at the nanoscale, AFM is applied. The nanostructure of the pure films (NP-free PS-*b*-PMMA) is shown in Figure 7.2, where the dark matrix and bright domains are the PS and PMMA blocks, respectively. According to our previous study on the DBC with a PMMA volume fraction of 0.09, the morphology of the pure film should be spherical [26].

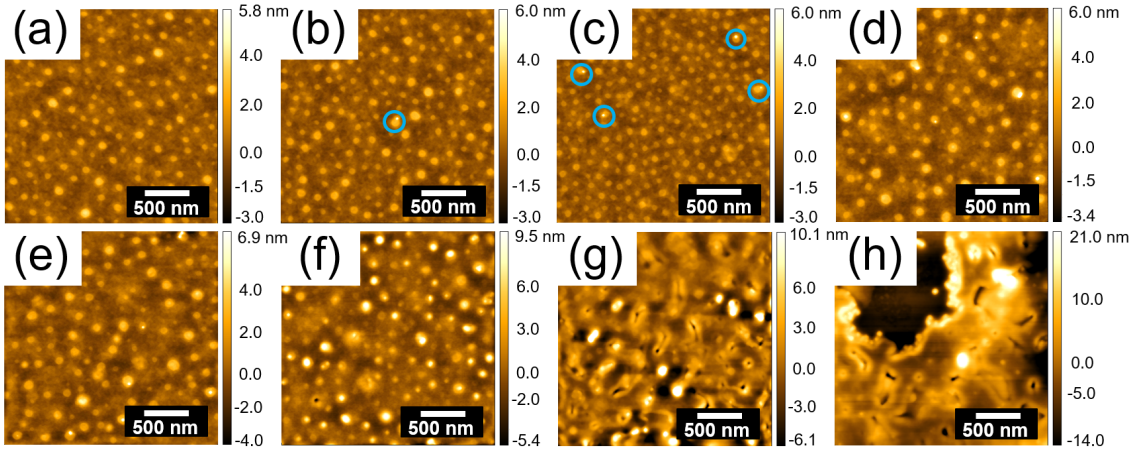

Figure 7.2: *AFM images of hybrid films with increasing iron oxide NP concentration. (a) 0, (b) 0.1, (c) 0.5, (d) 1, (e) 2, (f) 5, (g) 10 and (h) 20 wt %. The dark matrix, bright domains, and brighter dots are PS, PMMA, and iron oxide NPs, respectively. In (b) and (c), the blue circles show the NPs are selectively located at the interface between PS and PMMA domains. (Reprinted with permission from [87]. Copyright 2020 American Chemical Society.)*

With iron oxide NP loading, brighter dots (iron oxide NPs) appear at the interface

between the PS and the PMMA domains first (Figure 7.2b and 7.2c), then more and more white dots appear in the area of the PMMA spheres as shown in Figure 7.2d, 7.2e, 7.2f, 7.2g, and 7.2h. For a better view of the iron oxide NPs, the corresponding AFM phase images (Figure 7.3) and SEM images (Figure 7.4, 7.5 and 7.6) are also displayed.

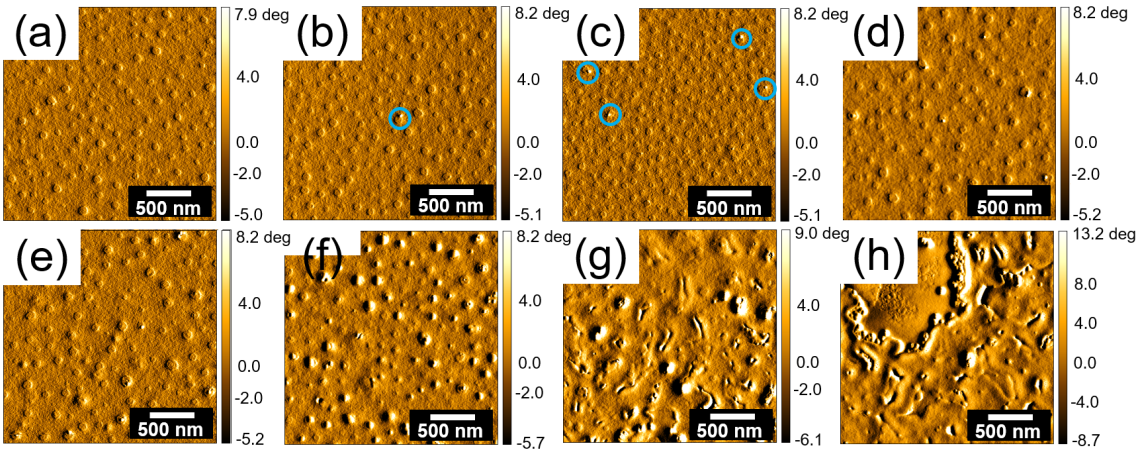

Figure 7.3: *AFM phase images of hybrid films with increasing iron oxide NP concentration. (a) 0, (b) 0.1, (c) 0.5, (d) 1, (e) 2, (f) 5, (g) 10 and (h) 20 wt %. In (b) and (c), the blue circles show the NPs are selectively located at the interface between PS and PMMA domains. (Reprinted with permission from [87]. Copyright 2020 American Chemical Society.)*

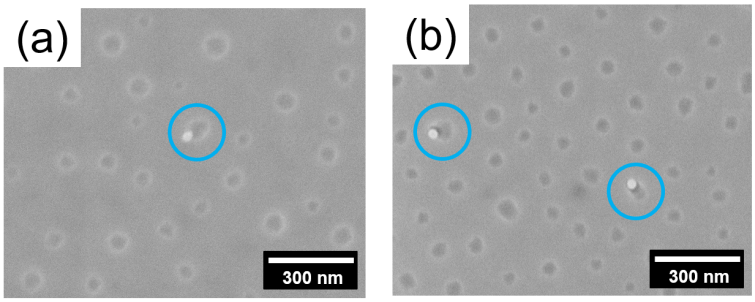

Figure 7.4: *SEM images of the NP-DBC hybrid films with iron oxide NP concentration of (a) 0.1 wt % and (b) 0.5 wt %. The NPs are selectively located at the interface between PS and PMMA domains, and are marked with blueorange circles. (Reprinted with permission from [87]. Copyright 2020 American Chemical Society.)*

Interestingly, instead of an increase of the PMMA sphere size, an obvious decrease is found with a NP concentration of 0.5 wt %. Such behavior can be explained by the location of the NPs. As seen in AFM (Figure 7.2b, 7.2c, 7.3b and 7.3c, marked with blue circles) and SEM (Figure 7.4a and 7.4b, marked with blue circles) images, the NPs are selectively located at the interface between PS and PMMA domains, due to a large

interfacial tension caused by the strong segregation strength χN of the UHMW DBC PS-*b*-PMMA [31, 201]. The selective localization of NPs at the interface is beneficial for reducing the interfacial tension [31]. Thus, in this case, less stretching of the polymer chains is necessary for accommodating the unfavorable contacts of PS and PMMA [202].

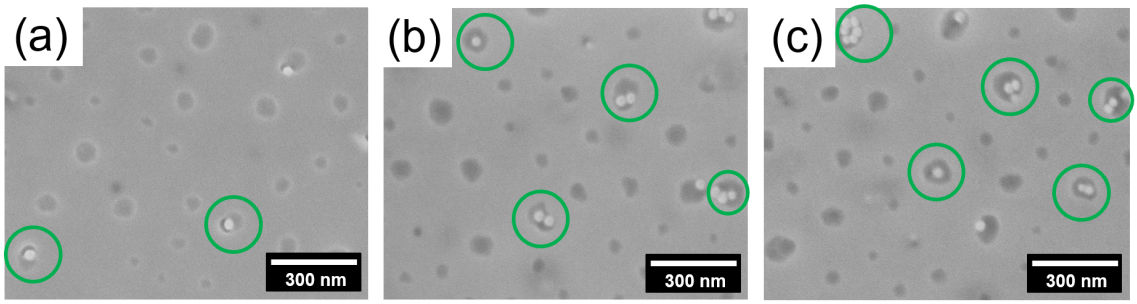

Figure 7.5: *SEM images of the NP-DBC hybrid films with iron oxide NP concentration of (a) 1 wt %, (b) 2 wt % and (c) 5 wt %. The NPs are located preferentially in the PMMA domains, and are marked with green circles. (Reprinted with permission from [87]. Copyright 2020 American Chemical Society.)*

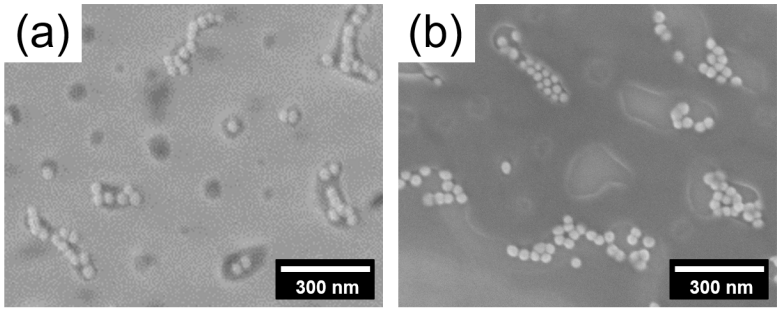

Figure 7.6: *SEM images of the NP-DBC hybrid films with iron oxide NP concentration of (a) 10 wt % and (b) 20 wt %. The formation of chain-like NP aggregates. (Reprinted with permission from [87]. Copyright 2020 American Chemical Society.)*

As the NP concentration increases from 0.5 to 5 wt %, more and more NPs and small NP aggregates (white dots in Figure 7.2d, 7.2e, and 7.2f) appear, resulting in a significant increase of the polymer elastic penalty. To minimize the polymer elastic penalty [31], the NPs and NP aggregates are preferentially located inside the PMMA spheres (Figure 7.2e-2f and 7.5b-c) due to the hydrogen bonding between the carboxylic acid ligands of NPs and the ester groups of PMMA. This is consistent with the results we observed in thick films, as shown in Figure 7.7 (cross-section TEM images). A further increase of the NP concentration to 10 wt % results in a deformation of the spherical structure of the PMMA domains, leading to the formation of PMMA ellipsoids (Figure 7.2g). Such ellipsoidal PMMA domain is caused by chain-like NP aggregates (a head-to-tail orientation, see

in Figure 7.6a), which are formed by strong dipolar coupling among the magnetic NPs at room temperature [203, 204]. The formation of such chain-like NP aggregates inside the PMMA block deforms the hosting domain. With the highest NP concentration, a discontinuous film appears (Figure 7.2h and 7.6b), which results from an overload of NPs.

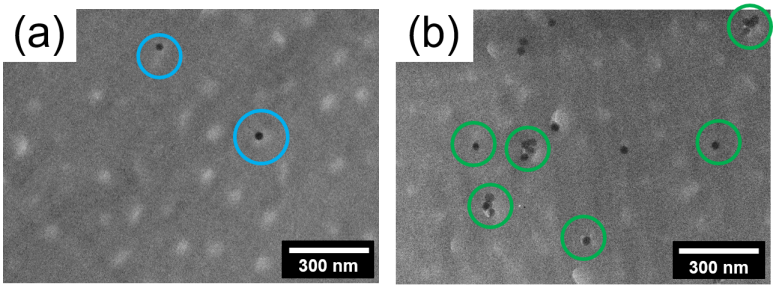

Figure 7.7: *Cross-sectional TEM images of thick NP-DBC hybrid films with iron oxide NP concentration of (a) 0.5 wt % and (b) 5 wt %. The NPs are located at the interface between PS and PMMA domains and in the PMMA domains, and are marked with blue circles and green circles, respectively. An ultramicrotom is applied to cut the thick film (around 30 m) into thin film (around 40 nm) on a Cu grid for the cross-sectional TEM measurements. (Reprinted with permission from [87]. Copyright 2020 American Chemical Society.)*

7.2 Film thickness

To accurately determine the thickness of the hybrid films, XRR measurements are performed for the homogenous films (< 10 wt %) and surface profilometry measurements for the rough films (≥ 10 wt %), because XRR is not suitable for rough films [166]. Thus, in Figure 7.8a XRR data of hybrid films with NP concentrations of 0, 0.1, 0.5, 1, 2, and 5 wt % are shown. Figure 7.8b shows the thickness of the hybrid films as a function of iron oxide NP concentration. At NP concentrations below 10 wt %, film thicknesses are extracted from the fits of corresponding XRR data. The film thickness increases linearly from 51 ± 0.3 nm (pure) to 74 ± 0.5 nm (5 wt %), due to the space required by the added NPs inside the films. For a further increase in the NP concentration the film thickness increases non-linearly from 74 ± 0.5 nm (5 wt %) to 92 ± 6 nm (20 wt %), because NPs are no longer mostly embedded inside the hybrid films. Instead, excessive NPs are on the sample surface at high NP concentrations [178].

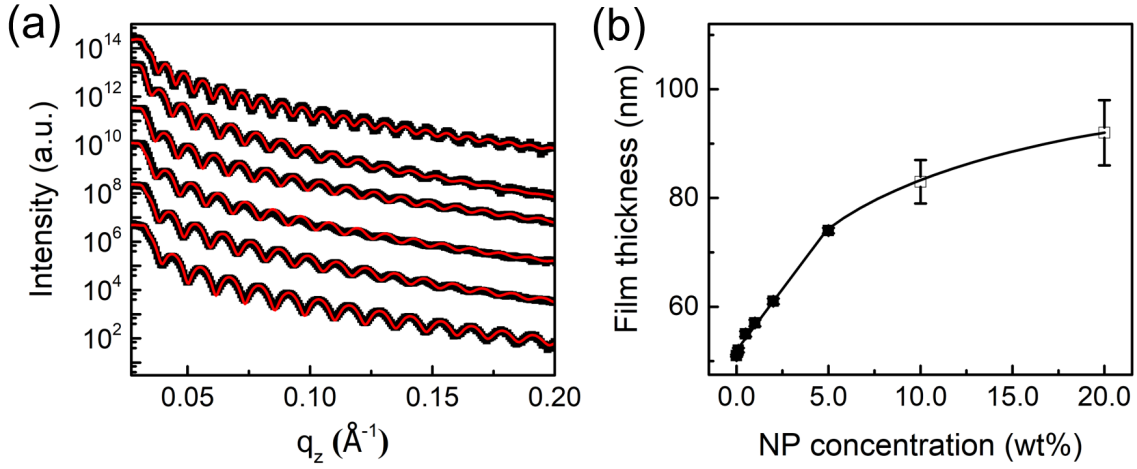

Figure 7.8: *(a) XRR data (black dots) of hybrid films at different iron oxide NP concentrations. Curves with fits (red solid lines) from bottom to top refer to hybrid films with NP concentrations of 0, 0.1, 0.5, 1, 2, and 5 wt %. (b) Film thickness plotted as a function of iron oxide NP concentration as measured by XRR (solid box) and surface profilometry (empty box). The black solid line serves as a guide to the eye. (Reprinted with permission from [87]. Copyright 2020 American Chemical Society.)*

7.3 Film inner morphology

The buried nanostructures are investigated with GISAXS [129]. Figure 7.9 shows the 2D GISAXS data of hybrid films with different iron oxide NP concentrations. With increasing NP concentration, the 2D GISAXS data change significantly. Interestingly, an extended intensity streak (Bragg rod, marked with red arrow) is observed at a NP concentration of 0.5 wt % (Figure 7.9c). This indicates a formation of a well-ordered nanostructure within the hybrid film. Moreover, the intensity becomes more and more prominent in the Yoneda region with increasing NP concentration, due to an enhancement of the electron density contrast with increasing NP content.

For a quantitative analysis, horizontal line cuts are performed at the Yoneda peak position from 2D GISAXS data and plotted together with the corresponding fits as shown in Figure 7.10a. In the fit procedure, the distorted-wave Born approximation (DWBA) based on the effective interface approximation (EIA) is applied for modeling the structures of the hybrid films [205]. Considering the observations from AFM and SEM, a spherical geometry is assumed for the PMMA domains and the iron oxide NPs [200].

In Figure 7.10a, in the GISAXS data two main features are observed. They are structure factors of the PMMA domains and the iron oxide NPs and are marked with I and II, respectively. For the NP-free (pure) PS-*b*-PMMA sample, a shoulder-like peak (q_y =

0.032 nm^{-1}, denoted as peak I, shown as a solid blue arrow in Figure 7.10a) is observed, which resembles the distance between two neighboring PMMA spheres. From the fit of the pure film, a structure with a PMMA sphere radius of 47 nm and an inter-domain distance of 195 nm is extracted. However, the film thickness is only 51 ± 0.3 nm (Figure 7.8b), which is less than the PMMA sphere diameter (94 nm). Thus, the film is highly confined and the formation of a full-sphere is not possible. The polymer blocks have to adopt a half-spherical morphology to realize the characteristic structure (L_0) in lateral direction [29, 57, 58].

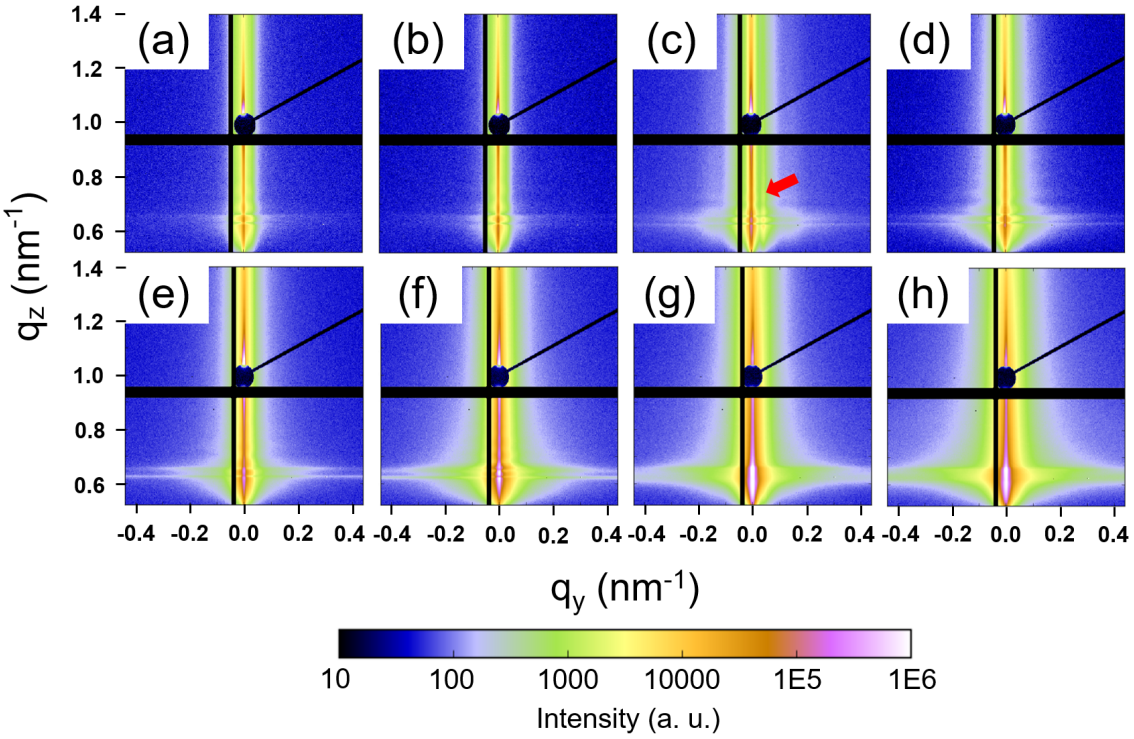

Figure 7.9: *2D GISAXS data of hybrid films with different iron oxide NP concentrations: (a) 0, (b) 0.1, (c) 0.5, (d) 1, (e) 2, (f) 5, (g) 10 and (h) 20 wt %. The specular peak is shielded by a beamstop. In (c), the red arrow shows the order peak. (Reprinted with permission from [87]. Copyright 2020 American Chemical Society.)*

As the NP concentration increases to 0.5 wt %, peak I shifts to higher q_y values and becomes more prominent, which indicates the formation of smaller inter-domain distances of PMMA spheres with higher ordered structures. The corresponding average PMMA sphere radius and inter-domain distance, extracted from peak I, decrease from around 47 nm to 35 nm (Figure 7.10b) and from around 195 nm to 137 nm (Figure 7.10c), respectively. Such decreases are consistent with the observation obtained from the AFM analysis discussed above. However, with increasing NP concentration from 0.5 to 10 wt %, peak I gets less prominent and shifts to lower q_y values (Figure 7.10a). The corresponding

average PMMA domain radius and inter-domain distance increase from around 35 nm to 53 nm and from around 137 nm to 210 nm, respectively. This increase can be explained by the incorporation of NPs inside the PMMA domains, resulting in an expansion of the PMMA domain radius and inter-domain distance. During SVA, the mobility of the polymer chains is enhanced. Thus, the mobile chains are able to adjust themselves for accommodating more NPs. As a result, the ordered spherical morphology is perturbed with increasing PMMA domain sizes.

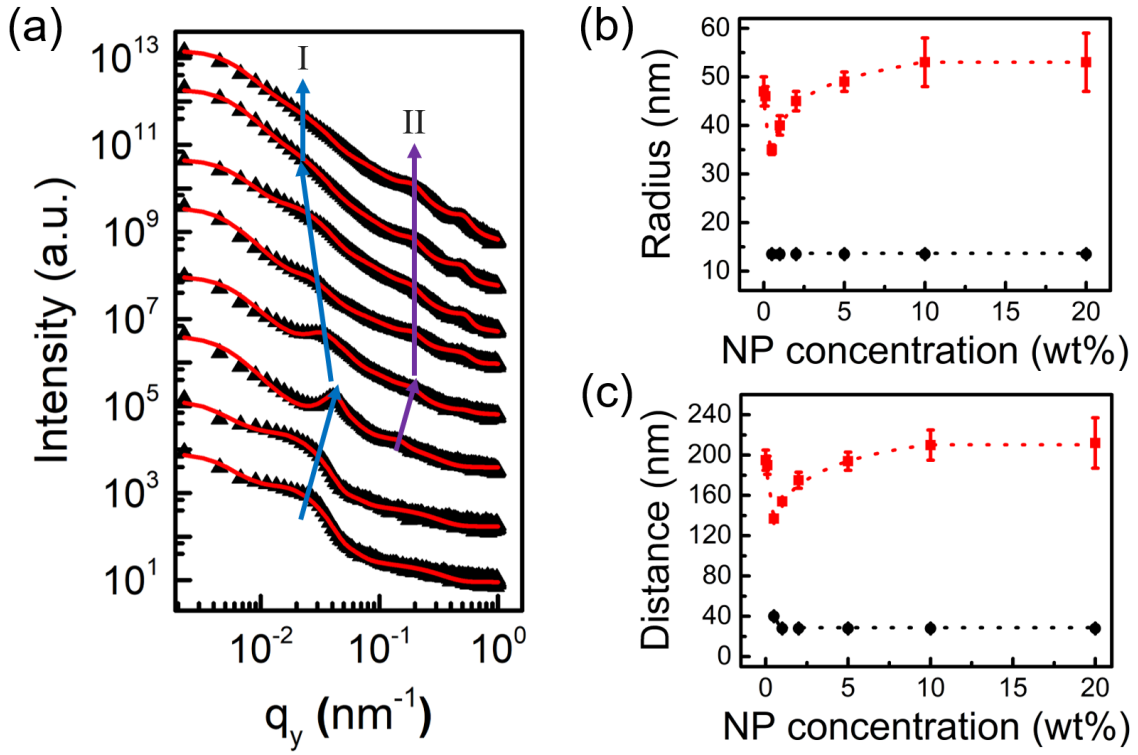

Figure 7.10: *(a) Horizontal line cuts obtained from the 2D GISAXS data for hybrid films with different iron oxide NP concentrations (from bottom to top: 0, 0.1, 0.5, 1, 2, 5, 10 and 20 wt %). The fits are indicated with red solid lines. For clarity, all curves are shifted along the intensity axis. Peak I and II are structure factors of PMMA spheres and iron oxide NPs, respectively. The structure results from a constant Ornstein-Zernike-like contribution at high qy, which is indicated with a dashed orange arrow. Feature structures extracted from the fits are (b) radius and (c) distance of the nanostructures. The dashed lines in (b) and (c) serve as a guide to the eye. (Reprinted with permission from [87]. Copyright 2020 American Chemical Society.)*

Moreover, as discussed above, from the AFM and SEM images (Figure 7.2g and 7.6), at a NP concentration of 10 wt %, part of the PMMA spheres are severely deformed into ellipsoids for accommodating the chain-like NP aggregates. These random ellipsoids accelerate the formation of ill-defined PMMA structures, as shown by the large error bars

in Figure 7.10b and 7.10c (NP concentration = 10 wt %). For further increase in the NP concentration from 10 to 20 wt %, peak I stays at a low q_y value. Figure 7.10b and 7.10c show the corresponding average PMMA domain radius and inter-domain distance, extracted from the fits, which are maintained at around 53 nm and 210 nm, respectively. Such constant values indicate the over-saturation of the PMMA domains with NPs.

In addition, with NP concentrations $\geq$ 0.5 wt %, another broad scattering feature (peak II, shown as a solid purple arrow) appears at higher q_y values (Figure 7.10a), which represents the structure factor of the iron oxide NPs. The corresponding NP radius stays constant at 13.5 $\pm$ 0.3 nm, while the center-to-center distance decreases from 40 $\pm$ 3 nm (0.5 wt %) to 28 $\pm$ 1 nm (1 wt %), and then remains constant at 28 $\pm$ 1 nm (Figure 7.10b and 7.10c).

Moreover, an additional scattering feature is seen at a rather high q_y value (shown as a dashed orange arrow), which is modelled with a constant Ornstein-Zernike-like contribution [170, 171]. The Ornstein-Zernike like contribution is the so-called correlation length, which can be considered as the distance between the neighboring entanglement points [171]. As the NP concentration increases, it becomes more prominent. Such phenomenon is caused by the redistribution of polymer chains due to more and more polymer chains stretching around the NPs at higher NP concentration.

7.4 Evolution of morphology

To present the entire morphological evolution of the NP-DBC hybrid films with increasing iron oxide NP concentration, a simplified sketch is shown in Figure 7.11. Via SVA, perpendicularly aligned large PMMA half-spheres are obtained in the pure (Figure 7.11a) UHMW DBC film. At low NP concentrations (0.1 and 0.5 wt %), the NPs are preferentially located at the interface of PS and PMMA phases (Figure 7.11b and 7.11c), the PMMA half-sphere size and inter-PMMA half-sphere distance decrease, and the order of the spherical structure is enhanced. It reaches the highest order at a NP concentration of 0.5 wt % (Figure 7.11c). At intermediate NP concentrations (Figure 7.11d), the previous ordered structure is perturbed, which is caused by the expansion of the PMMA domains for accommodating more NPs. However, further addition of NPs to a concentration of 10 wt % (Figure 7.11e) leads to a morphology change from half-sphere to half-ellipsoid for part of the PMMA domains. Such transition is caused by stronger dipoles among large iron oxide NPs, favoring the formation of NP chains. Finally, at very high NP concentration, a discontinuous film is observed (Figure 7.11f), due to the formation of larger NP aggregates on the film surface.

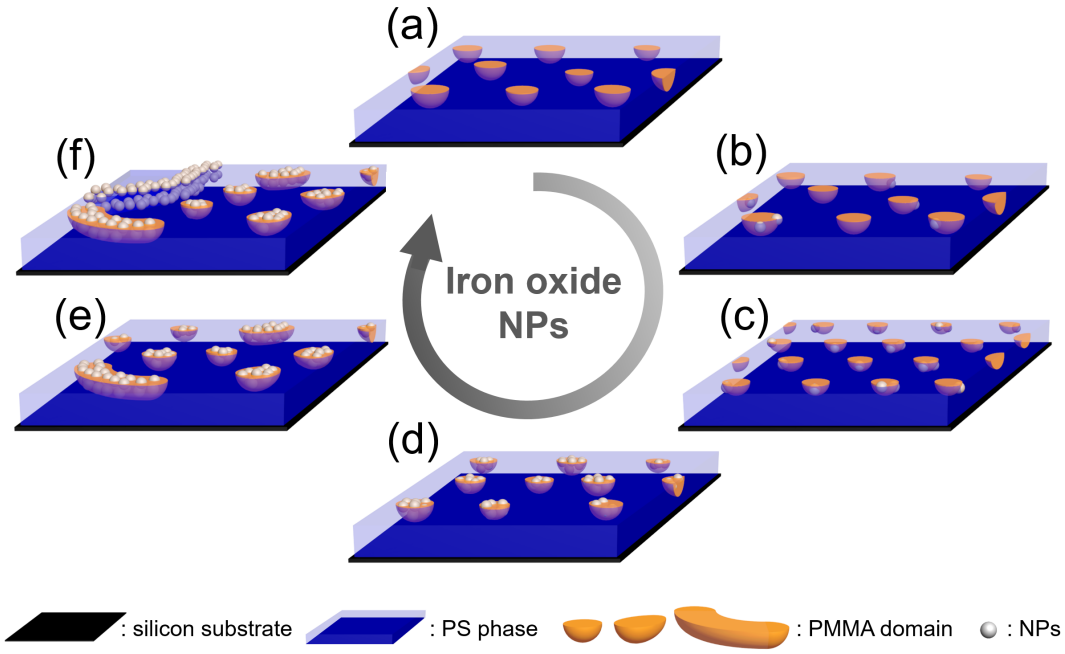

Figure 7.11: *Schematic representation of the morphology evolution of the (a) pure UHMW DBC film, and the NP-DBC hybrid films with (b) very low (0.1 wt %), (c) low (0.5 wt %), (d) intermediate (1 - 5 wt %), (e) high (10 wt %), and (f) very high (20 wt %) iron oxide NP concentrations. (Reprinted with permission from [87]. Copyright 2020 American Chemical Society.)*

7.5 Magnetic properties

7.5.1 Influence of temperature

Magnetization measurements are recorded by applying an external magnetic field (range from -7000 to 7000 Oe) parallel to the sample surface. To study the influence of the temperature on the magnetic behavior, a selected hybrid film with a NP concentration of 5 wt % is measured at different temperatures (Figure 7.12). The hybrid film is ferrimagnetic at all temperatures. As the temperature increases from 5 to 300 K, the hysteresis loop becomes narrower, especially for temperatures from 200 K (Figure Figure 7.12a). The corresponding remanence (M_r) and coercivity (H_c) decrease from around 0.95 to 0.64 emu cm^{-3} and from around 90 to 46 Oe, respectively (Figure Figure 7.12b). The observed behavior of Mr and Hc is caused by thermal fluctuations [196,206]. With increasing temperature, the magnetic moments fluctuate faster, causing an increase in random anisotropy of the magnetic domains. Moreover, a strong temperature dependence of the magnetic susceptibility (χ) is shown in Figure 7.12b. The higher the temperature, the

faster the magnetic response (higher χ), which is consistent with a previous study on magnetic NP-DBC films [13].

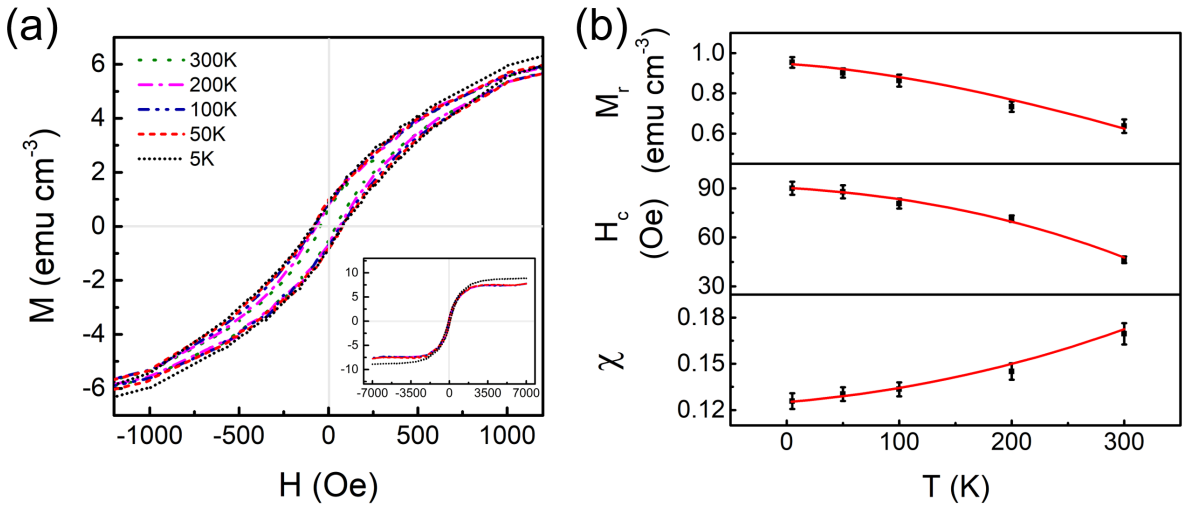

Figure 7.12: *Magnetic property of the NP-DBC hybrid film with an iron oxide NP concentration of 5 wt %. (a) Magnetic hysteresis loops recorded at different temperatures (from 5 to 300 K), and shown in the magnetic field range from -1200 to 1200 Oe. The hysteresis loops in the full field range from -7000 to 7000 Oe are displayed in the inset. (b) Remanence (M_r), coercivity (H_c) and magnetic susceptibility (χ) are extracted from the corresponding hysteresis loops and plotted as a function of temperature. The red solid lines serve as a guide to the eye. (Reprinted with permission from [87]. Copyright 2020 American Chemical Society.)*

7.5.2 Influence of NP concentration

Figure 7.13a shows the impact of the NP concentration on the magnetic properties of the NP-DBC hybrid films. The magnetic hysteresis loops are obtained at a temperature of 300 K, with an applied external magnetic field (from -7000 to 7000 Oe) parallel to the sample surface. All hybrid films are ferromagnetic at room temperature (300 K) with a coercivity (H_c) of about 46 Oe. The corresponding remanence (M_r), saturation magnetization (M_s) and relative remanence (M_r/M_s), extracted from Figure 7.13a, are plotted as a function of NP concentration (Figure 7.13b). With increasing NP concentration, both M_r and M_s increase evenly with similar tendency due to more NPs can provide more free flipping of magnetic moments. As a result, the ratio Mr/Ms remains unchanged, which is independent of NP concentration. This is consistent with previous studies of magnetic NP-DBC films [10, 164].

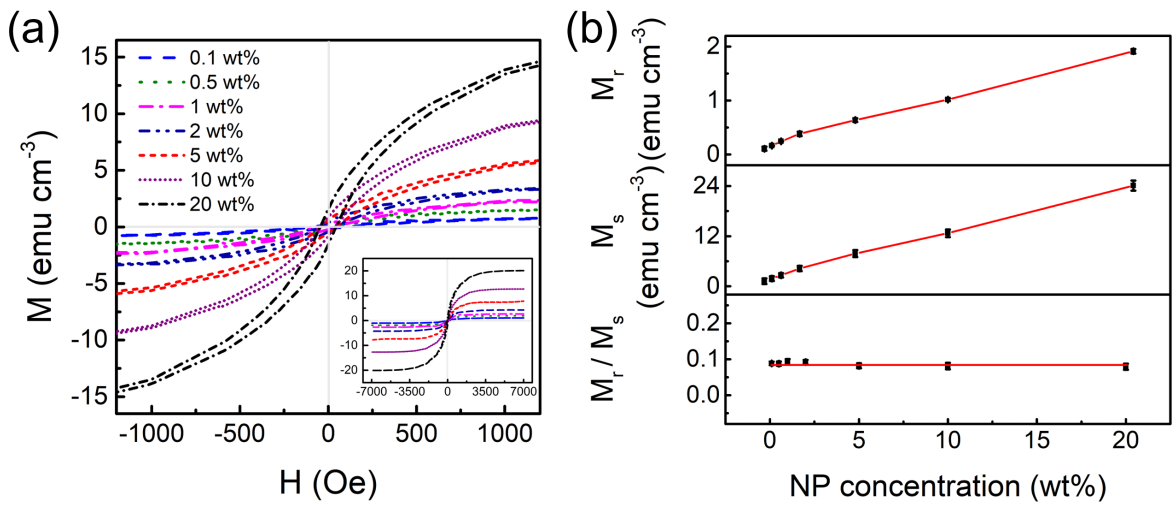

Figure 7.13: *(a) Magnetic hysteresis loops of the NP-DBC hybrid films with various iron oxide NP concentrations, in a magnetic field ranging from -1200 to 1200 Oe. All samples are measured at a temperature of 300 K. The hysteresis loops in the full field range from -7000 to 7000 Oe are displayed in the inset. (b) Remanence (M_r), saturation magnetization (M_s) and relative remanence (M_r/M_s) extracted from the corresponding hysteresis loops and plotted as a function of NP concentration. The red solid lines serve as a guide to the eye. (Reprinted with permission from [87]. Copyright 2020 American Chemical Society.)*

7.5.3 Magnetic anisotropy

As discussed earlier from the AFM and SEM images (Figure 7.2g, 7.6a and 7.14), at a NP concentration of 10 wt %, part of the NPs are aggregated to chain-like NP aggregates with a head-to-tail orientation. If the chain-like NP aggregates, as shown in Figure 7.14, are not randomly aligned in the film, they should exhibit a magnetic anisotropic behavior. In order to verify this, a magnetization curve is measured for the sample with a NP concentration of 10 wt %, in which the applied external magnetic field (B) is rotated by 90^o in the film plane, as shown in Figure 7.14 (from B_1 to B_2).

Figure 7.14 shows the NP chains are aligned closer to the B_2 direction compared to the B_1 direction (more blue rectangles versus red rectangles). For comparison, a reference sample (5 wt % NP) without chain-like NP aggregates is also measured under the same conditions. Figure 7.15a shows the effect of NP aggregate morphology on the magnetic properties of the NP-DBC hybrid films at T = 300 K. For the sample with a NP concentration of 5 wt %, no magnetic anisotropy is observed. However, for the sample with a NP concentration of 10 wt %, it shows a weak magnetic anisotropy. M_s and χ are slightly higher in the B_2 versus B_1 directions (Figure 7.15b), due to the alignment of NP chains closer to the B_2 direction (Figure 7.14), whereas a slightly lower H_c is observed

in the B_2 direction (Figure 7.14b). In general, a higher H_c should be obtained when the magnetic field is oriented closer to the easy axis (NP chain's direction). Thus, in addition to the effects of simple anisotropy, the possible mechanisms of magnetization reversal also need to be considered. There are two possible mechanisms, "parallel rotation mechanism" and "fanning mechanism", for the magnetization reversal [207, 208]. It has been reported that if the magnetization reversal follows a "fanning mechanism", H_c is decreased with decreasing ψ (an angle between the NP chain and the applied magnetic field B) from a critical angle ψ_0 (between 54.8^o and 49.8^o) [207]. Thus, a lower H_c is obtained when the applied magnetic field is oriented closer to the easy axis (NP chain's direction).

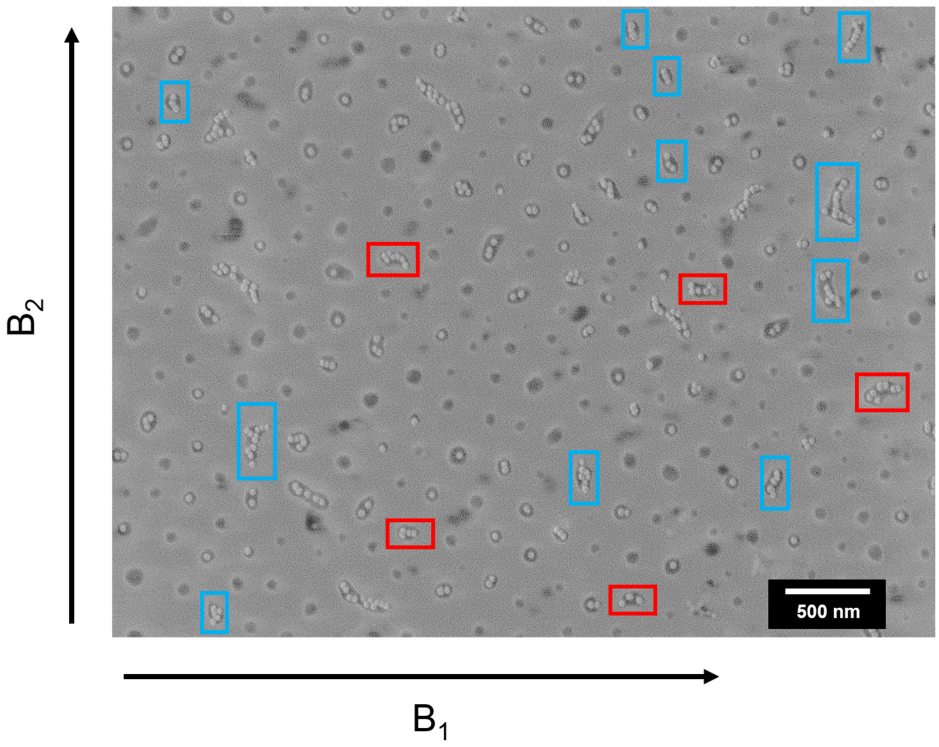

Figure 7.14: *SEM image of the NP-DBC hybrid film with iron oxide NP concentration of 10 wt %. B_1 and B_2 are external magnetic fields, which are applied in two orthogonal directions in the film plane to determine the magnetic property of the hybrid film at temperature of 300 K. The NP chains (with three or more single NPs) align along the directions of B1 and B2 are marked with red and blue rectangles, respectively. (Reprinted with permission from [87]. Copyright 2020 American Chemical Society.)*

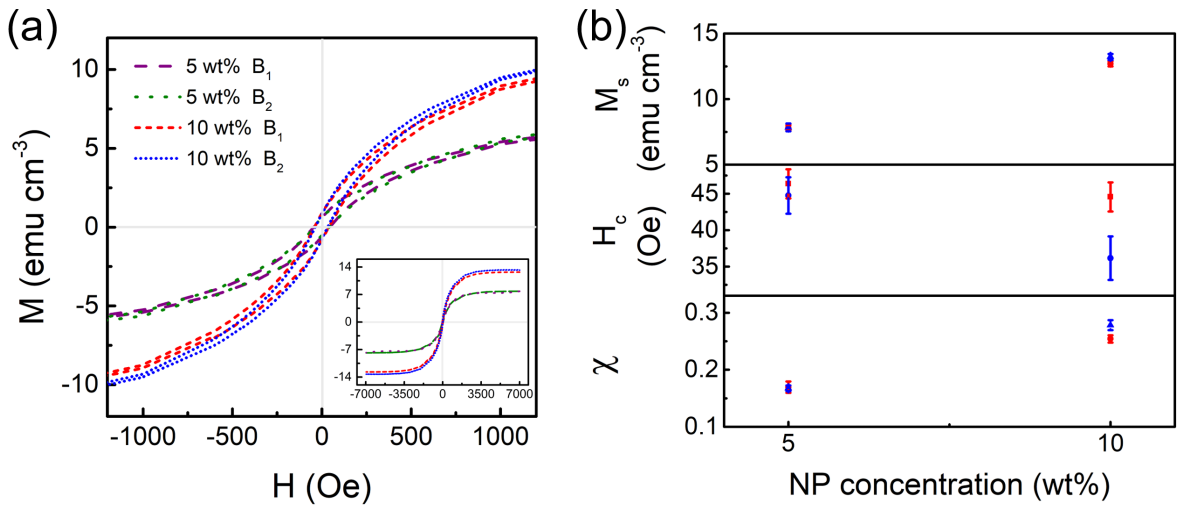

Figure 7.15: *(a) Magnetic hysteresis loops of the selected NP-DBC hybrid films with iron oxide NP concentrations of 5 and 10 wt % at a temperature of 300 K, and shown in the magnetic field range from -1200 to 1200 Oe. The hysteresis loops in the full field range from -7000 to 7000 Oe are displayed in the inset. B_1 and B_2 are external magnetic fields, which are applied in two orthogonal directions in the film plane. (b) Saturation magnetization (M_s), coercivity (H_c) and magnetic susceptibility (χ), are extracted from the corresponding hysteresis loops and plotted as a function of NP concentration. B_1 (red dots) and B_2 (blue dots) orientations are compared. (Reprinted with permission from [87]. Copyright 2020 American Chemical Society.)*

7.6 Summary

In this chapter, we report a facile method for the fabrication of ferromagnetic hybrid films containing large iron oxide NPs with diameters of 27.0 ± 0.6 nm.

The UHMW linear DBC PS-*b*-PMMA with large domains is utilized to template large iron oxide NPs. The localization of the NPs inside the UHMW DBC is investigated as a function of the NP concentration. For small amounts of NPs, the decrease in polymer interfacial tension is dominant. The NPs are located preferentially at the interface between the PS and PMMA domains, resulting in a decrease of PMMA domain sizes and inter-domain distances. Moreover, low NP loading helps to enhance the order of the half-spherical structure, and a well-ordered half-spherical morphology is observed at a NP concentration of 0.5 wt %. At high NP concentrations, the decrease in polymer elastic penalty becomes dominant. The NPs are preferentially located inside the PMMA domains, which leads to an expansion of the PMMA domains and inter-domain distances. As a result, the previously ordered half-spherical morphology is perturbed resulting in an

increased PMMA domain sizes. Interestingly, a change in the morphology from sphere to ellipsoid is seen for part of the PMMA domains at NP concentrations above 5 wt %. Such transition is caused by the formation of chain-like NP aggregates.

Magnetic properties of the hybrid films are probed via SQUID magnetometry. SQUID data show that the hybrid film containing chain-like NP aggregates exhibit a weak magnetic anisotropy at NP concentration of 10 wt %. All hybrid films are ferromagnetic at room temperature and are therefore good candidates for potential applications in magnetic data storage.

8 Spray deposited anisotropic ferromagnetic hybrid polymer films

Parts of this chapter have been published in the article: Spray-deposited anisotropic ferromagnetic hybrid polymer films of PS-*b*-PMMA and strontium hexaferrite magnetic nanoplatelets [146]. (Reprinted with permission from (W. Cao et al., *ACSAppl. Mater. Interfaces*, 2021, 13, 1592–1602.). Copyright 2021 American Chemical Society. DOI: 10.1021/acsami.0c19595).

In the previous chapter 7, magnetic hybrid polymer films containing iron oxide NPs and UHMW PS-*b*-PMMA DBC are fabricated. All hybrid films are ferromagnetic at room temperature. However, the coercivity of the obtained iron oxide NP-DBC hybrid film is only around 46 Oe, which is too small to meet advanced requirements in data storage applications.

To obtain films with high coercivity, M-type hexaferrite magnetic nanoplatelets with high coercivity can be utilized [34,120]. They are hard magnetic materials with a platelet-like shape and a high magnetic anisotropy [35]. Earlier works showed that coercivity depended on a favorable orientation of the magnetic nanoplatelets [119, 209]. To achieve the favorable orientation of the nanoplatelets, various approaches, such as anodic aluminum oxide (AAO) template, electrostatic attraction and external magnetic field, were used [119, 209, 210]. For instance, Lukatskaya et al. successfully controlled the arrangement of aluminum doped magnetic strontium hexaferrite nanoplatelets by using AAO membrane as a template [209]. Kushnir et al. prepared strontium hexaferrite nanoplatelets with positive charges and observed a fixed orientation of the nanoplatelets on a negatively surface charged glass substrate [119]. Such orientation was caused by the electrostatic attraction between the positive charges of the nanoplatelets and the negative charges of the substrate surface, which allowed the large facet of the nanoplatelets to align parallel to the surface of the substrate. Shuai et al. utilized an external magnetic field to align the moments of ferromagnetic nanoplatelets and investigated the mechanism of magnetomechanical effects [210]. Apart from these approaches, utilization of

DBC templates is also an efficient way to control the orientation of the nanoplatelets. For example, Krook et al. utilized a lamellar PS-*b*-PMMA to template the alignment of the rhombic nanoplatelets, which were gadolinium trifluoride doped with ytterbium and erbium [211, 212].

So far, concerning nanoplatelets-DBC hybrid films, less attention has been paid to the use of magnetic nanoplatelets and the study of kinetic processes during film fabrication. Due to the orientation-dependent magnetic properties of the magnetic nanoplatelets, it is of great significance to systematically investigate the kinetic processes during the film preparation process. GISAXS has proven to be a suitable approach for in situ morphology studies, which provided an in-depth understanding of fundamental kinetic processes [13, 154]. In a previous study, GISAXS was successfully applied to study the kinetics of superparamagnetic NPs-DBC hybrid films during spray deposition [13]. The effects of the magnetite NPs on the film formation and DBC morphology were identified. However, the used magnetic NPs were spherical, which limited the investigation of their orientation during spray deposition. Moreover, the hybrid film exhibited superparamagnetic behavior, instead of a ferromagnetic behavior that can be used in data storage applications [6, 213].

In the present study, spray deposition, a scalable technique, is applied to prepare ferromagnetic hybrid films from solution precursors, which contain UHMW DBC PS-*b*-PMMA and strontium hexaferrite nanoplatelets. Compared to DBCs with low or intermediate molecular weight, UHMW DBCs can provide more space to host the nanoplatelets due to the large nanostructures formed by microphase separation [18]. During spray deposition, kinetic processes of the DBC morphology and the orientation of the magnetic nanoplatelets are monitored by in situ GISAXS measurements. A pure DBC film without nanoplatelets is also prepared as a reference. The scattering data suggest that the average tilt angle between the nanoplatelet large facet and substrate surface normal is decreased over spray time, which is caused by the dipole-dipole interactions between magnetic nanoplatelets and the interaction among the substrate, PMMA block and nanoplatelets. The obtained final dried films are then solvent vapor annealed inside a closed chamber with tetrahydrofuran (THF) to study the influence of solvent vapor annealing (SVA). To probe the surface structures and magnetic properties of the final films before and after SVA, characterizations, with scanning electron microscopy (SEM) and superconducting quantum interference device (SQUID) magnetometry, are applied. Results show that ferromagnetic hybrid polymer films with high coercivity can be achieved via spray deposition, which is beneficial to scale up the fabrication of hybrid films for magnetic data storage applications [34]. Moreover, the hybrid film shows perpendicular magnetic anisotropy before SVA while a weak magnetic anisotropy remains after SVA,

which renders these hybrid films as interesting candidates for magnetic data storage and sensors [214].

8.1 Spray deposition

The solution used for spray deposition is prepared from a mixture of UHMW PS-*b*-PMMA DBC and strontium hexaferrite nanoplatelets dissolved in a solvent DMF with a fixed DBC concentration of 6 mg mL^{-1}. The weight ratio of nanoplatelets to the PS-*b*-PMMA is 3 wt %. The utilized PS-*b*-PMMA has an average molar mass of 870 kg mol^{-1} with the PMMA volume fraction of 0.173. The strontium hexaferrite nanoplatelets are synthesized by Trusov group and are functionalized with polyacrylic acid (PAA). The nanoplatelets' average diameter of the large facet is around 39 nm and average thickness is around 5.5 nm. For reference, a pure DBC solution without nanoplatelets is prepared with the same conditions. Silicon wafers are cut into the size of 20 mm × 20 mm and cleaned before spray deposition. The whole spray process is performed in a custom-made spray set up equipped with a spray gun. The spray protocol consists of 20 cycles. Each cycle is defined as 0.1 s spray-on (spraying) and 2.0 s spray-off (waiting). Details of the utilized materials and spraying can be seen from the chapter 4 (sample preparation).

To track the structure evolution of spray deposited films, GISAXS measurements are performed in situ during the 42 s spray time, which is calculated by (0.1 s spraying + 2.0 s waiting) × 20 cycles (Figure 4.9). The in situ measurements are performed at PETRA III (MiNaXS/P03 beamline) at DESY (Hamburg, Germany) [215] with an X-ray wavelength of 0.0965 nm. To avoid beam damage and to also obtain information on the measured samples over a large area, the sample stage keeps scanning in a 15 mm range along the sample surface y-direction, which is normal to the X-ray beam direction [13]. The scattering signal is collected on a 2D detector Pilatus 300 K (Dectris Ltd.; pixel size of 172 μm × 172 μm) with each frame of 0.1 s measurement time. The statistics of the scattering signal are improved by integrating 10 frames to 1 frame with 1 s because there is no morphological change in a time range of less than 1 s [13]. To probe the desirable nanostructures in the sprayed films with full depth, the sample-detector distance and incidence angle of the X-ray beam are set to 4340 mm and 0.4^o, respectively.

8.2 Surface morphology before solvent vapor annealing

For final spray deposited films (pure and hybrid), SEM is used to examine their surface morphologies before SVA, as shown in Figure 8.1. Figure 8.1a shows the SEM image of the

final pure PS-*b*-PMMA film, in which the bright and dark parts are the PS and PMMA blocks, respectively [187]. Due to the use of UHMW DBC, a very high segregation strength χN between PS and PMMA blocks is obtained [31]. According to the self-consistent field theory, [40] such very high segregation strength leads to the realization of a cylindrical morphology of the DBC, although the PMMA volume fraction of DBC is only 0.172. Thus, the morphology of the PMMA domains should be cylindrical. In Figure 8.1a, lying-down and perpendicular PMMA cylinders are observed. They can be better identified from Figure 8.1c, which is an enlarged view of Figure 8.1a. The average diameter of the PMMA cylinders and the average length of the lying-down PMMA cylinders are around 26 nm and 103 nm, respectively.

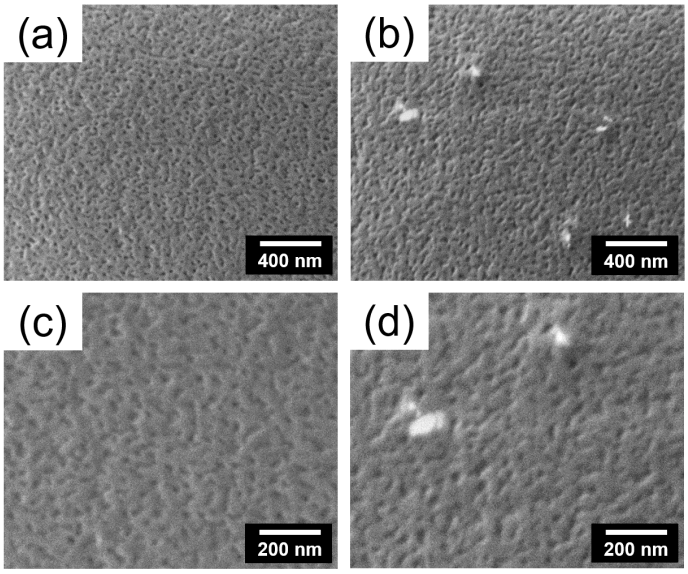

Figure 8.1: *SEM images of the spray deposited final films before SVA of (a, c) pure DBC reference film and (b, d) ferromagnetic hybrid film containing 3 wt % of magnetic nanoplatelets at (a, b) low and (c, d) high magnifications. (Reprinted with permission from [146]. Copyright 2020 American Chemical Society.)*

With magnetic nanoplatelets loading, brighter objects (magnetic nanoplatelets) appear in the area of PS matrix of the DBC film as shown in Figure 8.1b, 8.1d (an enlarged view of Figure 8.1b) and Figure 8.2. Due to the hydrogen bonds between ester groups of PMMA and polyacrylic acid (PAA) ligands of magnetic nanoplatelets, the nanoplatelets should be located preferentially inside the PMMA cylinders [145]. However, the size of the nanoplatelets is too large to be located inside the PMMA cylinders with an average diameter of around 26 nm. As shown in Figure 4.4, the nanoplatelets' average diameter of the large facet is around 39 nm and average thickness is around 5.5 nm. Moreover, during spray deposition, the film formation speed is too fast [216], causing the

nanoplatelets do not have sufficient time to undertake vigorous movements [217]. As a result, the nanoplatelets are trapped inside the PS matrix, which has sufficient space for the accommodation of nanoplatelets and the final sprayed films exhibit a non-equilibrium morphology.

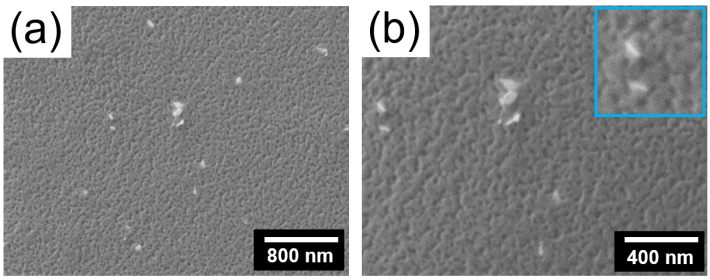

Figure 8.2: *SEM images of the spray deposited final ferromagnetic hybrid film containing 3 wt % of magnetic nanoplatelets before SVA at (a) low and (b) high magnifications. In (b), on the top right corner is a zoomed-in image, which is used to show the position of magnetic nanoplatelets. (Reprinted with permission from [146]. Copyright 2020 American Chemical Society.)*

8.3 Morphology evolution during spray deposition

To monitor the morphology evolution of the reference and hybrid films during spray deposition, in situ GISAXS measurements are applied. A schematic view of the spray deposition with simultaneous in situ GISAXS measurements is shown in Figure 4.9. In the selected spray protocol, 20 spray cycles are applied and each cycle consists of 0.1 s spraying (spray-on) and 2 s waiting (spray-off). The temperature of the substrate is controlled at 170 °C via a heating plate, which is slightly higher than the boiling point of dimethylformamide (DMF) (153 °C) [150], being used to dissolve PS-*b*-PMMA and the magnetic nanoplatelets. Therefore at 170 °C, the rapid drying of the deposited hybrid films means to operate the spray process in the dry-spray regime [13]. Moreover, the temperature of 170 °C is also higher than the glass transition temperature of both PS and PMMA blocks (around 105 °C). However, considering the utilized UHMW DBC with highly entangled chain conformations [25], significant movement of the DBC chains are not expected in the very short spray time (less than 1 minute). Thus, in the present study, the influence of the temperature on the DBC evolution can be ignored.

8.3.1 Pure DBC reference film

For the pure DBC reference film, the selected 2D GISAXS data with different spray times are shown in Figure 8.3. As the spray time increases, the overall scattering intensity increases, which is caused by a growing amount of DBC on the substrate over time [154].

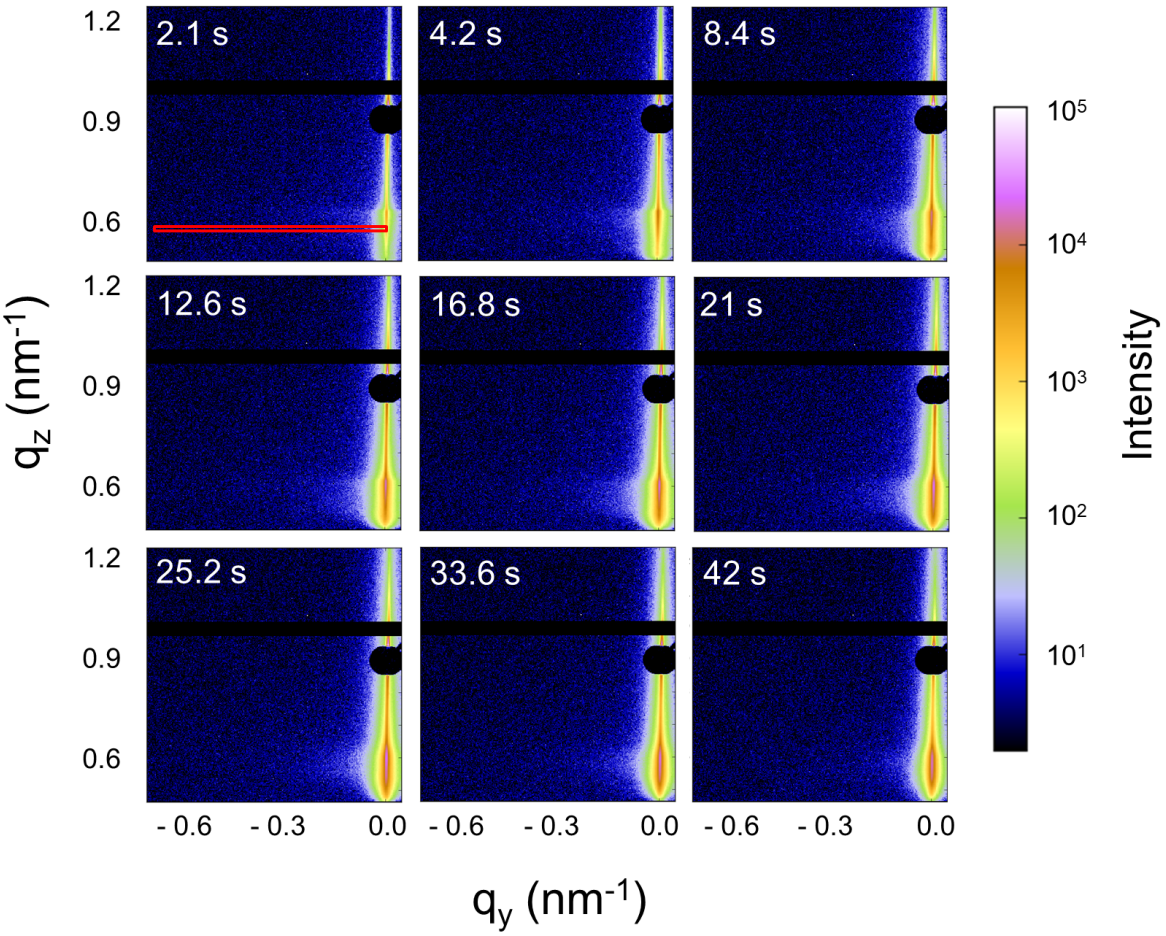

Figure 8.3: *Selected 2D GISAXS data of the pure DBC reference film measured during in situ spray deposition at different times as indicated (top left corner). A red rectangle in 2.1 s represents the horizontal line cut along qy direction. (Reprinted with permission from [146]. Copyright 2020 American Chemical Society.)*

In order to quantitatively analyze the structure evolution during spraying, horizontal line cuts of the 2D GISAXS data are taken as shown in Figure 8.3 (2.1s). The selected horizontal line cuts (Figure 8.4a, black dots) are modeled based on the distorted-wave Born approximation, which relates to the effective interface approximation [126, 192]. Considering the observations from SEM, two different cylindrical geometries (form factors), which represent the radii of PMMA elongated structure (half-length of lying-down

PMMA cylinder) and PMMA cylinders, are assumed in the model. Detailed modeling parameters can be found in the Supporting Information. The fits, extracted radii and distances are displayed in Figure 8.4a (red lines), 8.4b and 8.4c, respectively.

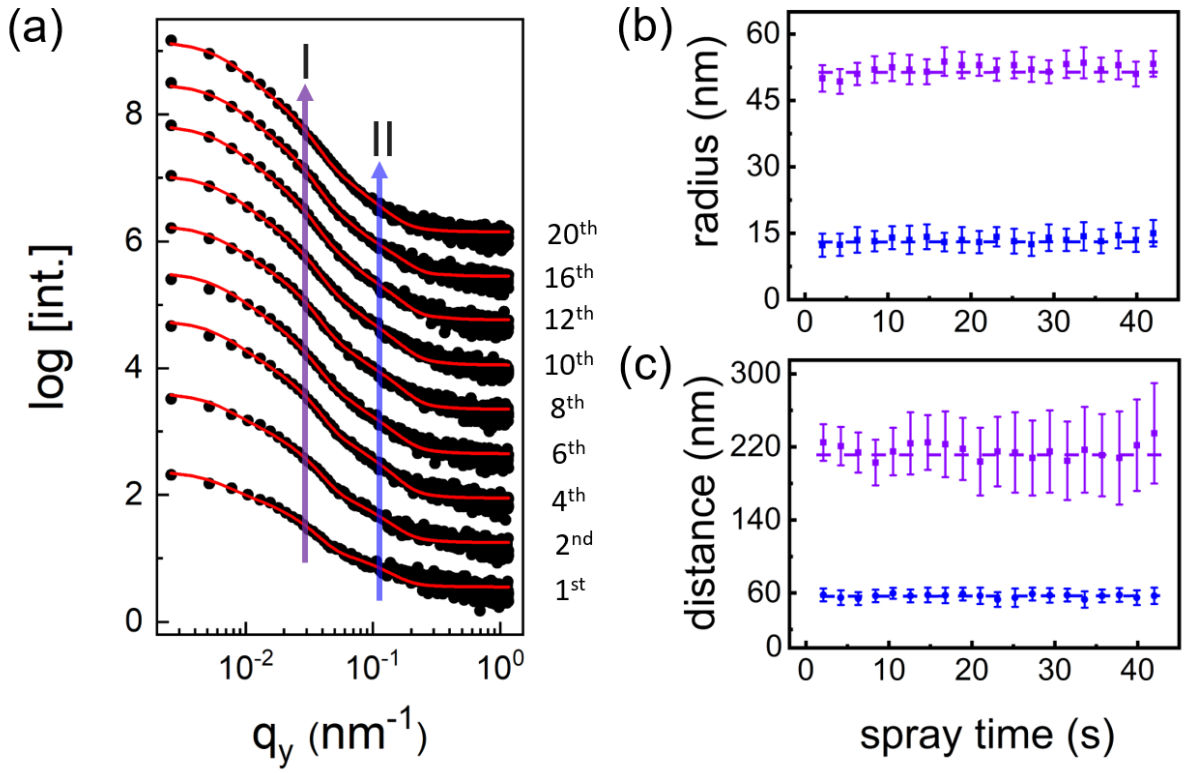

Figure 8.4: *(a) Selected horizontal line cuts (black dots) from the 2D GISAXS data of pure DBC reference film with increasing spray cycle number (1st, 2nd, 4th, 6th, 8th, 10th, 12th, 16th, and 20th from bottom to top, corresponding to the spray time of 2.1 s, 4.2 s, 8.4 s, 12.6 s, 16.8 s, 21 s, 25.2 s, 33.6 s, and 42 s). The red lines show the fits. Curves are shifted along the intensity axis for clarity of the presentation. Structure I (purple arrow) and II (blue arrow) are structure factors of PMMA elongated structure and PMMA cylinders, respectively. (b) Radius and (c) distance of the nanostructures extracted from the fits. The dashed lines in (b) and (c) serve as a guide to the eye. (Reprinted with permission from [146]. Copyright 2020 American Chemical Society.)*

In Figure 8.4a, two main features are observed and denoted with structure I and structure II in the GISAXS data, which correspond to the structure factors of PMMA elongated structure (lying-down PMMA cylinders along the length direction) and PMMA cylinders (all PMMA cylinders along the radius direction), respectively. As the spray cycle number increases, structure I remains constant and becomes weaker, indicating the formation of unchanged center-to-center distance of neighboring PMMA elongated structure with less ordered structures. The average radius and center-to-center distance of the PMMA

elongated structure remain stable at around 51 ± 3 nm (Figure 8.4b) and 211 ± 37 nm (Figure 8.4c) during the entire spray process. Such unchanged radius and distance are similar to our previous research on spraying DBC films [13].

During spraying, the DBC solution is first atomized into a multitude of droplets. These droplets are then carried onto the substrate driven by the nitrogen flow [218]. Due to the flying time of the droplets from the nozzle to the substrate surface, part of the solvent in the droplets has been evaporated before the droplets reach the substrate [154]. Moreover, the high temperature of the substrate (170 °C) causes an extremely rapid evaporation of the residual solvent (dry-spray regime) [13]. Thus, the average domain radius and average center-to-center distance remain constant over the spray deposition. However, as spray deposition progresses, less free substrate surface is exposed and more DBC material is deposited on the previously deposited discontinuous DBC film [13]. This change in surface coverage can cause a change in the orientation of the PMMA cylinders related to the effect of the substrate and free surface. The reason is as follows: Due to the presence of hydrophilic SiO_x on the silicon substrate surface caused by the acid cleaning process with an acid solution, the interfacial energy substrate-PMMA is lower than the interfacial energy substrate-PS, leading to segregation of the PMMA block at the substrate surface accompanied with the formation of lying-down PMMA cylinders [195, 219]. Since PMMA has a slightly higher surface energy than PS at 170 °C, on the film surface less lying-down PMMA cylinders remain [194]. The previous work by Ji et al. confirmed that the number of tilted (lying-down) cylinders decreased as they were close to the free surface [220]. In later spray stages, such difference between the substrate and film surface leads to the formation of less lying-down PMMA cylinders, causing a broader distribution of the center-to-center distance of the PMMA elongated structure. As a result, the structure order of the overall PMMA elongated structure in the entire film becomes weak (Figure 8.4a), as shown by the error bars in Figure 8.4c. In contrast, there are no obvious changes in the value and error bar extracted from structure II (structure factor of PMMA cylinders) during the entire spray process (Figure 8.4c). The corresponding average radius and center-to-center distance of the PMMA cylinders remain constant at around 13 ± 3 nm (Figure 8.4b) and 58 ± 7 nm (Figure 8.4c), respectively.

8.3.2 Hybrid polymer film

For the ferromagnetic hybrid film containing 3 wt % magnetic nanoplatelets, the selected 2D GISAXS data with different spray times are shown in Figure 8.5. As the spray time increases, the scattering intensity increases which is similar to the observations in case of the pure DBC reference film. However, 2D GISAXS data of the ferromagnetic hybrid film

show a higher intensity along the q_y direction compared to the reference film, because of the presence of magnetic nanoplatelets.

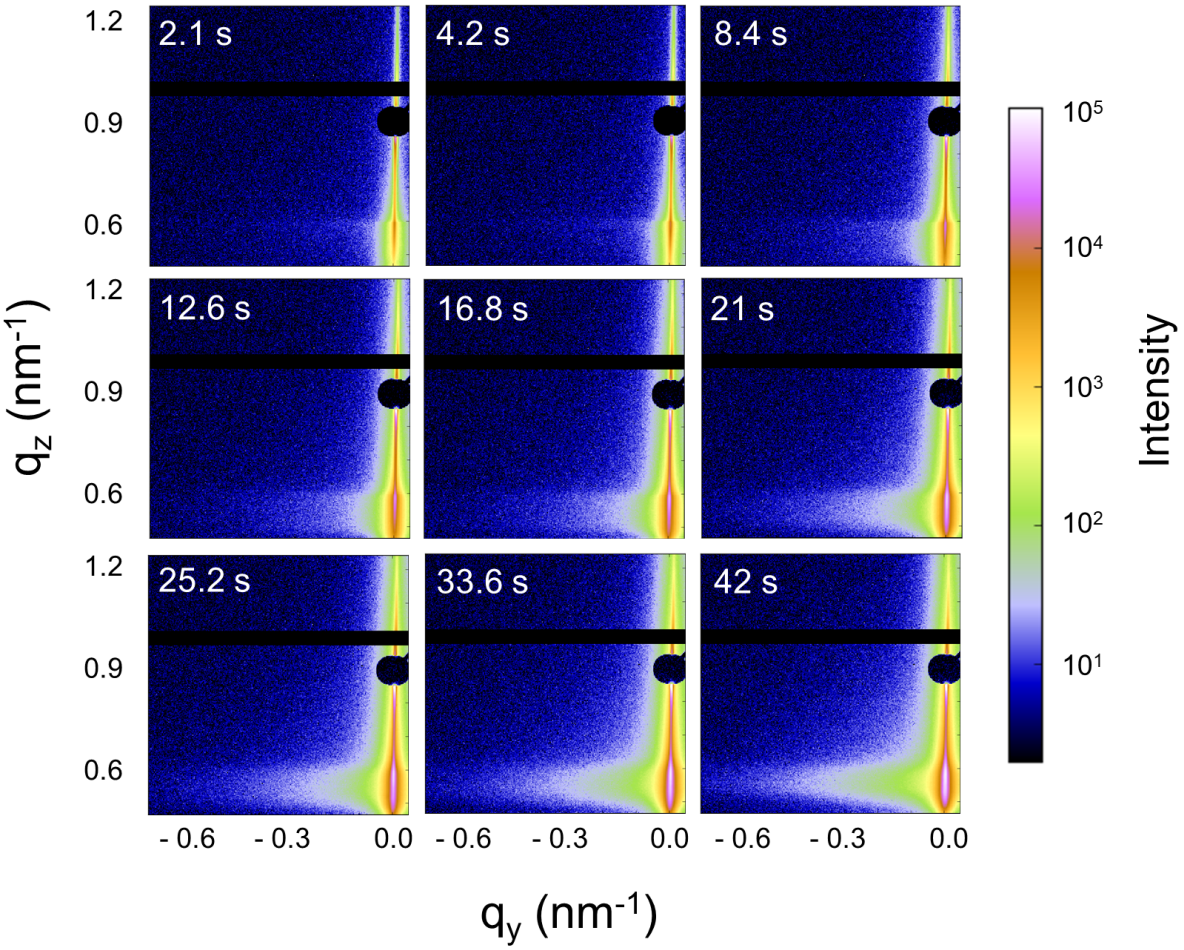

Figure 8.5: *Selected 2D GISAXS data of the ferromagnetic hybrid film measured during in situ spray deposition at different times as indicated (top left corner). (Reprinted with permission from [146]. Copyright 2020 American Chemical Society.)*

Figure 8.6a shows selected horizontal line cuts (black dots) and corresponding fits (red lines) from the 2D GISAXS data of ferromagnetic hybrid film (Figure 8.5). Due to the presence of the magnetic nanoplatelets, an additional cylindrical geometry is required in the model to fit the horizontal line cuts of the hybrid film. It is noticeable that three main features (denoted with structures I, II, and III) are observed in the GISAXS data (Figure 8.6a). Moreover, from the 2D mapping of the scattering data versus spray time as extracted from all horizontal line cuts (Figure 8.7), one can also observe the additional structure from magnetic nanoplatelets at high q_y values in the hybrid film compared to the pure film.

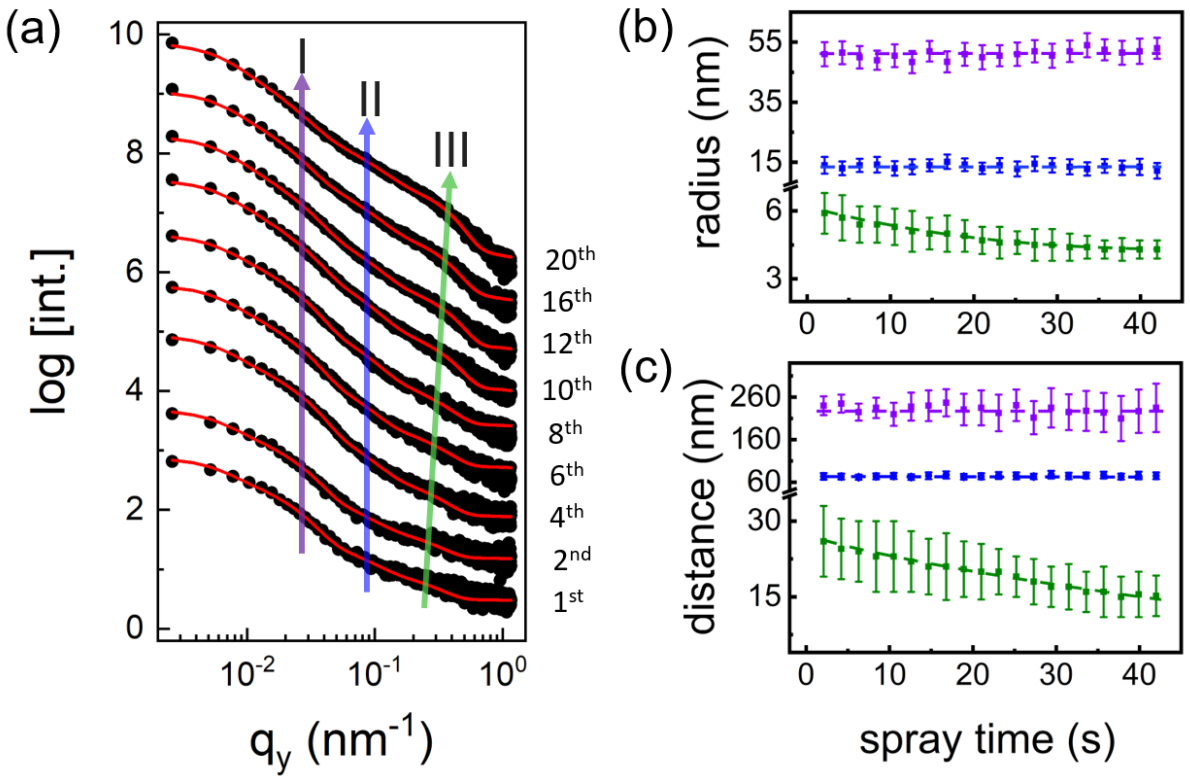

Figure 8.6: *(a) Selected horizontal line cuts (black dots) from the 2D GISAXS data of ferromagnetic hybrid film with increasing spray cycle number (1st, 2nd, 4th, 6th, 8th, 10th, 12th, 16th, and 20th from bottom to top, corresponding to the spray time of 2.1 s, 4.2 s, 8.4 s, 12.6 s, 16.8 s, 21 s, 25.2 s, 33.6 s, and 42 s). The red lines show the fits. Curves are shifted along the intensity axis for clarity of the presentation. Structure I (purple arrow), II (blue arrow) and III (green arrow) are structure factors of PMMA elongated structure, PMMA cylinders and magnetic nanoplatelets, respectively. (b) Radius and (c) distance of the PMMA elongated structure, PMMA cylinders and magnetic nanoplatelets extracted from the fits. The dashed lines in (b) and (c) serve as a guide to the eye. (Reprinted with permission from [146]. Copyright 2020 American Chemical Society.)*

Similar to the pure DBC reference film, structure I (structure factor of PMMA elongated structure) and structure II (structure factor of PMMA cylinders) remain constant with increasing spray cycle number. However, as compared to the reference film, structure I and structure II shift to lower q_y values (corresponding to 0.028 nm^{-1} and 0.087 nm^{-1}) due to the incorporation of magnetic nanoplatelets, caused by the expansion of the center-to-center distances of PMMA elongated structure and PMMA cylinders. The corresponding average center-to-center distances of the PMMA elongated structure and PMMA cylinders are around 229 ± 38 nm (Figure 8.6c) and 73 ± 7 nm (Figure 8.6c), respectively. In

contrast, their domain radii are the same as for the reference film. These findings confirm the observation in the SEM that the nanoplatelets are trapped inside the PS phase.

The width of the PS phase (w_{PS}) between two neighboring PMMA domains in the pure reference film is around 32 nm, as calculated via

$$w_{PS} = d_{II} - 2R_{II} \tag{8.1}$$

where d_{II} is the center-to-center distance of neighboring PMMA cylinders and R_{II} is the PMMA cylinder radius.

The available spacing of 32 nm is smaller than the average diameter of the large facet of the nanoplatelets (39 nm). However, the nanoplatelets are not standard discs as shown in Figure 4.4. The large facet of the nanoplatelet can be treated as a rectangle with an average width of around 28 nm, which provides possibilities to arrange them inside the PS matrix.

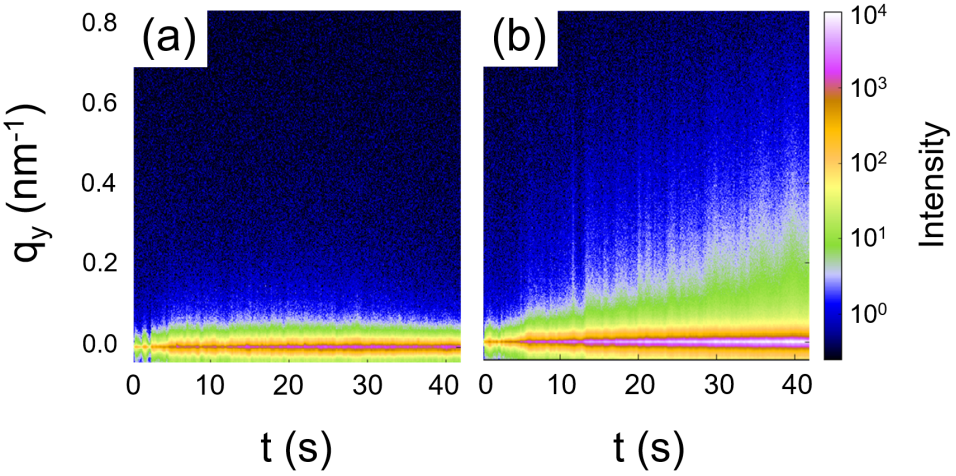

Figure 8.7: *Mapping extracted from horizontal line cuts from respective 2D GISAXS data of (a) pure polymer reference film and (b) hybrid ferromagnetic film. (Reprinted with permission from [146]. Copyright 2020 American Chemical Society.)*

At higher q_y values, an additional scattering feature (green arrow) is seen in Figure 8.6a. This feature originates from the structure factor of the magnetic nanoplatelets. As the spraying proceeds, the structure III shifts to higher q_y values and becomes more prominent. The corresponding average radius and center-to-center distance of the magnetic nanoplatelets, extracted from structure III, decrease from around 5.9 nm to 4.3 nm (Figure 8.6b) and from around 26 nm to 15 nm (Figure 8.6c), respectively. Obviously, the average diameter of the nanoplatelets extracted from GISAXS (from 11.8 nm to 8.6 nm)

is larger than the average thickness of the nanoplatelets obtained by TEM analysis (5.5 nm). This deviation indicates that the nanoplatelet large facet is oriented not normal to the substrate surface. Instead, they are tilted at an angle (α_β) of more than 45^o close to the substrate surface [221], as calculated and shown in Figure 8.8. α_β represents the angle between the nanoplatelet large facet and the substrate surface normal.

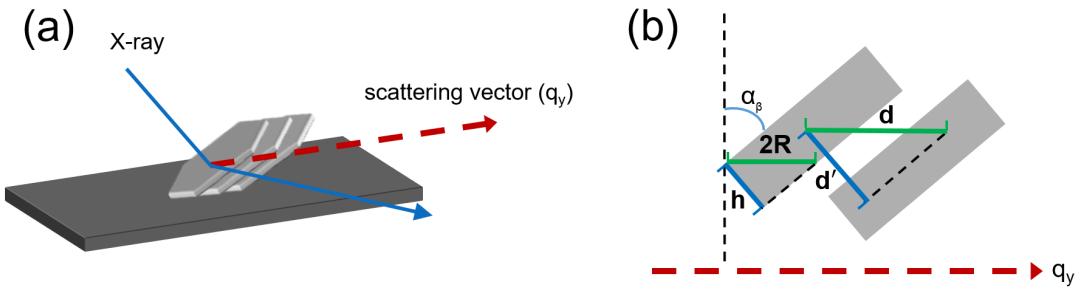

Figure 8.8: *(a) Simplified schematic representation of GISAXS measurements on tilted magnetic nanoplatelets. (b) A zoomed-in cross sectional schematic of the tilted nanoplatelets. (Reprinted with permission from [146]. Copyright 2020 American Chemical Society.)*

Such tilted nanoplatelets can be explained by the interactions between substrate, nanoplatelets and PMMA block [222–224]. Entropic force causes accumulation of the nanoplatelets at the substrate surface and the orientation of the nanoplatelets is limited by the arrangement of the PMMA block near the substrate surface. The PMMA block prefers to segregate to the substrate surface while the domain is limited in height due to a fast-dry process causing a limitation of the polymer chain stretching. As a result, the nanoplatelets have to adopt a lying-down way (with their large facets parallel to the substrate surface) on the substrate surface (marked with blue boxes in Figure 8.9) to realize the arrangement of the restricted PMMA blocks, due to the existence of hydrogen bonds between the PAA ligands of the nanoplatelets and the ester groups of PMMA. Moreover, magnetic dipole-dipole interactions cause most nanoplatelets in PS or subsequently deposited nanoplatelets to spontaneously rotate their orientation close to the orientation of the nanoplatelets that stay on the substrate surface during spraying, because every nanoplatelet can be seen as a permanent magnet with a spontaneous magnetization direction perpendicular to the large facet [209]. However, due to the binding effect of the polymer chains and the distance effect of the dipole-dipole interactions, the rotation of the subsequently deposited nanoplatelets is limited. This causes a decrease in the tilt angle of the nanoplatelets over spray time, leading to the observed decrease in the radius and distance extracted from the GISAXS fits. Here, it is undeniable that some nanoplatelets can also adopt a lying-down way inside the film as shown in the SEM images (Figure 8.1b, 8.1d and 8.2). However,

they are too sparsely dispersed inside the film to have sufficient scattering contribution to become visible in the GISAXS signal.

In Figure 8.8, α_β is the angle between the nanoplatelet large facet and substrate surface normal, h and d' are the thickness (height) of the nanoplatelets and center-to-center distance of neighboring nanoplatelets in thickness (height) direction, respectively. $2R$ and d are the values extracted from GISAXS, corresponding to the diameter of the nanoplatelets and center-to-center distance of neighboring nanoplatelets in lateral direction. The angle α_β can be calculated via

$$\alpha_\beta = \arccos \frac{h}{2R} = \arccos \frac{d'}{d} \tag{8.2}$$

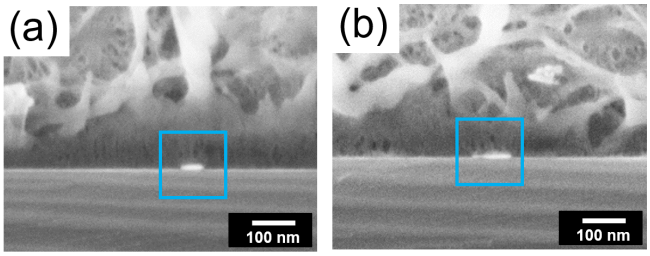

Figure 8.9: *Cross-sectional SEM images of spray deposited final ferromagnetic hybrid film containing 3 wt % magnetic nanoplatelets before SVA. Bright spots (marked with blue boxes) represent the lying-down magnetic nanoplatelets, which stay on the substrate surface. In the thin film, the porous structure might be caused by the solvent evaporation during sample preparation and subsequently breaking the sample for the cross-section study. (Reprinted with permission from [146]. Copyright 2020 American Chemical Society.)*

8.4 Surface morphology after solvent vapor annealing

To study the influence of SVA, the obtained final dried films are annealed inside a closed chamber with THF vapor at room temperature for 20 h. SEM is used to examine the surface morphology of both films (pure and hybrid) after SVA. Compared to the films before SVA, both films developed the relatively ordered larger nanostructures after SVA as shown in Figure 8.10. During annealing, the mobility of both polymer blocks, PS and PMMA, is enhanced, leading the average diameter of PMMA domains increases to around 85 ± 8 nm (Figure 8.10a). The increased size of the PMMA domains and a long time of SVA process (20 h) allow the magnetic nanoplatelets to migrate to the PMMA domains

(Figure 8.10b) via the hydrogen bonding between the ester groups of PMMA and the PAA ligands of magnetic nanoplatelets.

To better present the DBC morphology and position of the nanoplatelets, enlarged views of the SEM data of the pure and hybrid films are shown in Figure 8.10c and 8.10d, respectively. Additionally, a growing number of lying-down PMMA cylinders (PMMA elongated structure) is observed for the hybrid film (Figure 8.10b) compared to the pure reference film (Figure 8.10a). This can be attributed to the fact that the nanoplatelets prefer to aggregate at the substrate surface and attract more PMMA chains to the substrate side, resulting in more flipping of the PMMA cylinders from perpendicular to lying-down orientation [222].

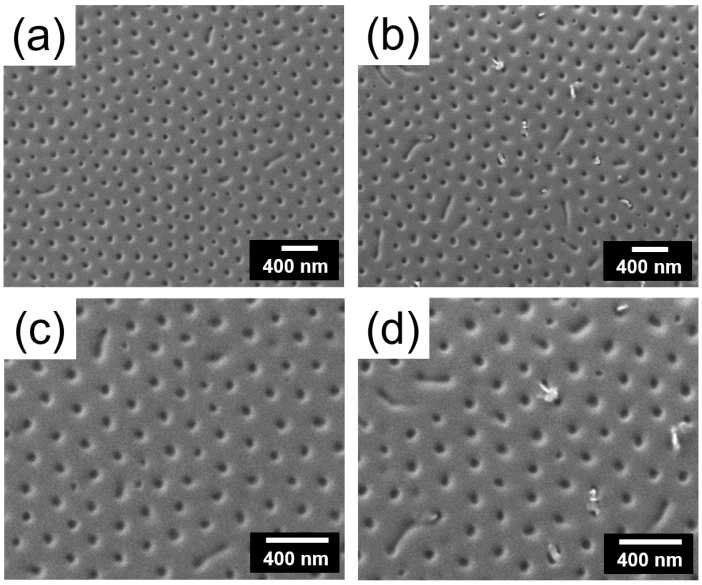

Figure 8.10: *SEM images of the spray deposited final films after SVA of (a, c) pure DBC reference film and (b, d) ferromagnetic hybrid film containing 3 wt % of magnetic nanoplatelets at (a, b) low and (c, d) high magnifications. (Reprinted with permission from [146]. Copyright 2020 American Chemical Society.)*

To probe inner morphologies of the solvent annealed final spray deposited films (pure and hybrid), static GISAXS measurements are applied. Figure 8.11a and 8.11b show the 2D GISAXS data of pure and hybrid films, respectively. A prominent Bragg scattering rod (marked with a red arrow in Figure 8.11a and 8.11b) is observed in both pure reference and hybrid films, indicating the formation of ordered nanostructures. Compared to the pure film (Figure 8.11a), the hybrid film (Figure 8.11b) exhibits a higher intensity along the q_y direction due to the presence of magnetic nanoplatelets enhancing the contrast. For quantitative analysis, horizontal line cuts and modeling are carried out as already explained before (in situ GISAXS). Figure 8.11c shows the horizontal line cuts (black

dots) and the corresponding fits (red lines). For the pure film, a strong main peak (q_y = 0.033 nm^{-1}) and a weak second-order peak (q_y = 0.059 nm^{-1}, marked with a dashed blue arrow) are seen, which originate from the structure of the PMMA cylinders. The presence of the second-order peak indicates that a well-ordered structure is obtained in the pure film.

With nanoplatelets loading (3 wt %), the peak (structure of PMMA cylinders) shifts slightly to a lower q_y value (q_y = 0.031 nm^{-1}) due to the incorporation of magnetic nanoplatelets, resulting in the expansions of the PMMA domain size and inter-PMMA distance. Moreover, the peak becomes less prominent and the second-order peak disappears. The well-ordered structure in the pure film is perturbed with growing PMMA domain sizes to accommodate the nanoplatelets and further perturbed by the appearance of more lying-down PMMA cylinders (shown in Figure 8.10d) in the hybrid film [10].

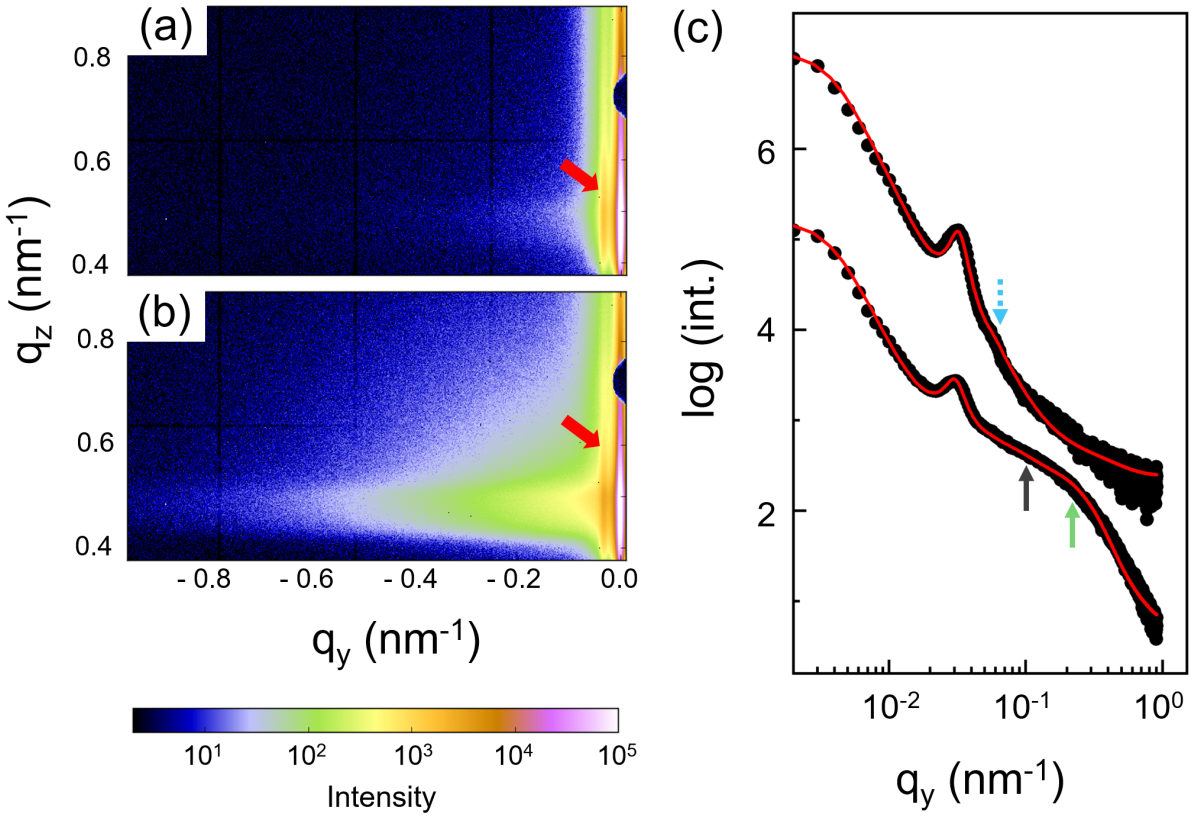

Figure 8.11: *2D GISAXS data of (a) pure film and (b) hybrid film after SVA of 20 h. (c) Corresponding horizontal line cuts of the 2D GISAXS data (black dots) and fits (red lines) of pure film (top) and hybrid film (bottom), respectively. (Reprinted with permission from [146]. Copyright 2020 American Chemical Society.)*

To model the horizontal line cut of the hybrid film, two additional cylindrical geometries with different sizes are required. As shown in Figure 8.11c, a broad and weak peak at q_y

around 0.1 nm^{-1} (marked with a black solid arrow) is observed, which is the structure of the nanoplatelet aggregates. Similar to the in situ GISAXS analysis, at a higher q_y value, a scattering feature from single nanoplatelets is also seen (marked with a green solid arrow). However, it shifts to a lower q_y value compared to the sample without SVA, because THF is a good solvent for the PAA chains, which are coated on the surface of nanoplatelets [225]. During SVA, the PAA chains stretch and cause a larger center-to-center distance between neighboring nanoplatelets. Moreover, the extracted average radius of the single nanoplatelet from GISAXS is around 3.8 ± 0.5 nm (Figure 8.12). If the calculation of the tilt angle of the nanoplatelet is applied, a tilt angle slightly less than 45^o can be obtained. However, considering the existence of lying-down nanoplatelets as shown in the SEM image (Figure 8.10d), the nanoplatelets are expected to be randomly located in the PMMA domains after SVA. Because the increased size of the PMMA domains after SVA allows the nanoplatelets to be arranged in any orientation, including those on the substrate surface.

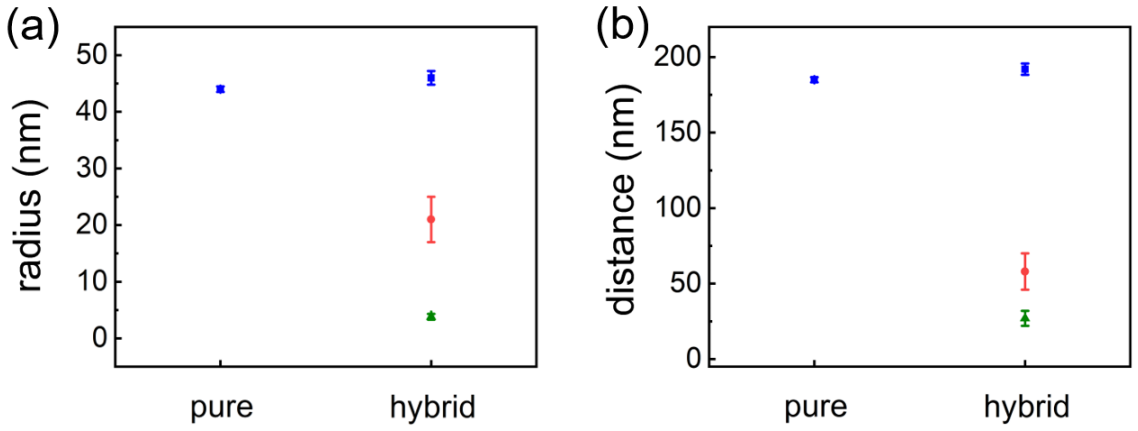

Figure 8.12: *(a) Radius and (b) distance of PMMA cylinders (blue squares), magnetic nanoplatelet aggregates (red circles) and magnetic nanoplatelets (green triangles) extracted from the fits (Figure 8.11c) of pure and hybrid films after SVA of 20 h. (Reprinted with permission from [146]. Copyright 2020 American Chemical Society.)*

8.5 Morphology evolution

To sketch the orientation of magnetic nanoplatelets during spraying and SVA processes, a simplified schematic is shown in Figure 8.13. With increasing spray time, the orientation of the nanoplatelets changes by a decrease in the average tilt angle (α_β). As described earlier, the nanoplatelets prefer to aggregate to the substrate and finally adopt a lying-down way on the substrate surface because of the interactions between substrate, nanoplatelets and

PMMA block. This drives the nanoplatelets so that they do not lie randomly inside the PS matrix but are tilted and lie close to the substrate surface at the initial spraying stage.

As spraying proceeds, such driving force becomes weaker and magnetic dipole-dipole interactions dominate. However, due to the binding effect of the polymer chains and distance effect of the dipole-dipole interactions, the rotation of the subsequently deposited nanoplatelets is limited, resulting in a decrease in the average α_β over spray time. With applying SVA, the mobility of polymer blocks is enhanced, causing a significant increase in the size of PMMA cylinders. Moreover, the hydrogen bonding between the PMMA and nanoplatelets allows the nanoplatelets to aggregate and lie randomly inside the PMMA domains after a long SVA time of 20 h.

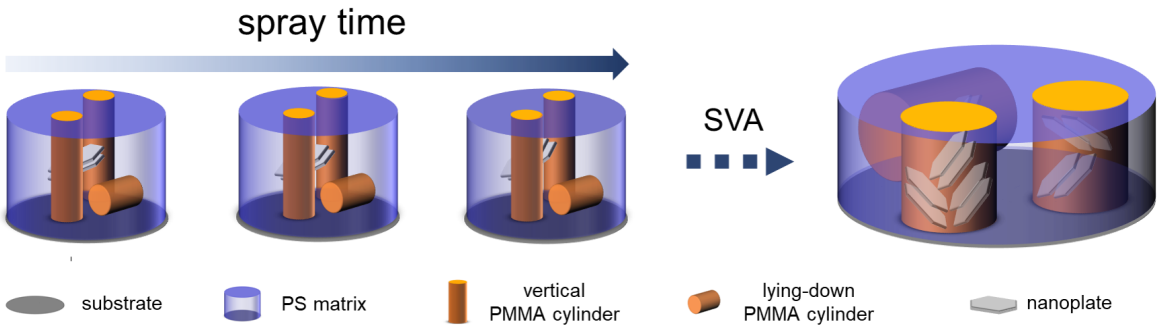

Figure 8.13: *Schematic representation of the orientation of magnetic nanoplatelets during spraying and SVA. For clarity, only the average state is shown. (Reprinted with permission from [146]. Copyright 2020 American Chemical Society.)*

8.6 Magnetic properties

8.6.1 Influence of temperature

To study the influence of temperature on the magnetic properties of the hybrid film, before SVA a final spray deposited hybrid film is measured at various temperatures as shown in Figure 8.14. The measurements are performed with the film surface parallel to the applied external magnetic field (from -15000 to 15000 Oe).

In Figure 8.14a, noticeable magnetic hysteresis loops with large loops are observed for all temperatures, indicating a strong ferromagnetic behavior of the hybrid film. With an increase in temperature, the hysteresis loop becomes narrower. The corresponding saturation magnetization (M_s), remanence (M_r) and coercivity (H_c) decrease from around 2.17 to 1.36 emu cm^{-3}, from around 1.05 to 0.67 emu cm^{-3} and from around 3609 to

3350 Oe, respectively. Such observation in M_s, M_r and H_c can be explained by thermal fluctuations [196]. The magnetic moments exhibit faster fluctuations with increasing temperature, which leads to higher random anisotropy in the magnetic domains, resulting in lower M_s, M_r and H_c at a higher temperature. Additionally, a slight S-shaped curve is observed in the hysteresis loops at low magnetic fields. This may be caused by residual superparamagnetic γ-Fe_2O_3, as described in our previous publication [119].

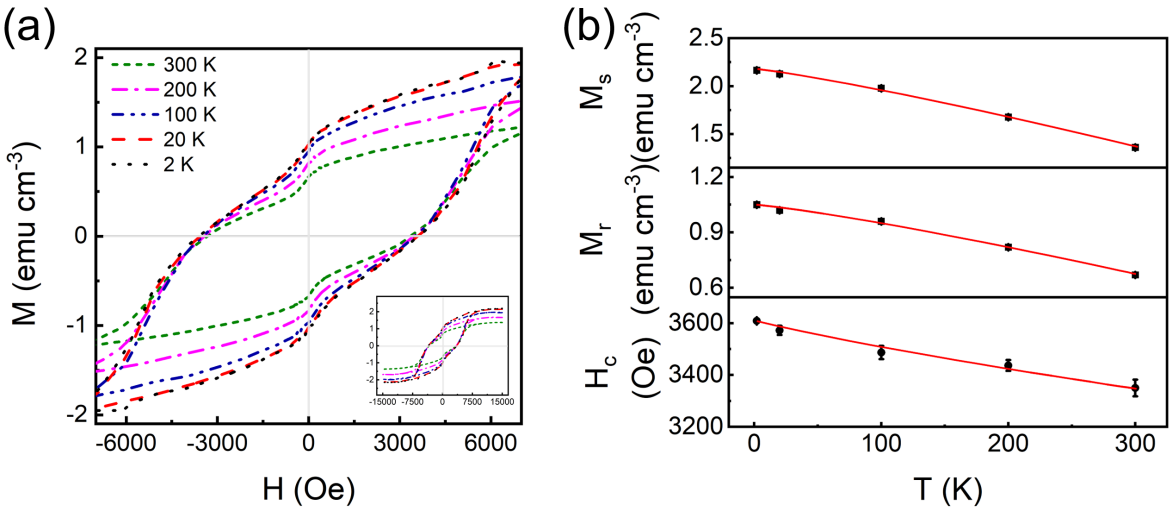

Figure 8.14: *Magnetic properties of the spray deposited final hybrid film before SVA. (a) Magnetic hysteresis loops collected at various temperatures (2, 20, 100, 200, and 300 K) as a function of the magnetic field (from -7000 to 7000 Oe). The inset shows the hysteresis loops with a full field range from -15000 to 15000 Oe. (b) Saturation magnetization (M_s), remanence (M_r), and coercivity (H_c) versus temperature are obtained from the corresponding hysteresis loops. The red solid lines serve as a guide to the eyes. (Reprinted with permission from [146]. Copyright 2020 American Chemical Society.)*

8.6.2 Magnetic anisotropy

As seen in GISAXS and SEM, in the hybrid film before SVA the magnetic nanoplatelets are tilted with a large facet being close to the substrate surface. In contrast, the nanoplatelets are oriented randomly after SVA. Moreover, the nanoplatelets used have a high uniaxial magnetic anisotropy with the easy magnetization axis perpendicular to their large facets [119]. Thus, a magnetic hybrid film with an easy magnetization axis close to the film surface normal should be obtained for the hybrid film before SVA. The hybrid film should exhibit magnetic isotropy after SVA.

To verify this, the hybrid films are measured in three orthogonal orientations (two in the film plane and one out of the film plane) by changing the direction of the applied external magnetic field (B), as shown in Figure 8.15. Two in-film orientations are marked with B_1 and B_2 (film surface parallel to the applied external magnetic field) and the out-of-film orientation is marked with B_3 (film surface perpendicular to the applied external magnetic field). The measurements are performed in the above mentioned three orthogonal orientations with an applied external magnetic field ranging from -15000 to 15000 Oe at 300 K via a SQUID magnetometry.

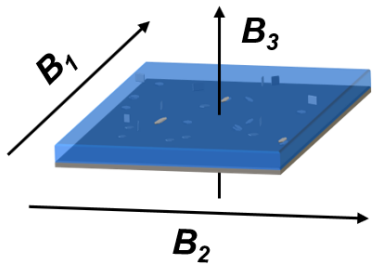

Figure 8.15: *Schematic to present the sample's magnetic properties measured with the magnetic field applied in three orthogonal orientations (two in the film plane marked with B_1 and B_2, and one out of the film plane marked with B_3). (Reprinted with permission from [146]. Copyright 2020 American Chemical Society.)*

Figure 8.16 shows the magnetic data of the obtained final hybrid film before SVA. For the sample measured in the film plane (B_1 and B_2), no magnetic anisotropy is seen, indicating that the orientation of the nanoplatelets in the film plane is random. However, an apparent change in the hysteresis loops is observed when changing the direction of the applied external magnetic field to out of the film plane (B_3). M_s, H_c, and χ are higher in the out-of-film orientation (B_3) versus in-film (B_1 and B_2) orientations (Figure 8.16b) due to the anisotropic behavior of the magnetic hybrid film [10]. As discussed above, the easy axis of the hybrid film is perpendicular to the film surface, i.e. out of the film plane. Therefore, higher M_s, H_c, and χ are obtained in the perpendicular direction (B_3) compared to the parallel direction (B_1 and B_2).

Figure 8.17a shows the magnetic hysteresis loops of the spray deposited final hybrid film after SVA at 300 K in three orthogonal orientations. Compared to the hybrid film without SVA, the annealed film exhibits weaker magnetic anisotropy due to the rearrangement of magnetic nanoplatelets during SVA. As seen in SEM and GISAXS, SVA helps to enhance the mobility of the polymer chains, leading to the average PMMA domain diameter increased to above 80 nm, which is sufficient for the incorporation of magnetic nanoplatelets with any orientation. Moreover, the annealing time of 20 h ensures that

the nanoplatelets have enough time to move in the hybrid film. In general, magnetic anisotropy is not supposed to be observed if the orientation of the magnetic nanoplatelets is random. However, in our case, the annealed film exhibits a weak magnetic anisotropy. Because the nanoplatelets are located inside the PMMA cylinders with a random orientation and most of the PMMA cylinders are vertically aligned on the substrate, resulting in an easy magnetization axis is aligned in the perpendicular (B_3) versus parallel directions (B_1 and B_2) [10]. Slightly higher M_s, H_c, and χ are obtained in the perpendicular direction (B_3) as shown in Figure 8.17b.

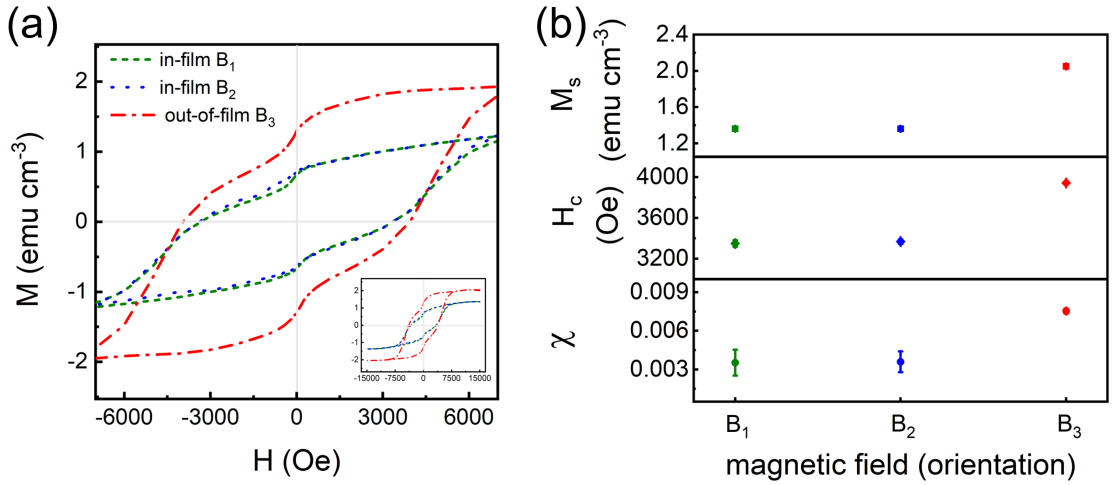

Figure 8.16: *(a) Magnetic hysteresis loops of the spray deposited final hybrid film before SVA are plotted at a temperature of 300 K in three orthogonal orientations of the magnetic field (from -7000 to 7000 Oe). The in-film orientations are marked with B_1 and B_2 and the out-of-film orientation is marked with B_3. The inset shows the hysteresis loops with a full field range from -15000 to 15000 Oe. (b) Saturation magnetization (M_s), coercivity (H_c), and magnetic susceptibility (χ) versus orientation. (Reprinted with permission from [146]. Copyright 2020 American Chemical Society.)*

From the observed magnetic behaviors of the hybrid films before and after SVA, a solvent-controlled magnetic property of the hybrid film has been proven. The hybrid film shows obvious perpendicular magnetic anisotropy before SVA while it exhibits extremely weak perpendicular magnetic anisotropy after SVA. Such solvent-controlled magnetic behavior will play an important role in the practical fabrication of magnetic solvent sensors.

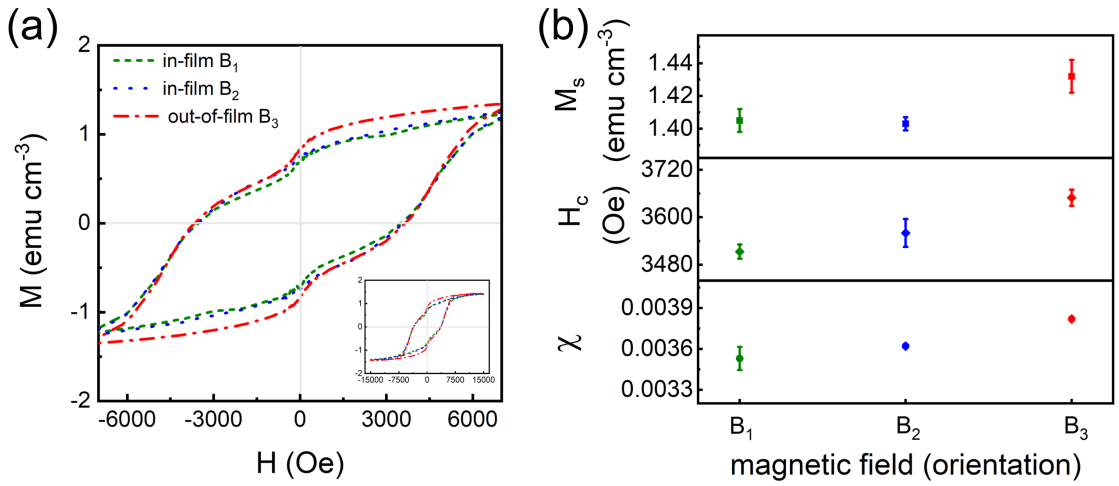

Figure 8.17: *(a) Magnetic hysteresis loops of the spray deposited final hybrid film after SVA are plotted at a temperature of 300 K as a function of magnetic field (from -7000 to 7000 Oe) in three orthogonal orientations. The in-film orientations are marked with B_1 and B_2 and the out-of-film orientation is marked with B_3. The inset shows the hysteresis loops with a full field range from -15000 to 15000 Oe. (b) Saturation magnetization (M_s), coercivity (H_c), and magnetic susceptibility (χ) obtained from the corresponding hysteresis loops. B_1 (green dots), B_2 (blue dots), and B_3 (red dots) orientations are compared. (Reprinted with permission from [146]. Copyright 2020 American Chemical Society.)*

8.7 Summary

In this chapter, anisotropic ferromagnetic hybrid polymer films of UHMW PS-b-PMMA and strontium hexaferrite magnetic nanoplatelets are prepared by spray deposition.

The morphology evolution of the hybrid film is monitored via GISAXS measurements in situ during spray deposition. A pure DBC film without nanoplatelets is also deposited under the same conditions as a reference. For both films, with and without nanoplatelets, the PMMA cylindrical structure remains stable during spray deposition, while the PMMA elongated structure becomes weaker over time. However, the hybrid film shows larger inter-domain distances and unchanged domain sizes compared to the pure film due to the hosting of nanoplatelets, which are trapped inside the PS matrix. Moreover, in the hybrid film, the scattering data suggest that the magnetic nanoplatelets are tilted with the large facet close to the substrate surface. A decrease in the average tilt angle between the nanoplatelet large facet and substrate surface normal is observed with increasing spray time. This is the result of the dipole-dipole interactions between magnetic nanoplatelets and the interaction among the substrate, PMMA block and magnetic nanoplatelets. After SVA, both films develope a relatively ordered and larger PMMA nanostructure, which

allows the magnetic nanoplatelets to migrate to the PMMA domains inside the hybrid film. This change in the film morphology is mainly driven by the hydrogen bonds between the ester groups of PMMA and the PAA ligands of magnetic nanoplatelets and a sufficient SVA time (20 h).

SQUID data show that both hybrid films, before and after SVA, are ferromagnetic and have a high coercivity above 3000 Oe at room temperature, which is beneficial for potential applications in the field of magnetic data storage. Moreover, the hybrid film shows perpendicular magnetic anisotropy before SVA while exhibits extremely weak perpendicular magnetic anisotropy after SVA, which endows it as a good candidate for magnetic sensors.

9 Conclusion and outlook

In the present thesis, the main aim is to optimize the morphology of pure UHMW DBCs and hybrid magnetic NP-DBC systems and to investigate the magnetic properties of the obtained hybrid magnetic NP-DBC systems. The investigation is focused on three main topics: the fabrication of UHMW DBC PS-*b*-PMMA templates with large domain sizes, the kinetic process of film formation during printing and spray deposition of magnetic NP-DBC films and the fabrication of ferromagnetic NP-DBC films. To obtain a desired DBC template, the structure evolution of the fabricated UHMW DBC PS-*b*-PMMA thin films is systematically investigated as a function of increasing film thickness and SVA time. For different investigated magnetic hybrid topics, different magnetic NPs are selected. Small fcc-FePt NPs and large Fe_3O_4 NPs are utilized for the hybrid systems showing superparamagnetism and ferromagnetism, respectively. To enhance the ability of the ferromagnetic hybrid films to withstand an external magnetic field without becoming demagnetized and to obtain a hybrid film with magnetic anisotropy, $SrFe_{12}O_{19}$ nanoplatelets are selected.

In a first study, an asymmetric linear UHMW PS-*b*-PMMA DBC is used for the fabrication of an ordered DBC template with a large domain size. The structural evolution of the fabricated UHMW DBC template is systematically investigated as function of increasing film thickness and SVA time using AFM and GISAXS measurements. GISAXS data suggest that the morphology changes from disorder to relativity ordered PMMA domains in a PS matrix as the film thickness increases ($\leq 0.5\ L_0$). With increasing SVA time, a rapid morphology evolution of locally hexagonal packed PMMA domains (from poorly ordered to locally ordered and then back to poorly ordered nanostructures) is observed. Thus, suitable film thickness and SVA time are crucial for the formation of ordered nanostructures also in the case of the UHMW DBCs. By controlling the film thickness and the SVA time, ordered DBC templates with domain sizes above 80 nm can be obtained. The obtained DBC-based large domain sized nanomaterials are attractive for use as templates.

Based on the study of pure UHMW PS-*b*-PMMA DBC thin films and to scale up the fabrication, a superparamagnetic NP-DBC film containing UHMW DBC PS-*b*-PMMA and small fcc-FePt NPs is fabricated by the slot-die printing technique. The kinetic process of the film formation during printing of the superparamagnetic NP-DBC film is investigated

via in situ GISAXS measurements. As a reference, a pure DBC PS-*b*-PMMA film is also printed. The scattering data suggest that the hybrid film exhibits a faster shrinkage of the PMMA domains and a faster formation of a relatively stable state compared to the pure film. This difference is due to the addition of FePt NPs which accelerates the solvent evaporation. A metastable state is installed as the scattering data changes slightly with increasing time. Due to the presence of the FePt NPs which inhibit the reorganization of the polymer chains, a longer metastable state is observed during the printing process of the hybrid film compared to the pure film. SQUID data reveal that the printed hybrid film is superparamagnetic and therefore is good candidate for potential applications in magnetic switches and sensors having a large scale.

To enable magnetic data storage application, magnetic films containing ferromagnetic NPs are required. Here, large Fe_3O_4 NPs with a diameter of around 27 nm, above the critical value of 20 nm, are utilized. Compared to FePt NPs, Fe_3O_4 NPs can be more easily synthesized and are nowadays commercially available. The localization of the large Fe_3O_4 NPs inside the UHMW DBC PS-*b*-PMMA and the corresponding magnetic preoperties are investigated as a function of NP concentration. Through AFM and SEM measurements, a change in the position of the NPs inside the UHMW DBC thin films depending on the NP concentration is observed. At low concentrations, the NPs are located at the interfaces between the PS and PMMA domains, and at high concentrations, the NPs are positioned preferentially inside the PMMA domains. GISAXS data suggests that low amount of Fe_3O_4 NPs helps to enhance the order of the UHMW DBC structure, and a well-ordered DBC morphology is observed at a Fe_3O_4 NP concentration of 0.5 wt %. SQUID data show that all hybrid films are ferromagnetic at room temperature and a weak magnetic anisotropy in the film plane is observed for the hybrid film containing chain-like NP aggregates at a NP concentration of 10 wt %.

In order to fabricate perpendicular magnetically anisotropic films and to enhance the ability of the magnetic hybrid films to withstand an external magnetic field without becoming demagnetized, large Fe_3O_4 NPs are replaced by $SrFe_{12}O_{19}$ nanoplatelets in the hybrid magnetic NP-DBC system. Because $SrFe_{12}O_{19}$ nanoplatelets are hard magnetic materials with high magnetic anisotropy and high coercivity, they are a optimal choice. By applying in situ GISAXS measurements, the orientation of $SrFe_{12}O_{19}$ nanoplatelets during spray deposition can be monitored. The scattering data suggest that the magnetic nanoplatelets are tilted with the large facet close to the substrate surface and a decrease in the average tilt angle between the nanoplatelet large facet and substrate surface normal is observed with increasing spray time. The final obtained hybrid film is then solvent-vapor-annealed inside a closed chamber with THF to study the influence of SVA on the film's properties. Obvious changes in the DBC morphology and nanoplatelet local-

ization are observed after SVA treatment. SQUID data show that ferromagnetic hybrid polymer films with high coercivity (above 3000 Oe) are obtained by using the $SrFe_{12}O_{19}$ nanoplatelets. The hybrid film exhibits a perpendicular magnetic anisotropy before SVA, which is strongly weakened after SVA. Such hybrid films appear highly promising for potential applications in magnetic data storage and sensors.

Based on the results obtained in this thesis, several topics are of interest for future research. First, as stated before, coercivity is the ability of magnetic films to withstand an external magnetic field without becoming demagnetized. It is of great significance to fabricate magnetic films based on NPs with ultrahigh coercivity, such as fct-FePt NPs. The coercivity of the fct-FePt NPs can reach 33 KOe. However, the conditions for fct-FePt NPs synthesis are intensive and complicated because a protective layer of robust oxide is required to avoid aggregation of the FePt NPs during the thermal annealing step. Since UHMW DBCs are effective templates to disperse NPs, it would be attractive to study and use such templates for the fabrication of fct-FePt NP films. Moreover, fct-FePt NPs can "duplicate" the structure of UHMW DBC, thereby achieving structural diversity. Secondly, the kinetic study of printed superparamagnetic NP-DBC system shows that the presence of magnetic NPs can accelerate the solvent evaporation, resulting in a faster formation of a relatively stable state in a hybrid film compared to the pure film. Thus, it would be interesting to study the influence of NP concentration on solvent evaporation and the structure evolution via in situ measurements such as GISAXS. Finally, considering the fact that the external magnetic field has a great influence on the morphology of magnetic NP-DBC films, it is also compelling to study the film formation kinetics of NP-DBC film in the presence of external magnetic fields of varying strengths.

Bibliography

[1] M. Melzer, J. I. Mönch, D. Makarov, Y. Zabila, G. S. Cañón Bermúdez, D. Karnaushenko, S. Baunack, F. Bahr, C. Yan, M. Kaltenbrunner, and O. G. Schmidt, "Wearable magnetic field sensors for flexible electronics," *Advanced Materials*, vol. 27, no. 7, pp. 1274–1280, 2015.

[2] H. Wu, M. Khdour, P. Apsangi, and H. Yu, "High-frequency magnetic thin-film inductor integrated on flexible organic substrates," *IEEE Transactions on Magnetics*, vol. 53, no. 11, pp. 1–7, 2017.

[3] M. Suda and Y. Einaga, "Sequential assembly of phototunable ferromagnetic ultrathin films with perpendicular magnetic anisotropy," *Angewandte Chemie International Edition*, vol. 121, no. 10, pp. 1786–1789, 2009.

[4] Q. Dai, D. Berman, K. Virwani, J. Frommer, P.-O. Jubert, M. Lam, T. Topuria, W. Imaino, and A. Nelson, "Self-assembled ferrimagnet-polymer composites for magnetic recording media," *Nano letters*, vol. 10, no. 8, pp. 3216–3221, 2010.

[5] A. Tokarev, J. Yatvin, O. Trotsenko, J. Locklin, and S. Minko, "Nanostructured soft matter with magnetic nanoparticles," *Advanced Functional Materials*, vol. 26, no. 22, pp. 3761–3782, 2016.

[6] G. Reiss and A. Hütten, "Applications beyond data storage," *Nature materials*, vol. 4, no. 10, pp. 725–726, 2005.

[7] Y. Zang, F. Zhang, D. Huang, C. Di, and D. Zhu, "Sensitive flexible magnetic sensors using organic transistors with magnetic-functionalized suspended gate electrodes," *Advanced Materials*, vol. 27, no. 48, pp. 7979–7985, 2015.

[8] X. Jiang, J. Feng, L. Huang, Y. Wu, B. Su, W. Yang, L. Mai, and L. Jiang, "Bioinspired 1d superparamagnetic magnetite arrays with magnetic field perception," *Advanced Materials*, vol. 28, no. 32, pp. 6952–6958, 2016.

[9] D. Toulemon, M. V. Rastei, D. Schmool, J. S. Garitaonandia, L. Lezama, X. Cattoën, S. Bégin-Colin, and B. P. Pichon, "Enhanced collective magnetic properties induced by the controlled assembly of iron oxide nanoparticles in chains," *Advanced Functional Materials*, vol. 26, no. 15, pp. 2454–2462, 2016.

[10] S. Xia, L. Song, V. Körstgens, M. Opel, M. Schwartzkopf, S. V. Roth, and P. Müller-Buschbaum, "Magnetic nanoparticle-containing soft-hard diblock copolymer films with high order," *Nanoscale*, vol. 10, no. 25, pp. 11930–11941, 2018.

[11] I. Hamley, "Ordering in thin films of block copolymers: Fundamentals to potential applications," *Progress in polymer science*, vol. 34, no. 11, pp. 1161–1210, 2009.

[12] Y. Mai and A. Eisenberg, "Self-assembly of block copolymers," *Chemical Society Reviews*, vol. 41, no. 18, pp. 5969–5985, 2012.

[13] S. Xia, L. Song, N. Hohn, K. Wang, S. Grott, M. Opel, M. Schwartzkopf, S. V. Roth, and P. Müller-Buschbaum, "Spray-coating magnetic thin hybrid films of PS-*b*-PNIPAM and magnetite nanoparticles," *Advanced Functional Materials*, vol. 29, no. 15, p. 1808427, 2019.

[14] W. I. Park, Y. K. Jung, Y. Kim, W. H. Shin, Y. J. Choi, T. W. Park, J. H. Shin, Y. H. Jeong, J. H. Cho, H.-S. Shin, S.-H. Kwon, Y. S. Jung, and K. H. Kim, "Individual confinement of block copolymer microdomains in nanoscale crossbar templates," *Advanced Functional Materials*, vol. 29, no. 5, p. 1805795, 2019.

[15] L. Upadhyaya, M. Semsarilar, R. Fernández-Pacheco, G. Martinez, R. Mallada, I. M. Coelhoso, C. A. Portugal, J. G. Crespo, A. Deratani, and D. Quemener, "Nano-structured magneto-responsive membranes from block copolymers and iron oxide nanoparticles," *Polymer Chemistry*, vol. 8, no. 3, pp. 605–614, 2017.

[16] P. Posocco, Y. M. Hassan, I. Barandiaran, G. Kortaberria, S. Pricl, and M. Fermeglia, "Combined mesoscale/experimental study of selective placement of magnetic nanoparticles in diblock copolymer films via solvent vapor annealing," *The Journal of Physical Chemistry C*, vol. 120, no. 13, pp. 7403–7411, 2016.

[17] I. Barandiaran and G. Kortaberria, "Synthesis and characterization of nanostructured PS-*b*-P4VP/Fe_2O_3 thin films with magnetic properties prepared by solvent vapor annealing," *RSC advances*, vol. 5, no. 116, pp. 95840–95846, 2015.

[18] J. K. D. Mapas, T. Thomay, A. N. Cartwright, J. Ilavsky, and J. Rzayev, "Ultrahigh molecular weight linear block copolymers: Rapid access by reversible-deactivation radical polymerization and self-assembly into large domain nanostructures," *Macromolecules*, vol. 49, no. 10, pp. 3733–3738, 2016.

[19] P. Mokarian-Tabari, R. Senthamaraikannan, C. Glynn, T. W. Collins, C. Cummins, D. Nugent, C. Owyer, and M. A. Morris, "Large block copolymer self-assembly for fabrication of subwavelength nanostructures for applications in optics," *Nano letters*, vol. 17, no. 5, pp. 2973–2978, 2017.

[20] Y. S. Jung and C. A. Ross, "Solvent-vapor-induced tunability of self-assembled block copolymer patterns," *Advanced Materials*, vol. 21, no. 24, pp. 2540–2545, 2009.

[21] J. Peng, D. H. Kim, W. Knoll, Y. Xuan, B. Li, and Y. Han, "Morphologies in solvent-annealed thin films of symmetric diblock copolymer," *The Journal of chemical physics*, vol. 125, no. 6, p. 064702, 2006.

[22] Y. S. Jung and C. A. Ross, "Orientation-controlled self-assembled nanolithography using a polystyrene-polydimethylsiloxane block copolymer," *Nano Letters*, vol. 7, no. 7, pp. 2046–2050, 2007.

[23] R. Guo, H. Huang, Y. Chen, Y. Gong, B. Du, and T. He, "Effect of the nature of annealing solvent on the morphology of diblock copolymer blend thin films," *Macromolecules*, vol. 41, no. 3, pp. 890–900, 2008.

[24] W. I. Park, K. Kim, H.-I. Jang, J. W. Jeong, J. M. Kim, J. Choi, J. H. Park, and Y. S. Jung, "Directed self-assembly with sub-100 degrees celsius processing temperature, sub-10 nanometer resolution, and sub-1 minute assembly time," *Small*, vol. 8, no. 24, pp. 3762–3768, 2012.

[25] E. Grune, T. Johann, M. Appold, C. Wahlen, J. Blankenburg, D. Leibig, A. H. Muler, M. Gallei, and H. Frey, "One-step block copolymer synthesis versus sequential monomer addition: A fundamental study reveals that one methyl group makes a difference," *Macromolecules*, vol. 51, no. 9, pp. 3527–3537, 2018.

[26] M. Appold and M. Gallei, "Bio-inspired structural colors based on linear ultrahigh molecular weight block copolymers," *ACS Applied Polymer Materials*, vol. 1, no. 2, pp. 239–250, 2019.

[27] L. Leibler, "Theory of microphase separation in block copolymers," *Macromolecules*, vol. 13, no. 6, pp. 1602–1617, 1980.

[28] G. H. Fredrickson, "Surface ordering phenomena in block copolymer melts," *Macromolecules*, vol. 20, no. 10, pp. 2535–2542, 1987.

[29] A. Knoll, A. Horvat, K. Lyakhova, G. Krausch, G. Sevink, A. Zvelindovsky, and R. Magerle, "Phase behavior in thin films of cylinder-forming block copolymers," *Physical Review Letters*, vol. 89, no. 3, p. 035501, 2002.

[30] K. W. Gotrik and C. Ross, "Solvothermal annealing of block copolymer thin films," *Nano letters*, vol. 13, no. 11, pp. 5117–5122, 2013.

[31] V. Pryamitsyn and V. Ganesan, "Strong segregation theory of block copolymer-nanoparticle composites," *Macromolecules*, vol. 39, no. 24, pp. 8499–8510, 2006.

[32] M. Colombo, S. Carregal-Romero, M. F. Casula, L. Gutiérrez, M. P. Morales, I. B. Böhm, J. T. Heverhagen, D. Prosperi, and W. J. Parak, "Biological applications of magnetic nanoparticles," *Chemical Society Reviews*, vol. 41, no. 11, pp. 4306–4334, 2012.

[33] F. Ozel and H. Kockar, "Growth and characterizations of magnetic nanoparticles under hydrothermal conditions: Reaction time and temperature," *Journal of Magnetism and Magnetic Materials*, vol. 373, pp. 213–216, 2015.

[34] L. Fu, X. Liu, Y. Zhang, V. P. Dravid, and C. A. Mirkin, "Nanopatterning of "hard" magnetic nanostructures via dip-pen nanolithography and a sol-based ink," *Nano Letters*, vol. 3, no. 6, pp. 757–760, 2003.

[35] L. A. Trusov, A. V. Vasiliev, M. R. Lukatskaya, D. D. Zaytsev, M. Jansen, and P. E. Kazin, "Stable colloidal solutions of strontium hexaferrite hard magnetic nanoparticles," *Chemical Communications*, vol. 50, no. 93, pp. 14581–14584, 2014.

[36] F. S. Bates and G. H. Fredrickson, "Block copolymer thermodynamics: theory and experiment," *Annual review of physical chemistry*, vol. 41, no. 1, pp. 525–557, 1990.

[37] M. L. Huggins, "Thermodynamic properties of solutions of long-chain compounds," *Annals of the New York Academy of Sciences*, vol. 43, no. 1, pp. 1–32, 1942.

[38] P. J. Flory, "Thermodynamics of high polymer solutions," *The Journal of chemical physics*, vol. 10, no. 1, pp. 51–61, 1942.

[39] M. W. Matsen and F. S. Bates, "Unifying weak-and strong-segregation block copolymer theories," *Macromolecules*, vol. 29, no. 4, pp. 1091–1098, 1996.

[40] J. M. Swann and P. D. Topham, "Design and application of nanoscale actuators using block-copolymers," *Polymers*, vol. 2, no. 4, pp. 454–469, 2010.

[41] E. W. Cochran, C. J. Garcia-Cervera, and G. H. Fredrickson, "Stability of the gyroid phase in diblock copolymers at strong segregation," *Macromolecules*, vol. 39, no. 7, pp. 2449–2451, 2006.

[42] S. Xia, *Investigation of nanostructured magnetic thin polymer films.* PhD thesis, Technische Universität München, München, Germany, 2019.

[43] T. P. Russell, G. Coulon, V. Deline, and D. Miller, "Characteristics of the surface-induced orientation for symmetric diblock PS/PMMA copolymers," *Macromolecules*, vol. 22, no. 12, pp. 4600–4606, 1989.

[44] E. Han, K. O. Stuen, M. Leolukman, C.-C. Liu, P. F. Nealey, and P. Gopalan, "Perpendicular orientation of domains in cylinder-forming block copolymer thick films by controlled interfacial interactions," *Macromolecules*, vol. 42, no. 13, pp. 4896–4901, 2009.

[45] C. Shin, H. Ahn, E. Kim, D. Y. Ryu, J. Huh, K.-W. Kim, and T. P. Russell, "Transition behavior of block copolymer thin films on preferential surfaces," *Macromolecules*, vol. 41, no. 23, pp. 9140–9145, 2008.

[46] S. Park, Y. Kim, W. Lee, S.-M. Hur, and D. Y. Ryu, "Gyroid structures in solvent annealed PS-*b*-PMMA films: controlled orientation by substrate interactions," *Macromolecules*, vol. 50, no. 13, pp. 5033–5041, 2017.

[47] R. A. Segalman, A. Hexemer, R. C. Hayward, and E. J. Kramer, "Ordering and melting of block copolymer spherical domains in 2 and 3 dimensions," *Macromolecules*, vol. 36, no. 9, pp. 3272–3288, 2003.

[48] G. E. Stein, E. J. Kramer, X. Li, and J. Wang, "Layering transitions in thin films of spherical-domain block copolymers," *Macromolecules*, vol. 40, no. 7, pp. 2453–2460, 2007.

[49] W. Li, C. Duan, and A.-C. Shi, "Nonclassical spherical packing phases self-assembled from ab-type block copolymers," 2017.

[50] C. Tang, J. Bang, G. E. Stein, G. H. Fredrickson, C. J. Hawker, E. J. Kramer, M. Sprung, and J. Wang, "Square packing and structural arrangement of abc triblock copolymer spheres in thin films," *Macromolecules*, vol. 41, no. 12, pp. 4328–4339, 2008.

[51] K. Kim, S. Park, Y. Kim, J. Bang, C. Park, and D. Y. Ryu, "Optimized solvent vapor annealing for long-range perpendicular lamellae in PS-*b*-PMMA films," *Macromolecules*, vol. 49, no. 5, pp. 1722–1730, 2016.

[52] C. Jin, B. C. Olsen, E. J. Luber, and J. M. Buriak, "Nanopatterning via solvent vapor annealing of block copolymer thin films," *Chemistry of Materials*, vol. 29, no. 1, pp. 176–188, 2017.

[53] W. I. Park, Y. Kim, J. W. Jeong, K. Kim, J.-K. Yoo, Y. H. Hur, J. M. Kim, E. L. Thomas, A. Alexander-Katz, and Y. S. Jung, "Host-guest self-assembly in block copolymer blends," *Scientific reports*, vol. 3, no. 1, pp. 1–10, 2013.

[54] X. Wei, W. Gu, W. Chen, X. Shen, F. Liu, J. W. Strzalka, Z. Jiang, and T. P. Russell, "Disorder-to-order transitions induced by alkyne/azide click chemistry in diblock copolymer thin films," *Soft Matter*, vol. 8, no. 19, pp. 5273–5282, 2012.

[55] W. Li and M. Müller, "Defects in the self-assembly of block copolymers and their relevance for directed self-assembly," *Annual review of chemical and biomolecular engineering*, vol. 6, pp. 187–216, 2015.

[56] S. H. Kim, M. J. Misner, and T. P. Russell, "Controlling orientation and order in block copolymer thin films," *Advanced Materials*, vol. 20, no. 24, pp. 4851–4856, 2008.

[57] D. Walton, G. Kellogg, A. Mayes, P. Lambooy, and T. Russell, "A free energy model for confined diblock copolymers," *Macromolecules*, vol. 27, no. 21, pp. 6225–6228, 1994.

[58] M. J. Fasolka, P. Banerjee, A. M. Mayes, G. Pickett, and A. C. Balazs, "Morphology of ultrathin supported diblock copolymer films: Theory and experiment," *Macromolecules*, vol. 33, no. 15, pp. 5702–5712, 2000.

[59] T. L. Morkved and H. M. Jaeger, "Thickness-induced morphology changes in lamellar diblock copolymer ultrathin films," *Europhysics Letters*, vol. 40, no. 6, p. 643, 1997.

[60] T. Russell, A. Menelle, S. Anastasiadis, S. Satija, and C. Majkrzak, "Unconventional morphologies of symmetric, diblock copolymers due to film thickness constraints," *Macromolecules*, vol. 24, no. 23, pp. 6263–6269, 1991.

[61] G. Coulon, T. Russell, V. Deline, and P. Green, "Surface-induced orientation of symmetric, diblock copolymers: a secondary ion mass-spectrometry study," *Macromolecules*, vol. 22, no. 6, pp. 2581–2589, 1989.

[62] G. Coulon, D. Ausserre, and T. Russell, "Interference microscopy on thin diblock copolymer films," *Journal de physique*, vol. 51, no. 8, pp. 777–786, 1990.

[63] W. H. Tang, "Confinement of symmetric diblock copolymer thin films," *Macromolecules*, vol. 33, no. 4, pp. 1370–1384, 2000.

[64] J.-U. Sommer, A. Hoffmann, and A. Blumen, "Block copolymer films between neutral walls: A monte carlo study," *The Journal of chemical physics*, vol. 111, no. 8, pp. 3728–3732, 1999.

[65] P. Müller-Buschbaum, E. Bauer, O. Wunnicke, and M. Stamm, "The control of thin film morphology by the interplay of dewetting, phase separation and microphase separation," *Journal of Physics: Condensed Matter*, vol. 17, no. 9, p. S363, 2005.

[66] S. Ham, C. Shin, E. Kim, D. Y. Ryu, U. Jeong, T. P. Russell, and C. J. Hawker, "Microdomain orientation of PS-*b*-PMMA by controlled interfacial interactions," *Macromolecules*, vol. 41, no. 17, pp. 6431–6437, 2008.

[67] G. Stein, E. W. Cochran, K. Katsov, G. Fredrickson, E. Kramer, X. Li, and J. Wang, "Symmetry breaking of in-plane order in confined copolymer mesophases," *Physical review letters*, vol. 98, no. 15, p. 158302, 2007.

[68] M.-S. She, T.-Y. Lo, and R.-M. Ho, "Long-range ordering of block copolymer cylinders driven by combining thermal annealing and substrate functionalization," *ACS nano*, vol. 7, no. 3, pp. 2000–2011, 2013.

[69] C. M. Bates, M. J. Maher, D. W. Janes, C. J. Ellison, and C. G. Willson, "Block copolymer lithography," *Macromolecules*, vol. 47, no. 1, pp. 2–12, 2014.

[70] X. Gu, I. Gunkel, A. Hexemer, and T. P. Russell, "Controlling domain spacing and grain size in cylindrical block copolymer thin films by means of thermal and solvent vapor annealing," *Macromolecules*, vol. 49, no. 9, pp. 3373–3381, 2016.

[71] T. Seshimo, R. Maeda, R. Odashima, Y. Takenaka, D. Kawana, K. Ohmori, and T. Hayakawa, "Perpendicularly oriented sub-10-nm block copolymer lamellae by atmospheric thermal annealing for one minute," *Scientific reports*, vol. 6, no. 1, pp. 1–8, 2016.

[72] J. N. Albert, T. D. Bogart, R. L. Lewis, K. L. Beers, M. J. Fasolka, J. B. Hutchison, B. D. Vogt, and T. H. Epps III, "Gradient solvent vapor annealing of block copolymer thin films using a microfluidic mixing device," *Nano letters*, vol. 11, no. 3, pp. 1351–1357, 2011.

[73] K. W. Gotrik, A. F. Hannon, J. G. Son, B. Keller, A. Alexander-Katz, and C. A. Ross, "Morphology control in block copolymer films using mixed solvent vapors," *ACS nano*, vol. 6, no. 9, pp. 8052–8059, 2012.

[74] C. Sinturel, M. Vayer, M. Morris, and M. A. Hillmyer, "Solvent vapor annealing of block polymer thin films," *Macromolecules*, vol. 46, no. 14, pp. 5399–5415, 2013.

[75] W. Bai, K. Yager, and C. Ross, "In situ characterization of the self-assembly of a polystyrene–polydimethylsiloxane block copolymer during solvent vapor annealing," *Macromolecules*, vol. 48, no. 23, pp. 8574–8584, 2015.

[76] Y. Xuan, J. Peng, L. Cui, H. Wang, B. Li, and Y. Han, "Morphology development of ultrathin symmetric diblock copolymer film via solvent vapor treatment," *Macromolecules*, vol. 37, no. 19, pp. 7301–7307, 2004.

[77] J. N. Albert and T. H. Epps III, "Self-assembly of block copolymer thin films," *Materials Today*, vol. 13, no. 6, pp. 24–33, 2010.

[78] Z. Di, D. Posselt, D.-M. Smilgies, and C. M. Papadakis, "Structural rearrangements in a lamellar diblock copolymer thin film during treatment with saturated solvent vapor," *Macromolecules*, vol. 43, no. 1, pp. 418–427, 2010.

[79] G. Kim and M. Libera, "Morphological development in solvent-cast Polystyrene-Polybutadiene-Polystyrene (SBS) triblock copolymer thin films," *Macromolecules*, vol. 31, no. 8, pp. 2569–2577, 1998.

[80] K. Fukunaga, H. Elbs, R. Magerle, and G. Krausch, "Large-scale alignment of abc block copolymer microdomains via solvent vapor treatment," *Macromolecules*, vol. 33, no. 3, pp. 947–953, 2000.

[81] H. Elbs, C. Drummer, V. Abetz, and G. Krausch, "Thin film morphologies of abc triblock copolymers prepared from solution," *Macromolecules*, vol. 35, no. 14, pp. 5570–5577, 2002.

[82] J. Hao, Z. Wang, Z. Wang, Y. Yin, R. Jiang, B. Li, and Q. Wang, "Self-assembly in block copolymer thin films upon solvent evaporation: a simulation study," *Macromolecules*, vol. 50, no. 11, pp. 4384–4396, 2017.

[83] A. Jain and U. Wiesner, "Silica-type mesostructures from block copolymer phases: formation mechanism and generalization to the dense nanoparticle regime," *Macromolecules*, vol. 37, no. 15, pp. 5665–5670, 2004.

[84] A. C. Balazs, T. Emrick, and T. P. Russell, "Nanoparticle polymer composites: where two small worlds meet," *Science*, vol. 314, no. 5802, pp. 1107–1110, 2006.

[85] T. N. Hoheisel, K. Hur, and U. B. Wiesner, "Block copolymer-nanoparticle hybrid self-assembly," *Progress in Polymer Science*, vol. 40, pp. 3–32, 2015.

[86] W. Cao, S. Xia, M. Appold, N. Saxena, L. Bießmann, S. Grott, N. Li, M. Gallei, S. Bernstorff, and P. Müller-Buschbaum, "Self-assembly in ultrahigh molecular weight sphere-forming diblock copolymer thin films under strong confinement," *Scientific reports*, vol. 9, no. 1, pp. 1–9, 2019.

[87] W. Cao, S. Xia, X. Jiang, M. Appold, M. Opel, M. Plank, R. Schaffrinna, L. P. Kreuzer, S. Yin, M. Gallei, M. Schwartzkopf, S. V. Roth, and P. Müller-Buschbaum, "Self-assembly of large magnetic nanoparticles in ultrahigh molecular weight linear diblock copolymer films," *ACS applied materials & interfaces*, vol. 12, no. 6, pp. 7557–7564, 2020.

[88] E. Kim, H. Ahn, S. Park, H. Lee, M. Lee, S. Lee, T. Kim, E.-A. Kwak, J. H. Lee, X. Lei, J. Huh, J. Bang, B. Lee, and D. Y. Ryu, "Directed assembly of high molecular weight block copolymers: highly ordered line patterns of perpendicularly oriented lamellae with large periods," *ACS nano*, vol. 7, no. 3, pp. 1952–1960, 2013.

[89] M. Appold, E. Grune, H. Frey, and M. Gallei, "One-step anionic copolymerization enables formation of linear ultrahigh-molecular-weight block copolymer films featuring vivid structural colors in the bulk state," *ACS applied materials & interfaces*, vol. 10, no. 21, pp. 18202–18212, 2018.

[90] B. Sohn and R. Cohen, "Processible optically transparent block copolymer films containing superparamagnetic iron oxide nanoclusters," *Chemistry of materials*, vol. 9, no. 1, pp. 264–269, 1997.

[91] A.-H. Lu, E. e. Salabas, and F. Schüth, "Magnetic nanoparticles: synthesis, protection, functionalization, and application," *Angewandte Chemie International Edition*, vol. 46, no. 8, pp. 1222–1244, 2007.

[92] W. Wu, Z. Wu, T. Yu, C. Jiang, and W.-S. Kim, "Recent progress on magnetic iron oxide nanoparticles: synthesis, surface functional strategies and biomedical applications," *Science and technology of advanced materials*, 2015.

[93] A. Akbarzadeh, M. Samiei, and S. Davaran, "Magnetic nanoparticles: preparation, physical properties, and applications in biomedicine," *Nanoscale research letters*, vol. 7, no. 1, pp. 1–13, 2012.

[94] D. L. Leslie-Pelecky and R. D. Rieke, "Magnetic properties of nanostructured materials," *Chemistry of materials*, vol. 8, no. 8, pp. 1770–1783, 1996.

[95] L. Wu, A. Mendoza-Garcia, Q. Li, and S. Sun, "Organic phase syntheses of magnetic nanoparticles and their applications," *Chemical reviews*, vol. 116, no. 18, pp. 10473–10512, 2016.

[96] C. Bean and I. Jacobs, "Magnetic granulometry and super-paramagnetism," *Journal of applied Physics*, vol. 27, no. 12, pp. 1448–1452, 1956.

[97] S. Bedanta and W. Kleemann, "Supermagnetism," *Journal of Physics D: Applied Physics*, vol. 42, no. 1, p. 013001, 2008.

[98] L. Néel, "Thermoremanent magnetization of fine powders," *Reviews of Modern Physics*, vol. 25, no. 1, p. 293, 1953.

[99] S. Xia, E. Metwalli, M. Opel, P. A. Staniec, E. M. Herzig, and P. Müller-Buschbaum, "Printed thin magnetic films based on diblock copolymer and magnetic nanoparticles," *ACS applied materials & interfaces*, vol. 10, no. 3, pp. 2982–2991, 2018.

[100] S. Bedanta, *Supermagnetism in magnetic nanoparticle systems*. PhD thesis, 2006.

[101] S. Evershed, "Permanent magnets in theory and practice," *Journal of the Institution of Electrical Engineers*, vol. 58, no. 295, pp. 780–825, 1920.

[102] T. Thomson, "Magnetic properties of metallic thin films," *Metallic Films for Electronic, Optical and Magnetic Applications*, pp. 454–546, 2014.

[103] S. Sun, "Recent advances in chemical synthesis, self-assembly, and applications of fept nanoparticles," *Advanced Materials*, vol. 18, no. 4, pp. 393–403, 2006.

[104] O. Gutfleisch, J. Lyubina, K.-H. Müller, and L. Schultz, "Fept hard magnets," *Advanced Engineering Materials*, vol. 7, no. 4, pp. 208–212, 2005.

[105] D. E. Laughlin, K. Srinivasan, M. Tanase, and L. Wang, "Crystallographic aspects of L10 magnetic materials," *Scripta Materialia*, vol. 53, no. 4, pp. 383–388, 2005.

[106] T. Burkert, O. Eriksson, S. I. Simak, A. V. Ruban, B. Sanyal, L. Nordström, and J. M. Wills, "Magnetic anisotropy of L10 FePt and Fe1-x Mnx Pt," *Physical Review B*, vol. 71, no. 13, p. 134411, 2005.

[107] J. Kim, C. Rong, J. P. Liu, and S. Sun, "Dispersible ferromagnetic FePt nanoparticles," *Advanced Materials*, vol. 21, no. 8, pp. 906–909, 2009.

[108] S. Sun, C. B. Murray, D. Weller, L. Folks, and A. Moser, "Monodisperse FePt nanoparticles and ferromagnetic FePt nanocrystal superlattices," *science*, vol. 287, no. 5460, pp. 1989–1992, 2000.

[109] M. Chen, J. Liu, and S. Sun, "One-step synthesis of FePt nanoparticles with tunable size," *Journal of the American Chemical Society*, vol. 126, no. 27, pp. 8394–8395, 2004.

[110] Q. Li, L. Wu, G. Wu, D. Su, H. Lv, S. Zhang, W. Zhu, A. Casimir, H. Zhu, A. Mendoza-Garcia, and S. Sun, "New approach to fully ordered fct-FePt nanoparticles for much enhanced electrocatalysis in acid," *Nano letters*, vol. 15, no. 4, pp. 2468–2473, 2015.

[111] S. Sun, H. Zeng, D. B. Robinson, S. Raoux, P. M. Rice, S. X. Wang, and G. Li, "Monodisperse MFe_2O_4 (M= Fe, Co, Mn) nanoparticles," *Journal of the American Chemical Society*, vol. 126, no. 1, pp. 273–279, 2004.

[112] E. Kang, J. Park, Y. Hwang, M. Kang, J.-G. Park, and T. Hyeon, "Direct synthesis of highly crystalline and monodisperse manganese ferrite nanocrystals," *The Journal of Physical Chemistry B*, vol. 108, no. 37, pp. 13932–13935, 2004.

[113] M.-H. Phan, J. Alonso, H. Khurshid, P. Lampen-Kelley, S. Chandra, K. Stojak Repa, Z. Nemati, R. Das, Ó. Iglesias, and H. Srikanth, "Exchange bias effects in iron oxide-based nanoparticle systems," *Nanomaterials*, vol. 6, no. 11, p. 221, 2016.

[114] A. Lak, *Synthesis and characterization of magnetic iron oxide nanoparticles*. PhD thesis, 2013.

[115] T. Hyeon, S. S. Lee, J. Park, Y. Chung, and H. B. Na, "Synthesis of highly crystalline and monodisperse maghemite nanocrystallites without a size-selection process," *Journal of the American Chemical Society*, vol. 123, no. 51, pp. 12798–12801, 2001.

[116] T. Hyeon, Y. Chung, J. Park, S. S. Lee, Y.-W. Kim, and B. H. Park, "Synthesis of highly crystalline and monodisperse cobalt ferrite nanocrystals," *The Journal of Physical Chemistry B*, vol. 106, no. 27, pp. 6831–6833, 2002.

[117] J. Park, K. An, Y. Hwang, J.-G. Park, H.-J. Noh, J.-Y. Kim, J.-H. Park, N.-M. Hwang, and T. Hyeon, "Ultra-large-scale syntheses of monodisperse nanocrystals," *Nature materials*, vol. 3, no. 12, pp. 891–895, 2004.

[118] D. Kim, N. Lee, M. Park, B. H. Kim, K. An, and T. Hyeon, "Synthesis of uniform ferrimagnetic magnetite nanocubes," *Journal of the American Chemical Society*, vol. 131, no. 2, pp. 454–455, 2009.

[119] S. E. Kushnir, D. S. Koshkodaev, P. E. Kazin, D. M. Zuev, D. D. Zaytsev, and M. Jansen, "Rapid formation of a monolayer of oriented hard-magnetic strontium hexaferrite nanoparticles on a solid substrate," *Advanced Engineering Materials*, vol. 16, no. 7, pp. 884–888, 2014.

[120] X. Wei, Y. Liu, D. Zhao, X. Mao, W. Jiang, and S. S. Ge, "Net-shaped barium and strontium ferrites by 3D printing with enhanced magnetic performance from milled powders," *Journal of Magnetism and Magnetic Materials*, vol. 493, p. 165664, 2020.

[121] M. Gopal, W. M. Chan, and L. De Jonghe, "Room temperature synthesis of crystalline metal oxides," *Journal of Materials Science*, vol. 32, no. 22, pp. 6001–6008, 1997.

[122] M. Tolan and M. Tolan, *X-ray scattering from soft-matter thin films: materials science and basic research*, vol. 148. Springer, 1999.

[123] A. Duparre, J. Ferre-Borrull, S. Gliech, G. Notni, J. Steinert, and J. M. Bennett, "Surface characterization techniques for determining the root-mean-square roughness and power spectral densities of optical components," *Applied optics*, vol. 41, no. 1, pp. 154–171, 2002.

[124] L. Nevot and P. Croce, "Characterization of surfaces by grazing X-ray reflection: Application to the study of the polishing of various silicate glasses," *Rev. Phys. Appl.*, vol. 15, pp. 761–779, 1980.

[125] H. Kiessig, "Studies on the total reflection of X-rays," *Annals of Physics*, vol. 402, no. 6, pp. 715–768, 1931.

[126] R. Lazzari, "IsGISAXS: a program for grazing-incidence small-angle X-ray scattering analysis of supported islands," *Journal of Applied Crystallography*, vol. 35, no. 4, pp. 406–421, 2002.

[127] V. Holỳ and T. Baumbach, "Nonspecular X-ray reflection from rough multilayers," *Physical Review B*, vol. 49, no. 15, p. 10668, 1994.

[128] S. Sinha, E. Sirota, Garoff, S, and H. Stanley, "X-ray and neutron scattering from rough surfaces," *Physical Review B*, vol. 38, no. 4, p. 2297, 1988.

[129] P. Müller-Buschbaum, "Grazing incidence small-angle X-ray scattering: an advanced scattering technique for the investigation of nanostructured polymer films," *Analytical and bioanalytical chemistry*, vol. 376, no. 1, pp. 3–10, 2003.

[130] R. Hosemann, W. Vogel, D. Weick, and F. Balta-Calleja, "Novel aspects of the real paracrystal," *Acta Crystallographica Section A: Crystal Physics, Diffraction, Theoretical and General Crystallography*, vol. 37, no. 1, pp. 85–91, 1981.

[131] C. M. Palumbiny, *Polymeric PEDOT: PSS electrodes for organic electronics: Understanding the conductivity-structure relation*. PhD thesis, Technische Universität München, München, Germany, 2015.

[132] D. Yang, *Influence of solvent additives on the morphological degradation in polymer-fullerene solar cells*. PhD thesis, Technische Universität München, München, Germany, 2020.

[133] M. D. Abramoff, "ImageJ as an image processing tool and library," *Microscopy and Microanalysis*, vol. 13, no. S02, pp. 1672–1673, 2007.

[134] G. Binnig, C. F. Quate, and C. Gerber, "Atomic force microscope," *Physical review letters*, vol. 56, no. 9, p. 930, 1986.

[135] D. Nečas and P. Klapetek, "Gwyddion: an open-source software for spm data analysis," *Open Physics*, vol. 10, no. 1, pp. 181–188, 2012.

[136] M. W. Fairbairn and S. R. Moheimani, "Control techniques for increasing the scan speed and minimizing image artifacts in tapping-mode atomic force microscopy: Toward video-rate nanoscale imaging," *IEEE Control Systems Magazine*, vol. 33, no. 6, pp. 46–67, 2013.

[137] L. G. Parratt, "Surface studies of solids by total reflection of X-rays," *Physical review*, vol. 95, no. 2, p. 359, 1954.

[138] G. Benecke, W. Wagermaier, C. Li, M. Schwartzkopf, G. Flucke, R. Hoerth, I. Zizak, M. Burghammer, E. Metwalli, P. Müller-Buschbaum, M. Trebbin, S. Förster, O. Paris, S. V Roth, and P. Fratzl, "A customizable software for fast reduction and analysis of large X-ray scattering data sets: applications of the new DPDAK package to small-angle X-ray scattering and grazing-incidence small-angle X-ray scattering," *Journal of applied crystallography*, vol. 47, no. 5, pp. 1797–1803, 2014.

[139] B. D. Josephson, "Possible new effects in superconductive tunnelling," *Physics Letters*, vol. 1, no. 7, pp. 251–253, 1962.

[140] M. Buchner, K. Höfler, B. Henne, V. Ney, and A. Ney, "Tutorial: Basic principles, limits of detection, and pitfalls of highly sensitive squid magnetometry for nanomagnetism and spintronics," *Journal of Applied Physics*, vol. 124, no. 16, p. 161101, 2018.

[141] W. Cao, S. Yin, M. Bitsch, S. Liang, M. Plank, M. Opel, M. A. Scheel, M. Gallei, O. Janka, M. Schwartzkopf, S. V. Roth, and P. Müller-Buschbaum, "In situ study of fept nanoparticles-induced morphology development during printing of magnetic hybrid diblock copolymer films," *Advanced Functional Materials*, p. 2107667, 2021.

[142] F.-K. Su, G.-F. Liau, and J.-L. Hong, "Restraining the aggregation of photoluminescent 1-pyrenecarboxylic acid by hydrogen bonding to poly (methyl methacrylate)," *Journal of Polymer Science Part B: Polymer Physics*, vol. 45, no. 8, pp. 920–929, 2007.

[143] W.-J. Lee, J.-G. Chang, and S.-P. Ju, "Hydrogen-bond structure at the interfaces between water/poly (methyl methacrylate), water/poly (methacrylic acid), and water/poly (2-aminoethylmethacrylamide)," *Langmuir*, vol. 26, no. 15, pp. 12640–12647, 2010.

[144] A. Sehgal, Y. Lalatonne, J.-F. Berret, and M. Morvan, "Precipitation-redispersion of cerium oxide nanoparticles with poly (acrylic acid): toward stable dispersions," *Langmuir*, vol. 21, no. 20, pp. 9359–9364, 2005.

[145] D. Das, E. Cha, S. Lee, H. Shin, and I. Noh, "Effects of molar ratios of two immiscible monomers toward development of an amphiphilic, highly stretchable, bioadhesive, self-healing copolymeric hydrogel and its mineral-active cellular behavior," *Biomacromolecules*, vol. 21, no. 2, pp. 892–902, 2020.

[146] W. Cao, S. Yin, M. Plank, A. Chumakov, M. Opel, W. Chen, L. P. Kreuzer, J. E. Heger, M. Gallei, C. J. Brett, M. Schwartzkopf, A. A. Eliseev, E. O. Anokhin, L. A. Trusov, S. V. Roth, and P. Müller-Buschbaum, "Spray-Deposited Anisotropic Ferromagnetic Hybrid Polymer Films of PS-*b*-PMMA and Strontium Hexaferrite Magnetic Nanoplatelets," *ACS Applied Materials & Interfaces*, 2020.

[147] P. Müller-Buschbaum, N. Hermsdorf, S. Roth, J. Wiedersich, S. Cunis, and R. Gehrke, "Comparative analysis of nanostructured diblock copolymer films," *Spectrochimica Acta Part B: Atomic Spectroscopy*, vol. 59, no. 10-11, pp. 1789–1797, 2004.

[148] L. Wan, R. Ruiz, H. Gao, K. C. Patel, T. R. Albrecht, J. Yin, J. Kim, Y. Cao, and G. Lin, "The limits of lamellae-forming PS-*b*-PMMA block copolymers for lithography," *ACS nano*, vol. 9, no. 7, pp. 7506–7514, 2015.

[149] Y.-S. Sun, C.-T. Wang, and J.-Y. Liou, "Tuning polymer-surface chemistries and interfacial interactions with UV irradiated polystyrene chains to control domain orientations in thin films of PS-*b*-PMMA," *Soft matter*, vol. 12, no. 11, pp. 2923–2931, 2016.

[150] L. Wang, Y. Li, F. Zou, H. Du, L. Sun, J. Zhang, X. Song, and G. Song, "Insight into crystallization process of rubrene by binary solvent mixtures," *RSC advances*, vol. 6, no. 5, pp. 3532–3538, 2016.

[151] C. Lawrence, "The mechanics of spin coating of polymer films," *The Physics of fluids*, vol. 31, no. 10, pp. 2786–2795, 1988.

[152] D. Schubert, "Spin coating as a method for polymer molecular weight determination," *Polymer Bulletin*, vol. 38, no. 2, pp. 177–184, 1997.

[153] D. W. Schubert and T. Dunkel, "Spin coating from a molecular point of view: its concentration regimes, influence of molar mass and distribution," *Materials Research Innovations*, vol. 7, no. 5, pp. 314–321, 2003.

[154] L. Song, W. Wang, V. Körstgens, D. M. González, F. C. Löhrer, C. J. Schaffer, J. Schlipf, K. Peters, T. Bein, D. Fattakhova-Rohlfing, S. V. Roth, and P. Müller-Buschbaum, "In situ study of spray deposited titania photoanodes for scalable fabrication of solid-state dye-sensitized solar cells," *Nano Energy*, vol. 40, pp. 317–326, 2017.

[155] W. Chen, H. Tang, Y. Chen, J. E. Heger, N. Li, L. P. Kreuzer, Y. Xie, D. Li, C. Anthony, Z. Pikramenou, K. W. Ng, X. W. Sun, K. Wang, and P. Müller-Buschbaum, "Spray-deposited pbs colloidal quantum dot solid for near-infrared photodetectors," *Nano Energy*, vol. 78, p. 105254, 2020.

[156] H. Jung, S. Woo, Y. Choe, D. Y. Ryu, J. Huh, and J. Bang, "Single step process for self-assembled block copolymer patterns via in situ annealing during spin-casting," *ACS Macro Letters*, vol. 4, no. 6, pp. 656–660, 2015.

[157] M. A. Chavis, D.-M. Smilgies, U. B. Wiesner, and C. K. Ober, "Widely tunable morphologies in block copolymer thin films through solvent vapor annealing using mixtures of selective solvents," *Advanced functional materials*, vol. 25, no. 20, pp. 3057–3065, 2015.

[158] I. Gunkel, X. Gu, Z. Sun, E. Schaible, A. Hexemer, and T. P. Russell, "An in situ gisaxs study of selective solvent vapor annealing in thin block copolymer films: Symmetry breaking of in-plane sphere order upon deswelling," *Journal of Polymer Science Part B: Polymer Physics*, vol. 54, no. 2, pp. 331–338, 2016.

[159] C. Lai, W. B. Russel, and R. A. Register, "Scaling of domain spacing in concentrated solutions of block copolymers in selective solvents," *Macromolecules*, vol. 35, no. 10, pp. 4044–4049, 2002.

[160] S. H. Kim, M. J. Misner, T. Xu, M. Kimura, and T. P. Russell, "Highly oriented and ordered arrays from block copolymers via solvent evaporation," *Advanced Materials*, vol. 16, no. 3, pp. 226–231, 2004.

[161] C.-C. Chang and C.-T. Lo, "Effect of particles on the structure of solvent-annealed block copolymer/nanoparticle composite thin film," *The Journal of Physical Chemistry B*, vol. 115, no. 11, pp. 2485–2493, 2011.

[162] T. Thurn-Albrecht, J. Schotter, G. Kästle, N. Emley, T. Shibauchi, L. Krusin-Elbaum, K. Guarini, C. Black, M. Tuominen, and T. Russell, "Ultrahigh-density nanowire arrays grown in self-assembled diblock copolymer templates," *Science*, vol. 290, no. 5499, pp. 2126–2129, 2000.

[163] S. Ji, L. Wan, C.-C. Liu, and P. F. Nealey, "Directed self-assembly of block copolymers on chemical patterns: A platform for nanofabrication," *Progress in Polymer Science*, vol. 54, pp. 76–127, 2016.

[164] Y. Yao, E. Metwalli, B. Su, V. Korstgens, D. Mosegui Gonzalez, A. Miasnikova, A. Laschewsky, M. Opel, G. Santoro, S. V. Roth, and P. Müller-Buschbaum, "Arrangement of maghemite nanoparticles via wet chemical self-assembly in PS-*b*-PNIPAM Diblock copolymer films," *ACS applied materials & interfaces*, vol. 7, no. 23, pp. 13080–13091, 2015.

[165] S.-W. Kim, E. Kim, H. Lee, B. C. Berry, H.-C. Kim, and D. Y. Ryu, "Thickness-dependent ordering of perpendicularly oriented lamellae in PS-*b*-PMMA thin films," *Polymer*, vol. 74, pp. 63–69, 2015.

[166] Y. Shao, Z. Guo, H. Li, Y. Su, and X. Wang, "Atomic layer deposition of iron sulfide and its application as a catalyst in the hydrogenation of azobenzenes," *Angewandte Chemie*, vol. 129, no. 12, pp. 3274–3279, 2017.

[167] J. Hahm and S. Sibener, "Time-resolved atomic force microscopy imaging studies of asymmetric PS-*b*-PMMA ultrathin films: Dislocation and disclination transformations, defect mobility, and evolution of nanoscale morphology," *The Journal of Chemical Physics*, vol. 114, no. 10, pp. 4730–4740, 2001.

[168] T. Pietsch, E. Metwalli, S. V. Roth, R. Gebhardt, N. Gindy, P. Müller-Buschbaum, and A. Fahmi, "Directing the self-assembly of mesostructured hybrid materials: Effect of polymer concentration and solvent type," *Macromolecular Chemistry and Physics*, vol. 210, no. 10, pp. 864–878, 2009.

[169] M. Li, I. Katsouras, C. Piliego, G. Glasser, I. Lieberwirth, P. W. Blom, and D. M. de Leeuw, "Controlling the microstructure of poly (vinylidene-fluoride)(PVDF) thin films for microelectronics," *Journal of Materials Chemistry C*, vol. 1, no. 46, pp. 7695–7702, 2013.

[170] M. Shibayama, T. Tanaka, and C. C. Han, "Small angle neutron scattering study on poly (N-isopropyl acrylamide) gels near their volume-phase transition temperature," *The Journal of chemical physics*, vol. 97, no. 9, pp. 6829–6841, 1992.

[171] N. S. Vishnevetskaya, V. Hildebrand, B.-J. Niebuur, I. Grillo, S. K. Filippov, A. Laschewsky, P. Muller-Buschbaum, and C. M. Papadakis, "Aggregation behavior of doubly thermoresponsive polysulfobetaine-*b*-poly (N-isopropylacrylamide) diblock copolymers," *Macromolecules*, vol. 49, no. 17, pp. 6655–6668, 2016.

[172] W. Li, M. Liu, F. Qiu, and A.-C. Shi, "Phase diagram of diblock copolymers confined in thin films," *The Journal of Physical Chemistry B*, vol. 117, no. 17, pp. 5280–5288, 2013.

[173] D. Posselt, J. Zhang, D.-M. Smilgies, A. V. Berezkin, I. I. Potemkin, and C. M. Papadakis, "Restructuring in block copolymer thin films: In situ GISAXS investigations during solvent vapor annealing," *Progress in polymer science*, vol. 66, pp. 80–115, 2017.

[174] Y. Tsori, E. Sivaniah, D. Andelman, and T. Hashimoto, "Orientational transitions in symmetric diblock copolymers on rough surfaces," *Macromolecules*, vol. 38, no. 16, pp. 7193–7196, 2005.

[175] M. Konefał, P. Cernoch, V. Patsula, E. Pavlova, J. Dybal, K. Załeski, and A. Zhigunov, "Enhanced ordering of block copolymer thin films upon addition of magnetic nanoparticles," *ACS Applied Materials & Interfaces*, vol. 13, no. 7, pp. 9195–9205, 2021.

[176] M. R. Hammond, H. Dietsch, O. Pravaz, and P. Schurtenberger, "Mutual alignment of block copolymer-magnetic nanoparticle composites in a magnetic field," *Macromolecules*, vol. 43, no. 20, pp. 8340–8343, 2010.

[177] S. Xia, L. Song, W. Chen, V. Korstgens, M. Opel, M. Schwartzkopf, S. V. Roth, and P. Muller-Buschbaum, "Printed thin diblock copolymer films with dense magnetic nanostructure," *ACS applied materials & interfaces*, vol. 11, no. 24, pp. 21935–21945, 2019.

[178] Y. Yao, E. Metwalli, M. Opel, M. Haese, J.-F. Moulin, K. Rodewald, B. Rieger, and P. Müller-Buschbaum, "Lamellar diblock copolymer films with embedded maghemite nanoparticles," *Advanced Materials Interfaces*, vol. 3, no. 8, p. 1500712, 2016.

[179] F. Liu, S. Ferdous, E. Schaible, A. Hexemer, M. Church, X. Ding, C. Wang, and T. P. Russell, "Fast printing and in situ morphology observation of organic photovoltaics using slot-die coating," *Advanced materials*, vol. 27, no. 5, pp. 886–891, 2015.

[180] S. Chung, K. Cho, and T. Lee, "Thin-film transistors: Recent progress in inkjet-printed thin-film transistors," *Advanced Science*, vol. 6, no. 6, p. 1970031, 2019.

[181] S. Pröller, F. Liu, C. Zhu, C. Wang, T. P. Russell, A. Hexemer, P. Müller-Buschbaum, and E. M. Herzig, "Following the morphology formation in situ in printed active layers for organic solar cells," *Advanced Energy Materials*, vol. 6, no. 1, p. 1501580, 2016.

[182] L. Zhu, W. Zhong, C. Qiu, B. Lyu, Z. Zhou, M. Zhang, J. Song, J. Xu, J. Wang, J. Ali, W. Feng, Z. Shi, X. Gu, L. Ying, Y. Zhang, and F. Liu, "Aggregation-induced multilength scaled morphology enabling 11.76% efficiency in all-polymer solar cells using printing fabrication," *Advanced Materials*, vol. 31, no. 41, p. 1902899, 2019.

[183] D. S. Marques, R. M. Dorin, U. Wiesner, D.-M. Smilgies, A. R. Behzad, U. Vainio, K.-V. Peinemann, and S. P. Nunes, "Time-resolved GISAXS and cryo-microscopy characterization of block copolymer membrane formation," *Polymer*, vol. 55, no. 6, pp. 1327–1332, 2014.

[184] Y. Gu, R. M. Dorin, K. W. Tan, D.-M. Smilgies, and U. Wiesner, "In situ study of evaporation-induced surface structure evolution in asymmetric triblock terpolymer membranes," *Macromolecules*, vol. 49, no. 11, pp. 4195–4201, 2016.

[185] W. Chen, H. Tang, N. Li, M. A. Scheel, Y. Xie, D. Li, V. Körstgens, M. Schwartzkopf, S. V. Roth, K. Wang, X. Sun, and P. Müller-Buschbaum, "Colloidal pbs quantum dot stacking kinetics during deposition via printing," *Nanoscale horizons*, vol. 5, no. 5, pp. 880–885, 2020.

[186] D. Yang, S. Grott, X. Jiang, K. S. Wienhold, M. Schwartzkopf, S. V. Roth, and P. Müller-Buschbaum, "In situ studies of solvent additive effects on the morphology development during printing of bulk heterojunction films for organic solar cells," *Small Methods*, vol. 4, no. 9, p. 2000418, 2020.

[187] S. O. Kim, H. H. Solak, M. P. Stoykovich, N. J. Ferrier, J. J. De Pablo, and P. F. Nealey, "Epitaxial self-assembly of block copolymers on lithographically defined nanopatterned substrates," *Nature*, vol. 424, no. 6947, pp. 411–414, 2003.

[188] K. E. Strawhecker, S. K. Kumar, J. F. Douglas, and A. Karim, "The critical role of solvent evaporation on the roughness of spin-cast polymer films," *Macromolecules*, vol. 34, no. 14, pp. 4669–4672, 2001.

[189] S. Cheng and G. S. Grest, "Dispersing nanoparticles in a polymer film via solvent evaporation," *ACS Macro Letters*, vol. 5, no. 6, pp. 694–698, 2016.

[190] Y. Lin, A. Böker, J. He, K. Sill, H. Xiang, C. Abetz, X. Li, J. Wang, T. Emrick, S. Long, Q. Wang, A. Balazs, and T. P. Russell, "Self-directed self-assembly of nanoparticle/copolymer mixtures," *Nature*, vol. 434, no. 7029, pp. 55–59, 2005.

[191] Y. Luo, D. Montarnal, S. Kim, W. Shi, K. P. Barteau, C. W. Pester, P. D. Hustad, M. D. Christianson, G. H. Fredrickson, E. J. Kramer, and C. J. Hawker, "Poly (dimethylsiloxane-*b*-methyl methacrylate): A promising candidate for sub-10 nm patterning," *Macromolecules*, vol. 48, no. 11, pp. 3422–3430, 2015.

[192] Y. Yoneda, "Anomalous surface reflection of X rays," *Physical review*, vol. 131, no. 5, p. 2010, 1963.

[193] B. Sarkar and P. Alexandridis, "Block copolymer-nanoparticle composites: Structure, functional properties, and processing," *Progress in Polymer Science*, vol. 40, pp. 33–62, 2015.

[194] S. Wu, "Surface and interfacial tensions of polymer melts. II. Poly (methyl methacrylate), poly (n-butyl methacrylate), and polystyrene," *The Journal of Physical Chemistry*, vol. 74, no. 3, pp. 632–638, 1970.

[195] K. Brassat, D. Kool, C. G. Nallet, and J. K. Lindner, "Understanding film thickness-dependent block copolymer self-assembly by controlled polymer dewetting on prepatterned surfaces," *Advanced Materials Interfaces*, vol. 7, no. 1, p. 1901605, 2020.

[196] W. F. Brown Jr, "Thermal fluctuations of a single-domain particle," *Physical review*, vol. 130, no. 5, p. 1677, 1963.

[197] S. Maenosono, T. Suzuki, and S. Saita, "Superparamagnetic FePt nanoparticles as excellent MRI contrast agents," *Journal of Magnetism and Magnetic Materials*, vol. 320, no. 9, pp. L79–L83, 2008.

[198] K. Wiemer, K. Dörmbach, I. Slabu, G. Agrawal, F. Schrader, T. Caumanns, S. Bourone, J. Mayer, J. Steitz, U. Simon, and A. Pich, "Hydrophobic superparamagnetic FePt nanoparticles in hydrophilic poly (N-vinylcaprolactam) microgels: a new multifunctional hybrid system," *Journal of Materials Chemistry B*, vol. 5, no. 6, pp. 1284–1292, 2017.

[199] N. T. Trang, T. T. Thuy, K. Higashimine, D. M. Mott, and S. Maenosono, "Magnetic-plasmonic FePt@Ag core–shell nanoparticles and their magnetic and SERS properties," *Plasmonics*, vol. 8, no. 2, pp. 1177–1184, 2013.

[200] Y. Yao, E. Metwalli, M. A. Niedermeier, M. Opel, C. Lin, J. Ning, J. Perlich, S. V. Roth, and P. Muller-Buschbaum, "Nano-and microstructures of magnetic field-guided maghemite nanoparticles in diblock copolymer films," *ACS applied materials & interfaces*, vol. 6, no. 7, pp. 5244–5254, 2014.

[201] J. Y. Lee, Z. Shou, and A. C. Balazs, "Modeling the self-assembly of copolymer-nanoparticle mixtures confined between solid surfaces," *Physical review letters*, vol. 91, no. 13, p. 136103, 2003.

[202] V. Ganesan, C. J. Ellison, and V. Pryamitsyn, "Mean-field models of structure and dispersion of polymer-nanoparticle mixtures," *Soft Matter*, vol. 6, no. 17, pp. 4010–4025, 2010.

[203] P. De Gennes and P. Pincus, "Pair correlations in a ferromagnetic colloid," *Physik der kondensierten Materie*, vol. 11, no. 3, pp. 189–198, 1970.

[204] K. Butter, P. Bomans, P. Frederik, G. Vroege, and A. Philipse, "Direct observation of dipolar chains in iron ferrofluids by cryogenic electron microscopy," *Nature materials*, vol. 2, no. 2, pp. 88–91, 2003.

[205] G. Renaud, R. Lazzari, and F. Leroy, "Probing surface and interface morphology with grazing incidence small angle X-ray scattering," *Surface Science Reports*, vol. 64, no. 8, pp. 255–380, 2009.

[206] Y. Yu, L. Tauxe, and B. M. Moskowitz, "Temperature dependence of magnetic hysteresis," *Geochemistry, Geophysics, Geosystems*, vol. 5, no. 6, 2004.

[207] I. Jacobs and C. Bean, "An approach to elongated fine-particle magnets," *Physical Review*, vol. 100, no. 4, p. 1060, 1955.

[208] M. Krajewski, W. S. Lin, H. M. Lin, K. Brzozka, S. Lewinska, N. Nedelko, A. Slawska-Waniewska, J. Borysiuk, and D. Wasik, "Structural and magnetic properties of iron nanowires and iron nanoparticles fabricated through a reduction reaction," *Beilstein journal of nanotechnology*, vol. 6, no. 1, pp. 1652–1660, 2015.

[209] M. R. Lukatskaya, L. A. Trusov, A. A. Eliseev, A. V. Lukashin, M. Jansen, P. E. Kazin, and K. S. Napolskii, "Controlled way to prepare quasi-1d nanostructures with complex chemical composition in porous anodic alumina," *Chemical Communications*, vol. 47, no. 8, pp. 2396–2398, 2011.

[210] M. Shuai, A. Klittnick, Y. Shen, G. P. Smith, M. R. Tuchband, C. Zhu, R. G. Petschek, A. Mertelj, D. Lisjak, M. Čopič, J. E. Maclennan, M. A. Glaser, and N. A. Clark, "Spontaneous liquid crystal and ferromagnetic ordering of colloidal magnetic nanoplates," *Nature communications*, vol. 7, no. 1, pp. 1–8, 2016.

[211] N. M. Krook, J. Ford, M. Marechal, P. Rannou, J. S. Meth, C. B. Murray, and R. J. Composto, "Alignment of nanoplates in lamellar diblock copolymer domains and the effect of particle volume fraction on phase behavior," *ACS Macro Letters*, vol. 7, no. 12, pp. 1400–1407, 2018.

[212] N. M. Krook, C. Tabedzki, K. C. Elbert, K. G. Yager, C. B. Murray, R. A. Riggleman, and R. J. Composto, "Experiments and simulations probing local domain bulge and string assembly of aligned nanoplates in a lamellar diblock copolymer," *Macromolecules*, vol. 52, no. 22, pp. 8989–8999, 2019.

[213] N. A. Frey, S. Peng, K. Cheng, and S. Sun, "Magnetic nanoparticles: synthesis, functionalization, and applications in bioimaging and magnetic energy storage," *Chemical Society Reviews*, vol. 38, no. 9, pp. 2532–2542, 2009.

[214] D. Maspoch, D. Ruiz-Molina, K. Wurst, N. Domingo, M. Cavallini, F. Biscarini, J. Tejada, C. Rovira, and J. Veciana, "A nanoporous molecular magnet with reversible solvent-induced mechanical and magnetic properties," *Nature materials*, vol. 2, no. 3, pp. 190–195, 2003.

[215] A. Buffet, A. Rothkirch, R. Döhrmann, V. Körstgens, M. M. Abul Kashem, J. Perlich, G. Herzog, M. Schwartzkopf, R. Gehrke, P. Müller-Buschbaum, and S. V. Roth, "P03, the microfocus and nanofocus X-ray scattering (MiNaXS) beamline of the PETRA III storage ring: the microfocus endstation," *Journal of synchrotron radiation*, vol. 19, no. 4, pp. 647–653, 2012.

[216] P. Zhang, G. Santoro, S. Yu, S. K. Vayalil, S. Bommel, and S. V. Roth, "Manipulating the assembly of spray-deposited nanocolloids: in situ study and monolayer film preparation," *Langmuir*, vol. 32, no. 17, pp. 4251–4258, 2016.

[217] Q. Li, J. He, E. Glogowski, X. Li, J. Wang, T. Emrick, and T. P. Russell, "Responsive assemblies: Gold nanoparticles with mixed ligands in microphase separated block copolymers," *Advanced Materials*, vol. 20, no. 8, pp. 1462–1466, 2008.

[218] P. Jenny, D. Roekaerts, and N. Beishuizen, "Modeling of turbulent dilute spray combustion," *Progress in Energy and Combustion Science*, vol. 38, no. 6, pp. 846–887, 2012.

[219] K. Brassat, D. Kool, J. Bürger, and J. K. Lindner, "Hierarchical nanopores formed by block copolymer lithography on the surfaces of different materials pre-patterned by nanosphere lithography," *Nanoscale*, vol. 10, no. 21, pp. 10005–10017, 2018.

[220] S. Ji, C.-C. Liu, W. Liao, A. L. Fenske, G. S. Craig, and P. F. Nealey, "Domain orientation and grain coarsening in cylinder-forming poly (styrene-*b*-methyl methacrylate) films," *Macromolecules*, vol. 44, no. 11, pp. 4291–4300, 2011.

[221] T. Paik, D.-K. Ko, T. R. Gordon, V. Doan-Nguyen, and C. B. Murray, "Studies of liquid crystalline self-assembly of GdF3 nanoplates by in-plane, out-of-plane SAXS," *ACS nano*, vol. 5, no. 10, pp. 8322–8330, 2011.

[222] R. Zhang, G. Singh, A. Dang, L. Dai, M. R. Bockstaller, B. Akgun, S. Satija, and A. Karim, "Nanoparticle-driven orientation transition and soft-shear alignment in diblock copolymer films via dynamic thermal gradient field," *Macromolecular rapid communications*, vol. 34, no. 20, pp. 1642–1647, 2013.

[223] M. Ganter, J. Kressler, W. Heckmann, N. Higashida, and T. Inoue, "Tem study of block copolymers confined in thin films," *Polymer*, vol. 36, no. 21, pp. 4167–4171, 1995.

[224] K. Brassat and J. K. Lindner, "Nanoscale block copolymer self-assembly and microscale polymer film dewetting: Progress in understanding the role of interfacial energies in the formation of hierarchical nanostructures," *Advanced Materials Interfaces*, vol. 7, no. 5, p. 1901565, 2020.

[225] S. L. Canning, J. M. Ferner, N. M. Mangham, T. J. Wear, S. W. Reynolds, J. Morgan, J. P. A. Fairclough, S. M. King, T. Swift, M. Geoghegan, and S. Rimmer, "Highly-ordered onion micelles made from amphiphilic highly-branched copolymers," *Polymer Chemistry*, vol. 9, no. 47, pp. 5617–5629, 2018.

List of publications

Publications related to the dissertation

- W. Cao, S. Yin, M. Bitsch, S. Liang, M. Plank, M. Opel, M. A. Scheel, M. Gallei, O. Janka, M. Schwartzkopf, S. V. Roth, P. Müller-Buschbaum, "In Situ Study of FePt Nanoparticles-Induced Morphology Development during Printing of Magnetic Hybrid Polymer Films", *Adv. Funct. Mater.*, pp. 2107667, 2021.
- W. Cao, S. Yin, M. Plank, A. Chumakov, M. Opel, W. Chen, L. P. Kreuzer, J. E. Heger, M. Gallei, C. J. Brett, M. Schwartzkopf, A. A. Eliseev, E. O. Anokhin, L. A. Trusov, S. V. Roth, P. Müller-Buschbaum, "Spray-Deposited Anisotropic Ferromagnetic Hybrid Polymer Films of PS-*b*-PMMA and Strontium Hexaferrite Magnetic Nanoplatelets", *ACS Appl. Mater. Interfaces.*, vol. 13, pp. 1592-1602, 2021.
- W. Cao, S. Xia, X. Jiang, M. Appold, M. Opel, M. Plank, R. Schaffrinna, L. P. Kreuzer, S. Yin, M. Gallei, M. Schwartzkopf, S. V. Roth, P. Müller-Buschbaum, "Self-Assembly of Large Magnetic Nanoparticles in Ultrahigh Molecular Weight Linear Diblock Copolymer Films", *ACS Appl. Mater. Interfaces*, vol. 12, pp. 7557–7564, 2020.
- W. Cao, S. Xia, M. Appold, N. Saxena, L. Bießmann, S. Grott, N. Li, M. Gallei, S. Bernstorff, P. Müller-Buschbaum, "Self-Assembly in ultrahigh molecular weight sphere-forming diblock copolymer thin films under strong confinement", *Sci. Rep.*, vol. 9, pp. 18269, 2019.

Further publications

- S. Yin, W. Cao, Q. Ji, Y. Cheng, L. Song, N. Li, C. L. Weindl, M. Schwartzkopf, S.V.Roth, P. Müller-Buschbaum, "Multidimensional Morphology Control for PS-*b*-P4VP Templated Mesoporous Iron (III) Oxide Thin Films", *Adv. Mater. Interfaces*, pp. 2100141, 2021.

- K. Wang, S. Xia, W. Cao, N. Hohn, S. Grott, L. P. Kreuzer, M. Schwartzkopf, S. V. Roth, P. Müller-Buschbaum, "Comparison of UV Irradiation and Sintering on Mesoporous Spongelike ZnO Films Prepared from PS-*b*-P4VP Templated Sol–Gel Synthesis", *ACS Appl. Nano Mater.*, vol. 1, pp. 7139-7148, 2018.
- N. Li, L. Song, N. Hohn, N. Saxena, W. Cao, X. Jiang, P. Müller-Buschbaum, "Nanoscale crystallization of a low band gap polymer in printed titania mesopores", *Nanoscale*, vol. 12, pp. 4085-4093, 2020.
- X. Jiang, H. Kim, P. S. Deimel, W. Chen, W. Cao, D. Yang, S. Yin, R. Schaffrinna, F. Allegretti, J. V. Barth, M. Schwager, H. Tang, K. Wang, M. Schwartzkopf, S. V. Roth, P. Müller-Buschbaum, "Internal nanoscale architecture and charge carrier dynamics of wide bandgap non-fullerene bulk heterojunction active layers in organic solar cells", *J. Mater. Chem. A*, vol. 8, pp. 23628-23636, 2020.
- W. Chen, S. Liang, F. C. Lohrer, S. J. Schaper, N. Li, W. Cao, L. P. Kreuzer, H. Liu, H. Tang, V. Körstgens, M. Schwartzkopf, K. Wang, X. Sun, S. V. Roth, P. Müller-Buschbaum, "In situ Grazing-Incidence Small-Angle X-ray Scattering Observation of Gold Sputter Deposition on a PbS Quantum Dot Solid", *ACS Appl. Mater. Interfaces*, vol. 12, pp. 46942-46952, 2020.
- L. Sun, M. Yang, X. Dong, L. Hu, L. Hu, C. Xie, T. Liu, F. Qin, W. Wang, Y. Jiang, M. Wu, W. Cao, F. A. Larrain, C. Fuentes-Hernandez, K. Meng, B. Kippelen, P. Müller-Buschbaum, Y. Zhou, "Efficient Electrical Doping of Organic Semiconductors Via an Orthogonal Liquid-Liquid Contact", *Adv. Funct. Mater.*, vol. 31, pp. 2009660, 2021.

Scientific reports

- W. Cao, S. Yin, M. Bitsch, M. Plank, M. Gallei, M. Schwartzkopf, S. V. Roth, P. Müller-Buschbaum, "In situ study of morphology development during printing of magnetic hybrid polymer films", *Lehrstuhl für Funktionelle Materialien, Annual Report*, 2020.
- W. Cao, S. Yin, M. Plank, A. Chumakov, C. J. Brett, M. Schwartzkopf, M. Gallei, S. V. Roth, P. Müller-Buschbaum, "In situ study of spray deposited ferromagnetic hybrid films containing PS-*b*-PMMA and strontium hexaferrite magnetic nanoplates", *Lehrstuhl für Funktionelle Materialien, Annual Report*, 2019.

- W. Cao, S. Xia, X. Jiang, M. Appold, M. Opel, M. Gallei, M. Schwartzkopf, S. V. Roth, P. Müller-Buschbaum, "Self-assembly of large iron oxide nanoparticles in ultrahigh molecular weight linear diblock copolymer films", *Lehrstuhl für Funktionelle Materialien, Annual Report*, 2018.
- W. Cao, S. Xia, M. Appold, M. Gallei, P. Müller-Buschbaum, "Thin films of ultrahigh molecular weight diblock copolymers", *Lehrstuhl für Funktionelle Materialien, Annual Report*, 2017.

Conference talks

- W. Cao, F. Jung, L. Bießmann, "AFM/SEM", *E13 Polymer Physics Summer School*, Obertauern (Austria), June 2018.
- W. Cao, S. Xia, P. Müller-Buschbaum, "Well-ordered magnetic thin films with large periods", *3rd Internal Biennial Science Meeting of the MLZ*, Grainau (Germany), June 2017.

Conference poster presentations

- W. Cao, S. Yin, M. Plank, M. Plank, A. Chemezov, M. Opel, M. Gallei, C. J. Brett, M. Schwartzkopf, A. A. Eliseev, L. A. Trusov, S. V. Roth, P. Müller-Buschbaum, "Spray deposited anisotropic magnetic hybrid thin films containing PS-*b*-PMMA and strontium hexaferrite magnetic nanoplatelets", *DPG-Frühjahrstagung*, virtual, March 2021.
- W. Cao, S. Yin, M. Plank, M. Plank, M. Opel, M. Gallei, A. Chemezov, C. J. Brett, M. Schwartzkopf, S. V. Roth, P. Müller-Buschbaum, "Spray deposited anisotropic magnetic hybrid thin films containing PS-*b*-PMMA and strontium hexaferrite magnetic nanoplates", *MLZ User Meeting*, Garching (Germany), December 2020.
- W. Cao, S. Xia, X. Jiang, M. Appold, M. Opel, M. Gallei, M. Schwartzkopf, S. V. Roth, P. Müller-Buschbaum, "Magnetic films based on ultrahigh molecular weight diblock copolymer", *MLZ User Meeting*, Marriott (Germany), December 2019.
- W. Cao, S. Xia, X. Jiang, M. Appold, M. Opel, M. Gallei, M. Schwartzkopf, S. V. Roth, P. Müller-Buschbaum, "Magnetic films based on ultrahigh molecular weight diblock copolymer", *DPG-Frühjahrstagung*, Regensburg (Germany), March 2019.

- W. Cao, S. Xia, M. Appold, N. Saxena, L. Bießmann, S. Grott, M. Gallei, P. Müller-Buschbaum, "Thin films of ultrahigh molecular weight diblock copolymers", *4th German SNI Conference*, Garching (Germany), September 2018.
- W. Cao, S. Xia, M. Appold, M. Gallei, P. Müller-Buschbaum, "Thin films of ultrahigh molecular weight diblock copolymers", *DPG-Frühjahrstagung*, Berlin (Germany), March 2018.
- W. Cao, S. Xia, P. Müller-Buschbaum, "Well-ordered magnetic thin films with large periods", *Kolloid-Tagung "Multiresponsive systems"*, Garching (Germany), October 2017.

Acknowledgments

First of all, I would like to thank my supervisor Prof. Dr. Peter Müller-Buschbaum for giving me the opportunity to work on the PhD project of magnetic hybrid films at his chair. He provided a nice working environment and gave helpful suggestions and guidance throughout my PhD training. Prof. Dr. Peter Müller-Buschbaum is always happy to share his experience and support my scientific research with his solid and vast knowledge. I am extremely grateful for his encouragement and trust that strengthen my self-confidence as a researcher. I also learned a lot from his regarding scientific writing and presentation, owing to his helpful and continuous feedback over the entire course of my PhD. Additionally, he gave me the chance to attend many conferences and beamtimes, from which I made new experiences. It was a pleasure to study under his guidance and many thanks to him again.

Furthermore, I would like to thank my mentor Prof. Dr. Christine M. Papadakis. Many thanks to her for the many friendly discussions, especially about diblock copolymers. I am grateful for the plethora of useful suggestions she gave me. Also, a great thank you to Dr. Senlin Xia, who patiently guided me through the experiments and all of the data processing techniques involved in my studies.

The research could not have been accomplished without the successful synthesis of the UHMW DBCs and magnetic NPs. The UHMW PS-*b*-PMMA and fcc-FePt NPs were provided by the group of Prof. Dr. Markus Gallei (Saarland University). Many thanks to Markus for the discussions, suggestions and help, especially during the preparation and revision of our manuscripts. I would also like to thank Michael Appold and Martina Plank (Technische Universität Darmstadt) for the synthesis of the UHMW PS-*b*-PMMA. Thanks to Martin Bitsch and Oliver Janka (Saarland University) for the synthesis and characterization of the fcc-FePt NPs. Additionlly, the strontium hexaferrite nanoplatelets were provided by Dr. Lev A. Trusov, Artem A. Eliseev and Evgeny O. Anokhin (Moscow State University). A great thanks to them for the discussions and help.

For the success of all the beamtimes, I would like to thank the beamline scientists for their discussion, patience and strong support. Many thanks to Dr. Sigrid Bernstorff (Elettra), Prof. Dr. Stephan V. Roth (DESY), Dr. Matthias Schwartzkopf (DESY) and

Dr. Andrei Chumakov (DESY). Also, the help from E13 colleagues was indispensable. In no specific order, I want to thank Dr. Nitin Saxena, Dr. Lorenz Bießmann, Sebastian Grott, Xinyu Jiang, Shanshan Yin and Tianxiao Xiao. Moreover, special thanks go out to the DESY colleagues, Calvin J. Brett and Marc Gensch, for their help in the in situ spray experiments.

None of the good science would have been successful without the discussions with my E13 colleagues. In no specific order, I want to thank Dr. Volker Körstgens, Dr. Lin Song, Dr. Johannes Schlipf, Dr. Bo Su, Dr. Nitin Saxena, Dr. Lorenz Bießmann, Dr. Senlin Xia, Dr. Kun Wang, Dr. Nuri Hohn, Dr. Dan Yang, Dr. Florian Jung, Dr. Wei Chen, Dr. Kerstin S. Wienhold, Franziska Löhrer, Lucas Kreuzer, Tobias Widmann, Sebastian Grott, Julian Heger, Simon Jakob Schaper, Shambhavi Pratap, Anna-Lena Oechsle, Roy Schaffrinna, Dominik Schwaiger, Lennart Reb, Christina Geiger, Manuel Scheel, Christian Weindl, Nian Li, Xinyu Jiang, Shanshan Yin, Renjun Guo, Suzhe Liang, Tianxiao Xiao, Peixi Wang, Ting Tian, Suo Tu, Yanan Li and Tianfu Guan. I could not have pushed my research forward without their help. Many thanks in particular to Dr. Lin Song and Dr. Florian Jung for the discussion and simulation of GISAXS data, respectively. A great thanks to Shanshan Yin, Xinyu Jiang and Nian Li for the SEM measurements. Besides E13 colleagues, I would like to thank Dr. Matthias Opel from the WMI, who performed the SQUID measurements. He provided strong and friendly support in the field of magnetism. Also many thanks to Prof. Dr. Alexander W. Holleitner (WSI) and Peter Weiser (WSI) for the possibility to carry out SEM and AFM measurements.

I am sincerely grateful to Dr. Volker Körstgens, Dr. Florian Jung, Lucas Kreuzer, Christopher Everett, Julian Heger, Julija Reitenbach, Shanshan Yin, Tianxiao Xiao, Suzhe Liang and Yanan Li for proof reading of the present thesis. All corrections are valuable for the improvement of my thesis.

A big thank to our secretaries Marion Waletzki and Carola Kappauf, who make science work behind-the-scenes. They offered great help to me on issues such as enrollment, reimbursements, visa extension and job contract. Also, many E13 non-scientific activities were organized by them. In addition, thanks to Julian Heger for helping to solve problems that arose due to German translation. Thanks to Dominik Schwaiger and Jia-Jhen Kang for their support on IT issues. Thanks to Dr. Florian Jung, Chia-Hsin Ko, Jia-Jhen Kang, Yanan Li and Bahar Yazdanshenas for their help in ordering experimental reagents.

The China Scholarship Council (CSC) is gratefully acknowledged for funding. Thanks a lot for the financial support from CSC.

Finally, I would like to thank my family. My wife, parents, parents-in-law, sisters and brother have always provided unconditional support to me whenever I in need. I

especially want to thank my fabulous wife Li Qiu for her patience, company and enormous endorsement. Life is colorful and enjoyable because of my family.